UNIVERSITAT DE BARCELONA

Bottom-up Engineering of Thermoelectric Nanomaterials and Devices from Solution-Processed Nanoparticle Building Blocks

Silvia Ortega Torres

Bottom-up Engineering of Thermoelectric Nanomaterials and Devices from Solution-Processed Nanoparticle Building Blocks

Tesi que presenta
Silvia Ortega Torres

per obtar al títol de Doctor per la Universitat de Barcelona

Directors
Prof. Dr. Andreu Cabot and Dr. Maria Ibáñez
Director Industrial
Mr. Germán Noriega
Tutor
Prof. Dr. Blas Garrido

Institut de Recerca en Energia de Catalunya – IREC
CIDETE Ingenieros S.L.
Departament d'Enginyeries: Secció d'Electrònica

Programa de Doctorats Industrials – Generalitat de Catalunya

Contents

Acknowledgements

I start writing these lines knowing that probably are the most important ones of the whole PhD thesis. Not because of the technical or scientific relevance, but because these lines are dedicated to my very important people, to the ones that made this journey a story that deserves to be told. Now is time to summarize and I cannot imagine a better starting than expressing my biggest and sincerest thanks to all those who shared with me every moment of these four years.

The first ones cannot be others than my supervisors, Andreu and Maria, who gave me the opportunity to start these studies some years ago and introduced me the fantastic and exciting world of thermoelectrics. Andreu opened the doors of his group for me and I will always be grateful for this. He is all passion in his job and inevitably this is transferred to the rest of members. He always worried about my career and had the patience to guide me across it and gave me confidence to grow. About Maria, I do not want to lose the opportunity to, like most of the members of the group did when writing these lines before me, say that she was the first one to show me how to do a synthesis. But saying only this would not be enough. She has shared with me more than syntheses, pellets, papers, hours, trips, talks and apps, and has been always close to discuss and help me in whatever matter. Probably she has been the person that has influenced me more within this time, and I want to thank her for that and for being my friend and almost part of my family.

To the company that I belong to, CIDETE Ingenieros S.L., and specially to Germán and his wife Almudena. He trusted in me when I was just a master student and gave me time and space to learn and develop many important skills. Today, thanks to him, I am not only a PhD candidate. He opened a new world to my eyes and I know that I do not want to leave it. Research is fascinating, and many things can and should be done from the flank of a company.

Also thanks to AGAUR and the Industrial Doctorates program of the Catalonia Government, for giving me the opportunity to learn abroad, show my work in first level international conferences and making my PhD easier thanks to the funding.

Of course, I cannot forget the Functional Nanomaterials group, my second family during this time. For all the hours working hard and the funny moments. To the present members (Doris, Marcos, Evgenii, Taisiia, Michaela, Mike and our big and

nicest Chinese community, Liu, Peter, Xiaoting, Junfeng, Yong, and Junshan) and the ones that have belonged to it at some moment during this time, like Zhishan, that left us alone. Thank you all *aaa lot*. I know that some of you will just not be colleagues, but friends for life. Pablo, mi Pablito, for all the talks, laughs and high-fives. The student never beat the teacher. And of course, Doris. Thank you for being my friend in capital letters, all the support and teas. The doors of my new home will be always open for you, no matter the oceans.

To all the scientists and researchers that I met working in the European research projects with CIDETE. From each of them I could learn something important, and made me grow as a professional. Thank you for the complicity in the difficult moments, specially to the ones that became friends: Matteo and Fabrizio. Also, to the IREC family. Maybe we are not the biggest research centre, but for sure we are the best one.

To my friends, the lifelong ones, the ones that never change and were always there in my best and worst moments to celebrate the days with just being together: Elena, Silvia, Luís, Adri and Agus, Laia and Ferdi, Dani and Cris. I am sure they would be happy to know that now, with almost 30 years old, I finished studying. Also to my friends from the years studying Physics at the University, because they made a big contribution for me to arrive here: Edu, Yolanda, Clara, Toni and Marc. We learnt to trust in ourselves.

To my family. My father Emiliano, my mother Isabel and my brother Germán. Vosotros os merecéis el más gigante de todos los gracias que escribo aquí. Por aguantarme y animarme en los malos días y hacer aún mejores los buenos. Todo lo que tengo y todo lo que soy es gracias a vosotros. Sois lo más grande siempre. El mejor de los consejos viene de casa, y, como decía mi amigo Alejandro, nos vamos pa'lante y llegamos hasta el final.

To David, because he makes me happy. Alohomora.

Sant Joan Despí, April 2017.

Preface
Publications and summary of the thesis

The work included in this PhD thesis covers part of the work developed in the period 2013-2017 by the PhD candidate Silvia Ortega Torres at the Catalonia Institute for Energy Research – IREC, in Sant Adrià de Besòs, Barcelona, and the SME CIDETE Ingenieros S.L. in Vilanova i la Geltrú, Barcelona. The research has been performed under the framework of the Industrial Doctorate Program from the Catalonia Government and partially supported by AGAUR (2014 DI-10). These aspects have fostered a research which strongly focuses on technology transfer. In this regard, the project was also admitted into the InnoEnergy PhD School, in order to strength the business and innovation skills of the student.

The research has been focused on the bottom-up engineering and development of thermoelectric nanomaterials from solution-processed nanoparticle building blocks and its application into new and adaptable cost-effective devices with improved efficiency. This dissertation will cover all the aspects from the synthesis and engineering of the nanomaterials to the device manufacturing and integration.

The thesis includes a general introduction as Chapter 0, were the topic and the objectives are presented, and a wrap up final chapters with the main conclusions and future work. The core of the dissertation, chapters from 1 to 4, are built around 6 articles published, accepted or submitted in peer-review journals that are in agreement with the requirements of the Physics doctoral program of the University of Barcelona for a thesis presented as a compilation of publications.

List of publications

Publications included in this thesis

1. Silvia Ortega, Maria Ibáñez, Doris Cadavid and Andreu Cabot. Bottom-up processing of PbTe-PbS thermoelectric nanocomposites. *Int. J. Nanotechnol., 2014, 11, 955-970.*

2. Maria Ibáñez, Rachel J. Korkosz, Zhishan Luo, Pau Riba, Doris Cadavid, Silvia Ortega, Andreu Cabot and Mercouri G. Kanatzidis. Electron doping in bottom-up engineered thermoelectric nanomaterials through HCl-mediated ligand displacement. *J. Am. Chem. Soc., 2015, 137, 4046-4049.*

3. Pedro C. Dias, Doris Cadavid, Silvia Ortega, Alejandro Ruiz, Maria Bernadete M. França, Flavio J. O. Morais, Elnatan C. Ferreira and Andreu Cabot. Autonomous soil moisture sensor based on nanostructured thermosensitive resistors powered by an integrated thermoelectric generator. *Sens. Actuators A, 2016, 239, 1-7.*

4. Maria Ibáñez, Zhishan Luo, Aziz Genç, Laura Piveteau, Silvia Ortega, Doris Cadavid, Oleksandr Dobrozhan, Yu Liu, Maarten Nachtegaal, Mona Zebarjadi, Jordi Arbiol, Maksym V. Kovalenko and Andreu Cabot. High-performance thermoelectric nanocomposites from nanocrystal building blocks. *Nat. Commun., 2016, 7, 10766.*

5. Silvia Ortega, Maria Ibáñez, Yu Liu, Yu Zhang, Maksym V. Kovalenko, Doris Cadavid and Andreu Cabot. Bottom-up engineering of thermoelectric nanomaterials and devices from solution-processed nanoparticle building blocks. *Chem. Soc. Rev., 2017, DOI: 10.1039/c6cs00567e.*

6. Doris Cadavid, Silvia Ortega, Sergio Illera, Yu Liu, Oscar Juan Durá, Maria Ibáñez, Alexey Shavel, Yu Zhang, Antonio M. López, M. A. López de la Torre, Joan Daniel Prades, Germán Noriega, Maksym V. Kovalenko and Andreu Cabot. Influence of the ligand striping on the transport properties of nanoparticle-based PbSe bulk nanomaterials, *ACS Appl. Mater. Interfaces, 2017, Submitted.*

Publications not included in this thesis

1. Maria Ibáñez, Reza Zamani, Stéphane Gorsse, Jiandong Fan, Silvia Ortega, Doris Cadavid, Joan Ramon Morante, Jordi Arbiol and Andreu Cabot. Core-shell nanoparticles as building blocks for the bottom-up production of functional nanocomposites: PbTe-PbS thermoelectric properties. *ACS Nano, 2013, 7, 2573-2586.*

2. Yu Liu, Doris Cadavid, Maria Ibáñez, Jonathan de Roo, Silvia Ortega, Oleksandr Dobrozhan, Maksym V. Kovalenko and Andreu Cabot. Colloidal AgSbSe$_2$ nanocrystals: surface analysis, electronic doping and processing into thermoelectric nanomaterials. *J. Mater. Chem. C, 2016, 4, 4756-4762*.

3. Yu Liu, Doris Cadavid, Maria Ibáñez, Silvia Ortega, Sara Martí-Sánchez, Oleksandr Dobrozhan, Maksym V. Kovalenko, Jordi Arbiol and Andreu Cabot. Thermoelectric properties of semiconductor-metal composites produced by particle blending. *APL Mater., 2016, 4, 104813*.

4. Yu Liu, Gregorio García, Silvia Ortega, Doris Cadavid, Pablo Palacios, Jinyu Lu, Maria Ibáñez, Lili Xi, Jonathan De Roo, Antonio M. López, Sara Martí-Sánchez, Ignasi Cabezas, María de la Mata, Zhishan Luo, Chaochao Dun, Oleksandr Dobrozhan, David L. Carroll, Wenqing Zhang, José Martins, Maksym V. Kovalenko, Jordi Arbiol, Germán Noriega, Jiming Song, Perla Wahnón and Andreu Cabot. Solution-based synthesis and processing of Sn- and Bi-doped Cu$_3$SbSe$_4$ nanocrystals, nanomaterials and ring-shaped thermoelectric generators. *J. Mater. Chem. A, 2017, 5, 2592-2602*.

Summary of results

In the world around us, it is easy to think in different situations in which there are temperature gradients available. These could be converted into a great source of energy if using the proper technology. Thermoelectric devices are environmentally friendly solid-state harvesters able to play this role by converting temperature differences into an electric voltage and vice-versa. These devices, besides being highly reliable since they have no moving parts, if engineered and fabricated in a shape-adaptable manner, are able to fit in countless industrial or domestic applications to improve their efficiency or power low-consumption devices like sensors. If, on top of it, the whole fabrication process is cost-effective and easily scalable, the outcoming thermoelectric devices could potentially reach numerous markets banned to date due to a mix of low efficiencies and high prices of the currently existing solutions.

The first milestone towards cost-effective thermoelectric devices relies on the improvement of the thermoelectric conversion efficiency of the constituents materials. However, such improvement cannot be at all costs. New materials with significant improved performance need to be designed and engineered with relatively low production cost. In this framework, solution-processed techniques are an outstanding alternative for the production of thermoelectric materials and devices. In particular, the bottom-up assembly of colloidal nanoparticles, with controlled size, shape, crystal phase and composition, has no competing technology to precisely design functional metamaterials without the need of a high capital equipment or complex procedures, not only for thermoelectrics, but also for a wide range of applications. Nevertheless, some limitations still need to be overcome to exploit the full potential of solution-processed assembly technologies, and two different challenges should be addressed. The first one is regarding materials efficiency enhancement, and the second one to the device development itself. In this work, we undertake a journey from the material development to the engineering of the final device.

The thesis is structured in 5 chapters, starting from the Chapter 0 or General Introduction. This introductory chapter intends to situate the reader into the broader context of the technology and present the main objectives of the work. Firstly, the current energy paradigm is presented so that the application of thermoelectrics becomes a necessity. Even such devices are already present in

some niche applications, its further development and increase of efficiency turns unavoidable for its definitive market widespread. Some basic concepts over this technology are introduced together with an historical overview and the most significant advances during the years. Especial attention is paid to the challenges to tackle within the production of efficient materials and the difficulty to optimize many tightly interrelated parameters at the same time. Different techniques for the production of these materials are presented, making especial emphasis on their capacity to control materials properties at the nanoscale, and the out-of-the-lab production opportunities. Finally, solution-processed techniques are introduced, and their suitability for the fabrication of engineered nanomaterials at the large scale with high efficiency is presented. The availability of these materials in the form of ink may open the door for a further production of shape-adaptable thermoelectric devices.

Chapter 1 is based on the publication that shares the name with this PhD dissertation: *Bottom-up engineering of thermoelectric nanomaterials and devices from solution-processed nanoparticle building blocks*, accepted for its publication in the journal *Chemical Society Reviews* on 16th April 2017. This chapter presents a general view of the solution-processed route for the development of bottom-up engineered nanoparticle-based thermoelectric nanomaterials and devices. It is an extended and comprehensive text where main concepts, challenges, advantages and opportunities that the technology offers are exposed. Starting from the necessity of materials engineering for the development of efficient thermoelectric nanomaterials, this chapter explores the different steps for the nanoparticles production: from the synthesis of different materials to the purification and surface design, continuing with the assembly routes and material consolidation and paying further attention to the main doping strategies available within the technique and the new ways that it has fostered for the development of new and shape-adaptable solution-processed thermoelectric devices.

Chapter 2 is the most extensive one of this dissertation, since it is built around 3 publications that cover the three different steps of the solution-processed nanomaterials preparation, and how the efficiency can be enhanced within each one. First article is focused on the synthesis stage, and presents the production of core-shell nanoparticles as a way to design nanocomposites. Results are presented in the publication under name *Bottom-up processing of PbTe-PbS thermoelectric nanocomposites*, published in the *International Journal of Nanotechnology* in 2014. The second one is related to the purification step,

showing how, taking advantage of the nanoparticle surface, an HCl-mediated ligand displacement is able to introduce controlled amounts of dopants in the nanoparticle. These results were published in 2015 in the *Journal of the American Chemical Society* with the title *Electron doping in the bottom-up engineered thermoelectric nanomaterials through HCl-mediated ligand displacement*. Last one, published in 2016 in *Nature Communications*, focused on the final assembly phase, in which by properly assembling two different kinds of nanoparticles, a semiconductor and a metal, the efficiency could be greatly enhanced. The title for this third publication is *High-performance thermoelectric nanocomposites from nanoparticle building blocks*.

After showing the different possibilities of the performance optimization for solution processed materials to develop efficient thermoelectric materials, in Chapter 3 a step is made towards the production of a ring-shape device. Taking PbSe as a model material, this chapter presents a whole engineering story from the synthesis of the nanoparticles to the fabrication of the device, passing through the surface engineering step for the enhancement of the materials efficiency. These results have been submitted for their publication in *ACS Applied Materials and Interfaces*. However, considering the especial deadline conditions in the deposit of this thesis, the final acceptance letter has not yet arrived.

The final chapter, Chapter 4, presents the integration of a thermoelectric device together with a nanoparticle-based temperature sensor. This integrated assembly, including an ultra-low-power electronic management, was implemented as an autonomous soil moisture sensor, and shows the great opportunity that both solution-processed techniques and thermoelectrics technology offer for the development of new applications. This work, *Autonomous soil moisture sensor based on nanostructured thermosensitive resistors powered by an integrated thermoelectric generator* was published in *Sensors and Actuators A* in 2016.

Finally, some conclusions over the presented project and future work are listed.

x

Authors' contribution to the publications included

The 6 articles here considered have been produced with the collaboration of different authors and have not been previously presented in any other PhD dissertation. The impact factor of 2015 of each journal is provided and, except one, all of them belong to the first quartile regarding the Science Citation Index, thus being in compliance with the regulations of the Physics doctoral program of the University of Barcelona for a PhD thesis presented as a compilation of publications. The contribution of each author is hereby exposed. Overall, in all the publications, Andreu Cabot and Maria Ibáñez planned, coordinated and strongly participated in the design and writing of all the papers, while the PhD candidate, Silvia Ortega, contributed to the development of the experimental work, data analysis and manuscript writing.

Chapter 1:

1. Silvia Ortega, Maria Ibáñez, Yu Liu, Yu Zhang, Maksym V. Kovalenko, Doris Cadavid and Andreu Cabot. Bottom-up engineering of thermoelectric nanomaterials and devices from solution-processed nanoparticle building blocks. *Chem. Soc. Rev., 2017, DOI: 10.1039/c6cs00567e.*

* Impact factor 2015: 34.09

Silvia Ortega reviewed the existing literature, designed the work and wrote the manuscript. Doris Cadavid and Maksym V. Kovalenko contributed to the literature review and to the manuscript writing. Yu Liu and Yu Zhang contributed to the discussion.

Chapter 2:

2. Silvia Ortega, Maria Ibáñez, Doris Cadavid and Andreu Cabot. Bottom-up processing of PbTe-PbS thermoelectric nanocomposites. *Int. J. Nanotechnol., 2014, 11, 955-970.*

* Impact factor 2015: 0.502

Silvia Ortega designed and developed the experiments and wrote the manuscript. Doris Cadavid participated in the thermoelectric analysis. This

publication does not belong to the first quartile of the Science Citation Index, nevertheless, it is included for the well understanding of the thesis as a whole.

3. Maria Ibáñez, Rachel J. Korkosz, Zhishan Luo, Pau Riba, Doris Cadavid, Silvia Ortega, Andreu Cabot and Mercouri G. Kanatzidis. Electron doping in bottom-up engineered thermoelectric nanomaterials through HCl-mediated ligand displacement. *J. Am. Chem. Soc., 2015, 137, 4046-4049*.

* Impact factor 2015: 13.038

Silvia Ortega contributed to the materials synthesis and thermoelectric characterization and discussion. Rachel J. Korkosz performed the SPS densification of the materials. Zhishan Luo and Pau Riba helped with the materials synthesis. Doris Cadavid contributed during the thermoelectric measurements. Mercouri G. Kanatzidis participated in the manuscript writing and discussion.

4. Maria Ibáñez, Zhishan Luo, Aziz Genç, Laura Piveteau, Silvia Ortega, Doris Cadavid, Oleksandr Dobrozhan, Yu Liu, Maarten Nachtegaal, Mona Zebarjadi, Jordi Arbiol, Maksym V. Kovalenko and Andreu Cabot. High-performance thermoelectric nanocomposites from nanocrystal building blocks. *Nat. Commun., 2016, 7, 10766*.

* Impact factor 2015: 11.329

Silvia Ortega produced the nanocomposites and performed the thermoelectric characterization. Zhishan Luo helped with the synthesis of materials. Doris Cadavid, Oleksandr Dobrozhan and Yu Liu contributed to the thermoelectric characterization. Aziz Genç, Jordi Arbiol, Laura Piveteau and Maarten Nachctegaal performed structural nanocomposite characterization. Mona Zebarjadi performed band alignment calculations. Maksym V. Kovalenko together with Maria Ibáñez and Andreu Cabot planned and supervised the work and had a major input in the writing of the manuscript.

Chapter 3:

5. Doris Cadavid, Silvia Ortega, Sergio Illera, Yu Liu, Oscar Juan Durá, Maria Ibáñez, Alexey Shavel, Yu Zhang, Antonio M. López, M. A. López de la Torre, Joan Daniel Prades, Germán Noriega, Maksym V. Kovalenko and Andreu Cabot. Influence of the ligand striping on the transport properties of nanoparticle-based PbSe bulk nanomaterials, *ACS Appl. Mater. Interfaces, 2017, Submitted*.

* Impact factor 2015: 7.145

Silvia Ortega produced the materials at the large scale, designed and manufacture the device and the test station and planned the experiments and analysis in these regards. Doris Cadavid designed and developed the materials optimization work and its analysis. Silvia Ortega and Doris Cadavid contributed equally to this work and wrote the manuscript together. Sergio Illera and Joan Daniel Prades developed the charge transport model. Yu Liu and Yu Zhang contributed to the materials synthesis. Oscar Juan Durá and M. A. López de la Torre performed the thermal characterization of the materials. Alexey Shavel, Antonio M. López, Germán Noriega and Maksym V. Kovalenko participated in the discussion.

Chapter 4:

6. Pedro C. Dias, Doris Cadavid, Silvia Ortega, Alejandro Ruiz, Maria Bernadete M. França, Flavio J. O. Morais, Elnatan C. Ferreira and Andreu Cabot. Autonomous soil moisture sensor based on nanostructured thermosensitive resistors powered by an integrated thermoelectric generator. *Sens. Actuators A, 2016, 239, 1-7.*

* Impact factor 2015: 2.201

Silvia Ortega produced the nanomaterials, contributed to the integration of the sensor and the thermoelectric device in the experiment and helped with the manuscript writing. Pedro C. Dias designed the work and the circuit, took care of the experiments with the prototype and wrote the manuscript. Doris Cadavid and Alejandro Ruiz participated in the sensor production. Maria Bernadete M. França, Flavio J. O. Morais and Elnatan C. Ferreira contributed to the electronics integration and the discussion of the results.

Prof. Dr. Andreu Cabot and Dr. Maria Ibáñez certify that the information provided over these lines is reliable. In recognition whereof, sign in Barcelona, 21st April 2017.

Prof. Dr. Andreu Cabot

Dr. Maria Ibáñez

Resum de la tesi

Al mon que ens envolta és fàcil pensar en situacions en què hi ha gradients de temperatura disponibles. Aquests, es podrien convertir en fonts d'energia molt interessants mitjançant l'ús adequat de la tecnologia. Els dispositius termoelèctrics son conversors d'estat sòlid capaços de jugar aquest important paper, ja que son capaços de transformar diferències de temperatura en energia elèctrica i vice-versa. A més a més, son altament fidedignes ja que no tenen cap part mòbil i poden ser instal·lats a qualsevol emplaçament si son adaptats a l'aplicació en qüestió, ja sigui a escala domèstica o industrial, per millorar la seva eficiència energètica o, per exemple, alimentar altres dispositius de baix cost com ara sensors. Si, a més a més, el conjunt del procés de fabricació és de baix cost i fàcilment escalable per la seva producció en massa, els dispositius termoelèctrics resultants tindran la possibilitat d'entrar dins de nous mercats, fins ara impossibles degut a una barreja fatal d'alts preus i baixes eficiències dels productes comercials disponibles actualment.

El primer pas cap a la fabricació de mòduls termoelèctrics més efectius en tots els sentits, és la millora de la seva eficiència a través de la recerca de nous o més efectius materials dels quals estan constituïts. Tanmateix, però, aquesta millora no pot ser a qualsevol cost. És necessari que aquests nous materials mantinguin alhora l'eficiència i baix cost en la seva fabricació. En aquest sentit, les tècniques de processat en solució son una gran alternativa per la producció de materials i dispositius termoelèctrics, i, en particular, la utilització de nanopartícules col·loïdals, amb mida, forma, fase i composició controlada. No hi ha cap altra tecnologia que aconsegueixi el seu nivell de control sobre el disseny de materials funcionals sense la necessitat de costosos equipaments o procediments complexes, no només per termoelèctrics sinó per un ampli ventall d'aplicacions. No obstant això, algunes limitacions encara han de ser superades per tal de poder explotar plenament el potencial que les tècniques de processat en solució ofereixen. Els dos majors reptes als quals la tecnologia s'enfronta son: primer, millorar l'eficiència dels materials, i, segon, en el desenvolupament de nous models de dispositius.

Aquest manuscrit inclou una introducció general o Capítol 0, on el tema és introduït dins d'un context més general i els objectius son presentats, i un capítol final amb les principals conclusions extretes de la investigació i les vies de continuació d'aquesta. El pes d'aquesta tesi es troba entre els capítols de 1 i 4.

Estan construïts al voltant de 6 articles publicats, acceptats o enviats per la seva publicació a revistes arbitrades i es troben en consonància amb els requeriments del programa de doctorat en Física de la Universitat de Barcelona per una tesi publicada com a compendi de publicacions.

El Capítol 1 està basat en la publicació que comparteix nom amb aquesta tesi doctoral: *Bottom-up engineering of thermoelectric nanomaterials and devices from solution-processed nanoparticle building blocks*, acceptat per la seva publicació a la revista *Chemical Society Reviews* el 16 d'Abril de 2017. Aquest capítol presenta una visió general de les rutes de processat en solució pel desenvolupament *bottom-up* de nanomaterials i dispositius termoelèctrics basats en nanopartícules. És un text ampli que exposa en profunditat els principals conceptes, reptes, avantatges i oportunitats que aquesta tecnologia ofereix. Començant per la necessitat de produir materials dissenyats específicament per la obtenció de materials termoelèctrics eficients, aquest capítol explora els diferents passos dins la producció de nanopartícules: des de la síntesi de diferents famílies de materials a la purificació i enginyeria de la superfície, continuant amb les possibles rutes per el seu assemblatge i parant especial atenció a les principals estratègies de dopatge disponibles. Finalment, mostrant la porta que aquesta tecnologia ha obert a la fabricació de nous dispositius termoelèctrics adaptables processats en solució.

El Capítol 2 és el més extens d'aquest manuscrit, ja que està construït al voltant de 3 articles ja publicats que tracten sobre la síntesi i enginyeria dels nanomaterials termoelèctrics processats en solució: *Bottom-up processing of PbTe-PbS thermoelectric nanocomposites*, publicat a l'*International Journal of Nanotechnology*, *Electron doping in the bottom-up engineered thermoelectric nanomaterials through HCl-mediated ligand displacement*, publicat al *Journal of the American Chemical Society* i *High-performance thermoelectric nanocomposites from nanocrystal building blocks*, publicat a la revista *Nature Communications*. Aquest capítol vol mostrar les diferents rutes pel disseny dels nanomaterials termoelèctrics, tenint en compte el que prèviament s'havia presentat al Capítol 1. Primer, durant la síntesi, amb la producció de nanopartícules del tipus *core-shell*. Segon, durant el procés de purificació de la superfície, mitjançant un procés de desplaçament dels lligams basat en la utilització de HCl per tal d'introduir quantitats controlades de dopants a les nanopartícules. I tercer, durant el procés d'assemblatge, presentant la formació de nanocompostos mitjançant una determinada mescla de nanopartícules metàl·liques i semiconductores.

Després de mostrar las possibilitats que la tècnica utilitzada durant aquest treball de doctorat té pel desenvolupament de nanomaterials termoelèctrics, al Capítol 3 es fa un pas endavant i es produeix un dispositiu en forma d'anella capaç de recuperar energia de superfícies tubulars com ara tubs d'escapament de vehicles. Prenent el PbSe com a material model, aquest capítol presenta una història completa des de la síntesi de les nanopartícules fins a la fabricació del dispositiu. Aquest resultats han estat enviats per la seva publicació a la revista *ACS Applied Materials and Interfaces*. Desafortunadament, tenint en compte les condicions especials en les dates límit de dipòsit que aquesta tesi ha patit, la carta d'acceptació final no ha arribat a temps.

El capítol final, Capítol 4, presenta la integració d'un dispositiu termoelèctric conjuntament amb un sensor de temperatura basat en nanopartícules. Incloent un circuit electrònic de control de l'energia de baix cost, aquest nou dispositiu va ser dissenyat com un sensor autònom d'humitat del sòl, demostrant així les grans oportunitats que tant les tècniques de processat en solució com els termoelèctrics ofereixen pel desenvolupament de noves i interessants aplicacions. Aquest treball, *Autonomous soil moisture sensor based on nanostructured thermosensitive resistors powered by an integrated thermoelectric generator*, va ser publicat a la revista *Sensors and Actuators A* al 2016.

Els treballs inclosos dins d'aquesta tesi doctoral cobreixen part de la feina desenvolupada durant el període 2013-2017 per la doctoranda Silvia Ortega Torres a l'Institut de Recerca en Energia – IREC, a Sant Adrià de Besòs, Barcelona, i l'empresa CIDETE Ingenieros S.L. a Vilanova i la Geltrú, Barcelona. La recerca es troba englobada dins del programa Doctorats Industrials de la Generalitat de Catalunya i ha estat parcialment finançada per l'AGAUR (2014 DI-10). Aquests han aspectes han fet que la recerca estigui focalitzada cap un procés de transferència de tecnologia.

Chapter 0   General introduction:
Broader context and objectives

The energy challenge, its production and efficient consumption, is one of the greatest issues that our world is currently facing. The European Commission, in its 2020 Energy Strategy,[1] and through the 2012 Energy Efficiency Directive,[2] aims at the 20% improvement in energy efficiency, while achieving a 20% reduction in greenhouse gas emissions and reaching a 20% of renewable EU energy production, but more in detail, pointing towards energy efficiency as the most cost-effective route to reduce emissions and make energy consumption more affordable for consumers. Such situation and the fact that more than the 60% of the produced energy is rejected in the form of heat (Figure 0.1),[3] has been translated into an extensive research over the necessity of efficient thermoelectric devices able to generate electricity from the otherwise wasted heat.

Thermoelectric devices are able to convert temperature gradients into available electrical power; and reversely, when applying an electrical current, a thermal energy gradient is generated, thus permitting their use also for precise and localized temperature control.[4-6] When considering their energy harvesting function, such devices are especially useful in order to improve the overall energy

efficiency of countless industrial and domestic processes. Among them, thermoelectrics are not limited only to high power consumption or production markets, being also considered in the very interesting and day-by-day growing sub-watt or low power generation world (Figure 0.2),[7] i.e. the so-called wearables market or within autonomous remote sensor nodes.
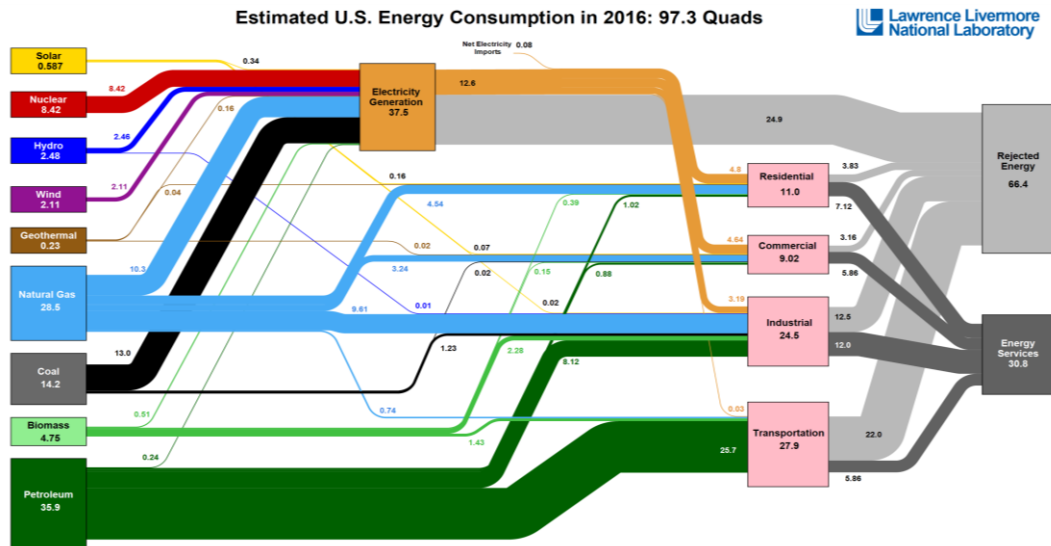

Figure 0.1   United States energy flow chart of the energy consumption in 2016. Lawrence Livermore National Laboratory, published in March 2017.[3]
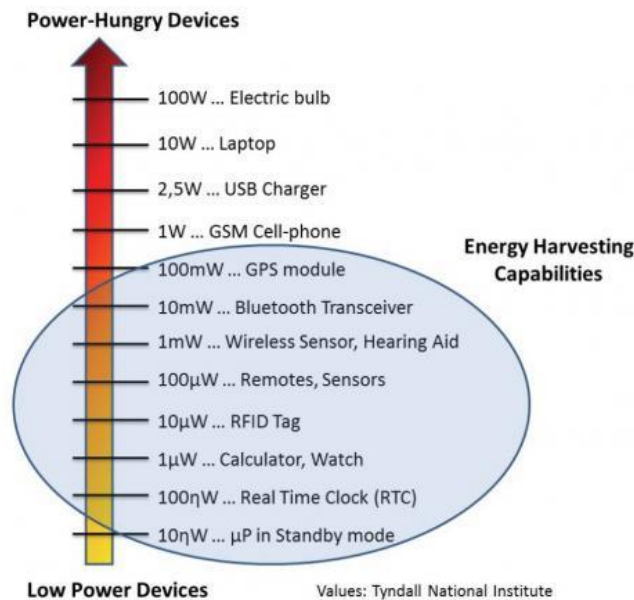

Figure 0.2   Low power thermoelectrics energy harvesting capabilities. "Sub-watt thermoelectric energy harvesting: industry and market analysis" report, Infinergia Consulting, 2014.[7]

Within the different applications in which thermoelectrics are today present, the space one is probably the most well established. Since 1960 NASA has been using radioisotope thermoelectric generators in a variety of missions, where a radioactive source provides the heat that is afterwards converted into electricity by the thermoelectric device. Many well-known missions such as Apollo, Cassini, Voyager or most recently the Curiosity Rover on Mars, include such assemblies.[8] In a similar way, Gentherm is fabricating thermoelectric generators for its installation in remote locations such as natural gas offshore platforms or gas pipe lines. Burning gas to produce heat is enough to power safety lights or for valve control.[9]

A second field in which thermoelectrics are being widely introduced is the automobile industry. Similarly to the behaviour shown in the energy consumption chart, the 40% of the energy produced by a vehicle combustion engine is wasted in the exhaust in the form of heat. Such big percentage could be translated into 900 W of power if the heat is harvested with only a 3% efficiency by the thermoelectric assembly. BMW, General Motors or Ford are some of the producers that already installed this kind of devices in their units. In this field, thermoelectrics have been also used for localized cooling of the, for instance, vehicle seat.[10-12]

Of course, the are other daily-use examples in current thermoelectrics applications. For instance, in Amazon, for 137 €, it is possible to acquire a camp stove able to produce power from fire to recharge the battery of a mobile phone or any other USB-connected device.[13] In this direction too, a recently created Spanish company is working on a device able to produce electrical power from the combustion of biomass systems.[14] Other daily-use examples on cooling applications of thermoelectrics can be found in CMOS sensors and telecommunications optic fibre lasers temperature stabilization, in portable fridges that can be connected to a car power source, or in the biomedical field, devices for temperature control and refrigeration of medical and pharmaceutical products such as insulin.[10, 15]

In the low power regime, the recent and enormous growth of wearable electronics market and autonomous sensors has opened the door for a new paradigm for thermoelectrics applications.[16] While Seiko or Citizen are examples of watches producers with pioneering role in this field,[17] commercial estimations situated the market for wireless sensor networks powered with thermoelectrics to reach 25M $ by 2016.[18] Being able to generate power from the temperature of the human body if attached directly into the skin, or directly form the

environment, these new applications also revealed the necessity for new and shape-adaptable devices.[16, 19-21]

Unfortunately, the quite spread list of applications, is still very far from reaching its full magnitude due to the low efficiencies that thermoelectric devices show, together with the relatively high price of these devices in the market, commonly built with scarce materials produced by energy-intensive procedures, and its difficulty to be adapted to the wide range of required shapes.[22-24]

For the better understanding of such drawbacks and challenges that thermoelectric industry is nowadays facing, at this point it is necessary to make a deeper step into the topic.

0.1 Thermoelectrics technology

0.1.1 Basics of thermoelectric devices

Thermoelectric (TE) converters are solid-state devices that allow the direct and reversible conversion between temperature gradients and electrical power. By this, we talk about the Seebeck effect when producing a voltage from a temperature difference, and, in the other way around, when the TE material or device creates a temperature difference when applying a voltage, the Peltier effect.[4, 25]

One of the main features of these devices is that, having no moving parts, they are hugely reliable and maintenance free. Prove of this quasi-everlasting operation is the TE generator installed on board of the Voyager 1 space probe launched by NASA in 1977. After almost 40 years installed, and having the probe almost escaped from the Solar System, it is still working and allowing the signal transmission. But this is not the only advantage that TE devices present. They are acoustically silent, lightweight, and environmentally friendly since no emission comes from their operation due to their solid-state nature. In addition, as already presented, TE devices are ideal when precise temperature control is required (<0.1 ºC), being able to operate in any orientation.[8, 25]
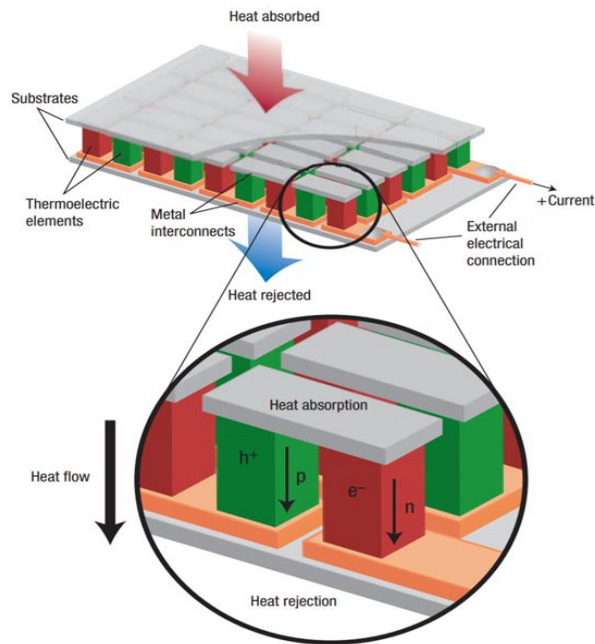
Figure 0.3   Assembly and working principle of a TE module.[26]

TE modules contain a series of n- and p-type semiconductors connected electrically in series and thermally in parallel sandwiched between two electrically insulating and thermally conductive sheets (Figure 0.3), in which the main building block is called TE couple or pair. Multiple pairs are then joined in order to generate a larger voltage. Nevertheless, as previously seen, TE devices can work reversely in Peltier or Seebeck mode (Figure 0.4). When working as a power generator, a temperature difference is stablished across the TE material and the major carriers of each of the TE semiconductor materials move from the hot to the cold side, where usually a heat sink is placed, thus resulting in a net current flow or power output. On the other hand, when working as a cooler, the power comes from an external source, and the heat flow is created by the current flow across the circuit.[27]
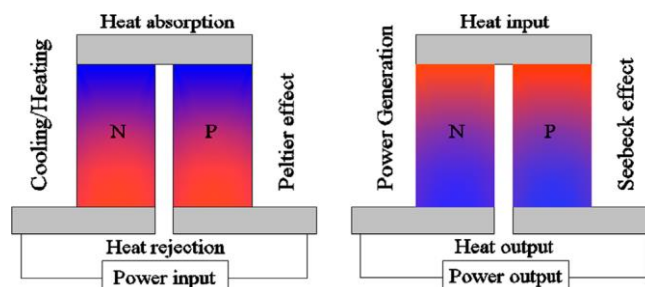
Figure 0.4   Reversible modes of a TE module: Peltier or cooling mode and Seebeck or power generation mode.[12]

Both the efficiency (η) and the coefficient of performance (COP) of a TE device depend solely on the temperature at the cold and hot sides and on an intrinsic material figure of merit usually expressed in its adimensional form (ZT).

$$\eta = \frac{\Delta T}{T_{hot}} \frac{\sqrt{1 + ZT} - 1}{\sqrt{1 + ZT} + \frac{T_{cold}}{T_{hot}}}$$

$$COP = \frac{T_{cold}}{\Delta T} \frac{\sqrt{1 + ZT} - \frac{T_{hot}}{T_{cold}}}{\sqrt{1 + ZT} + 1}$$

$$ZT = \frac{\sigma S^2}{\kappa} T$$

Where ΔT is the difference of temperature between the hot and the cold sides, σ is the electrical conductivity of the material, S is the Seebeck coefficient and κ the thermal conductivity. Thus, being the temperatures established by the application, the larger is the value of the ZT, the larger would be the efficiency of the device. However, even if the efficiency is only limited by the Carnot efficiency, and the ZT can be as high as infinite, the material-dependent parameters are strongly interrelated, as will be introduced in further sections, and this is translated in low values for the ZT.[26]
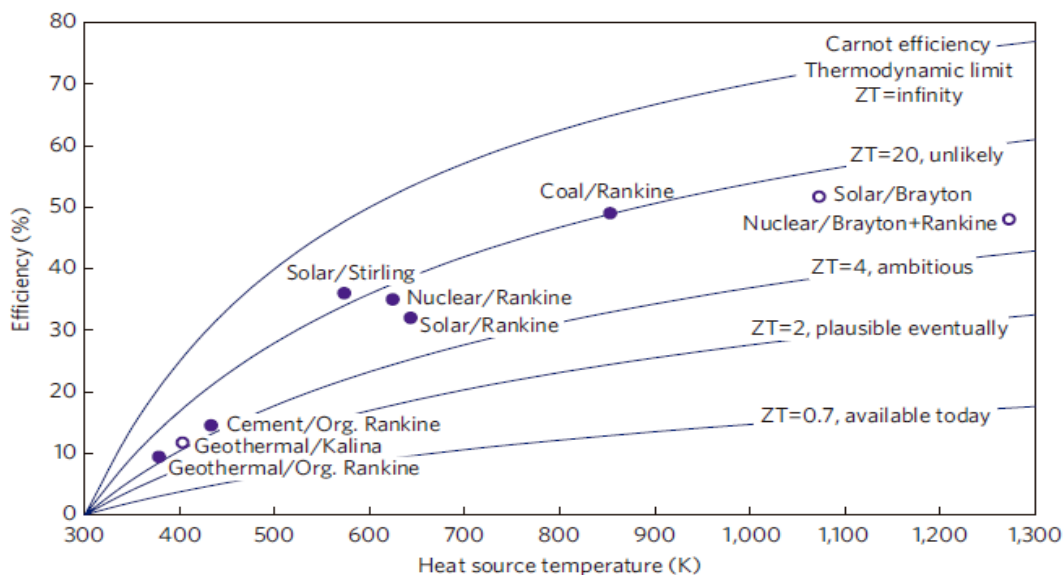
Figure 0.5   Efficiency expressed in % for TE power generators with different values of ZT and comparison with current competing technologies.[24]

Nowadays, at the lab-scale, record high ZT for TE materials is 2.6 for a SnSe single crystal.[28] However, even promising, these results cannot be directly transferred to the market due to the great difficulty that fabricating a single crystal suppose. For commercially available materials ZT values are still around or below the unity. Hence, market available TE devices exhibit an efficiency below 5% (Figure 0.5). An increase in the ZT value is therefore required if this technology wants to compete against other power sources such as geothermal or the well-stablished photovoltaics. Generally speaking, an increase of the value over 2 would change drastically the possible amounts of TE applications.[24, 29] It is because of this situation that TE devices currently mostly find their niche applications into the low power energy-autonomous embedded systems industry, as previously explained.

0.1.2 Historical overview

In the first half of the 19th century the TE effects were discovered, mainly by Thomas Seebeck, Jean Charles A. Peltier and William Thomson. Some years later, at the beginning of the following century, Altenkirch was the first one to identify the ZT relation as the most important parameter for the enhancement of the efficiency of TE devices. The technology, even slowly, was further studied during and after the first and second world wars for military and civilian use, and by the 50's, generators with 5% efficiency and coolers able to decrease temperature from ambient to negative values were achieved. Such early devices, mostly developed in the United States and URSS, were either ZnSb- or Bi_2Te_3-based with ZT values around the unity.[8, 30]

The research for more efficient TE materials continued. While Abram Ioffe promoted the use of semiconductors and was one of the first ones suggesting the use of alloying for the reduction of the thermal conductivity, it was not until the 90's when new concepts on materials development were introduced. Hicks and Dresselhaus theoretically postulated in 1993 the opportunities of the enhancement of ZT values by quantum confinement.[31, 32] This new concept became a revolution within the field, and supposed the consideration of the use of nanostructures. Three years later, Glen Slack introduced the phonon-glass electron-crystal (PGEC) approach, leading to the development of new materials families such as Skutterudites or Clathrates.[33] Advances around these two new paradigms will be further discussed in next section.

Even if the TE materials technology has greatly advanced across the years until our days (Figure 0.6), reaching ZT values over 2, for the most of the market of commercial TE modules the situation has remained almost intact. With some exceptions, such as the tetrahedrite- and silicon- based TE assemblies commercialized by Alphabet Energy[34] or the module developed by Otego[35] comprising the new organic materials, commercially available modules are mainly limited to Bi_2Te_3 legs grown in the form of ingot from a melting process and PbTe for higher temperature applications.[36, 37] The challenge that the technology transfer from the lab to the industry supposes in terms of scalability and reproducibility together with the difficulties related to the proper soldering process, makes the introduction of new TE materials into the market a non-trivial matter.[38]
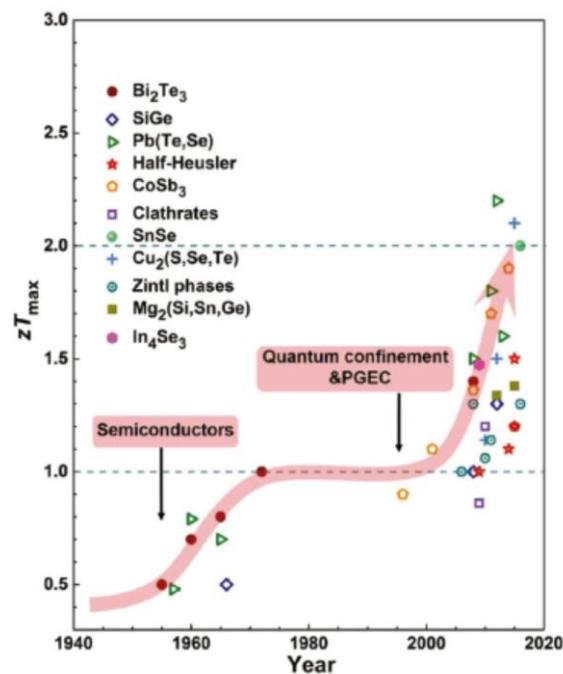
Figure 0.6   TE materials development through the years.[39]

0.1.3   The efficiency enhancement challenge

For two centuries, scientists have been struggling for the achievement of higher ZT values. A good TE material has to present high σ and S while keeping a low κ. The key point of this challenge is the strong interrelation between such properties related in the ZT equation and the difficulty to achieve a good balance between all of them at the same time.[39-41]

For a degenerated semiconductor, S is given by the Pisarenko relation:

$$S = \frac{8\pi^2 \kappa_B^2}{3eh^2} m^* T \left(\frac{\pi}{3n}\right)^{2/3}$$

Where κ_B and h are the the Boltzmann and Plank constants respectively, m^* is the effective mass of the density of states, e is the electron charge and n the carrier concentration. At the same time, σ is also related to n by:

$$\sigma = ne\mu$$

Where μ is the carrier mobility.
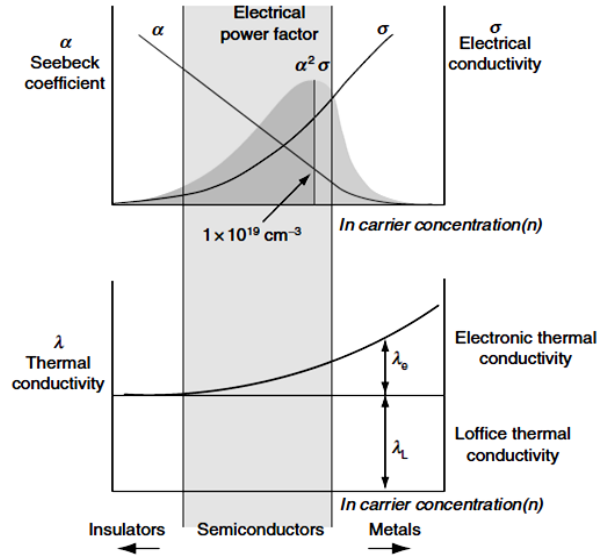
Figure 0.7   Dependence of the ZT-related properties with the carrier concentration.[4]

Being σ and S both connected to n, in the case of σ the relation is directly proportional while in S is an inverse one. By this, when n increases, S decreases and σ increases, as shown in Figure 0.7. The compromise is found for heavily doped semiconductors, where the power factor ($PF=S^2\sigma$) is maximized.

Regarding κ, it is in fact the addition of two contributions, κ_e and κ_l, which are the heat transported by the charge carriers and phonons respectively:

$$\kappa = \kappa_e + \kappa_l$$

And, as expected, κ_e is as well related to n via the Wiedemann-Franz relation:

$$\kappa_e = \sigma L T$$

Where L is the Lorenz number. This means that the more σ is increased, the higher value of the κ_e and hence, of κ. Moreover, if this was not enough, the only at first glance independent parameter, κ_l, is also related to μ. Most strategies used to decrease κ also affect μ since defects introduced in the lattice for phonon scattering also scatter carriers and this is translated into a potential decrease of σ when decreasing κ. However, this last drawback could be diminished with the proper engineering of the TE materials.

Coming back to the attempts on ZT enhancing made within the past years, they are of course related to the optimization of the mentioned TE properties. In this direction, most of the strategies have been focused in optimizing n and minimizing κ_l. For the optimization of the first one, its value should be set at around 10^{19} cm^{-3} by means of the introduction of dopants into the material.

Once optimized n, the most straightforward strategy to increase ZT is to minimize κ_l. For this, the use of materials with layered or complex crystal structures was proposed together with the PGEC concept; semiconductors designed so that the efficient transmission of charge carriers is allowed (crystal) while effectively impeding the conduction of heat across it (glass). Such materials usually include cages in which heavy atoms are trapped and rattle to block the phonons. In addition, scattering centers need to be introduced in the material. Several approaches have been followed, starting with alloying, to bring κ to the alloy limit.[42] However, this strategy is just useful to scatter short-wavelength phonons, being thus not enough for an overall κ decrease.[26, 43] Besides all the effective advances in such approaches, nanostructuring has been proved to be the most efficient method used to date to reduce κ_l. The introduction of crystal domains at the nanometer scale or the inclusion of nanoparticles (NPs) within a crystalline matrix, are effective strategies to scatter also mid-and long-wavelength phonons at the grain boundaries (Figure 0.8).[44-49]

Hicks and Dresselhaus also played an important role in the launching of nanostructuring as a hot topic within the TE community by proposing its use for the quantum confinement of the carriers, increasing the density of states, thus potentially decoupling σ and S so that the PF is maximized as a whole. Until 2014, materials considered record high ZT published in earlies 2000's were based on the nanostructuring approach. However, none of them could truly demonstrate the desired quantum confinement effect and to date is yet to be experimentally proved.[50, 51]
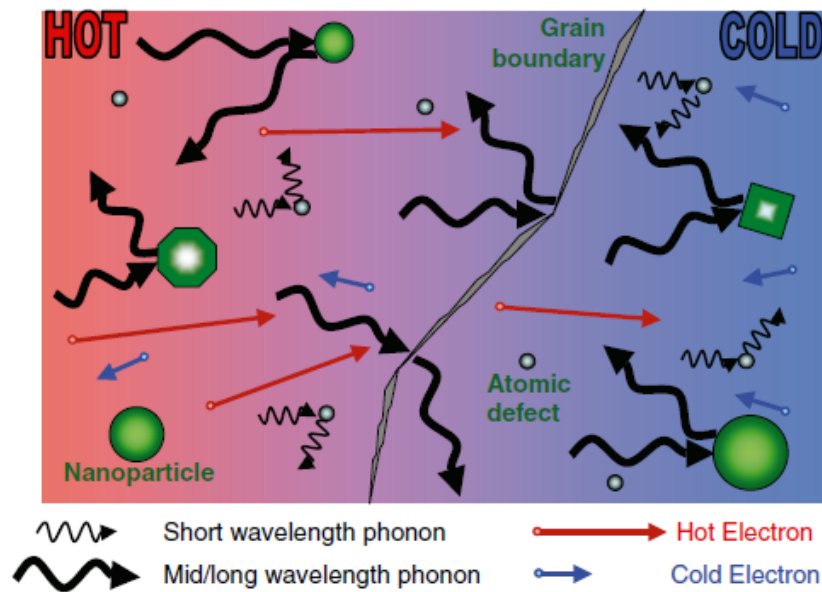
Figure 0.8   Phonon scattering mechanisms in a nanostructured TE material. Point defects are useful short-wavelength phonons while larger NPs and grain boundaries contribute to the scattering of mid- and long-wavelength ones.[45]

The energy filtering concept, another strategy proposed for the enhancement of S, is also related to the effects of nanostructuring in TE materials. Within this approach, theoretically predicted and experimentally observed, low energy carriers are selectively filtered at potential barriers introduced by nanostructures so that only carriers with higher energies are transmitted.[52]

The discussion on the optimization of material parameters, including the unavoidable necessity of manipulation of the density of states[53] in order to increase the PF and specially focused on nanostructures, will further continue in Chapter 1.

0.1.4 Production of bulk TE materials

Even nowadays there is an increasing interest on printed TE materials and devices,[54] bulk TE materials have been until our days the most studied and developed ones for its easy integration into classical TE device architectures and because of its production possibilities at the large scale. As this thesis will present the production of TE nanomaterials from the bottom-up assembly of colloidal nanoparticles, this section will be focused in the most deeply explored synthesis

techniques for bulk TE materials, like solid-state reaction synthesis or mechanical alloying.[4, 41]

In solid state melting reactions, elemental materials of the highest purity are mixed and loaded into ampoules, usually made of quartz or fused silica. Here, once evacuated and sealed, temperature is raised above the material melting point, and maintained there for several hours, most of times, more than 10 h. This method also allows the creation of nanoprecipitates by spinodal decomposition.[55]

Other possibility for the preparation of nanostructured materials is the use of the ball milling-technique.[56] It is considered a top-down approach because firstly materials are grown in bulk, usually by solid-state reaction, and then are smashed into a ball milling apparatus for hours, until achieving a nanopowder. This step is does not need any temperature control but can be carried out under inert atmosphere to avoid oxidation. The nanopowder is later compacted into bulk by means of, for example, hot press or SPS. A good example of this technique is the p-type BiSbTe alloy reported by Poudel et al. in 2008,[57] in which an ingot made of the alloy is crushed into a ball milling and further densified by hot pressing. The ZT = 1.4 at around 373 K mainly comes from the reduction of the κ due to the introduction of nanograins, resulting in higher values than the ones obtained for the ingot itself.
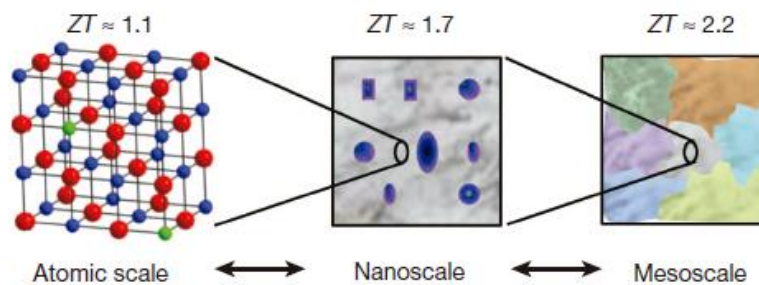
Figure 0.9 Enhancement of the ZT value of a material at the different scales: atomic, nanoscale and mesoscale.[48]

Sometimes both strategies are combined to enlarge scattering. An example of this is the PbTe-PbS alloy (3 at% Na doped), with PbS nanoprecipitates in the PbTe matrix, presenting ZT = 2.3 at 923 K.[49] This material, grown in the form of ingot in quartz tubes and afterward crushed to powders that were further pressed under spark plasma sintering (SPS). Authors relate their high values to the "all-scale hierarchical architecture" of the final materials. In these regards, previous to

this work, ZT = 2.2 at 915 K were reported for Na-doped PbTe with, in this case, SrTe nanoprecipitates, fabricated under the same method (Figure 0.9).[48]

Mechanical alloying is another route for the development of TE nanomaterials, but in this case, a bottom-up one, that has been used extensively and not only at the lab-scale. It is englobed also within the solid-sate techniques but it is performed in the same type of ball milling apparatus presented before. Elemental powders are placed into jars together with the grinding balls and are milled for hours in dry or wet conditions, and sometimes under inert atmosphere, where fracturing and welding between the starting materials turns into the desired final composition. Some of the best results obtained for Skutterudites are from mechanically alloyed materials.[58] This is the case of the n-type Te-doped $CoSb_3$ with reported ZT = 0.93 at 820 K.[59] In this work, authors prepared different compositions of the doped materials by mechanical alloying pure elemental materials during 15 h followed by a compaction of the final bulk noanomaterials by SPS. This technique has found its market into the large production of nanomaterials, and companies like Matres in Italy are already supplying nanostructured powders for different applications.[60]
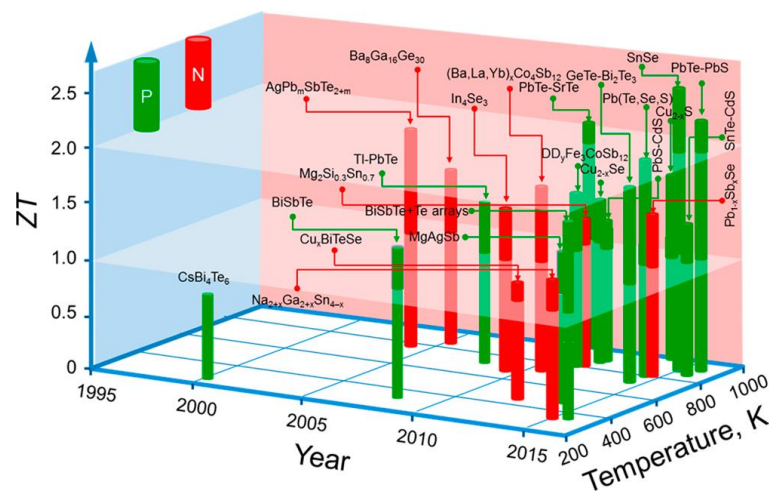
Figure 0.10   State-of-the art bulk TE materials.[41]

Besides the great enhancements that nanostructuring has supposed to the TE materials development, the highest ZT values ever reported are for SnSe single crystals.[28] It is also an example of solid-state melting reaction synthesis, followed by the Bridgman technique to grow the single crystal itself (Figure 0.10). This material never woke up too many interest within the TE community until 3 years ago, when the publication saw the light. SnSe is a compound with layered and anisotropic structure that present intrinsic low κ_l with superior TE performance

along a preferential crystal orientation, resulting in ZT = 2.62 at 923 K. When comparing these results with its counterpart polycrystalline version, ZT is only able to reach 1.2 at approximately the same temperature.[61] However, the fact that it is a single crystal and the difficulties that it involves for its fabrication, make its mass production unlikely.

For the large-scale fabrication of TE materials, it is highly important its easy scalability and cost-effectiveness.[62, 63] However, as shown in the previous section, the development of truly efficient TE materials is not an easy job. Many parameters have to be optimized and this requires an absolute control over the synthesis and thus over the final materials characteristics. While methods like mechanical alloying or ball milling do not allow any control over material properties, solid state reactions neither allow the control at the nanometer scale needed. In addition, these techniques are energy-intensive and time consuming, comprising high temperatures and long reaction times, and not affordable for the mass production of TE devices reaching the market. On the other hand, vacuum-based techniques, such as molecular beam epitaxy or chemical vapor deposition, for the production of thin-films nanomaterials do allow the huge control required. However, their low production rates and the very expensive working costs, push into the background its interesting results, being just useful as proof-of-concept of different nanostructuring approaches.

0.2 Bottom-up TE nanomaterials and devices from solution-processed NP building blocks

NP-based solution-processed bottom-up routes offer the best combination of control over nanomaterials parameters and the cost-effective production at the large scale. Among them, colloidal synthesis, that involves low reaction temperatures and times and does not need the intervention of ultra-pure starting reactants, while achieving the highest control over size, shape, composition and crystal phase of the NPs synthesized, is the most suitable technology for the production of efficient engineered TE nanomaterials (Figure 0.11).[64-70] In Chapter 1, it is possible to consult the state-of-the-art ZT chart of solution processed TE materials.

This technique is based on the reaction of molecular precursors in the appropriate concentration of solvents and organic surfactants at temperatures

between 150 and 300 °C, under inert atmosphere to avoid oxidation and at ambient pressure. It is possible to differentiate between three main events within the NP synthesis: nucleation, growth and purification.[71-73] Being possible to control each of them, it opens the door to the precise design of the characteristics of the final products.[74] Furthermore, as the scalability is also a crucial point for the suitability of the technique for the large-scale production, in different occasions it has been proved its high throughput together with the development of a continuous production method or flow reactor.[75-77]
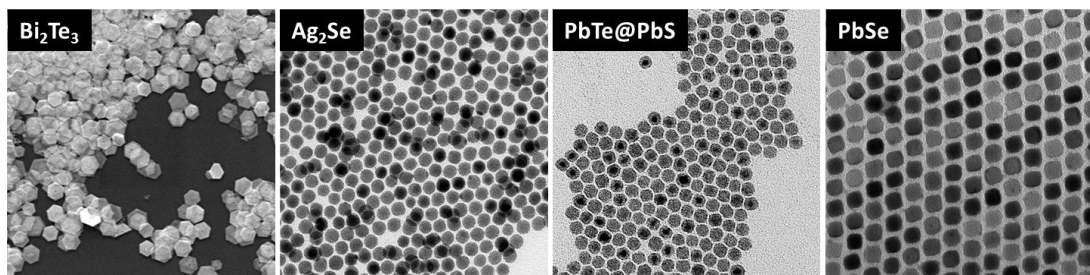
Figure 0.11 Representative transmission and scanning microscope micrographs of some of the bottom-up solution-processed TE NPs produced by the PhD candidate.

The large control over colloidal NPs properties achieved has allowed the exploration of their use for a wide range of applications; such as solar cells, light emitting devices, photodetectors, catalysis, TE or biological/medical.[78-86]

Regarding TE, solution-processed nanomaterials are especially attractive for the production of the new generation of devices. They give to access to low-cost and efficient materials in solution or in the form of inks.[87, 88] Based on that, solution-based printing processes, such as inkjet printing or screen printing, open the door to the fabrication, with simple and affordable techniques and at the large scale, of new flexible or shape-adaptable TE devices.[54, 89-92] Such adaptability is important for the improvement of the thermal contact between the TE and the surfaces in which ubiquitous temperature gradients may be found. Conventional TE devices, with planar architectures and comprising ceramic plates as substrates, are not useful to directly match the wide range of surfaces in which TE modules could be integrated. Moreover, the cost of such plates it is not negligible, being comparable to the material development cost.[23] Hence, for the definitive widespread of TE devices into the market, besides the development of efficient, cost-effective and scalable materials, it is necessary to reach a new paradigm with shape-adaptable substrates and architectures, and solution-processed techniques may be the key (Figure 0.12).
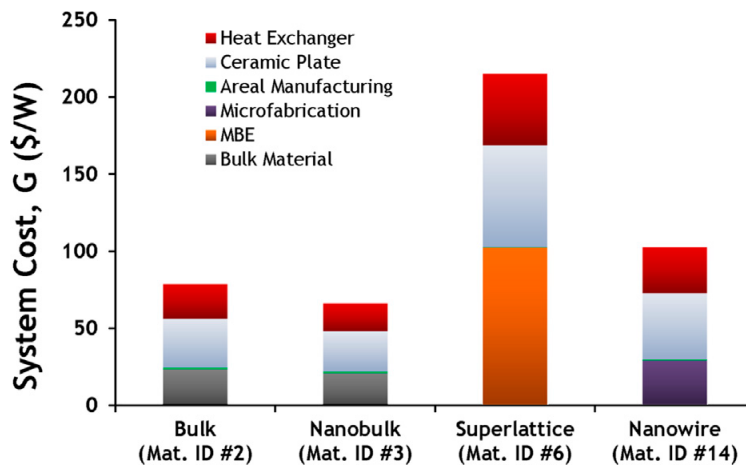
Figure 0.12 Estimated cost ($/W) of TE devices based on different materials developed by four different synthesis techniques.[23] Being bulk referred to zone-melting solid state synthesis, nanobulk to melt-spinning, superlattice to molecular beam epitaxy and nanowire to electrochemical synthesis, colloidal synthesis techniques should present lower cost than all of the compared technologies.

Besides many interesting examples that have been published during the last years (complete available list in Chapter 1), Otego,[35] a new creation spin-off from the Karlsruhe Institute of Technology, is already commercialising flexible TE modules developed by solution-processed printing techniques, based on organic materials printed onto thin polymer foils. To date, no conformable devices based on inorganic materials are available in the market. Within this PhD thesis, it has been developed a new process for the fabrication of a shape-adaptable TE device based on the solution-processed engineered nanomaterials here presented. Such device and process are currently under patent pending process and, considering the time restrictions over the deposit of this dissertation, it could not be included in this text.

This thesis will focus on the solution-processed production of TE nanomaterials from NP building blocks grown, more in detail, by colloidal synthesis. As will be shown in the following chapters, this technique has offered us the possibility to precisely design the NP building blocks parameters, reaching not only more efficient nanomaterials, but also the goal of a device fabrication and integration. Therefore, showing the huge and real potential that this approach presents to reach the TE market in the short-term.

0.3 Objectives

This thesis will cover a complete journey from the materials development to the device fabrication and integration. In this context, and taking into account the broader context in which this dissertation is included, the main objectives of this work have been:

1. To review the existing literature on the topic and present a comprehensive summary of it to pave the way for the technology development and evaluate the starting point of this work. (Chapter 1)

2. To smooth the way from the lab to the market, presenting a complete route from the synthesis to the device, the main advantages, challenges and opportunities. (Chapter 1-4)

3. To develop efficient TE materials from the engineering of colloidal nanomaterials. (Chapter 2)

4. To show the versatility of this route by controlling the TE properties at three different levels: within the synthesis, during the purification of the nanocrystals and during the assembly. (Chapter 2)

5. To extend the synthesis of the nanomaterials to the large scale making a step forward for the fabrication of a TE device. (Chapter 3)

6. To go beyond the fabrication processes and propose the integration of solution-processed nanomaterials and TE devices into applications. (Chapter 4)

Chapter 1   The journey over engineered nanoparticle-based solution-processed thermoelectric nanomaterials and devices
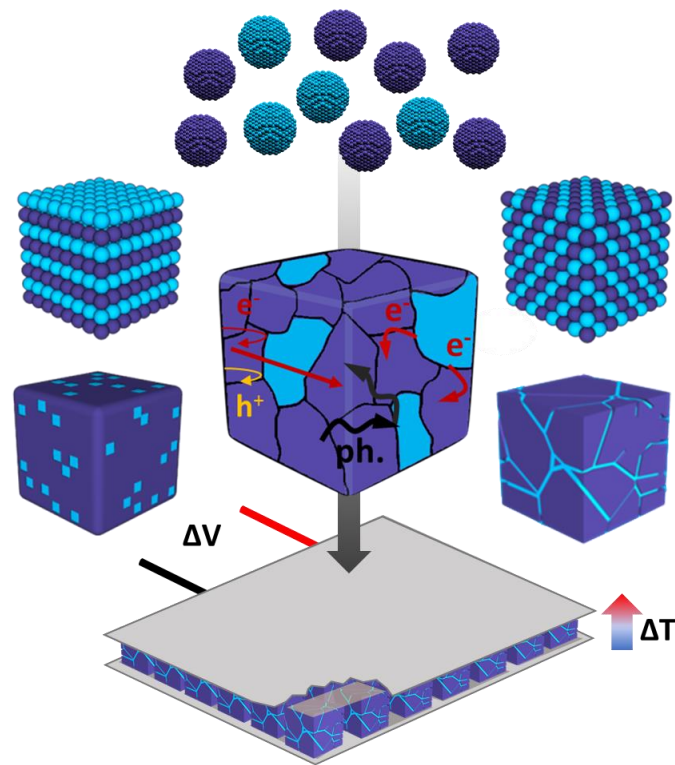
The development of solution-processed NP-based TE nanomaterials from a bottom-up engineering approach is an exciting topic still in its infant stage, therefore many different challenges need to be attended to exploit its possibilities to its full potential.

This chapter is the result of a deep literature research transformed into a compressive analysis of the convergence of two different fields: TE and solution-processed NPs.[93]

After a brief introduction in which the needs of TE materials are presented (Section 1), four relevant topics are discussed: i) the design, synthesis and surface chemical engineering of inorganic NPs as building blocks to produce nanomaterials (Sections 2 and 3); ii) the production of nanomaterials, and particularly nanocomposites, with unprecedented nanometre scale control over crystallite size, facets, orientation and phase distribution by means of facile, scalable, potentially low-cost, high-yield and extremely versatile NP-based bottom-up processing approaches (Section 4); iii) the rational control of charge carrier concentration in NP-based bottom-up engineered materials (Section 5); iv) the application of such nanomaterials to fabricate cost-effective TE devices able to convert heat into electricity and vice versa and thus susceptible to improve efficiency of a plethora of industrial and domestic processes, to power autonomous electronic systems and to control temperature and cool several applications (Section 6).

Finally, in the last part of the Chapter (Section 7); a realistic view of the opportunities and future prospects of this technology is discussed taking into account its advantages, limitations and challenges.

Additionally, an annex (Supplementary Information) is included, in which we show different state-of-the-art data of the technology: i) a record high ZT values chart similar to the one for bulk TE materials (Figure 0.10); and ii) a summary of the main attempts for the production of solution-processed TE devices until early 2017, showing the deposition method and substrate used, number of pairs and architecture, output power and if flexible.

Despite the focus is solely on TE materials and devices, an important part of this chapter describes synthesis and surface engineering strategies to optimize functional properties of NP and NP-based bottom-up assembly approaches, with emphasis on their main advantages, challenges and limitations. These topics are common to a wide range of research fields and applications beyond TE. In particular, the surface engineering of NPs, the assembly and consolidation of nanomaterials, their doping and the limitations of thermal processes in terms of crystal domain growth and compositional changes are topics of great importance in photovoltaics, catalysis or energy storage among others.

This chapter provides the reader with a solid background and the required tools to understand the following chapters. Even though, considering the time-line of this PhD, this chapter should be the last one since it is a collection of all the knowledge gained during this time, it has been created with the solid intention of showing the complete journey from the solution-processed TE nanomaterials and devices engineering, and will be referred along the upcoming chapters.

Chem Soc Rev

TUTORIAL REVIEW

Bottom-up engineering of thermoelectric nanomaterials and devices from solution-processed nanoparticle building blocks†

Silvia Ortega, [a] Maria Ibáñez,*[bc] Yu Liu,[a] Yu Zhang,[a] Maksym V. Kovalenko, [bc] Doris Cadavid *[a] and Andreu Cabot *[ad]

The conversion of thermal energy to electricity and *vice versa* by means of solid state thermoelectric devices is extremely appealing. However, its cost-effectiveness is seriously hampered by the relatively high production cost and low efficiency of current thermoelectric materials and devices. To overcome present challenges and enable a successful deployment of thermoelectric systems in their wide application range, materials with significantly improved performance need to be developed. Nanostructuration can help in several ways to reach the very particular group of properties required to achieve high thermoelectric performances. Nanodomains inserted within a crystalline matrix can provide large charge carrier concentrations without strongly influencing their mobility, thus allowing to reach very high electrical conductivities. Nanostructured materials contain numerous grain boundaries that efficiently scatter mid- and long-wavelength phonons thus reducing the thermal conductivity. Furthermore, nanocrystalline domains can enhance the Seebeck coefficient by modifying the density of states and/or providing type- and energy-dependent charge carrier scattering. All these advantages can only be reached when engineering a complex type of material, nanocomposites, with exquisite control over structural and chemical parameters at multiple length scales. Since current conventional nanomaterial production technologies lack such level of control, alternative strategies need to be developed and adjusted to the specifics of the field. A particularly suitable approach to produce nanocomposites with unique level of control over their structural and compositional parameters is their bottom-up engineering from solution-processed nanoparticles. In this work, we review the state-of-the-art of this technology applied to the thermoelectric field, including the synthesis of nanoparticles of suitable materials with precisely engineered composition and surface chemistry, their combination and consolidation into nanostructured materials, the strategies to electronically dope such materials and the attempts to fabricate thermoelectric devices using nanoparticle-based nanopowders and inks.

Key learning points
(1) Nanostructuring approaches to increase thermoelectric performance.
(2) Possibilities and limitations of the synthesis of thermoelectric materials in nanoparticle form.
(3) Significance of the nanoparticle surface chemical engineering to control nanomaterial properties.
(4) Strategies and current challenges for the bottom-up assembly of solution-processed nanoparticles.
(5) Electronic doping approaches in nanomaterials produced by assembly of solution-processed nanoparticles.

[a] Catalonia Institute for Energy Research – IREC, 08930 Sant Adrià de Besòs, Barcelona, Spain. E-mail: dcadavid@irec.cat, acabot@irec.cat
[b] Institute of Inorganic Chemistry, Department of Chemistry and Applied Biosciences, ETH Zürich, CH-8093, Switzerland.
E-mail: ibanez@inorg.chem.ethz.ch
[c] Empa-Swiss Federal Laboratories for Materials Science and Technology, Dübendorf, CH-8600, Switzerland
[d] ICREA, Pg. Lluis Companys 23, 08010 Barcelona, Spain
† Electronic supplementary information (ESI) available. See DOI: 10.1039/c6cs00567e

1. Introduction

Thermoelectric devices, allowing the solid-state and reversible conversion between heat and electricity, offer numerous advantages over competing technologies in the fields of temperature control and thermal energy harvesting. Advantages include no fluids or moving parts, high durability and reliability with

Chem. Soc. Rev., 2017, **00**, 1–19 | 1

The journey

23

virtually no maintenance cost, silent operation, reduced volume, and a very flexible design with wide size/power adaptability. Accordingly, numerous applications have been proposed for this technology. Beyond temperature sensing, the heat flow generated in a thermoelectric module when an electric potential is applied is used in portable fridges, car seat climate control systems and to actively cool optoelectronic and electronic devices. Besides, the capacity of thermoelectric modules to generate electricity from temperature gradients can be used to power autonomous electronic systems by harvesting energy from ubiquitous temperature gradients, to improve energy efficiency of domestic and industrial processes and vehicles by recovering wasted heat, and to generate electric power in deep-space missions.[1]

While proposed applications of thermoelectric devices are countless, most of them are yet to be successfully commercialized. What currently constrains thermoelectrics to few niche markets is a fatal combination of a relatively high price related to the used materials and poor performance compared with competing technologies, both as heat pump and electricity generator. In either direction, the maximum coefficient of performance (COP) or energy conversion efficiency (η) depends on the temperature at the cold and hot side (T_c, T_h; $\Delta T = T_h - T_c$; $T_a = \Delta T/2$), and a sole material-related figure of merit, Z:[1]

$$\text{COP} = \frac{T_c}{\Delta T} \frac{\sqrt{1 + ZT_a} - \frac{T_h}{T_c}}{\sqrt{1 + ZT_a} + 1}$$

$$\eta = \frac{\Delta T}{T_h} \frac{\sqrt{1 + ZT_a} - 1}{\sqrt{1 + ZT_a} + \frac{T_c}{T_h}}$$

Silvia Ortega

Silvia Ortega graduated in Physics in 2012 and received her MSc in Nanotechnology from the University of Barcelona. In 2014 she enrolled an Industrial PhD program between the Functional Nanomaterials Group in IREC and the company CIDETE Ingenieros S. L. in Barcelona. Since then, she is a PhD student under the supervision of Prof. A. Cabot and Dr M. Ibáñez. Her field of work is the preparation and characterization of solution-processed bottom-up thermoelectric materials, the design of new thermoelectric modules and their application for cooling and energy harvesting.

Maria Ibáñez

Maria Ibáñez (born in La Sénia, Spain) is a postdoctoral research fellow at ETH Zürich since 2014 when she joined Prof. Kovalenko group. She obtained her PhD in Physics in 2013 from the University of Barcelona, under the supervision of Prof. Cabot and Prof. Morante. She has worked as a visiting researcher in California Institute of Technology (Caltech), Cornell University, the University of Chicago, Northwestern University and the Commissariat à l'Energie Atomique et aux Energies Alternatives (CEA). Her research focus is to develop new nanomaterials, in particular nanocomposites, from the bottom-up assembly of precisely designed nanoparticles and to characterize their functional properties for different applications in the field of energy conversion and energy storage.

Yu Liu

Yu Liu received his Master's degree in Applied Chemistry from Anhui University, China in 2014. Then, he started his PhD studies in Nanoscience under the supervision of Prof. A. Cabot and Dr D. Cadavid at IREC in Barcelona, Spain. His research focuses on the development of high performance nanostructured thermoelectric materials and understanding the parameters and their underlying mechanisms that enhance the thermoelectric performance.
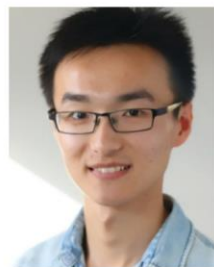
Yu Zhang

Yu Zhang received his Erasmus Mundus Joint Master Degrees from University of Barcelona and Heriot-Watt University. During his master's degree, he studied the toxic effects of nanoclay on immune system in the school of Life Science under supervision of Dr H. Johnston. In 2016, he enrolled the Nanoscience PhD program at the University of Barcelona in the Functional Nanomaterials Group under the guidance of Prof. A. Cabot and Dr D. Cadavid, focusing in the bottom-up engineering of nanostructures applied for energy storage and conversion.

The thermoelectric figure of merit, usually expressed in its dimensional form, ZT, is a particular combination of only three material parameters, Seebeck coefficient (S), electrical conductivity (σ) and thermal conductivity (κ):

$$ZT = \frac{\sigma S^2}{\kappa} T$$

There is no known limitation to ZT and thus, except for the Carnot limit, to the maximum η of thermoelectric devices. Yet, thermoelectric materials struggle to simultaneously display large S, high σ and low κ, being these three parameters tightly interrelated.

1.1. Optimization of the material parameters

To maximize ZT, the carrier concentration is a key parameter that needs to be adjusted, as not only σ but also S and the electronic $\kappa(\kappa_e)$ strongly but inversely depend on it. This is successfully accomplished by doping the material with extrinsic donor or acceptor impurities, through tuned off-stoichiometric compositions or through manipulation of electronically active intrinsic defects. Because the charge carrier concentrations required to optimize thermoelectric performance are relatively high, around 10^{19} cm^{-3}, usually large amounts of ionized impurities or defects need to be introduced, what negatively impacts charge carrier mobility and thus limits the maximum power factors (σS^2) reached. Such drawback can be avoided by removing impurities from the matrix material where charge transport takes place and concentrating them in nanoinclusion. While electrons can still be scattered at the nanoinclusion interfaces, the use of charge nanoreservoirs able to donate carriers allows to significantly increase electrons mean free path when compared to conventional doping. Such approach, known as modulation doping, has been demonstrated effective not only in superlattices but also in materials incorporating nanoinclusions, reaching up to a 40% increase of σ.[2,3]

Heat is transported both by charge carriers and phonons ($\kappa = \kappa_e + \kappa_L$). κ_e is proportional to the electrical conductivity *via* the Wiedemann–Franz law ($\kappa_e = L\sigma T$, L being the Lorenz number). The lattice $\kappa(\kappa_L)$ depends on the ability of phonons to propagate through the material, but it is indirectly related to σ in the sense that the introduction of phonon scattering mechanisms may negatively affect charge carrier mobility. One first approach to minimize heat transport is to identify materials with crystal structures providing intrinsically low κ_L.[1,4,5] κ_L decreases with increasing atomic mass due to a reduction of the sound velocity. It also decreases with increasing

Maksym V. Kovalenko has been tenure-track Assistant Professor of Inorganic Chemistry at ETH Zürich (Swiss Federal Institute of Technology) since July 2011 and Associate Professor from January 2017. He received his PhD degree in 2007 from the Institute of Solid State Physics, at Johannes Kepler University (Linz, Austria). He then moved to USA (2008–2011, Department of Chemistry, University of Chicago) for postdoctoral training.

Maksym V. Kovalenko

His present scientific focus is on the development of new synthesis methods for inorganic bulk and nanoscale materials, their surface chemistry and self-organization, and energy-related applications such as in batteries.

Doris Cadavid is a physicist and a MSc in physics from the National University of Colombia. She holds a PhD degree in Physics from the University of Barcelona since 2014. During her doctoral research she was focused in the development of solution-processed bottom-up strategies for the production of efficient thermoelectric nanostructured materials. In 2013 she was a visiting scientist at the Novel Materials Laboratory of the

Doris Cadavid

University of South Florida. Since 2014 she is a research engineer in the Advanced Materials Department at IREC. Her current research interests are the production and characterization of nanostructured materials with different electronic, structural and thermal properties for the application in the field of energy conversion and storage.

Andreu Cabot received his PhD from the University of Barcelona in 2003. From 2004 to 2007, he worked as a postdoctoral researcher in Prof. A. Paul Alivisatos group in the University of California at Berkeley and the Lawrence Berkeley National Laboratory. In 2009 he formed the Functional Nanomaterials Group and joined the Catalonia Institute for Energy Research – IREC, where he is currently ICREA Research Professor. His research

Andreu Cabot

interests include the design and preparation of nanomaterials, the characterization of their functional properties and their use in the field of energy conversion.

interatomic distances and lattice periodicity, as those characterizing multinary compounds with complex structures and large unit cells. κ_L is also strongly reduced by intrinsic atomic disorder as in amorphous materials or in materials with a quasi-random distribution of one of the elements. Additionally, a strong bond anharmonicity and anisotropy is particularly effective to reduce κ in specific crystallographic directions. To further reduce κ_L, additional point defects introducing fluctuations in mass, size and interatomic coupling forces can be created through alloying, partial atomic substitution or the addition of elements in proper lattice sites, such as filling structural voids with "rattling" atoms.[4] However, to effectively minimize κ_L, blocking all the phonon spectra is necessary, which requires phonon scattering mechanisms at all scales.[6] While point defects effectively scatter high frequency phonons, an effective strategy to scatter medium- and long-wavelength phonons is the introduction of grain boundaries. In this direction, the use of nanocrystalline materials has been demonstrated successful to reduce κ_L even below the alloy limit. Due to a more efficient phonon scattering at interphases of two different materials with an acoustic impedance mismatch, best performances have been obtained using nanocomposites. In such nanocomposites, to minimize the effect of interfaces on the mobility of the majority carriers and at the same time increase scattering of the minority carriers, to reduce its contribution to κ_e, a proper electronic band engineering is necessary. It is actually possible to design nanodomains with a specific potential function profile which minimizes the electron scattering cross section within the Fermi window, making these nanoinclusions visible for phonons but invisible for the majority carriers.[7]

Beyond optimizing charge carrier concentration and minimizing κ_L, strategies to produce truly efficient thermoelectric materials inevitably rely on increasing S, i.e. the average energy per electron within the Fermi window.[5] A first strategy to increase S is to maximize the asymmetry of the density of states (DOS) with respect to the Fermi level. Among several approaches to distort the DOS, the introduction of resonant impurity levels have been demonstrated particularly successful. Another approach to simultaneously provide high S and σ is to increase the number of energy valleys participating in the transport of majority carriers by forcing band convergence, while eventually also forcing the divergence of valleys contributing to the transport of minorities. Quantum confined structures also allow enhancing the DOS for electrons near the Fermi level, which has been demonstrated efficient in increasing S in superlattices.[8,9] An alternative strategy to increase S is to change the distribution of carriers contributing to charge and heat transport by introducing energy- and type-dependent scattering mechanisms. In this direction, beyond phonon scattering, nanocomposite interfaces can be used as such charge carrier energy- and type-dependent filters, selectively
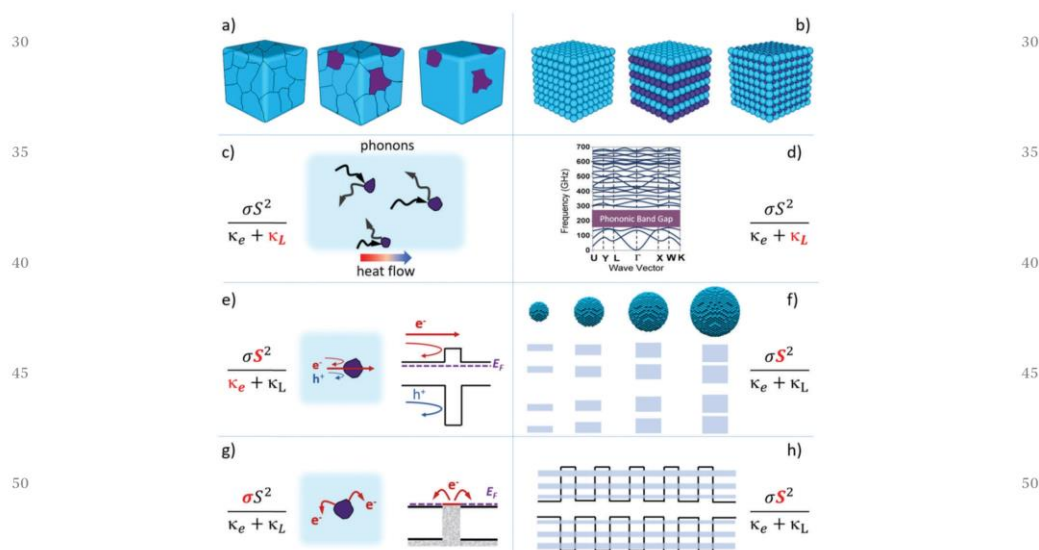
Fig. 1 Cartoons of different types of disorganized and organized nanomaterials (a and b) and schemes of the effect of nanostructures on the thermoelectric figure of merit: (c) phonon scattering; (d) phononic band gap; (e) charge carrier type- and energy-dependent filtering; (f) DOS modification by quantum confinement in QDs; (g) modulation doping; (h) DOS modification within QD superlattices.

4 | *Chem. Soc. Rev.,* 2017, **00**, 1–19

This journal is © The Royal Society of Chemistry 2017

blocking minority and low energy majority carriers, thus reducing bipolar effects and increasing the average energy per majority charge carrier.[8]

1.2. Nanomaterial engineering

Summarizing, nanomaterials and particularly nanocomposites can help improving ZT by increasing σ through modulation doping, decrease κ though scattering of phonons (κ_L) and minority charge carriers (κ_e) and increase S by manipulating the DOS or filtering charge carriers according to their sign and energy (Fig. 1). Additionally, nanomaterials have associated more favorable mechanical properties including reduced brittleness and improved machining, as grain boundaries disrupt the motion of dislocations.

However, to design and engineer a nanomaterial with optimized thermoelectric performance presents an extraordinary challenge. The strong interrelation between the relevant material transport properties makes the range of material parameters maximizing ZT extremely narrow, which demands the ability to adjust them with very high accuracy. Reaching the required precision in the manipulation of material parameters is particularly challenging in such complex materials as nanocomposites, with many additional degrees of freedom when compared to single crystals. Parameters such as size, shape, composition and phase of each nanodomain type, their distribution and orientation and their interface properties including coherency, band alignment, defects and roughness are not considered on crystalline materials, but determine the functional properties of nanocomposites.

A precise design of thermoelectric nanocomposites requires to significantly improve our understanding of the influence of each material parameter on its functional properties. To reliably establish such structure–property relationships, the development of powerful multi-scale modeling tools able to handle nanocomposites with affordable computational costs is necessary. Besides, the availability of trustworthy experimental results from model nanocomposites having precisely adjusted parameters is essential. Overall, the ability to produce such model materials would enable both a systematic study and thus a better fundamental understanding of the influence of material parameters on thermoelectric properties, and the later design, engineering and mass production of high performance materials for their commercialization and use.

Vacuum-based thin film deposition tools are the only current mature technologies able to produce nanomaterials that are compositionally engineered at the nanometer-scale. The accurate composition control of such technologies, based on an atom-by-atom growth, has translated into thermoelectric thin films with some of the highest figures of merit ever reported.[10] However, from a commercial point of view, vacuum-based technologies are characterized by relatively low yields, low production rates, and high capital, operational and maintenance costs. Furthermore, these technologies are not able to provide the relatively thick thermoelectric modules required by most applications. Additionally, from a research and development point of view, the lack of reliable tools to characterize the thermoelectric properties of thin films strongly hinders their potential to provide well-founded data on the influence of material parameters on thermoelectric performance. Actually, the reproducibility of thermoelectric superlattices has become an important issue and a vivid controversy still exists on the real gains associated to quantum confinement.

To overcome the limitations of vacuum-processed thin films, methods to prepare bulk thermoelectric nanocomposites with identical or improved compositional engineering capability are required. However, conventional strategies to produce bulk thermoelectric nanocomposites, such as ball milling or phase segregation within solid solutions, provide a poor level of control over nanomaterial parameters. Additionally, these strategies are energy- and time-intensive, what reduces their cost-effectiveness.

The bottom-up engineering of nanomaterials from solution-processed nanoparticles, like vacuum-based thin film deposition technologies, is based on a material growth by atomic or molecular addition, which potentially provides this technology with a similar level of control over composition. However, not requiring a substrate to support growth, nanoparticle-based bottom-up processes are characterized by much higher material production rates. At the same time, this strategy allows an exquisite surface/interface engineering, which provides additional mechanisms to modulate transport properties in the final nanocomposite. The availability of materials in nanoparticle form also enables a simple and cost-effective production of thermoelectric devices through printing technologies.

1.3. Objectives, target audience and review distribution

This tutorial review provides an overview of the advantages, remaining challenges and present opportunities of nanoparticle-based bottom-up processes to produce efficient and cost-effective thermoelectric nanomaterials and devices. We review the nanoparticle synthesis and assembly strategies, with emphasis on the particularities that thermoelectric application imposes: $i.e.$ the synthesis of intermetallic/intermetalloid nanoparticles, an accurate compositional engineering including high electronic doping levels, the purification of air-sensitive nanoparticles and their assembly into bulk nanocomposites with precisely modulated parameters and eventually crystallographic texture. We also review here the attempts to produce thermoelectric devices based on solution-processed nanoparticles and discuss their advantages and limitations (Fig. 2).

It is not the goal of this review to give an overview of recent advances on thermoelectric nanomaterials or of nanoparticle synthesis methods; to provide an exhaustive list of all works on solution-processing of thermoelectric materials; or to cover advances on thermoelectric materials grown by solution-processed approaches that do not involve nanoparticles, such as electrochemical deposition. While some organic materials could fit in the topic of this review, we chose to leave them out due to the different problematic they face when compared with inorganics.

This review is directed both to the thermoelectric and solution-processing communities. We aim at attracting interest from the thermoelectric community on the potential of

This journal is © The Royal Society of Chemistry 2017

Chem. Soc. Rev., 2017, **00**, 1–19 | 5

Fig. 2 Scheme of the process to manufacture thermoelectric devices from solution-processed nanoparticles.

nanoparticle-based solution processing technologies to engineer efficient thermoelectric materials for fundamental studies and commercial purposes. At the same time, we aim at demonstrating thermoelectrics as an extremely exciting and well-fitted target application for the nanoparticle solution-processing community.

2. Nanoparticle synthesis

Thermoelectric nanoparticles can be produced by several processes, which can be rationalized as top-down or mechanical, gas-phase or liquid-phase. A fourth category, the solid phase or formation of nanoparticles within solid matrixes by, for instance, phase-separation during cooling of solid solutions or ionic implantation, does not provide free-standing nanoparticles to be used as building blocks for the engineering of nanocomposites. Therefore, although successfully used in the thermoelectric field,[6] this approach will be omitted from the further discussion.

Top-down approaches produce nanoparticles by fragmentation of extended solids, harnessing the compositional (including doping) and structural engineering of starting bulk materials. Particularly, grinding is one of the most popular and industrialized nanoparticle production technologies due to its relatively moderate cost, simplicity and versatility. As drawbacks, top-down methods are energy-intense and lack mechanisms to precisely control nanoparticle size, shape and surface chemistry.

Gas-phase or aerosol synthesis methods include a relative large variety of approaches where atomic or molecular monomer decomposition/reaction can take place at high temperatures and mediating very high heating and cooling rates. These conditions allow producing high crystallinity nanoparticles, with potentially complex crystallographic phases and incorporating a range of impurities, as required for thermoelectric applications. However, as they typically require vacuum, their drawbacks include relatively high production costs and reduced scalability. These techniques also lack of control over nanoparticle surface properties, which limits its assembly and the tuning of the nanocomposite interfaces.

2.1. Solution-based synthesis of nanoparticles

In liquid-phase methods, the decomposition/reaction of atomic or molecular monomers takes place within a solvent heated to moderate temperatures.[11-13] The selection of the proper type and concentrations of the chemicals used, including solvents, precursors, surfactant and redox agents; and the temperature profile, considering time and temperature of addition of each component to the reaction mixture, is essential to obtain high quality nanoparticles, *i.e.* with parameters tuned at will, high yield and purity. The selection of chemicals needs to take into account the compatibility in terms of solubility/polarity and reactivity (temperature range) of the different components, to avoid unwanted chemical reactions. Chemicals should be ideally accessible commercially or *via* well-documented and simple preparation; stable at room temperature; not sensitive to light, air and moisture (*i.e.* ease of handling); safe, and cost- and environmentally-friendly. Compounds purity is particularly important to ensure reliability/repeatability of the final product since the amount and type of impurities can play an important role during the nanoparticle synthesis, and also influence key thermoelectric properties such as charge carrier concentration and electronic band structure of the final material. Finally, selected components should enable the posterior nanoparticle purification from possible side products, unreacted species and the solvent, which presence in the final thermoelectric nanomaterial may be strongly detrimental.

The solvent provides the media where all components diffuse and react while in atomic or molecular form. The use of a liquid solvent generally restricts the reaction temperature to below 400 °C, as most liquid solvents evaporate or decompose above this temperature. While the use of relatively low temperatures is one of the bases of the simplicity, potential low cost and relatively easy scalability of solution-based methods, it certainly limits the palette of thermoelectric materials that can be produced using commercial precursors. The relatively low temperatures used also translate in high defect densities and poor crystallinities in some materials, which could result in nanomaterials with lower thermal conductivities, but also reduced charge carrier mobilities. To increase the reaction temperature range of particular solvents and improve product crystallinity, the chemical reaction can take place within a sealed vessel at above ambient pressure in the so-called hydro- and solvo-thermal syntheses processes. Temperature can be also punctually much higher with proper excitation, *e.g.* sonochemical synthesis. Alternatively, ionic liquids/molten salts

6 | *Chem. Soc. Rev.*, 2017, **00**, 1—19

This journal is © The Royal Society of Chemistry 2017

with a potentially very wide temperature range and the ability to dissolve most ionic precursors have been also used as solvents.[14] However, their cost, difficult nanoparticle purification and the lack of proper ligands to control nanoparticle growth are still major limitation to be overcome.

Among the different solution-based synthesis procedures, colloidal synthesis routes are characterized by maintaining the nanoparticles suspended in solution, without aggregation, during the whole nanoparticle synthesis process. This strategy allows to simultaneously grow huge numbers of nanoparticles in the exact same conditions and thus to obtain extremely narrow size, shape and composition distributions.[11,12,15,16] Colloidal routes offer the highest level of control over nanoparticle parameters, what makes them especially suitable to produce the building blocks required for the bottom-up engineering of thermoelectric nanomaterials. In this regard, they strongly resemble the synthesis of organic molecules, both sharing compositional tunability at the atomic/molecular level, exquisite product monodispersity, and the convenient availability of the products in solution for subsequent assembly/use.

Colloidal stability is accomplished through the use of suitable surface ligands.[15] In non-polar solvents colloidal stability is generally provided through steric repulsion using organic molecules that contain both solvophobic (e.g. amines, thiols, silanes or phosphines) and solvophilic coordinating groups such as an alkyl chain. In polar solvents, colloids are stabilized electrostatically through charged surface ligands or using surfactant micelles with polar groups facing the solvent medium. To balance charge in electrostatically stabilized nanoparticles, oppositely charged counterions in solution are located in a diffuse region around the particle. These counterions may be incorporated to the nanoparticle-based nanocomposite during aggregation/assembly and consolidation thus also influencing the thermoelectric properties of the final material.

To date, best quality nanoparticles have been obtained using non-polar or weakly polar organic solvents where a broader range of coordination chemistries is available. However, polar solvents may be more cost-effective, especially water, and provide easier dissolution of low cost salts. The main limitations of polar solvents is that tuning the reactivity parameters is much more challenging and the concentration of colloidal nanoparticles produced, a key parameter determining costs and throughput, is much lower due to the nature of the electrostatic stabilization requiring larger distances between nanoparticles. Water is the cheapest and most environmental-friendly solvent, but it has serious shortcomings such as limited synthesis temperature range as well as oxidative and hydrolyzing abilities and instability in front of very strong reductants as those potentially needed to produce nanoparticles of some of the main thermoelectric families, e.g. Skutterudites, silicides, half-Heuslers or clathrates.

2.1.1. Size and shape control. While still mostly unexplored, the density and characteristics of interfaces must play a key role in determining thermoelectric properties in nanocomposites. Additionally, tuning the crystal domain sizes in the proper range also allows modifying the electronic band structure through quantum confinement effects. In bottom-up assembly strategies, these parameters can be modulated by adjusting the size and shape of the nanoparticle building blocks.

Nanoparticle size can be effectively tuned by adjusting the surface ligand amount and binding strength, which determines surface coverage and thus protection toward monomer addition. Larger amounts and/or strongly binding surfactants result in smaller nanoparticles. Size can be also tuned by adjusting the nucleation and growth balance though properly selecting the type and concentration of precursors and the reaction conditions. In general, the higher the monomer concentration injected at the reaction temperature (hot injection), the higher the number of formed nuclei, and thus the smaller the final nanoparticle size. Similarly, due to the favorable heterogeneous over homogeneous nucleation, a slow increase of temperature in heating-up procedures generally result in larger nanoparticles.

On the other hand, the nanoparticle shape is thermodynamically determined by the minimization of its surface energy. It thus depends on the material crystal structure and free energy of each facet, which can be controlled through the proper selection of type and amount of surfactants. Surfactants allow directing the nanoparticle shape by selectively blocking the delivery of reagents to specific surfaces or modifying the free energy of particular facets. Besides, shape directing templates, either solids that are afterward dissolved, or organic such as micelles, are also used to direct the nanoparticle geometry. Additionally, post nanoparticle synthesis processes such as oriented attachment and selective etching are also effective in modulating the nanoparticle geometry.

2.1.2. Composition and phase control. To simultaneously adjust all the parameters required to optimize thermoelectric properties (including charge carrier concentration, phonon scattering, mobilities and band convergences/divergences of majority and minority carriers), generally complex multinary compounds with particular crystal structures and which include one or several additional/substitutional elements are required. This makes the precise phase and compositional engineering not only particularly fundamental to optimize thermoelectric properties but also especially challenging. In this direction, nanoparticle-based bottom up assembly technologies potentially offer an unprecedented level of control, at the nanometer scale, of the phase and composition distribution within bulk nanocomposites. The nanoparticle crystal phase for example can be controlled through the use of proper type and concentration of precursors, surface ligands and growth conditions. Even metastable phases not reached through any other method have been produced using solution processing techniques in nanometer size crystals.[16] Being the synthesis temperature generally constrained to below 400 °C, limitations are found when attempting to produce nanoparticles with highly complex crystallographic structures requiring high energies, thus temperatures, for atomic organization.

Nanoparticles with the multinary compositions required to optimize thermoelectric properties may be produced by

This journal is © The Royal Society of Chemistry 2017

Chem. Soc. Rev., 2017, **00**, 1–19 | 7

selecting proper precursors and adjusting the reaction conditions to simultaneously react all the elements. However, it is generally more feasible to successively incorporate the different elements in the growing nanoparticle or to use a multiple-step growth process to reach the desired composition. In this last direction, the tiny size of nanoparticles, in the same order of magnitude or even smaller than atomic diffusion lengths, conveniently enables an ample post-synthetic compositional adjustment, though adding, replacing, removing or redistributing atoms (Fig. 3).[16–19] Such post-synthetic processes are very effective in producing nanoparticles with increased degrees of compositional complexity as the ones required to optimize thermoelectric properties.

New elements can be added into pre-grown nanoparticles by atomic diffusion from solution. This strategy is particularly interesting to produce thermoelectric intermetallic nanoparticles and is used to produce for example silicate nanoparticles through the incorporation of silicon atoms to preformed metal nanoparticles.[20] A new element can be also incorporated through additive reaction. This is the case when oxidizing a metal nanoparticle with a chalcogen for example.
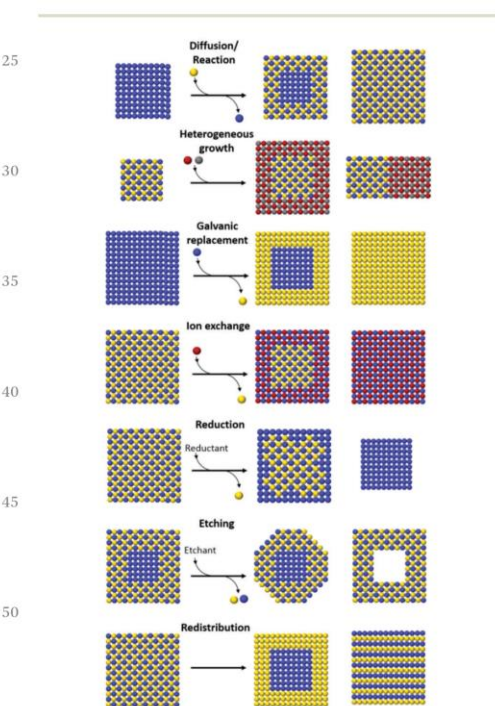
Fig. 3 Scheme of possible post-synthetic compositional adjustments, including atomic addition, substitution, removal and redistribution.

Heterostructured nanoparticles can be produced by the heterogeneous nucleation of new phases at the surface of preformed nanoparticles.[21] Their formation requires selecting a set of reaction conditions that avoid homogeneous nucleation of the new phase. Overall, when adding precursor to preformed nanoparticles under reaction conditions, the phase miscibility, the interface energy between the phases and the surface energy of each phase will determine the compositional distribution of the final nanoparticles. Being dependent on surface energies, this phase distribution can be directed by the use of surface ligands and modulated by the reaction conditions.

Substitution reactions are extremely powerful to adjust the nanoparticle composition, and even to create materials with new crystallographic phases. Generally, two types of substitutions are differentiated depending on the involvement or not of a redox process in the replacement of an atom from the crystal by one in solution. Substitutions not involving a redox reaction are referred as cation or anion exchange reactions.[18] These ion exchange reactions are driven by the energy balance between the lattice and surface energies of the initial and final phases and the desolvation and solvation energies of the replacing and replaced ions. The reaction can be thus controlled by adjusting ion solvation energies through incorporating proper solvating elements in the solution. When the substitution reaction involves a redox reaction, it is referred to as galvanic replacement.[19] In this case, typically a cation in solution incorporates into the nanoparticle lattice after being reduced with electrons provided by a former lattice atom which simultaneously moves to solution in a more oxidized chemical state. Being most elements solvated in an ionic form, galvanic replacement reactions are generally used to modify the composition of metals and metalloids that include zerovalent elements. However, this substitution reaction has been also demonstrated effective in ionic compounds such as oxides. Galvanic replacement is driven by the difference in reduction potential between the replacing and replaced elements, and thus generally proceeds in a unique direction. Substitution reactions can be used to replace completely an element by another to reach a new composition, or just partially to introduce controlled amounts of dopants, phonon scattering centers or elements that modify the band structure of the former material. Heterostructured nanoparticles can be also efficiently produced by partial atomic replacement.

The composition of pre-grown nanoparticles can be also adjusted by subtractive reactions, such as a reduction of an oxide to a metal using H_2 for instance or a selective etching to eliminate a template for example. Additionally, thermal treatments can be used to improve or change nanoparticle crystallinity or to redistribute the composing elements, transforming a core–shell structure into an alloy for instance or introducing a surface ion within the nanoparticle lattice to play a doping role.

2.2. Solution synthesis of thermoelectric nanoparticles

An extensive collection of solution-based protocols to produce nanoparticles is available and has been exploited to produce nanoparticles of several potential thermoelectric materials (Fig. 4).

8 | Chem. Soc. Rev., 2017, 00, 1–19

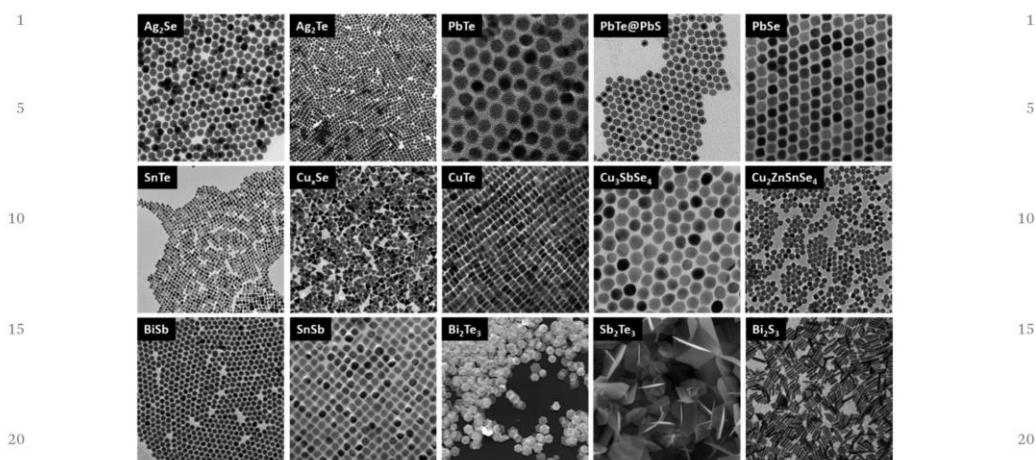This journal is © The Royal Society of Chemistry 2017

Fig. 4 Electron microscopy micrographs of a selection of solution processed nanoparticles with sizes in the range from 5 nm to around 100 nm produced by the authors of this review. See Fig. S2 (ESI†) for further details.

However, most nanoparticle synthetic routes have been developed for the production of elemental nanoparticles, particularly novel metals, and chalcogenides, including oxides. More recently the synthesis of antimonides and Si–Ge has been also pursued, but protocols to produce nanoparticles of numerous potential thermoelectric compounds are still to be defined.

2.2.1. Metal chalcogenides. Among the different thermoelectric material families, chalcogenides are by far the most explored in nanoparticle form. This fact is related to their relatively ease of growth in solution and at low temperature, the wide range of suitable commercial precursors in the proper oxidation state and to their multiple applications beyond thermoelectricity.[16] Numerous solution-based protocols to produce not only binary but also much more complex chalcogenides including multinary compounds with substitutional dopants and heterostructured nanoparticles have been produced with excellent quality.[16,21,22] Within the chalcogenide group, tellurides are generally characterized by the largest σ and lowest band gaps and κ, but higher costs and a smaller range of commercial tellurium sources for the production. Thus, most tellurides are produced using non-commercial, but easily synthesized precursors, such as tellurium complexes with trioctyl- or tributyl-phosphine, K_2Te or $Te(SiEt_3)_2$. At the other end, besides oxides, sulfides provide the lowest σ and the largest band gaps and κ, but at the lowest cost and making use of a very abundant element, with a very large variety of commercial precursors.

2.2.2. Metal oxides. Metal oxides, with high electronegativity differences, are generally characterized by low charge carrier mobilities, high κ_L (stiff lattices) and relatively large band gaps. Thus they generally provide moderate ZT values peaking at relatively high temperatures. However, some metal oxides are considered promising candidates for high temperature applications due to their low-toxicity, abundance and good stability at high temperatures even at ambient atmosphere.[1] Oxide nanoparticles are generally produced by the decomposition of a precursor molecule containing the required oxygen ions (e.g. oleates) or by the reaction of salts in the presence of ambient oxygen.[13] Water-based synthesis protocols and air atmospheres can be used, what represents an important advantage in terms of production cost. However, to obtain a proper crystallinity, hydrothermal synthesis protocols at pressures above ambient are generally required.[23] Being generally used at high temperatures, relatively severe nanomaterial consolidation processes may be required thus compromising the precise control over nanomaterial parameters obtained from the assembly of high-quality nanoparticles.

2.2.3. Intermetallic and intermetalloid compounds with zerovalent or low-oxidation-state elements. To this category belong several of the most promising classes of thermoelectric materials, including Skutterudites, clathrates, half-Heuslers, silicides, and Si–Ge alloys, most of them having Sb, Sn, Si or Ge as the most electronegative element. However, compared with covalent but polar chalcogenides and ionic oxides, the synthesis of nanoparticles of non-polar or weakly polar compounds containing zerovalent or low-oxidation-state elements is much less developed. This is in part attributed to the reduced number of alternative applications for these compounds in nanoparticle form and their high sensitivity to the ambient atmosphere. An additional difficulty is their high synthetic complexity requiring, in most cases, a change of precursor chemical state, since usually metals and metalloids are solvated either as ions or as

polar monomers and only few commercial organometallics containing metals in zerovalent state exist, *e.g.* carbonyls.

As weak reducing agents, amides, carboxylates, amines and alcohols, and particularly oleylamine and ethylene glycol, are very commonly used. When stronger reductants are required to produce nanoparticles containing elements with highly negative reduction potentials, hydrazine complexes, or alkali metal borohydrides and trialkylborohydrides are usually selected.[13] In terms of contamination, it should be noted that borohydrides may leave some boride behind, tetrabutylammonium bromide some bromide and the decomposition of carbonyls significant amounts of carbon. In terms of precursors, M–N bonded precursors, *e.g.* metal and metalloid alkyamides $M(NR_2)$ and silylamides $M[N(SiMe_3)_2]_n$, are particularly suitable to produce highly reduced nanoparticles.[24] They are characterized by a high reactivity, the absence of oxygen atoms that could form metal oxides, and a facile thermal decomposition or reduction. M–N compounds also provide lower level of carbonization than M–C compounds. However, $M(NR_2)$ are highly sensitive to oxygen and moisture. Also, silyl- and alkylamides, which are commercially available as precursors for atomic layer deposition or chemical vapor deposition, are exceedingly expensive for applications requiring large active materials volumes such as thermoelectrics. In this regard, the *in situ* formation of M–N bonds from lower cost and readily available salts represents a strong advantage.[25] Besides its high reactivity and proper chemical state of the decomposition product, an additional advantage of such complexes is the use of the amide as surface ligand controlling the nanoparticle nucleation and growth.[24]

Skutterudites. The term Skutterudites refer to MA_3 compounds, where M is a metal atom such as Co or Fe and A is a pnictogen, having the $CoAs_3$ cubic crystal structure. The particular interest on Sb-based Skutterudites in large part relies on their low κ_L associated to the presence of two voids per unit cell which in the case of antimonides are large enough to accommodate guest ions of alkaline earth or rare earth elements: $E_yT_4X_{12}$ (E = alkaline earth or rare earth element; T = transition metal; X = pnictogen). The filling has a double goal; to strongly decrease κ_L through the rattling of the guest ion and to control the charge concentration within the material through charge injection from the filler to the structure. Additional substitutions, particularly at the pnictogen site result in an important additional reduction of κ_L through the lattice distortion. Overall, nanoparticles with relatively complex compositions are thus required. Generally, antimony and antimonide nanoparticles have been produced by the reduction of an antimony salt using strong reducing agents such as sodium borohydride or $Li[Et_3BH]$.[26] Additionally, the synthesis of Skutterudite nanoparticles by hydrothermal methods has been reported in few works.[27] However, the compositional engineering required to optimize thermoelectric properties has not been reached at the nanoparticle level.

Si and Ge. Si, Ge and Si–Ge solid solutions show excellent optical, optoelectronic and ion intercalation properties, which make them suitable for several applications. Thus, several solution synthesis protocols for the production of nanoparticles of these materials have been developed in the last decade.[28] These nanoparticles are generally produced by the decomposition of organometals, the reduction of salts using a strong reductant, such as $LiAlH_4$, or the reaction of an alkali silicide and/or germanide with ammonium salts. Nanowires of these materials have been also produced, typically using metal nanoparticles as catalyst.

Metal silicides. Few reports detail solution-synthesis routes to produce nanoparticles of metal silicides, most of them with a focus on the catalytic application of these materials. In solution, silicide nanoparticles have been formed by silicification of elemental nanoparticles through the reaction of an organosilane or even $SiCl_4$ with the preformed nanoparticle.[20] This approach resembles the strategy to produce silicon nanowires in solution using a catalyst but properly adjusting the ratio of the two elements. Such strategy is however limited to metal silicides where an initial elemental nanoparticle can be easily formed, which is not the case for a number of potential thermoelectric compounds, *e.g.* Mg_2Si.

Clathrates. Clathrates are characterized by open host frameworks consisting of polyhedral cages made by tetrahedrally coordinated Si, Ge and Sn, and less frequently Al and Ga. Within these cages, guest atoms, generally alkali metal or alkali earth metals, accommodate and are ionized providing large charge carrier densities. The additive strategy used to produce metal silicides cannot be used to produce such intermetallic clathrates, due to the very different crystal structures involved and the limitations in the production of template alkali metal or alkaline earth metal nanoparticles where Si, Ge or Sn can diffuse. Nanoparticles of clathrate-II phases have been produced using an ionic liquid as a solvent and other phases of the K_xGe_y and Na_xSi_y as precursors in the presence of 18-crown-6.[29] Recently synthetic routes for the preparation of nanoparticles of bimetallic compounds containing Ga and especially Sn have been also developed for catalytic applications. As an example, Ga- and Sn-based nanoparticles were formed in the presence of oleylamine using tetrabutylammonium bromide and *n*-BuLi as reductants, respectively.[30] Sn-Based intermetallics for catalytic uses have been also very recently produced in water through a hydrothermal process using stannous chloride and sodium hydroxide.[31] These procedures may show the way to produce nanoparticles with proper composition and clathrate phases for thermoelectric application.

Half-Heuslers. Among the main currently proposed thermoelectric materials, half-Heusler phases, with a MgAgAs crystal phase, probably represent the most challenging material to be produced in nanoparticle form by solution-based methods. The most investigated thermoelectric compounds are solid solutions of MNiSn and MCoSb (M = Ti, Zr, Hf), with a high compositional complexity, *e.g.* $Hf_{1-x}Zr_xCoSn_{1-y}Sb_y$.[32] Such compositional complexity requires defining new protocols for either the simultaneous reduction of the different precursors to

10 | *Chem. Soc. Rev.*, 2017, **00**, 1–19

This journal is © The Royal Society of Chemistry 2017

form the alloy or the intricate and perhaps unfeasible successive addition of each element.

3. Nanoparticle purification and surface engineering

The use of liquid solvents demands additional post-synthesis processing steps when compared with solvent-free strategies. Nanoparticles need to be collected from the solution and purified to remove both the compounds used to control their nucleation and growth and the reaction side products that cannot escape from the liquid phase. Depending on specific properties and chemical stability, nanoparticles can be collect from the solution by precipitation and decantation of the liquid, magnetic separation, filtration and electrophoresis. This step also separates them from soluble reaction side-products, unbound ligands and non-reacted precursors. Generally, additional purification steps are required to completely remove organic and inorganic impurities, especially those bonded to the nanoparticle surface. Among them, the simplest and most widely used approach to remove organics is their thermal decomposition by means of an annealing process under inert gas or vacuum. Annealing definitively results in nanomaterials with enhanced transport properties, but at the cost of partially sintering the nanoparticles, potentially modifying the distribution and even nature of phases, and leaving a residual carbon layer that may limit thermoelectric performance. To minimize the effect of the annealing process and the amount of residual carbon, the original surface ligands can be replaced in a previous step with shorter and weak coordinating molecules such as pyridine, hydrazine, ammonia and n-butylamine. Once the original bulky ligands have been fully replaced, a mild thermal treatment, generally with the nanoparticles already assembled/aggregated, can be applied.

Beyond simply removing surface organic ligands, during the purification process, the nanoparticle surface chemistry can be engineered to reach improved thermoelectric performance.[11,12,15,33–35] Ligands chemically bonded to surface atoms should be thought as part of the nanoparticle since when removed or replaced, the overall nanoparticle stoichiometry and valence balance can significantly change. Notice that surface atoms typically account for densities in the range of 10^{20}–10^{21} cm^{-3}, which is one or two orders of magnitude above the optimum charge carrier concentration for thermoelectric application.

Both the ligand (and thus ligand removal) influence on the nanoparticle properties and the suitability of the strategy to remove/replace it depend on the type of bonding to the nanoparticle surface. Taking into account the nomenclature of coordination complexes, surface ligands can be classified in three types (Fig. 5).[15,33] L-type ligands are neutral two-electron donors with a lone electron pair that datively coordinate neutral surface metal ions (cations): $e.g.$ amines (RH$_2$), phosphines (R$_3$P) and phosphine oxides (R$_3$PO). X-type ligands require one electron from the nanoparticle surface site to form a two-
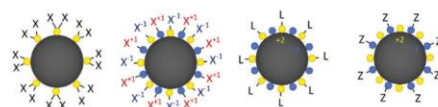

Fig. 5 Covalent bond classification of surface ligands.

electron covalent bond and coordinate with non-neutral cationic sites, $e.g.$ carboxylates (RCOO$^-$), thiolates (RS$^-$), phosphonates (RPO(OH)O$^-$) and inorganic ions such as Cl$^-$. Z-type ligands, generally inorganic cations, bind as two-electron acceptors at non-neutral anionic sites, $e.g.$ Pb(OOCR)$_2$ or CdCl$_2$. In general, growth in the presence of X-type ligands results in nanoparticles with non-stoichiometric compositions, with an excess of cations, thus n-type electrical conductivity. In non-polar solvents there should be electrostatic neutrality and thus the number of X-type ligands must compensate the off-stoichiometry and/or $vice\ versa$. In polar solvents nanoparticles can carry a certain amount of charge, around one elemental charge per nm^2 of surface or a few tens of charges per particle, which is compensated by counterions from the diffuse ions cloud around each nanoparticle in solution that could also end up in the final nanomaterial. Some molecules can bind both as L-type or X-type ligand. As an example, oleic acid can bind as a bidentate L-type ligand on stoichiometric or neutral surfaces
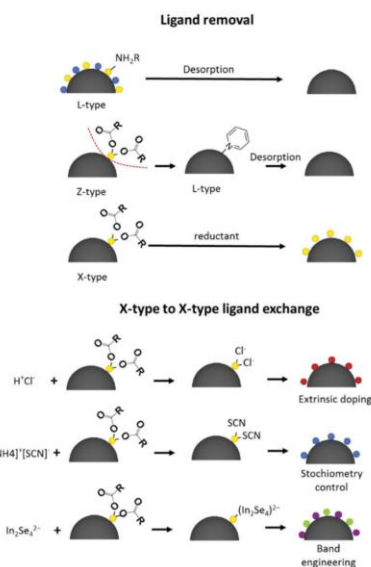

Fig. 6 Examples of possible surface engineering processes for nanoparticles, including ligand removal and ligand exchange for extrinsic doping, stoichiometry control and band engineering.

and as X-type oleate ions on Pb-terminated surfaces.[33] Frequently, combinations of ligands are intentionally or unintentionally used. As an example, relatively large organic ligands such as oleate cannot pack densely enough to saturate all metal dangling bonds on polar surfaces, thus OH⁻ and Cl⁻ groups may play an important role.[36]

The manipulation of the surface chemistry to adjust nanoparticle and nanomaterials properties is currently a highly dynamic research area. Major breakthroughs in modifying the nanoparticle surface chemistry to tune transport properties have been recently achieved through the use of inorganic surface ligands such as metal–chalcogenide complexes, thiocyanate and tetrafluoroborate salts, inorganic oxoanions and Lewis acid–base adduct, which allowed producing nanomaterials with relatively high charge carrier mobilities (Fig. 6).[34] In the same direction, atomic replacing ligands such as halides, chalcogens or metal ions, have been also explored to improve transport properties and particularly thermoelectric performance. In this case, the ligand removal takes place simultaneously to a cation or anion exchange.[37]

4. From nano to macro: nanoparticle assembly and nanomaterial consolidation

To fabricate nanoparticle-based thermoelectric devices, it is necessary to assemble the nanoparticles at a macroscopic scale, either in film or bulk form. The thermoelectric properties of the final material will depend on the nature and properties of the individual nanoparticles, but also on their organization, interconnection, packing density and relative crystal orientation within the nanocomposite. Nanoparticles can be assembled into ordered or disordered films or bulk nanostructured solids (Fig. 7). In thermoelectric nanocomposites, the suitability of an organized or random phase distribution is a topic of debate. Randomly organized phases and wide nanocrystal size distributions will effectively scatter a wider range of the phonon spectrum. On the other hand, an organized distribution of nanoinclusions will provide lower charge carrier scattering and could beneficially modify the DOS if in the quantum confinement regime.

4.1. Organized superlattices

One of the most exciting research areas within the thermoelectric field is the investigation of quantum confinement effects on the thermoelectric properties of single quantum dots, nanowires and superlattices. Identical excitement awakes in the nanoparticle community the fabrication of single quantum dot or nanowire devices and especially the assembly of nanoparticles into organized supercrystals.

Organized nanoparticle superstructures, eventually assemblies of coupled quantum dots forming 2D or 3D quantum dot or quantum well arrays, can be produced by inducing self-assembly of very high quality colloidal nanoparticles directly in
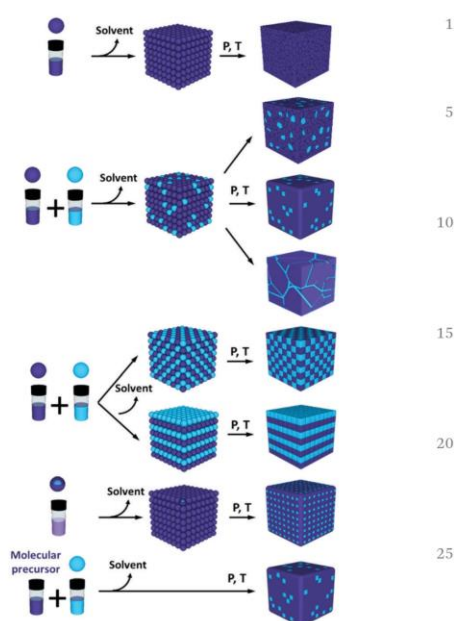

Fig. 7 Examples of the multiple possibilities for nanoparticles consolidation into ordered and disordered nanocomposites.

solution, by changing a parameter that compromises colloidal stability, or through solvent removal.[11,12,38,39]

Like the synthesis of nanoparticles, the self-assembly process or superlattice nucleation and growth depends both on interactions between building blocks, *i.e.* nanoparticles in this case, and on the process kinetics. The interactions between nanoparticles can be van der Waals or dipole–dipole, magnetic, electrostatic and ligand related. van der Waals and magnetic interactions present in certain materials are core-related interactions, thus difficult to modulate and rarely used to control assembly. Assembly is thus usually triggered by adjusting the surface/ligand-based interactions.

Ligand related interactions include electrostatic, steric, osmotic, elastic solvophilic, solvophobic and depletion interactions. These interactions are suitable to trigger nanoparticle assembly as they can be externally modulated through several processes, including ligand desorption or exchange, addition of an antisolvent, increase of concentration by solvent evaporation or modification of the relative binding energy and thus colloidal stability through temperature control.

The most used strategy to produce organized superlattices is to force a slow nanoparticle assembly in solution by increasing concentration through solvent evaporation. This requires nanoparticles with a very high colloidal stability as the assembly

process may take up to several days. Since ligands are key to keep the nanoparticles in solution during the superlattice growth, they need to be removed *a posteriori* to produce assemblies with proper thermoelectric properties. This removal may create abundant cracks, which need to be filled with additional nanoparticles. By this method, single component thin film assemblies driven by entropy maximization are easily produced from highly monodisperse nanoparticles.[9] To produce multicomponent superlattices with virtually any composition from the self-assembly of different nanoparticles types, a driving force for nanoparticles to organize in a dictated order is necessary. This driving force could be again the maximization of the entropy when using particles of different sizes/shapes,[39] electrostatic between differently charged particles or provided by organic linkers that covalently interact, *e.g.* using click chemistry.[38] Alternatively, a simpler approach to produce organized nanocomposites is the use of building blocks that already contain the different components in the correct ratio, *i.e.* heterostructured nanoparticles.

Electrostatic interactions are particularly well suited to produce organized nanocomposites. Electrostatic forces arise from the presence of charge on the nanoparticle surface associated to the presence of charged ligands in polar solvents, including absorption of ions and protonation/deprotonation of surface groups. Such charged nanoparticles in polar solvents attract counterions from the solution, resulting in an electrical double layer which screens charge at relatively long distances, but has associated strong interaction potentials at short ranges. The strength and sign of this interaction depends on the total nanoparticle surface charge and on the screening capability of the solution which is determined by the ion concentration. Both, the nanoparticle charge and the screening capability can be adjusted to properly drive electrostatic assembly. Particularly interesting to trigger electrostatic assembly while in solution is the use of pH-sensitive surface ligands which protonation or deprotonation can be triggered to adjust the surface charge density.

The assembly kinetics or rate of superlattice growth is another key parameter to produce extended assemblies. The formation of organized assemblies requires close to equilibrium conditions. Attractive energies need to be moderate to do not block the nanoparticle position at the first arrival site, but to allow some degree of reversibility in the binding of the nanoparticles, for them to properly rearrange. When an external stimulus or a change in conditions triggers a too rapid, diffusion-limited, aggregation, the final superstructure is disordered, often fractal.

Overall, organized multicomponent superlattices with a large variety of crystal structures have been obtained by several groups at length scales up to 100 micrometers generally by entropy maximization.[39] 3D nanocomposite crystals in the micrometer scale have been also produced by electrostatic assembly. However, while the study of the influence of compositional and organizational parameters on the functional properties of nanoparticle assemblies is one of the most appealing research areas in the nanomaterials field, the transport

properties of current non-consolidated assemblies are far away from those required to reach competitive thermoelectric performances. This fact and the difficulties in measuring transport properties of the relatively small assemblies produced, especially heat transport, have prevented obtaining complete and reliable data sets of the thermoelectric properties of such assemblies. Nevertheless, we foreseen this to be a major field of development in the short and medium term.

4.2. Nanoparticles random aggregation and consolidation

Nanoparticle-based thermoelectric nanomaterials are more generally produced by the random aggregation and subsequent consolidation of solution-processed and surface-engineered nanoparticles (Fig. S1 (ESI†) and Fig. 7). In this strategy, nanocomposites are easily produced by randomly blending in solution different types of nanoparticles. Such versatile approach can yield nanocomposites with virtually any composition. Not mediating any precise assembly strategy, the distribution of phases within the final material will be random. Alternatively, the phase distribution and component ratio can be also set at the nanoparticle level, within heterostructured nanoparticles.[21]

The availability of nanoparticles in solution allows a straightforward production of nanocrystalline films by conventional ink-based deposition technologies. On the other hand, bulk nanomaterials are generally produced by hot pressing dried nanoparticles, *i.e.* a nanopowder, into a dense pellet using uniaxial pressures from tens to hundreds of MPa while simultaneously heating the material at a temperature between 200 and 400 °C. An alternative consolidation technique is spark plasma sintering, which involves flowing a relatively high pulsed DC current through a graphite die containing the nanopowder while a uniaxial pressure is simultaneously applied.

The use of thermal treatments may rearrange ions within each crystal domain, reshaping it, potentially changing its phase and eventually forming secondary phases. It can also enable ion diffusion between adjacent crystals, resulting in crystal domain growth, alloying and phase redistribution. Also, off-stoichiometries can be created by the evaporation of particular elements.

Atomic diffusion during the consolidation process can also be used in ones favor to incorporate and/or activate electronic impurities located at the nanoparticle surface. It can be also used to selectively grow the crystal domains of one of the nanocomposite phases to favor charge transport, while maintaining a second phase with nanometric dimensions to provide efficient phonon scattering, potential energy filtering and/or modulation doping. Alternatively, such matrix-nanoinclusion nanocomposites can be produced by crystallizing a metal–organic precursor in the presence of nanoparticles functionalized with the same metal–organic.[40] In this case, a fast crystallization is required to kinetically trap the nanoparticles within the crystal. While this very appealing strategy has been used for the production of thin films for optoelectronic

applications, to the best of our knowledge, its use to produce relevant thermoelectric systems is yet to be explored.

4.3. Crystallographic texture

One main limitation of nanoparticle-based bottom-up approaches is the difficult formation of crystallographically textured nanomaterials, which is a necessary property in the numerous thermoelectric compounds that have highly anisotropic thermal and electronic transport properties, *e.g.* Bi–Sb–Se–Te alloys and SnSe. Texture or orientational order can be induced during assembly/aggregation (alignment) or during the consolidation process (reorienting/recrystallizing). Owing to the different surface energies and chemistries along different facets, orientational order can be reached during positional organization when using high quality and highly asymmetric nanoparticles, such as disks or nanorods.[39] Additionally, the application of external fields, *e.g.* electrostatic or magnetic, during the nanoparticle assembly/aggregation process may aid the crystallographic alignment.[41] As an example nanorods of polar semiconductors generally present a permanent dipole moment that can be used to align them under an external electrostatic field. Alternatively, crystallographic texture can be potentially reached during the consolidation process, also by applying external fields to reorganize the ions within the crystals or consolidating the material under severe plastic deformation conditions, *e.g.* high pressure torsion.[42] However, as these processes involve ion rearrangement, crystallographic texture may be accomplished at expenses of losing the parameter control acquired at the nanoparticle synthesis level.

5. Charge carrier concentration modulation

A precise adjustment of the charge carrier concentration is essential to optimize thermoelectric performance. Within a nanoparticle-based bottom-up engineering strategy, this parameter can be modulated at different processing steps (Fig. 8). At the nanoparticle level, the charge carrier concentration can be
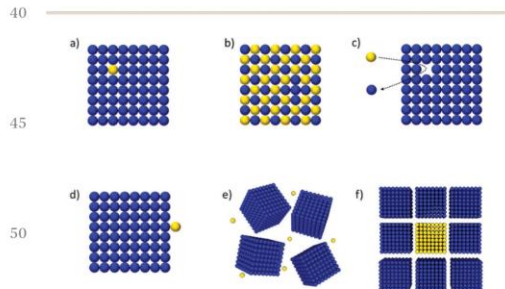
Fig. 8 Scheme of possible strategies to tune doping in nanoparticle-based solution-processed nanomaterials: (a) extrinsic dopants; (b) stoichiometry control; (c) atomic substitution; (d) surface chemistry; (e) dopant additives during consolidation; and (f) modulation doping.

tuned by introducing electronically active extrinsic impurities, adjusting the material stoichiometry and/or exploiting the intrinsic defect chemistry of the material. Such compositional and defect adjustment can be performed during synthesis or through post-synthesis processes (Fig. 3). Alternatively, the charge carrier concentration can be modulated by controlling the nanoparticle surface chemistry during the ligand removal/exchange process (Fig. 5). Additionally, during assembly and consolidation, electronically active additives can be introduced or compounds with suitable electronic band alignment can be combined, either by blending or using heterostructures containing both materials, so one of them injects charge into the other, *i.e.* modulation doping (Fig. 8).

5.1. Doping during nanoparticle synthesis

Reaching proper charge carrier concentrations for thermoelectric application, $\sim 10^{19}$ cm^{-3}, requires a heterovalent impurity concentration, off-stoichiometry balances or electronically active defect concentrations of around 0.01–0.1%, which in 10 nm nanoparticles corresponds to 1–30 electronically active species per particle. Several strategies have been developed to modulate the charge carrier concentration at the nanoparticle level. The most common is the inclusion of the appropriate amount of a dopant precursor in the initial reaction solution.[22,43,44] In this approach, the dopant and host precursors are intimately mixed even before the nucleation step, what should provide a highly homogeneous doping. However, the selection of the proper precursors, coordinating ligands and reaction conditions is critical to enable an effective incorporation of the extrinsic element. The reactivity of the dopant precursor need to be very similar to that of the host precursor for both to be incorporated to the growing nanoparticle. The simultaneous incorporation can be favored by choosing doping and host precursors that are chemically similar and/or proper coordination ligands that allow balancing reactivities. Surfactants, which determine surface energies, may also favor or hamper the incorporation of particular external ions. In most cases, the introduction of impurities inevitably calls for a kinetic control of the nanoparticle growth to block the foreign ion within the lattice.

An alternative approach to facilitate dopant insertion and its homogeneous distribution is the use of metal–organic molecules incorporating inorganic clusters that contain the already bound host and doping ions in the proper ratio. While the use of such single source precursors is a valid strategy to produce nanoparticles with extremely high dopant concentrations, the incorporation of 0.01–0.1% impurities required in the thermoelectric field calls for excessively large precursor molecule or obligates to combine these compounds with other host precursors, which brings on the same reactivity problems described above.

Another approach is to introduce the dopant ions within preformed nanoparticles. This can be carried out by means of precisely controlled partial ion exchange processes, an strategy somehow comparable to ion implantation in thin film technologies.[18] Being the overall material lattice easily

accessible through the very large and homogeneously distributed surface of colloidal nanoparticles, this strategy is very effective, even at room temperature. The impurity concentration can be controlled here by just tuning the amount of foreign ions in solution. However, limitations are found with particular ion exchange reactions which may not be energetically favorable, the potentially limited selectivity on the exchanged ion in multinary materials, and the eventual condensation of impurities to nucleate secondary phases.

Besides introducing impurities, an alternative strategy to tune the charge carrier concentration at the nanoparticle level is to unbalance its stoichiometry. This doping strategy is limited by the possible change of valence of elements within the structure and the creation of paired defects with a counteracting electronic role. The nanoparticle stoichiometry can be modulated by just tuning the amount of precursors in the initial solution or using proper multicomponent metal–organic precursors. Alternatively, in synthesis processes where not all ions incorporate simultaneously, the reaction time can be used as a convenient parameter to easily adjust stoichiometry.

Finally, off-stoichiometric compositions and electronically active defects can also be created by introducing isovalent impurities that distort the lattice and reduce the energy of formation of such defects, as is the case in the most used thermoelectric alloys, i.e. Bi–Sb–Te–Se.

5.2. Surface doping

The nature of nanoparticle-based thermoelectric nanomaterials is such that the required doping level (0.01–0.1%) is well below the concentration of surface atoms that are non-fully coordinated or are coordinated with external elements ($>1\%$). Therefore, to properly engineer the nanoparticle surface chemistry suffices to reach charge carrier concentrations in the required range. The drawback is that a non-proper control may also result in large unwanted charge carrier densities. As an example, despite the intrinsic n-type nature of lead chalcogenide nanoparticles due to preferential cation-terminated surfaces, when removing surface ligands in the presence of even very small amounts of oxygen, acceptor states are created on the surface, changing the electronic character to p-type.[44]

The charge carrier concentration can be adjusted by balancing the ratio of surface cations and anions in polar compounds through the use of proper surface ligands. Surface ligands can also act themselves as donating or accepting dopants.[44] For instance, halide passivation and metal cations on the surface have been proven to control the net nanoparticle surface charge while at the same time preventing the formation of deep electronic traps by avoiding oxygen absorption.[45] Despite this approach has produced outstanding results for quantum dot solar cells and photodetectors, little work has been done in this direction in the thermoelectric field. As one of the few examples in the thermoelectric field, a strong inorganic acid (HCl) was recently demonstrated to be able to strip carboxylic acids from the nanoparticle surface forming oleic acid in solution and leaving chlorine ions on the nanoparticle surface. During a subsequent consolidation step, Cl^-

ions diffused inside the crystal structure to act as a donor, providing the nanomaterial with n-type electrical conductivity and a tunable charge carrier concentration.[37]

5.3. Doping during consolidation

Another strategy to control the charge carrier concentration in nanomaterials produced by the aggregation of nanoparticles and its subsequent consolidation is to simply introduce the electronic dopant, generally in the form of a salt, within the nanopowder to be consolidated or the ink to be printed. This very simple strategy is only useful when applying a consolidation treatment at a sufficient temperature for the dopant to homogeneously diffuse and eventually activate within the crystal lattice. In order not to condition the temperature of the consolidation treatment to this process, small ions and proper precursors containing a counterion that is volatile, e.g. $NaNH_2$, or it is matched with the nanomaterial composition, e.g. Na_2Se, are used.[16]

5.4. Modulation doping

Maximized electrical conductivities at a given charge carrier concentration can be obtained by combining different types of nanoparticles of different materials, such that one of them is able to inject charge into the other.[2,3] This strategy allows removing ionized impurities from the host material thus providing higher charge carrier mobilities than equivalent ionically doped materials. Ideally the host material provides high S and charge carrier mobility, and the charge injecting nanoinclusions are homogeneously distributed throughout the host and contain very high charge carrier concentrations and a proper electronic band structure for them to spill over the host. In this regard, a particularly interesting class of nanocomposites is that of a semiconductor matrix with metal or semi-metal nanoinclusions. These nanocomposites can be produced by combining semiconductor and metal nanoparticles in the proper ratio or using metal-semiconductor nanostructures.[3] So far, this strategy has been demonstrated effective only to produce n-type nanocomposites from the combination of a semiconductor host with low work function metal nanoparticles, and it remains to be demonstrated for p-type materials potentially obtained by combining a semiconductor host with metal nanoparticles characterized by a large enough work function.

6. Solution-processed thermoelectric devices

Nanoparticle-based bulk nanomaterials can be sliced into cubes and used to manufacture thermoelectric modules with the conventional pellet-based architecture. However, the availability of thermoelectric materials in the form of nanoparticles, and particularly colloids, also enables the use of ink-based technologies for the high throughput fabrication of cost-effective thermoelectric devices.[46] In this regard, the fabrication of nanoparticle-based thermoelectric devices shares advantages
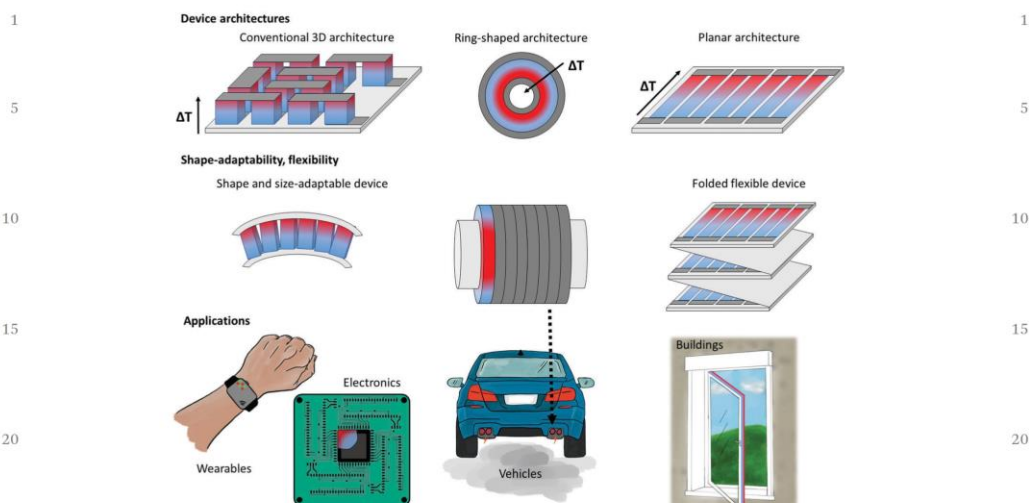
Fig. 9 Thermoelectric device architectures and examples of their applications.

with the processing of organic modules. The use of solution-based processes for the device fabrication also provides extended device versatility in terms of size and shape, including flexible, conformable or rigid modules with specific geometries. In this way, compared with conventional ceramic-based devices, solution-processed thermoelectric modules could be not only more cost-effective and lighter, but also provide an improved thermal contact (Table S1, ESI†).

For thermoelectric modules to operate at reasonable voltages, they have to include a significant number of semiconducting elements, alternating p- and n-type, that are connected thermally in series and electrically in parallel (Fig. 9). Another main particularity of most thermoelectric modules is their three-dimensional architecture as they usually generate/harvest temperature gradients that are orthogonal to the device plane. Therefore, the fabrication of thermoelectric modules generally requires depositing materials with proper 3D spatial resolution. The higher the spatial resolution in the placement or deposition of the thermoelectric elements, the larger the number of elements that can be placed in a given area and thus the higher operation voltages potentially used. The density of thermoelectric elements is especially critical when generating/harvesting small temperature gradients, *i.e.* being controlled/generating a very small voltage per thermoelectric element. Due to the historically manual fabrication of thermoelectric modules, they are generally produced with lower densities of thermoelectric elements than would be desirable for a number of applications. Conventional ink-based technologies such as screen printing or inkjet printing provide high enough resolutions to increase at least one order of magnitude the density of

elements of current modules, what would result in one order of magnitude higher open circuit voltages. However, the limitation of conventional ink-based technologies is that they typically produce relatively thin features, which complicates their contact in two different planes and may limit the supported temperature gradients.

A planar architecture, *i.e.* with the temperature gradient in the support plane, simplifies manufacturing and allows producing longer thermoelectric elements using solution processing technologies.[47] However, the main disadvantage of this architecture is the contribution of the support to the heat conduction, reducing the available temperature gradient. To get rid of the support limitation, self-supported layers, generally incorporating a percentage of a polymer to improve mechanical properties, have been also produced. A second disadvantage of the planar architecture is the low density of thermoelectric elements printed when compared with 3D devices. This reduce number of thermoelectric elements generally calls for the assembly of multiple planes, by folding the substrate for example, what may require not obvious solutions for automated manufacturing and for proper thermal contact.

The convenient fabrication of flexible devices is one of the most appealing characteristics of solution processing technologies. In this direction, nanoparticles have been deposited in several flexible supports including polyimides or infiltrated in textiles or even paper.[48,49] All these supports impose a limit on the temperature of the post-deposition processes and on the operation temperature of the device. Alternatively properly electrically isolated metal foils could provide advantages in terms of thermal contact with the heat source/sink (in 3D device architectures) and operation temperature range.

Alternatively, rigid modules with specific geometries adapted to particular heat sinks/sources such as pipes could provide equally effective thermal contacts and optimized form factors. As an example, for radial applications, such as energy harvesting in pipes, ring-shaped TE device have been also developed (Fig. 9).[22]

7. Challenges, opportunities and future prospects

Breakthrough nanomaterials enabling the fabrication of more-efficient thermoelectric devices will be reached through the control of material parameters and the understanding of mechanisms and phenomena at the atomic level. At the same time, the outcoming industrial innovation will be necessarily supported on cost-effective technologies able to transform this control and understanding into optimized products. In this framework, the bottom-up engineering of nanomaterials using nanoparticles with precisely modulated parameters is a particularly suited strategy for both the development of model materials for basic research and the high-throughput, high-yield and cost-effective fabrication of such complex materials and devices. However to fully access the extremely exciting possibilities that bottom-up nanoparticle-based technologies offer, several challenges remain to be overcome.

First of all, while an exquisite control over material parameters has been achieved at the nanoparticle level, we are still far from extending the same level of control to the macroscopic scale. Consolidation processes currently used to improve charge transport generally activate atomic self-diffusion through considerable distances compared with the nanoparticle size. This translates into considerable atomic redistribution including crystal domain growth, alloying or phase segregation, stoichiometric changes and interface redefinition. To overcome this issue, consolidation processes at mild temperatures should be used, but this requires major advances in the engineering of the surface chemistry of nanoparticles to reach competitive charge transport properties. Additionally, high temperature applications inevitably call for severe stabilization processes that discard the use of unstable nanoparticle assemblies. In all cases, it should be taken into account that nanocomposites are intrinsically metastable materials and their stability over relevant periods of time (tens of years) should be determined for each given composition, crystal phases and crystal domain sizes.

Most current high-performance thermoelectric materials consist of a crystalline semiconductor host with high S and charge carrier mobility that contains nanoinclusions for modulation doping, phonon scattering and charge carrier energy filtering. The production of such host-nanoinclusion nanocomposites by bottom-up assembly is not straightforward and has been very rarely attempted. The combination of molecular precursors with low crystallization temperatures to produce the host with properly functionalized nanoparticles as the final nanoinclusion, combined with a proper crystallization process may be the most facile strategy to produce the targeted

architecture. Alternatively, core–shell nanoparticles, containing a relatively low melting point material as host in the shell and a high melting point material as nanoinclusion in the core, could also result in the targeted nanocomposite after proper consolidation.

The charge carrier concentration is a particular important parameter that can be intentionally or unintentionally modified at different processing steps. At the nanoparticle level, the charge carrier concentration will depend on the type and concentration of extrinsic dopants and defects and on the overall stoichiometry and surface chemistry, including the crystal atomic termination and the concentration and type of ligands. It will also depend on the presence of intentionally or unintentionally introduced impurities, compositional variations and atomic reorganization during the assembly/consolidation steps and on the combination of materials within a nanocomposite. All these parameters and the effect of the processing atmosphere need to be properly controlled to be able to reliably modulate the final charge carrier concentration with the precision required to optimize performance. While significant progress have been done in the last decade in this direction, reaching nanoparticle-based materials with record thermoelectric figures of merit, still major advances both in terms of fundamental understanding and nanoparticle engineering abilities are required to precisely modulate such key parameter.

Another important challenge is the production of intermetallic or intermetalloid nanoparticles that include zerovalent or low-chemical-state elements with the compositional complexity required for thermoelectric application. The little work done in this direction, in spite of its interest and the availability of suitable chemicals and synthetic strategies to produce these compounds, offers a clear opportunity to develop and study new technologically relevant materials potentially transcending the thermoelectric field. Besides, beyond producing nanoparticles of materials previously proposed by the solid state chemistry community, the versatility and ease of material screening of bottom-up processes provide a high potential to produce new, unexplored and eventually rationally designed thermoelectric materials with enhanced performances.

A critical difficulty to engineer improved thermoelectric nanocomposites is the poor understanding we actually have on the transport properties of such complex systems. To enable a more rational nanocomposite design, information on the precise effect of crystal domain size, interfaces, phase distribution and quantum confinement on the thermoelectric performance is necessary. This requires extensive computational modelling combined with experimental characterization of a large number of model systems with systematically tuned parameters.

The main current weakness of nanoparticle-based bottom-up assembly processes is the not straightforward production of materials with crystallographic texture. This is particularly limiting in several of the main thermoelectric materials showing highly anisotropic properties, such as Bi–Sb–Se–Te alloys and SnSe. To overcome this challenge, major improvements on the design and engineering of the assembly/consolidation

processes are required. Possible strategies that need to be further developed are the assembly of nanoparticles mediating oriented attachment, the use of external fields to crystallographically align the nanoparticles during assembly/consolidation and the use of nanoparticles with highly anisotropic shapes, particularly nanoplates, nanorods or nanowires.

Particularly interesting opportunities are found on the manipulation of the nanoparticle surface chemistry. A proper surface engineering is necessary to control nanoparticle growth, drive their assembly and modulate their functional properties. This requires additional understanding not only of the surface influence on each process/property, but on the effect of each surface treatment on the final surface composition. To take advantage of the surface chemistry of nanoparticles to improve nanomaterial functional properties, systematic characterization of these surfaces by nuclear magnetic resonance spectroscopy for instance should become as much of a routine as the characterization of the nanoparticles size and shape by transmission electron microscopy or of their crystal structure by X-ray diffraction. We should additionally generalize the definition of nanoparticles by their core and surface composition, besides size, shape and phase.

The industrialization of nanoparticle-based bottom-up engineering technologies will require major engineering advances. The scale-up of the processes used to produce high quality nanoparticles is not fully solved, especially for applications with huge markets that require low costs and large volumes of functional nanomaterials, as thermoelectricity. Scale-up will inevitably require automated processes with 100% yields, very high nanoparticle concentrations in solution, low cost and safe solvents, surfactants, precursors and reductants and the recycling of solvents and possibly side products. Moving toward large scale industrialization paradoxically also requires improving our atomistic understanding of the precursor-to-nanoparticle reaction pathways *via* mechanistic experimental study and fundamental quantum chemistry simulations, to be able to optimize the process not only in terms of product parameters but also cost and reliability. Equally challenging may result the definition of automated processes for the purification and careful control of the surface chemistry of nanoparticles.

Another particularly important challenge is the scale-up of the processes to produce organized and macroscopic nanoparticle assemblies. While the idea of using nanoparticles as atoms to create supercrystals is extremely appealing, fascinating but slow progress is being achieved in this field. While we have the tools to drive assembly, an improved control on surface chemistry and proper crystallizers and crystallization strategies are required. An alternative solution could be the use of heterostructured nanoparticles to produce such organized nanocomposites.

In the thermoelectrics field, performance is generally measured and compared through a material figure of merit, without the need to fabricate prototype devices and test their efficiency. While this probably helped to accelerate the development of new materials, it has conversely delayed the progress on the design and engineering of thermoelectric devices, especially for new processing technologies. In printed thermoelectric devices, besides common difficulties such as crack formation and layer adhesion, the challenge to produce dense layers with sufficient thickness and especially to contact them at to different planes need to be overcome. Additive manufacturing technologies based on material jetting, *i.e.* 3D printing, may significantly help to progress in this area. However, it is not clear if such technologies will be able to reach the production throughputs required for industrialization.

Thermoelectric devices should be designed taking into account their most plausible final application. Taking into account cost-efficiency, thermoelectrics cannot currently compete and it is unlikely they will ever do with steam engines in large-scale energy conversion in Earth or with relatively large-scale non-portable compressor-based refrigerators. The unique advantages of thermoelectric modules are the very precise temperature control they offer, the potential to harvest small temperature gradients, their broad scalability, the portability and their potential cost-effectiveness at small scale. Particularly proper markets are those involving small scale temperature control (*e.g.* electronic devices cooling) and energy harvesting (*e.g.* autonomous self-powered sensors) where the performance of mechanical engines drops off. These applications generally require very high densities of thermoelectric elements to reach proper open circuit voltages. Notice also that particular applications such as active cooling of high power consumption devices may require thermoelectric materials with completely different properties, such as a high κ, which are yet to be developed.[50]

Overall, the future of thermoelectrics strongly depends on our ability to develop new materials with improved performance. Nanoparticle-based solution processing technologies can significantly contribute to this endeavor, while at the same time improving our fundamental understanding of the transport properties of nanomaterials. Efforts invested in this highly multidisciplinary area will be also highly valuable for the development of several other technologies, including photovoltaics, energy storage and sensing.

Acknowledgements

Notes and references

1 *Thermoelectrics Handbook: Macro to Nano*, ed. D. M. Rowe, CRC Press, Boca Raton, FL, 2006.
2 M. Zebarjadi, G. Joshi, G. Zhu, B. Yu, A. Minnich, Y. Lan, X. Wang, M. Dresselhaus, Z. Ren and G. Chen, *Nano Lett.*, 2011, **11**, 2225–2230.

18 | *Chem. Soc. Rev.,* 2017, **00**, 1–19

This journal is © The Royal Society of Chemistry 2017

3 M. Ibáñez, Z. Luo, A. Genç, L. Pivetau, S. Ortega, D. Cadavid, O. Dobrozhan, Y. Liu, M. Nachtegaal, M. Zebarjadi, J. Arbiol, M. V. Kovalenko and A. Cabot, *Nat. Commun.*, 2016, **7**, 10766.

4 G. J. Snyder and E. S. Toberer, *Nat. Mater.*, 2008, **7**, 105–114.

5 W. G. Zeier, A. Zevalkink, Z. M. Gibbs, G. Hautier, M. G. Kanatzidis and G. J. Snyder, *Angew. Chem., Int. Ed.*, 2016, **55**, 6826–6841.

6 K. Biswas, J. He, I. D. Blum, C.-I. Wu, T. P. Hogan, D. N. Seidman, V. P. Dravid and M. G. Kanatzidis, *Nature*, 2012, **489**, 414–418.

7 M. Zebarjadi, B. Liao, K. Esfarjani, M. Dresselhaus and G. Chen, *Adv. Mater.*, 2013, **25**, 1577–1582.

8 A. Shakouri, *Annu. Rev. Mater. Res.*, 2011, **41**, 399–431.

9 R. Y. Wang, J. P. Feser, J.-S. Lee, D. V. Talapin, R. Segalman and A. Majumdar, *Nano Lett.*, 2008, **8**, 2283–2288.

10 R. Venkatasubramanian, E. Siivola, T. Colpitts and B. O'Quinn, *Nature*, 2001, **413**, 597–602.

11 D. V. Talapin, J.-S. Lee, M. V. Kovalenko and E. V. Shevchenko, *Chem. Rev.*, 2010, **110**, 389–458.

12 M. V. Kovalenko, L. Manna, A. Cabot, Z. Hens, D. V. Talapin, C. R. Kagan, V. I. Klimov, A. L. Rogach, P. Reiss, D. J. Milliron, P. Guyot-Sionnnest, G. Konstantatos, W. J. Parak, T. Hyeon, B. A. Korgel, C. B. Murray and W. Heiss, *ACS Nano*, 2015, **9**, 1012–1057.

13 B. L. Cushing, V. L. Kolesnichenko and C. J. O'Connor, *Chem. Rev.*, 2004, **104**, 3893–3946.

14 X. Liu, N. Fechler and M. Antonietti, *Chem. Soc. Rev.*, 2013, **42**, 8237–8265.

15 M. A. Boles, D. Ling, T. Hyeon and D. V. Talapin, *Nat. Mater.*, 2016, **15**, 141–153.

16 C. Coughlan, M. Ibáñez, O. Dobrozhan, A. Singh, A. Cabot and K. M. Ryan, *Chem. Rev.*, 2017, DOI: 10.1021/acs.chemrev.6b00376.

17 M. R. Buck and R. E. Schaak, *Angew. Chem., Int. Ed.*, 2013, **52**, 6154–6178.

18 L. De Trizio and L. Manna, *Chem. Rev.*, 2016, **116**, 10852–10887.

19 X. Xia, Y. Wang, A. Ruditskiy and Y. Xia, *Adv. Mater.*, 2013, **25**, 6313–6333.

20 J. M. McEnaney and R. E. Schaak, *Inorg. Chem.*, 2015, **54**, 707–709.

21 M. Ibáñez, R. Zamani, S. Gorsse, J. Fan, S. Ortega, D. Cadavid, J. R. Morante, J. Arbiol and A. Cabot, *ACS Nano*, 2013, **7**, 2573–2586.

22 Y. Liu, G. García, S. Ortega, D. Cadavid, P. Palacios, J. Lu, M. Ibáñez, L. Xi, J. De Roo, A. M. López, S. Martí-Sánchez, I. Cabezas, M. de la Mata, Z. Luo, C. Dun, O. Dobrozhan, D. L. Caroll, W. Zhang, J. Martins, M. V. Kovalenko, J. Arbiol, G. Noriega, J. Song, P. Wahnón and A. Cabot, *J. Mater. Chem. A*, 2017, **5**, 2592–2602.

23 F. Dang, C. Wan, N.-H. Park, K. Tsuruta, W.-S. Seo and K. Koumoto, *ACS Appl. Mater. Interfaces*, 2013, **5**, 10933–10937.

24 M. He, L. Protesescu, R. Caputo, F. Krumeich and M. V. Kovalenko, *Chem. Mater.*, 2015, **27**, 635–647.

25 M. Yarema, R. Caputo and M. V. Kovalenko, *Nanoscale*, 2013, **5**, 8398–8410.

26 A. Datta and G. S. Nolas, *Eur. J. Inorg. Chem.*, 2012, 55–58.

27 A. Gharleghi, P.-C. Hung, F.-H. Lin and C.-J. Liu, *ACS Appl. Mater. Interfaces*, 2016, **8**, 35123–35131.

28 B. F. P. McVey, S. Prabakar, J. J. Gooding and R. D. Tilley, *ChemPlusChem*, 2017, **82**, 60–73.

29 P. Simon, Z. Tang, W. Carrillo-Cabrera, K. Chiong, B. Böhme, M. Baitinger, H. Lichte, Y. Grin and A. M. Guloy, *J. Am. Chem. Soc.*, 2011, **133**, 7596–7601.

30 Y. Liu, X. Liu, Q. Feng, D. He, L. Zhang, C. Lian, R. Shen, G. Zhao, Y. Ji, D. Wang, G. Zhou and Y. Li, *Adv. Mater.*, 2016, **28**, 4747–4754.

31 Y. Zhang, L. Li, Q. Li, J. Fan, J. Zheng and G. Li, *Chem. – Eur. J.*, 2016, **22**, 14196–14204.

32 F. Casper, T. Graf, S. Chadov, B. Balke and C. Felser, *Semicond. Sci. Technol.*, 2012, **27**, 063001.

33 N. C. Anderson, M. P. Hendricks, J. J. Choi and J. S. Owen, *J. Am. Chem. Soc.*, 2013, **135**, 18536–18548.

34 A. Nag, H. Zhang, E. Janke and D. V. Talapin, *Z. Phys. Chem.*, 2015, **229**, 85–107.

35 J. De Roo, K. De Keukeleere, Z. Hens and I. Van Driessche, *Dalton Trans.*, 2016, **45**, 13277–13283.

36 D. Zherebetskyy, M. Scheele, Y. Zhang, N. Bronstein, C. Thompson, D. Britt, M. Salmeron, P. Alivisatos and L.-W. Wang, *Science*, 2014, **344**, 1380–1384.

37 M. Ibáñez, R. J. Korkosz, Z. Luo, P. Riba, D. Cadavid, S. Ortega, A. Cabot and M. G. Kanatzidis, *J. Am. Chem. Soc.*, 2015, **137**, 4046–4049.

38 J. K. Stolarczyk, A. Deak and D. F. Brougham, *Adv. Mater.*, 2016, **28**, 5400–5424.

39 M. A. Boles, M. Engel and D. V. Talapin, *Chem. Rev.*, 2016, **116**, 11220–11289.

40 R. Tangirala, J. L. Baker, A. P. Alivisatos and D. J. Milliron, *Angew. Chem., Int. Ed.*, 2010, **49**, 2878–2882.

41 Y. Min, Y. Akbulut, K. Kristiansen, Y. Golan and J. Israelachvili, *Nat. Mater.*, 2008, **7**, 527–538.

42 G. Rogl, D. Setman, E. Schafler, J. Horky, M. Kerber, M. Zehetbauer, M. Falmbigl, P. Rogl, E. Royanian and E. Bauer, *Acta Mater.*, 2012, **60**, 2146–2157.

43 R. Buonsanti and D. J. Milliron, *Chem. Mater.*, 2013, **25**, 1305–1317.

44 A. Stavrinadis and G. Konstantatos, *ChemPhysChem*, 2016, **17**, 632–644.

45 O. Voznyy, D. Zhitomirsky, P. Stadler, Z. Ning, S. Hoogland and E. H. Sargent, *ACS Nano*, 2012, **6**, 8448–8455.

46 M. Orrill and S. LeBlanc, *J. Appl. Polym. Sci.*, 2017, **134**, 44256.

47 T. Varghese, C. Hollar, J. Richardson, N. Kempf, C. Han, P. Gamarachchi, D. Estrada, R. J. Mehta and Y. Zhang, *Sci. Rep.*, 2016, **6**, 33135.

48 C. Sun, A. H. Goharpey, A. Rai, T. Zhang and D.-K. Ko, *ACS Appl. Mater. Interfaces*, 2016, **8**, 22182–22189.

49 S. J. Kim, J. H. We and B. J. Cho, *Energy Environ. Sci.*, 2014, **7**, 1959–1965.

50 M. Zebarjadi, *Appl. Phys. Lett.*, 2015, **106**, 203506.

The journey

41

SUPPLEMENTARY INFORMATION

Bottom-up engineering of thermoelectric nanomaterials and devices from solution-processed nanoparticle building blocks

Silvia Ortega,[a] Maria Ibáñez,*[b,c] Yu Liu,[a] Yu Zhang,[a] Maksym V. Kovalenko,[b,c] Doris Cadavid*[a] and Andreu Cabot*[a,d]

[a] Catalonia Institute for Energy Research – IREC, 08930 Sant Adrià de Besòs, Barcelona, Spain. E-mail: dcadavid@irec.cat; acabot@irec.cat

[b] Institute of Inorganic Chemistry, Department of Chemistry and Applied Biosciences, ETH Zürich, CH- 8093, Switzerland. E-mail: ibanez@inorg.chem.ethz.ch

[c] Empa-Swiss Federal Laboratories for Materials Science and Technology, Dübendorf, CH-8600, Switzerland

[d] ICREA, Pg. Lluis Companys 23, 08010 Barcelona, Spain

Contents
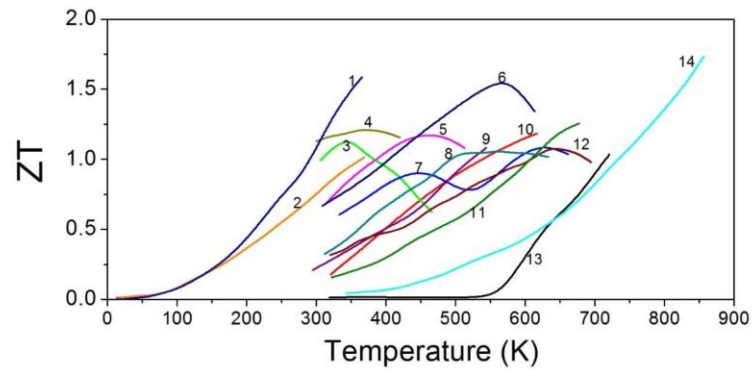
1. State-of-the-art solution-processed ZT materials

Figure S1. State-of-the-art ZT values obtained from solution-processed nanoparticle-based thermoelectric materials. **p-type**: **1.** $Bi_{0.5}Sb_{1.5}Te_3$[1], **4.** $Bi_{0.5}Sb_{1.5}Te_3$[2], **6.** $(Ag_2Te)_5(Sb_2Te_3)_5$[3], **8.** PbTe-BiSbTe[4], **9.** $AgBi_{0.5}Sb_{0.5}Se_2$[5], **11.** $Cu_3Sb_{0.88}Sn_{0.10}Bi_{0.02}Se_4$[6] and **12.** $AgSb_{0.98}Bi_{0.02}Se_2$[7]. **n-type**: **2.** $Bi_2Te_{2.7}Se_{0.3}$[1], **3.** $K_{0.06}Bi_2Te_{3.18}$[8], **5.** $Bi_2Te_{2.5}Se_{0.5}$[9], **7.** $PbTe_{0.66}Se_{0.33}$[10], **10.** PbTe-Bi_2Te_3[11], **13.** $(PbTe)_{0.72}(PbS)_{0.28}$[12] and **14.** PbS-Ag 4.4%[13]

2. Solution-processed nanoparticle-based thermoelectric devices

Table S1. Key parameters from solution-processed nanoparticle-based thermoelectric devices.

Reference / Material	Deposition Method	Substrate	n° pairs & architecture	Output Power	Flexible?
[14] Bi_2Te_3-epoxy Sb_2Te_3-epoxy	Dispenser Printing	Polyimide	50 in-plane	171.6 mV, 10.5 µW, 75 µW/cm² @ ΔT= 20 °C	Yes
[15] ZnSb $CoSb_3$	Screen Printing	Alumina	2 through-plane	27 mV, 0.1 mW/cm² @ ΔT= 50 °C	No
[16] PbTe	Dip Coating	Glass Fibers	-	1.7 mV @ ΔT= 58 °C	Yes
[17] -	Dispenser Printing	PDMS	- through-plane	7 mV, 2.1 µW @ ΔT= 19 °C	Yes
[18] $Bi_{0.5}Sb_{1.5}Te_3$/ Te-epoxy	Dispenser Printing	Polyimide	60 in-plane	152 µW/cm² @ ΔT= 20 °C	Yes
[19] $Sb_{1.5}Bi_{0.5}Te_3$ $Bi_2Te_{2.7}Se_{0.3}$	Inkjet Printing	Polyimide	3 in-plane	PF @ 75 °C p-type 77 µWm⁻¹K⁻² n-type 183 µWm⁻¹K⁻²	Yes
[20] Bi_2Te_3 Sb_2Te_3	Screen Printing	Glass Fabric	11 through-plane	2.9 mV, 3 µW @ ΔT= 20 °C	Yes
			8 through-plane	90 mV, 3.8 mW/cm² @ ΔT= 50 °C	
[21] I-doped PbTe	Dip Coating	Glass	2 in-plane	43 mV @ ΔT= 27 °C	No
[22] Bi_2Te_3 Sb_2Te_3	Screen Printing	Polyimide	8 in-plane	36.4 mV, 40.3 nW @ ΔT= 20 °C	Yes
[23] Bi-epoxy $Bi_{0.5}Sb_{1.5}Te_3$/ Te-epoxy	Dispenser Printing	Polyimide	10 in-plane	1230 µW/cm² @ ΔT= 70 °C	Yes
[24] Bi_2Te_3 Sb_2Te_3 PEDOT:PSS	Screen Printing	Polyimide	7 in-plane	85.2 mV, 1.22 mW/cm² @ ΔT= 50 °C	Yes
[25] Bi_2Se_3 nanoplates/ PVDF	Drop-casting	Free-standing TE foil	N/A	90 mV @ ΔT= 1.2 °C	Yes
[26] Ag_2Te/	Dip Coating	Nylon fibers	2 in-plane	3.5 mV, 5 nW, 0.6 µW/cm² @ ΔT= 20 °C	Yes

PEDOT:PSS					
[27] Bi_2Te_3 $Bi_{0.5}Sb_{1.5}Te_3$	Dispenser Printing	Polyimide	25 in-plane	33 μW, 2.8 W/m^2 @ ΔT= 20 °C	Yes
[28] $Cu_{1.75}Te$ NWs /PVDF	Vacuum Filtration	Free-standing TE foil	N/A	PF = 23 μWm^{-1}K^{-2} @ 25 °C	Yes
[29] WS_2 NSs $NbSe_2$ NSs	Vacuum Filtration/ Contact Printing	PDMS	100 through-plane	38 nW @ ΔT= 60 °C	Yes
[30] Bi_2Te_3 Sb_2Te_3	Dispenser Printing	Polyimide	1 through-plane	1.54 nW @ ΔT= 20 °C	Yes
[31] $Ca_3Co_4O_9$	Screen Printing	Alumina	10 in-plane	PF = 0.16 mWm^{-1}K^{-2} @ 300 °C	No
[31] $(ZnO)_5In_2O_3$			10 in-plane	PF = 1.4 μWm^{-1}K^{-2} @ 300 °C	No
[32] $Bi_{0.5}Sb_{1.5}Te_3$	3D Printing	Free-standing TE pellet	N/A	ZT = 0.12 @ 43 °C	No
[33] $Bi_2Te_{2.8}Se_{0.2}$	Screen Printing	Polyimide	5 in-plane	ZT = 0.43 @ 175 °C 6.1 μW/cm^2, 4.1 mW/cm^2 @ ΔT= 60 °C	Yes
[34] $TiS_2/$ hexylamine	Drop-casting	Free-standing TE foil	N/A	32 μW/cm^2 @ ΔT= 20 °C	Yes
[35] PbS QDs Bi-doped PbTe QDs	Dip Coating	Cellulose paper	3 in-plane	21.1 mV @ ΔT= 33 °C	Yes
			3 through-plane	14.2 mV @ ΔT= 33 °C	Yes
[36] Bi_2Te_3 Sb_2Te_3	Dispenser Printing	Silk Fabric	12 through-plane	10 mV, 15 nW @ ΔT= 35 °C	Yes
[37] $Bi_2Te_3/$ Sb_2Te_3 ChaM	Brush-painting	Polyimide or Glass	5 in-plane	2.43 mW/cm^2 @ ΔT= 50 °C	Yes/No
		Alumina	1 through-plane	4 mW/cm^2 @ ΔT= 50 °C	No
[38] Ag Ni	Screen Printing	Polyimide	15 in-plane	22 mV, 14.6 μW @ ΔT= 113 °C	Yes
[39] $Bi_{1.8}Te_{3.2}$ Sb_2Te_3	Screen Printing	Polyimide	8 in-plane	26.6 mV, 455.4 nW @ ΔT= 20 °C	Yes
		Glass fibers fabric	8 in-plane	42 mV, 2.3 μW @ ΔT= 20 °C	Yes
[40] $(Bi_{0.98}Sb_{0.02})_2$ $(Te_{0.9}Se_{0.1})_3$ $(Bi_{0.25}Sb_{0.75})_2$ $(Te_{0.95}Se_{0.05})_3$	Dispenser Printing	Polyester fabric	12 through-plane	23.9 mV, 3.11 nW @ ΔT= 22.5 °C	Yes
[41]	Screen Printing	PDMS	72	4.78 mW/cm^2 @ ΔT= 25 °C	Yes

S4

			through-plane		
$Bi_{0.3}Sb_{1.7}Te_3$ $Bi_2Se_{0.3}Te_{2.7}$ [42]					
$Bi_2Te_{2.7}Se_{0.3}$ $Bi_{0.5}Sb_{1.5}Te_3$ [43]	Brush-painting	Alumina	4 in-plane	ΔT= 3.7 °C @ 0.3 A cooling performance	No
$Bi_{1.8}Te_{3.2}$ Sb_2Te_3 [44]	Screen Printing	Polyimide	8 in-plane	32 mV, 444nW @ ΔT= 20 °C	Yes
TiS_2/organic PEDOT:PSS [45]	Contact Printing	PET	5 in-plane	33 mV, 2.5 W/m^2 @ ΔT= 70 °C	Yes
Bi_2Te_3 NWs Te-PEDOT:PSS [6]	Vacuum Filtration	Free-standing TE foil	6 in-plane	56 mV, 32 $\mu W/cm^2$ @ ΔT= 60 °C	No
Sn- Bi-doped Cu_3SbSe_4	Filling	Cu rings	N/A	20 mV, 1 mW @ ΔT= 160 °C	No

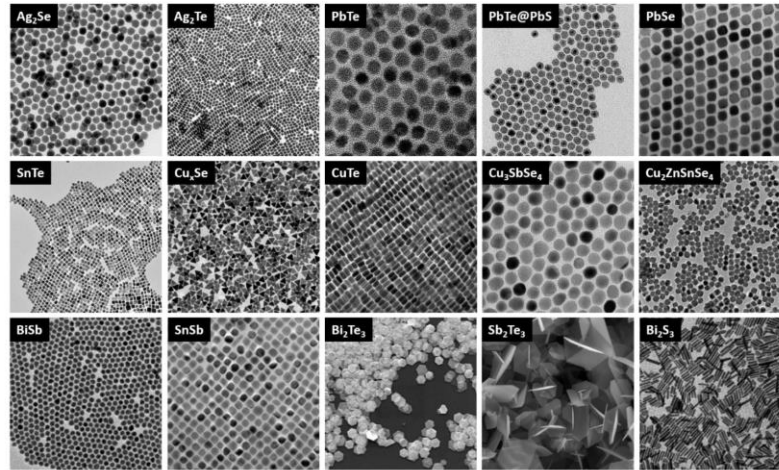## 3. Electron microscopy micrographs of solution-processed nanoparticle building blocks

Figure S2. Selection of solution-processed nanoparticles produced by the authors of this review following reported synthesis procedures: Ag_2Se,[46] Ag_2Te,[46] $PbTe$,[12] $PbTe@PbS$,[12] $PbSe$,[12] $SnTe$,[47] Cu_xSe,[48] $CuTe$,[49] Cu_3SbSe_4,[6] $Cu_2ZnSnSe_4$,[50] $BiSb$,[51] $SnSb$,[51] Bi_2Te_3,[2] Sb_2Te_3,[2] Bi_2S_3.[52]

4. References

1.   C. Zhang, M. de la Mata, Z. Li, F. J. Belarre, J. Arbiol, K. A. Khor, D. Poletti, B. Zhu, Q. Yan and Q. Xiong, *Nano Energy*, 2016, **30**, 630-638.

2.   R. J. Mehta, Y. Zhang, C. Karthik, B. Singh, R. W. Siegel, T. Borca-Tasciuc and G. Ramanath, *Nat. Mater.*, 2012, **11**, 233-240.

3.   J. Xu, H. Li, B. Du, X. Tang, Q. Zhang and C. Uher, *J. Mater. Chem.*, 2010, **20**, 6138-6143.

4.   B. Xu, M. T. Agne, T. Feng, T. C. Chasapis, X. Ruan, Y. Zhou, H. Zheng, J.-H. Bahk, M. G. Kanatzidis, G. J. Snyder and Y. Wu, *Adv. Mater.*, 2017, **29**, 1605140.

5.   C. Xiao, J. Xu, B. Cao, K. Li, M. Kong and Y. Xie, *J. Am. Chem. Soc.*, 2012, **134**, 7971-7977.

6.   Y. Liu, G. Garcia, S. Ortega, D. Cadavid, P. Palacios, J. Lu, M. Ibanez, L. Xi, J. De Roo, A. M. Lopez, S. Marti-Sanchez, I. Cabezas, M. d. l. Mata, Z. Luo, C. Dun, O. Dobrozhan, D. L. Carroll, W. Zhang, J. Martins, M. V. Kovalenko, J. Arbiol, G. Noriega, J. Song, P. Wahnon and A. Y. Cabot, *J. Mater. Chem. A*, 2017, **5**, 2592-2602.

7.   Y. Liu, D. Cadavid, M. Ibáñez, J. De Roo, S. Ortega, O. Dobrozhan, M. V. Kovalenko and A. Cabot, *J. Mater. Chem. C*, 2016, **4**, 4756-4762.

8.   K. Park, K. Ahn, J. Cha, S. Lee, S. I. Chae, S.-P. Cho, S. Ryee, J. Im, J. Lee and S.-D. Park, M. J. Han, I. Chung and T. Hyeon, *J. Am. Chem. Soc.*, 2016, **138**, 14458-14468.

9.   B. Xu, T. Feng, M. T. Agne, L. Zhou, X. Ruan, G. J. Snyder and Y. Wu, *Angew. Chem.*, 2017, **129**, 3600-3605.

10.   C. Zhou, Z. Shi, B. Ge, K. Wang, D. Zhang, G. Liu and G. Qiao, *J. Mater. Chem. A*, 2017, **5**, 2876-2884.

11.   H. Fang, T. Feng, H. Yang, X. Ruan and Y. Wu, *Nano Lett.*, 2013, **13**, 2058-2063.

12.   M. Ibáñez, R. Zamani, S. Gorsse, J. Fan, S. Ortega, D. Cadavid, J. R. Morante, J. Arbiol and A. Cabot, *ACS Nano*, 2013, **7**, 2573-2586.

13.   M. Ibáñez, Z. Luo, A. Genç, L. Piveteau, S. Ortega, D. Cadavid, O. Dobrozhan, Y. Liu, M. Nachtegaal, M. Zebarjadi, J. Arbiol, M. V. Kovalenko and A. Cabot, *Nat. Commun.*, 2016, **7**, 10766.

14.   A. Chen, D. Madan, P. Wright and J. Evans, *J. Micromech. Microeng.*, 2011, **21**, 104006.

15.   H.-B. Lee, H. J. Yang, J. H. We, K. Kim, K. C. Choi and B. J. Cho, *J. Electron. Mater.*, 2011, **40**, 615-619.

16.   D. Liang, H. Yang, S. W. Finefrock and Y. Wu, *Nano Lett.*, 2012, **12**, 2140-2145.

17.   S. Jo, M. K. Kim, M. S. Kim and Y. J. Kim, *Electron. Lett.*, 2012, **48**, 1013-1015.

18.   D. Madan, Z. Wang, A. Chen, P. K. Wright and J. W. Evans, *ACS Appl. Mater. Interfaces.*, 2013, **5**, 11872-11876.

19.   Z. Lu, M. Layani, X. Zhao, L. P. Tan, T. Sun, S. Fan, Q. Yan, S. Magdassi and H. H. Hng, *Small*, 2014, **10**, 3551-3554.

20.   S. J. Kim, J. H. We and B. J. Cho, *Energy Environ. Sci.*, 2014, **7**, 1959-1965.

21.   H. Fang, Z. Luo, H. Yang and Y. Wu, *Nano Lett.*, 2014, **14**, 1153-1157.

22.   Z. Cao, E. Koukharenko, R. N. Torah, J. Tudor and S. P. Beeby, *J. Phys.: Conf. Ser.*, 2014, **557**, 012016.

23.   D. Madan, Z. Wang, A. Chen, R. Winslow, P. K. Wright and J. W. Evans, *Appl. Phys. Lett.*, 2014, **104**, 013902.

24.   J. H. We, S. J. Kim and B. J. Cho, *Energy*, 2014, **73**, 506-512.

25.   C. Dun, C. A. Hewitt, H. Huang, J. Xu, D. S. Montgomery, W. Nie, Q. Jiang and D. L. Carroll, *ACS Appl. Mater. Interfaces*, 2015, **7**, 7054-7059.

26.   S. W. Finefrock, X. Zhu, Y. Sun and Y. Wu, *Nanoscale*, 2015, **7**, 5598-5602.

27.   D. Madan, Z. Wang, P. K. Wright and J. W. Evans, *Appl. Energy*, 2015, **156**, 587-592.

28.   C. Zhou, C. Dun, Q. Wang, K. Wang, Z. Shi, D. L. Carroll, G. Liu and G. Qiao, *ACS Appl. Mater. Interfaces*, 2015, **7**, 21015-21020.

29.   J. Y. Oh, J. H. Lee, S. W. Han, S. S. Chae, E. J. Bae, Y. H. Kang, W. J. Choi, S. Y. Cho, J.-O. Lee, H. K. Baik and T. I. Lee, *Energy Environ. Sci.*, 2016, **9**, 1696-1705.

30.   Z. Cao, J. J. Shi, R. N. Torah, M. J. Tudor and S. P. Beeby, *J. Phys.: Conf. Ser.*, 2015, **660**, 012096.

31.   R. Rudež, P. Markowski, M. Presečnik, M. Košir, A. Dziedzic and S. Bernik, *Ceram. Int.*, 2015, **41**, 13201-13209.

32.   M. He, Y. Zhao, B. Wang, Q. Xi, J. Zhou and Z. Liang, *Small*, 2015, **11**, 5889-5894.

33.   T. Varghese, C. Hollar, J. Richardson, N. Kempf, C. Han, P. Gamarachchi, D. Estrada, R. J. Mehta and Y. Zhang, *Sci. Rep.*, 2016, **6**, 33135.

34.   C. Wan, R. Tian, A. B. Azizi, Y. Huang, Q. Wei, R. Sasai, S. Wasusate, T. Ishida and K. Koumoto, *Nano Energy*, 2016, **30**, 840-845.

35.   C. Sun, A. H. Goharpey, A. Rai, T. Zhang and D.-K. Ko, *ACS Appl. Mater. Interfaces*, 2016, **8**, 22182-22189.

36.   Z. Lu, H. Zhang, C. Mao and C. M. Li, *Appl. Energy*, 2016, **164**, 57-63.

37.   S. H. Park, S. Jo, B. Kwon, F. Kim, H. W. Ban, J. E. Lee, D. H. Gu, S. H. Lee, Y. Hwang, J.-S. Kim, D.-B. Hyun, S. Lee, K. J. Choi, W. Jo and J. S. Son, *Nat. Commun.*, 2016, **7**, 13403.

38.   K. Ankireddy, A. K. Menon, B. Iezzi, S. K. Yee, M. D. Losego and J. S. Jur, *J. Electron. Mater.*, 2016, **45**, 5561-5569.

39.   Z. Cao, M. J. Tudor, R. N. Torah and S. P. Beeby, *IEEE Trans. Electron Dev.*, 2016, **63**, 4024-4030.

40.   A. R. M. Siddique, R. Rabari, S. Mahmud and B. Van Heyst, *Energy*, 2016, **115**, 1081-1091.

S8

41.   S. J. Kim, H. E. Lee, H. Choi, Y. Kim, J. H. We, J. S. Shin, K. J. Lee and B. J. Cho, *ACS Nano*, 2016, **10**, 10851-10857.

42.   H. Wu, X. Liu, P. Wei, H.-Y. Zhou, X. Mu, D.-Q. He, W.-T. Zhu, X.-L. Nie, W.-Y. Zhao and Q.-J. Zhang, , *J. Electron. Mater.*, 2016, doi:10.1007/s11664-016-5076-2.

43.   Z. Cao, E. Koukharenko, M. J. Tudor, R. N. Torah and S. P. Beeby, *Sens. Actuator A-Phys.*, 2016, **238**, 196-206.

44.   R. Tian, C. Wan, Y. Wang, Q. Wei, T. Ishida, A. Yamamoto, A. Tsuruta, W. Shin, S. Li and K. Koumoto, *J. Mater. Chem. A*, 2017, **5**, 564-570.

45.   C. Li, F. Jiang, C. Liu, W. Wang, X. Li, T. Wang and J. Xu, *Chem. Eng. J.*, 2017, doi:10.1016/j.cej.2017.03.023.

46.   D. Cadavid, M. Ibáñez, A. Shavel, O. J. Dura, M. A. Lopez de la Torre and A. Cabot, *J. Mater. Chem. A*, 2013, **1**, 4864-4870.

47.   M. Ibáñez, A. Cabot et al., *unpublished results*.

48.   W. Li, R. Zamani, M. Ibáñez, D. Cadavid, A. Shavel, J. R. Morante, J. Arbiol and A. Cabot, *J. Am. Chem. Soc.*, 2013, **135**, 4664-4667.

49.   W. Li, R. Zamani, P. Rivera Gil, B. Pelaz, M. Ibáñez, D. Cadavid, A. Shavel, R. A. Alvarez-Puebla, W. J. Parak, J. Arbiol and A. Cabot, *J. Am. Chem. Soc.*, 2013, **135**, 7098-7101.

50.   M. Ibáñez, R. Zamani, W. Li, A. Shavel, J. Arbiol, J. R. Morante and A. Cabot, *Cryst. Growth Des.*, 2012, **12**, 1085-1090.

51.   M. He, L. Protesescu, R. Caputo, F. Krumeich and M. V. Kovalenko, *Chem. Mater.*, 2015, **27**, 635-647.

52.   M. Ibáñez, P. Guardia, A. Shavel, D. Cadavid, J. Arbiol, J. R. Morante and A. Cabot, *J. Phys. Chem. C*, 2011, **115**, 7947-7955.

Chapter 2   Solution processing and engineering of thermoelectric nanomaterials
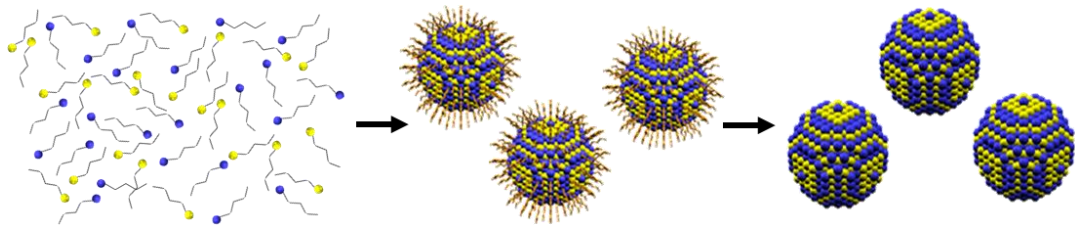
This chapter gets on with what explained in Chapter 1 regarding synthesis and surface-engineering of the NP building blocks and the assembly into nanocomposites. Including 3 publications, each of them is focused on one of those points.[94-96]

All the works (including also the ones reported in Chapter 3 and 4) are based on Pb-chalcogenides (PbS, PbTe, PbSe). This is mainly due to two reasons. First one is that such family is one of the best performing TE materials (Figure 0.10).[41] Second, is their suitability for the scaled-up production, thus being the perfect model materials to pave the way for the development of the solution-processing route to produce TE materials.

2.1   Composition control within the NP synthesis

Being the PbTe-PbS system one of the most reported ones, showing large ZT (Figure 0.10),[49, 97-100] this chapter shows the production of core-shell PbTe@PbS

NPs by the heterogeneous nucleation of PbS at the surface of the PbTe as-grown NPs. The production of heterostructures is used as an elegant way to produce homogeneous bulk nanocomposites from their bottom-up assembly. In addition, such nanocomposites present clearly higher ZT values than their counterparts PbTe and PbS pure phases.[101]

The first part of this work relates the synthesis of the NPs at the large scale, producing over 2 g of NPs per batch. Afterwards, cold press and hot press compaction methods are compared in order to obtain dense bulk nanocomposites from the random assembly of the colloidal NPs. In addition, it is developed a ligand displacement (LD) method to get rid of the organic surfactants presents at the NPs surface. A whole protocol based on the use of a lead (II) nitrate salt is presented.

2.2 NP purification and surface engineering

Following the Chapter 1 line, after having reached the proper control over composition of the NPs synthesized, next step is its purification to remove side products of the reaction and the surfactants used to direct its growth, some of them attached to the NP surface. However, besides only removing, taking advantage of the surface chemical engineering, it is also possible to modify the NP surface to tailor the properties of the final materials.[102]

Having proved the effectivity of LD in the previous section for the improvement of TE properties by removing carbonaceous species from the nanoparticles, the second part of Chapter 2 goes one step beyond, using the LD to simultaneously remove the organic ligands and introduce controlled amounts of dopants within the Pb-chalcogenides by the use of halides as atomic replacing ligands.

Two main parts can be differentiated in this work. In the first one, PbS is used as model material to develop the LD method and evaluate its effectivity in enhancing its electrical TE properties. Cl is a well-known dopant of this and other Pb-chalcogenides.[100, 103] Even in other works it is directly introduced as $PbCl_2$, here is done by means of a solution of HCl. When displacing the organic ligands, Cl ions would remain attached to the NP surface, and will later penetrate into the lattice during the consolidation step. This will allow the effective doping of the material in a controlled manner.

Based on the success obtained for the model material, the LD route is further tested in another Pb-chalcogenide NPs. The second test material is built on $PbTe_xSe_{x-1}$@PbS core-shell NP building blocks, that were synthesized by modifying the procedure presented in the previous section.[101, 104]

The Supporting Information is also included as an annex after the article because of the valuable information that contains. As the article is published as a Communication, detailed explanations over NP synthesis are here available. In addition, thermogravimetric analysis showing the effectivity of the HCl treatment in displacing the organic ligands and evidence on chlorine ions remaining into the original NPs can be found here.

The ZT values obtained in this work are comparable to the ones obtained for other PbSe-PbS systems produced by energy intensive strategies.[105] Moreover, these results are among the state-of-the-art ZT values for solution-processed materials (Figure S.1 in Chapter 1).

2.3 NP assembly and nanocomposite formation

The last step within the fabrication of solution-processed nanomaterials from NP-building blocks is its assembly into bulk nanomaterials. In the two previous sections nanocomposites were produced by consolidating core-shell NPs, however in this sub-chapter a simpler way is presented: the assembly of two different types of NPs.

In this publication, the two chosen materials are PbS and Ag, where PbS, the most inexpensive of all the Pb-chalcogenides, acts as matrix material and Ag acts as charge carrier nanoreservoirs. This choice it is not random. As introduced in Chapter 1, it is possible to modulate the doping by the blending of NPs of different materials so that one injects charge into the other. This is related to the band alignment associated to the relative position of the semiconductor and the metal Fermi level. In this case, the Ag Fermi level is above of the intrinsic PbS one. Having Ag a suitable working function, is able to inject electrons into the PbS conduction band.

Homogeneous PbS-Ag nanocomposites with adjusted metal concentrations were produced by combining PbS NPs with different amounts of Ag suspension in chloroform. Followed by the subsequent solvent evaporation. In this case, NPs

were used without further purification than the usual precipitation and redispersion steps, being possible to find the Ag in between the PbS grains. This system is deeply studied through all the article, giving evidence of the flat band alignment for the whole nanocomposite. Further studies on the PbS-Cu system have been also reported, showing the same charge transfer effect.[106]

At the end of this section the Supplementary Information is also attached with, for example, complementary transmission microscopy micrographs, XRD patterns of the PbS-Ag nanocomposites produced with different relative concentrations of PbS and Ag, system stability and other fitting parameters.

To close this chapter, it is worth to stress the importance of the results obtained from this work. To date, the ZT value reached here is the highest ever reported for solution-processed nanomaterials (Figure S.1 in Chapter 1). This and the other interesting outcomes from the former works included in this Chapter are the best cover letter to the huge versatility and potential that bottom-up solution-processed NP-based nanomaterials present for the facile development of the upcoming efficient TE materials and devices.

Bottom-up processing of PbTe-PbS thermoelectric nanocomposites

Silvia Ortega, Maria Ibáñez and Doris Cadavid

Catalonia Institute for Energy Research – IREC,
Jardins de les Dones de Negre, 1,
Sant Adrià de Besòs, Barcelona, 08930, Spain
E-mail: sortega@irec.cat
E-mail: mibanez@irec.cat
E-mail: dcadavid@irec.cat

Andreu Cabot*

Institució Catalana de Recerca i Estudis Avançats – ICREA,
08010 Barcelona, Spain

and

Catalonia Institute for Energy Research – IREC,
Jardins de les Dones de Negre, 1,
Sant Adrià de Besòs, Barcelona, 08930, Spain
E-mail: acabot@irec.cat
*Corresponding author

Abstract: Thermoelectricity is a key technology with the potential to improve the efficiency of energy conversion processes, which may strongly benefit from advances in the field of nanotechnology. Nanostructured materials are very appealing for thermoelectric applications, but the full development of their potential requires precise control of their properties at the nanoscale. Bottom-up assembly of nanoparticles provides access to a three-dimensional composition control at the nanoscale not attainable in any other technology. In particular, colloidal nanoheterostructures are especially interesting building blocks for the bottom-up production of functional nanomaterials. In the present work, we use PbTe@PbS core-shell nanoparticles as building blocks for the bottom-up production of PbTe-PbS nanocomposites. We used a ligand exchange strategy and a hot press process to promote the electrical conductivity of the nanocomposite and to increase its density. These two approaches allowed us to improve the performance of bottom-up assembled PbTe-PbS bulk nanostructured materials.

Keywords: colloidal synthesis; core-shell nanoparticles; hot press; ligand displacement; thermoelectricity; nanocomposite; PbTe; PbS; bottom-up assembly; nanotechnology.

Biographical notes: Silvia Ortega graduated in Physics in 2012 and received her MSc in Nanotechnology from the Faculty of Physics, University of Barcelona. Since 2013, she is a PhD student at the Functional Nanomaterials Group in IREC and Project Manager at Cidete Ingenieros SL. Her field of work is preparation of new thermoelectric materials and design of new thermoelectric modules.

Maria Ibáñez graduated in Physics in 2008, received her MSc in Physical Engineering in 2009 and her PhD in 2013 from the University of Barcelona. Currently, she is a postdoctoral researcher at the Catalonia Institute for Energy Research – IREC. Her research interest is focused on synthesis and self-assembly of semiconductor and metallic nanocrystals and energy-related applications of nanomaterials.

Doris Cadavid received her BSc in Physics from the Department of Physics at National University of Colombia in 2005, continued her MSc in Physics at the same department until 2008 and received her PhD in 2014 from the University of Barcelona. Her research focus is on thermoelectric materials; she had been working in a bottom-up approach for the fabrication of nanostructured materials to engineer their transport properties in order to enhance their thermoelectric performance.

Andreu Cabot graduated in Physics in 1998 and received his PhD in 2003 from the University of Barcelona. He did his postdoctoral research at the University of California, Berkeley, under Professor A. Paul Alivisatos guidance. He returned to the Electronics Department, University of Barcelona in 2007 and joined the Catalonia Institute for Energy Research – IREC in 2009 to form the Functional Nanomaterials Group. His research interests include the preparation, characterisation and assembly of nanocrystals and their application in energy conversion and storage.

1   Introduction

More than half of the energy used in energy conversion processes is wasted in the form of heat. In this scenario, thermoelectric (TE) energy conversion constitutes an alternative solution to improve the efficiency of current industrial and domestic processes. Besides the endless applications where TE generators could use the otherwise wasted thermal energy, these solid-state devices have no moving parts and are highly reliable, acoustically silent, small, lightweight and maintenance-free [1].

TE materials directly convert thermal into electrical energy. This phenomenon is based on the Seebeck effect, which involves the generation of an electrical voltage by a temperature gradient across a material. The TE device performance depends on the temperature gradient (ΔT) and three intrinsic material parameters combined in the so-called TE figure of merit (ZT)

$$ZT = \frac{S^2 \sigma T}{\kappa} \tag{1}$$

where S is the Seebeck coefficient, σ is the electrical conductivity, κ is the thermal conductivity and T is the absolute temperature. Being the ΔT established by the specific application, the highest the ZT, the highest the device efficiency. Notwithstanding the extraordinary potential of TE devices, the lack of high efficiencies has banned them from multiple potential markets [2].

Significant efforts have been made to maximise ZT. However, the main problem to increase TE efficiency is the difficult optimisation of a variety of interdependent properties. S, σ and κ are tightly interrelated and they all strongly depend on the electronic density of states. Therefore, an increase in S usually results in a decrease in σ, and an increase in σ produces an increase in κ and a decrease of S.

Nanocomposites, composite materials with crystallographic domains with sizes in the nanometre scale, potentially permit to decouple S and σ and to strongly decrease κ by phonon scattering at grain boundaries. However, while composite materials may allow improving thermoelectric performances, current top-down and vacuum-based technologies do not offer enough composition control and versatility or are not cost-effective.

Solution based techniques open an opportunity to produce bulk nanostructured composites in a cost-effective manner. The bottom-up assembly of nanocrystal building blocks not only allows the cost-effective production of nanocomposites but also permits to produce them with a large degree of control over their structural and chemical properties [3–17]. No other technology has the potential to produce nanocomposites with a comparable level of control over the size, shape, composition and phase of the crystal domains at the nanoscale [18–26]. In this scenario, nanoheterostructures are particularly interesting building blocks, as they allow producing highly homogeneous bulk nanocomposites in an easier manner (see Figure 1) and nanomaterial-based devices that take advantage of the best qualities of distinct materials [27–34].

Figure 1   Steps for the production of nanocomposites from the bottom-up assembly of core-shell nanoparticles (see online version for colours)
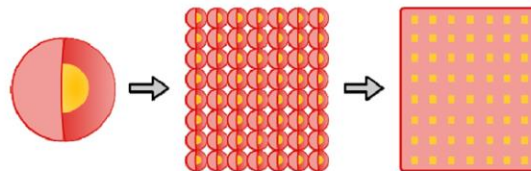
In spite of the great advantage that solution-based techniques offer to the TE field, they also have some challenges to overcome. The first one is the relatively low densities obtained. The second problem is the presence of organic surfactants used during nanoparticle (NP) synthesis. Surfactant molecules limit NP growth, direct its morphology and provide it with stability in an organic medium. However, they introduce an electrical insulating barrier between NPs with the corresponding detrimental effects on the electrical properties of the nanomaterials. The simplest methodology to get rid of these highly insulating molecules is by thermal decomposition. Despite its partial effectiveness, the carbon species remaining in the final nanomaterials may adversely affect their electrical properties.

In this work, we produced PbTe@PbS core-shell NPs with narrow size distributions and controlled PbTe/PbS ratios as building blocks for the bottom-up production of PbTe-PbS nanocomposites. We used a ligand exchange procedure to displace the organics used during the synthesis and a hot-press process to obtain highly dense pellets, which TE properties were characterised. Our studies prove that the electronic performance of nanocomposites was enhanced by the higher densities obtained and by the complete elimination of carbon from the final nanocomposite.

2   Experimental

2.1   Chemicals

Lead (II) oxide (99.9%), lead (II) nitrate (≥99%), oleic acid (OA, tech. 90%), 1-octadecene (ODE, 90%), tellurium shots (99.999%), thioacetamide (ACS reagent, ≥99.0%), hexamethyldisilathiane (TMS$_2$S, synthesis grade), *N,N*-dimethylformamide (DMF, ≥99%), anhydrous methanol (99.8%) and anhydrous chloroform (≥99%) were purchased from Aldrich. Tri-*n*-octylphosphine (TOP, 97%) was purchased from Strem. Hexane and ethanol were of analytical grade and obtained from Panreac. All chemicals were used as received without further purification. Syntheses were carried out using standard airless techniques: a vacuum/dry argon gas Schlenk line was used for syntheses and an argon-filled glove box for storing and handling air- and moisture-sensitive chemicals and during ligand displacement process.

2.2   Preparation of PbS NPs

A modified approach of that used by Hines et al. (2003) [35] was used for the preparation of PbS nanocrystals. Lead (II) oxide (2.94 g, 13 mM) and oleic acid (90 mL, 48 mM) were dissolved in 90 mL of ODE. This mixture was degassed at room temperature (RT) and 100ºC for 0.5 h each to form a lead oleate complex. Afterwards, the transparent solution was flashed with argon and heated to the reaction temperature (135ºC). At this temperature, 1.26 mL of TMS$_2$S dissolved in 40 mL of ODE was rapidly injected under argon gas flow. For the crystal growth, the reaction mixture was kept for 3 more min and then quickly cooled to RT using a water bath.

2.3   Preparation of PbTe NPs

A modified approach by Murphy et al. (2006) [36] was used for the preparation of PbTe nanocrystals. PbO (4.5 g, 20 mM) and OA (22.22 g, 79 mM) were dissolved in 150 mL of ODE. This mixture was degassed at RT and 100ºC for 0.5 h each to form a lead oleate complex. The transparent solution was flushed with Ar, and the temperature was raised to 160ºC. Tri-n-octylphosphine telluride (TOP:Te, 1.5 M) was prepared by dissolving 19.05 g of tellurium in 100 mL of TOP inside the glove box. Afterwards, 13.3 mL of 1.5 M TOP:Te was rapidly injected to the solution with the lead oleate complex. The reaction mixture was maintained at 160ºC between 1.5 min and 3 min and then quickly cooled to RT using a water bath. At this point, an aliquot was extracted to analyse the PbTe morphology.

2.4 Preparation of PbTe@PbS core-shell NPs

For the preparation of PbTe@PbS core-shell NPs, we follow a large scale approach of that used by Ibáñez et al. (2013) [3]. Once the crude solution containing the PbTe NPs was at RT, 189 mg of thioacetamide dissolved in 10 mL of DMF was added into the flask. The NPs solution containing the sulphur precursor was heated to 80ºC at 1.7ºC/min and maintained at this temperature for 30 min. After cooling to RT, NPs were precipitated by centrifugation and thoroughly washed by multiple precipitation and re-dispersion steps using ethanol and hexane, until they could not be redispersed in organic solvents. At this point, most of the surfactants initially used to control the NP size, shape and solubility had been already removed. NPs were finally redispersed in anhydrous chloroform and stored in the glove box for further use.

2.5 Ligand displacement

The ligand displacement (LD) procedure was performed at RT, with anhydrous solvents (chloroform and methanol), and in an inert atmosphere to prevent any oxidation of the NPs.

90 mL of PbTe@PbS core-shell NPs solution in chloroform (~9 g/L) was mixed with 80 mL of 0.02 M $Pb(NO_3)_2$ solution in methanol. The mixture was vigorously shaken for 1 min to promote the LD and then NPs were precipitated by centrifugation. Afterwards, they were washed several times with chloroform and methanol alternatively to drag all the remaining organic ligands surrounding the NPs and the possible excess of Pb and nitrate species not attached to their surface. Once the LD was completed, NPs were no longer soluble in non-polar solvents.

2.6 Preparation of PbTe-PbS nanomaterials

NPs were dried under vacuum to obtain a dark grey nanopowder. Dried NPs were heated to 500ºC for 1 h under an argon flow inside a tube furnace. Two different methods were used for the pressing of the annealed material.

RT-pressed nanomaterials: the nanopowder was pressed under a load of 2 tons at RT during 1.5 min in air.

HP-pressed nanomaterials: A custom-made hot-press (HP) instrument, with an induction heater coupled to a hydraulic press, was used for the nanopowder densification. We introduced the annealed material into a graphite die and placed it into the HP chamber. With a thermocouple in contact with the graphite, we monitored the material temperature. Finally, and after several purging steps (vacuum/argon), we pressed it under a load of 2 tons at 320ºC during 1.5 min in argon, obtaining a dense disc-shaped nanomaterial with 10 mm diameter and 2 mm thickness.

To estimate the densities, we performed geometric measurements and weighed all the nanomaterials accurately. Using the percentage of PbS and PbTe present, we calculated the expected theoretical density of each nanomaterial. Nanomaterials produced at RT and at 320ºC presented densities around 80 and 90%, respectively, with respect to the theoretical value.

2.7   TE characterisation

The Seebeck coefficient was measured using a static DC method. Electrical resistivity data were obtained by the standard four-probe method. Both S and electrical resistivity were measured simultaneously in an LSR-3 LINSEIS system in the range between RT and 710 K, under a helium atmosphere.

2.8   Structural characterisation

X-ray power diffraction (XRD) analyses were carried out on a Bruker AXS D8 Advance X-ray diffractometer with Cu Kα1 radiation ($\lambda = 1.5406$ Å). The size and shape of the nanoparticles were examined by transmission electron microscope (TEM) using a Zeiss Libra 120. Scanning electron microscopy (SEM) was performed using a Zeiss Auriga SEM with an energy dispersive X-ray spectroscopy (EDX) detector to study composition. Thermal gravimetric analyses (TGAs) were done using Perkin-Elmer TGA 4000 equipment. The dried PbTe@PbS nanopowders were heated up to 450ºC under a nitrogen flow and with a heating ramp of 5ºC/min.

3   Results and discussion

3.1   PbTe@PbS NPs

A two-step procedure was used to prepare PbTe@PbS NPs. Firstly, PbTe NPs were prepared by reacting Pb oleate with TOP:Te in ODE. In a second step, without purifying or exposing the PbTe NPs to air, the sulphur precursor was added to the crude solution containing PbTe NPs at RT. Then, the temperature was gradually increased to 80ºC at 1.7ºC/min in order to grow the PbS shell. Figure 2 shows a TEM micrograph of the PbTe (A) and PbTe@PbS (B) NPs produced with exceptionally low dispersion in size distribution, <10% (C). It must be pointed out that all NPs prepared were obtained from large scale synthesis, producing up to 2.1–2.5 g of size-monodispersed material in a single pot.

Figure 2   TEM micrographs of PbTe (A) and $(PbTe)_{0.68}$@$(PbS)_{0.32}$ (B) NPs with average sizes of 11 ± 1 nm and 16 ± 2 nm, respectively. (C) Histograms with the particle size distribution (see online version for colours)
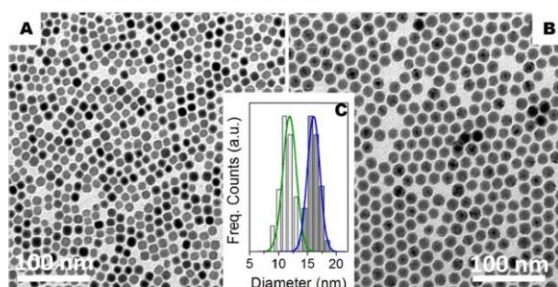
3.2 PbTe-PbS nanocomposites pressed at RT

Two different NPs with similar overall size but different PbTe/PbS ratios (see Figure 3) were used to produce $(PbTe)_{1-x}(PbS)_x$ nanomaterials with $x = 0.32$ and 0.6. As references, we also produced pure PbTe and PbS nanomaterials from the processing of PbTe and PbS NPs.

Figure 3 TEM micrographs of the two batches of $(PbTe)_{1-x}@(PbS)_x$ core-shell NPs with $x = 0.32$ (A) and 0.6 (B)
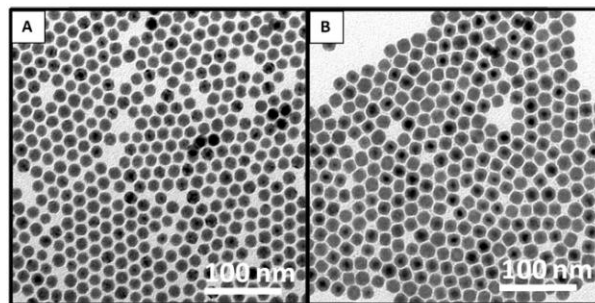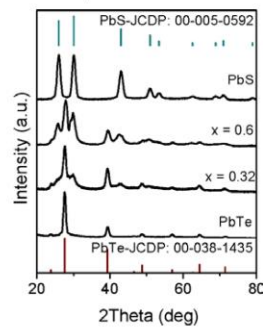

Figure 4 displays the XRD patterns of the $(PbTe)_{x-1}@(PbS)_x$ ($x = 0, 0.32, 0.6, 1$) NPs. We observed the coexistence of two crystal structures: altaite PbTe (JCDP: 00-038-1435) and galena PbS (JCDP: 00-005-0592). No evidence of alloying or oxidation could be obtained.

Figure 4 XRD patterns of $(PbTe)_{1-x}@(PbS)_x$ core-shell NPs with $x = 0, 0.32, 0.6$ and 1 (see online version for colours)

Once prepared, NPs were purified by multiple precipitation and re-dispersion steps and they were finally dried under vacuum to obtain a dark nanopowder. The nanopowder

was annealed at 500ºC for 1 h under an argon flow to completely remove organics. Figure 5 presents the XRD pattern of the nanopowder after the thermal treatment.

Annealed nanopowders were pressed under 2 tons of force at RT, to produce $(PbTe)_{1-x}(PbS)_x$ ($x = 0$, 0.32, 0.6, 1) nanomaterials. The relative densities obtained by this procedure were around 80% of the theoretical value calculated taking into account the material composition.

Figure 5   XRD pattern of the annealed $(PbTe)_{1-x}(PbS)_x$ nanomaterials with $x = 0$, 0.32, 0.6 and 1 (see online version for colours)
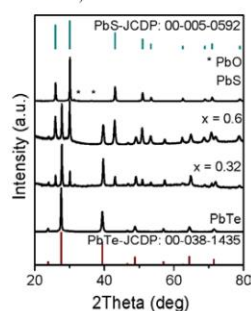
3.3   PbTe-PbS nanocomposites hot pressed

One of the main problems observed with the RT pressed nanomaterials was their low densities and high fragility. In order to overcome such problems, we compacted the materials using a custom-made HP instrument operated under argon.

In order to study the effect of temperature during the compacting of the nanomaterials, we produced several grams of the exact same composition and pressed them using the HP system. HP conditions were carefully adjusted to maximise the nanomaterial density, but minimise crystal domain growth and fragility. The best results were obtained when the temperature was set at 320ºC, with a load of around 2 tons during 1.5 min. Under such conditions, densities obtained were around 90% with respect to theoretical value. Despite the increase in density observed when compared with the RT press, we did not appreciate any increase of the crystal domains with the HP process. In both cases (RT and HP nanomaterials), the average crystal domain estimated by the Scherrer formula was around 45 nm. The increase of particle size respect to the initial NPs provided from the thermal treatment at 500ºC.

Figure 6 shows the XRD patterns from PbTe NPs, PbTe@PbS NPs, $(PbTe)_{1-x}(PbS)_x$ annealed nanomaterial and the corresponding HP nanomaterial. The effects of the annealing procedure were as we observe in the previous section: i) a narrowing of the peaks; ii) a partial alloying and iii) the appearance of tiny PbO peaks.

The crystal structure of the HP-nanomaterial did not present any alteration with respect to the XRD spectra of $(PbTe)_{1-x}(PbS)_x$ annealed nanomaterial, neither any constriction of the peaks, proving that no crystal growth was induced by the HP.

Figure 6   XRD patterns of PbTe NPs, $(PbTe)_{0.68}@(PbS)_{0.32}$ core-shell NPs, $(PbTe)_{0.68}(PbS)_{0.32}$
annealed nanomaterial and the corresponding $(PbTe)_{0.68}(PbS)_{0.32}$ dense nanomaterial
pressed with a HP system (see online version for colours)
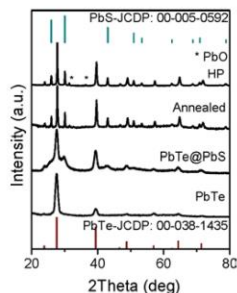
The thermoelectric properties of the higher and lower density nanomaterials with
the same exact PbTe/PbS ratio are compared in Figure 7. Significantly higher σ was
obtained for HP nanomaterials. The increase in σ was related to the higher density of the
nanocomposite and the related enhancement of the charge transfer between grains.

Figure 7 σ, S and PF for $(PbTe)_{0.68}(PbS)_{0.32}$ nanomaterial. Comparison between the nanomaterial
pressed at RT and the one pressed at 320ºC (HP) (see online version for colours)
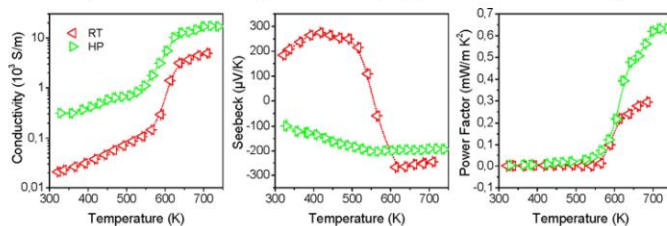
Surprisingly, the behaviour observed for S was very different between both samples.
The HP sample did not present any sign inversion. The values of S were negative in
the whole temperature range studied. We attribute this behaviour to the higher density of
electrons participating in the charge transport within this material. However, other side
effects determining such behaviour need to be studied with more detail. In the high
temperature range, S was slightly lower for HP nanomaterials. This result was expected
due to the higher σ obtained. Nonetheless, the final electrical performance was enhanced
by the increase of density obtained with the HP procedure and two-fold larger PF was
achieved.

3.4   PbTe-PbS nanocomposites hot pressed after metal LD

The huge capacity of colloidal synthesis to create new complex nanocomposites introduces the possibility to design new materials that can boost the TE performance. However, most of the current synthetic routes to produce NPs make use of organic surfactants, essential molecules to control growth, shape and composition of the final NPs. These organic molecules represent a problem due to their electrical insulator character.

During the last years, several alternative post-synthetic treatments have been developed to displace or replace these molecules by shorter organic groups or inorganic ligands at the NPs surface [37–42]. However, the practical application of such methods is still far to be truly useful at large scale. Problems such as oxidation of NPs surface, toxicity or/and highly reactivity of the compounds involved in the removal/replacement of the long-chain organic ligands need to be completely avoided. The approach we propose is based on the dissolution of a metal salt in an anhydrous polar solvent, which could be miscible with our colloidal solution (see Figure 8). In the case of lead nitrate: PbTe@PbS NPs were dried under vacuum to obtain a dark grey nanopowder and dispersed in anhydrous chloroform. This was mixed at room temperature with the $Pb(NO_3)_2$ solution in anhydrous methanol. Afterwards, NPs were precipitated by centrifugation. After several washing steps, organic ligands were completely displaced from NPs surface.

Figure 8   Schematic view of the displacement of oleic acid molecules from the surface of PbTe@PbS NPs (see online version for colours)
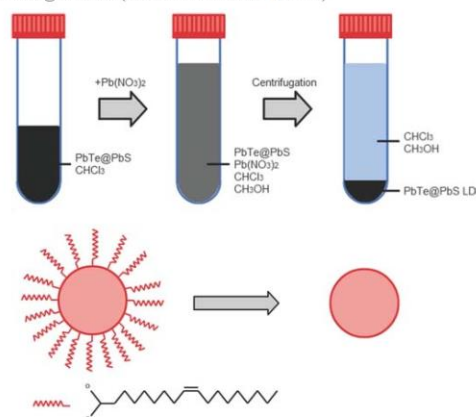
Different metal salts such as bismuth (III) nitrate, silver nitrate or lead (II) nitrate were successfully tested. After the proper treatment with each of these salts, we could not find any carbon present on the surface of the NPs. Among the different metal salts studied for the LD, lead (II) nitrate was proved to be the most effective.

Figure 9 shows the mass loss as a function of temperature for organic and inorganic (dashed-line) capped NPs. A relative mass decrease of a 10% was measured for organic caped NPs when heated to 450ºC under a nitrogen flow. On the other hand, after LD NPs showed a mass loss of less than 2%. The higher mass loss measured for organic caped NPs was consistent with the thermal decomposition of the bulky oleic acid molecules, not present once the displacement with metal ions was done.

Figure 9   TGA of organic and inorganic (dashed-line) capped NPs (see online version for colours)
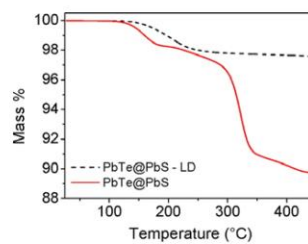
The percentage of carbon left after annealing PbTe@PbS NPs in a nitrogen atmosphere was measured by elemental analysis. A 1–2% of carbon was obtained from the analysis of annealed organic caped NPs. Nevertheless, the carbon percentage measured from annealed inorganic caped NPs was below the detection limit of the system: <0.1%. In the same way, no nitrogen was detected in the sample.

Figure 10 shows a TEM micrograph of the PbTe@PbS NPs after LD. NPs preserved their original shape and composition, they partially aggregated. Original NPs were stabilised by oleic acid. The length of these molecules kept NPs apart when they were dried out from solution. However, once the displacement was successfully done, the NPs were just stabilised in polar solvents by electrostatic repulsion. Thereby, the distance between these dried NPs is shorter than in the case of organic molecules, as can be seen in Figure 10.

Figure 10   TEM micrograph of the PbTe@PbS core-shell NPs after the LD process
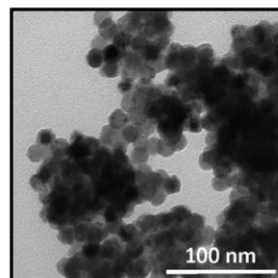
After the LD process, we followed the exact same procedure developed in the previous section to produce bulk nanoheterostructured materials and test their TE electrical properties. Nanopowders were annealed at 500ºC for 1 h and pressed under a load of 2 tons at 320ºC (HP) during 1.5 min under argon atmosphere, obtaining a dense disc-shaped nanomaterial with 10 mm diameter and 2 mm thickness. Figure 11 shows a SEM micrograph of the final nanocrystalline nanomaterials obtained. The inset presents a picture of the nanocomposite obtained. Despite the annealing and HP processes, the final material still preserved its nanostructuration and crystal domain sizes were found to be around 45 nm.

Figure 11   SEM micrograph of the $(PbTe)_{0.4}(PbS)_{0.6}$ nanomaterial obtained after pressing the $(PbTe)_{0.48}@(PbS)_{0.6}$ core-shell NPs using a HP. The inset shows the original pressed nanomaterial (see online version for colours)
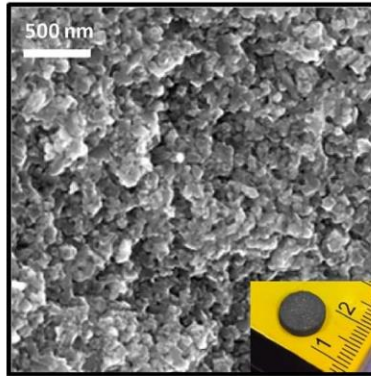

Figure 12 displays the XRD pattern of the PbTe and PbTe@PbS NPs, and the final HP nanomaterial. As expected, the final nanomaterial presents narrower peaks related to the crystal growth involved in the annealing process. Additionally, a slight shift corresponding to partial alloying was observed. No additional peaks were observed despite the slight excess of Pb present on the surface of the NPs during the annealing.

The thermoelectric properties of the produced nanocomposite were finally characterised and the results compared with a nanocomposite produced with the exact same initial PbS@PbTe NPs but without LD and HP (see Figure 13).

Higher σ was obtained for HP-LD-nanocomposite. In the lower temperature regime, two orders of magnitude enhancements were achieved for high-density carbon-free bulk nanocomposites. This large increase was associated to the absence of residual carbon at the NPs surface and the possible doping introduced by the Pb^{2+} ions.

For the HP-LD-nanocomposite, S was negative in the whole temperature range with no change in the sign of the majority charge carriers. We associate this different behaviour to an increase of electrons charge transfer, either by an increase of the density of charges or the enhancement of the mobility between grains. The distinction of these two possible effects will require a further investigation. The electrical behaviour of this

nanomaterial was clearly improved by means of the LD and HP processes leading to a PF close to $0.6 \text{ mWm}^{-1}\text{K}^{-2}$.

Figure 12 XRD patterns of PbTe NPs, $(PbTe)_{0.4}@(PbS)_{0.6}$ core-shell NPs and $(PbTe)_{0.4}(PbS)_{0.6}$ nanomaterial pressed with a HP system after a LD process (see online version for colours)

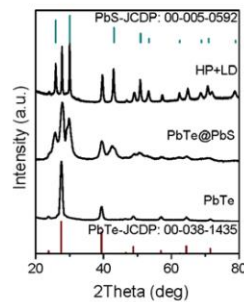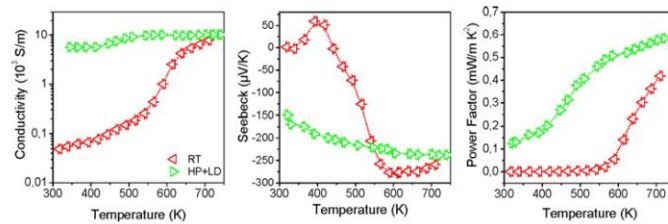**Figure 13** σ, S and PF for $(PbTe)_{0.4}(PbS)_{0.6}$ nanomaterial. Comparison between the nanomaterial pressed at RT and the one pressed at 320°C after a LD process (HP+LD) (see online version for colours)

4   Conclusions

PbTe@PbS core-shell NPs with narrow size distributions and different PbTe/PbS ratios were produced. Two different compaction methods of the $(PbTe)_{1-x}@(PbS)_{x}$ NPs for the bottom-up assembly of $(PbTe)_{1-x}(PbS)_{x}$ nanocomposites were compared. Furthermore, an organic LD by means of a $Pb(NO_3)_2$ metal salt solution was performed, removing carbonaceous species from final materials. Because of the higher values in densities obtained and complete removal of carbon from the final nanomaterial, electrical conductivities were enhanced without any significant decrease of S. As a proof, higher values of the PF were found for high-dense nanomaterials, with or without carbon, than for low-dense nanomaterials with low carbon content.

References

1 Rowe, D.M. (Ed.) (1995) *CRC Handbook of Thermoelectrics*, CRC, Boca Raton, FL.

2 Vining, C.B. (2009) 'An inconvenient truth about thermoelectrics', *Nat. Mater.*, Vol. 8, pp.83–85.

3 Ibáñez, M., Zamani, R., Gorsse, S., Fan, J., Ortega, S., Cadavid, D., Morante, J.R., Arbiol, J. and Cabot, A. (2013) 'Core-shell nanoparticles as building blocks for the bottom-up production of functional nanocomposites: PbTe-PbS thermoelectric properties', *ACS Nano*, Vol. 7, pp.2573–2586.

4 Mehta, R.J., Zhang, Y., Karthik, C., Singh, B., Siegel, R.W., Borca-Tasciuc, T. and Ramanath, G. (2012) 'New class of doped nanobulk high-figure-of-merit thermoelectrics by scalable bottom-up assembly', *Nat. Mater.*, Vol. 11, pp.233–240.

5 Kovalenko, M.V., Spokoyny, B., Lee, J.S., Scheele, M., Weber, A., Perera, S., Landry, D. and Talapin, D.V. (2010) 'Semiconductor nanocrystals functionalized with antimony telluride zintl ions for nanostructured thermoelectrics', *J. Am. Chem. Soc.*, Vol. 132, pp.6686–6695.

6 Scheele, M., Oeschler, N., Veremchuk, I., Peters, S.O., Littig, A., Kornowsky, A., Klinke, C. and Weller, H. (2011) 'Thermoelectric properties of lead chalcogenide core-shell nanostructures', *ACS Nano*, Vol. 5, pp.8541–8551.

7 Ibáñez, M., Zamani, R., Lalonde, A., Cadavid, D., Li, W., Shavel, A., Arbiol, J., Morante, J.R., Gorsse, S., Snyder, G.J. and Cabot, A. (2012) '$Cu_2ZnGeSe_4$ nanocrystals: synthesis and thermoelectric properties', *J. Am. Chem. Soc.*, Vol. 134, pp.4060–4063.

8 Ibáñez, M., Zamani, R., Li, W., Cadavid, D, Gorsse, S., Katcho, N.A., Shavel, A., López, A.M., Morante, J.R., Arbiol, J. and Cabot, A. (2012) 'Crystallographic control at the nanoscale to enhance functionality: polytypic Cu_2GeSe_3 nanoparticles as thermoelectric materials', *Chem. Mater.*, Vol. 24, pp.4615–4622.

9 Ibáñez, M., Cadavid, D., Zamani, R., García-Castelló, N., Izquierdo-Roca, V., Li, W., Fairbrother, A., Prades, J.D., Shavel, A., Arbiol, J., Pérez-Rodríguez, A., Morante, J.R. and Cabot, A. (2012) 'Composition control and thermoelectric properties of quaternary chalcogenide nanocrystals: the case of stannite $Cu_2CdSnSe_4$', *Chem. Mater.*, Vol. 24, pp.562–570.

10 Ibáñez, M., Cadavid, D., Tamburini, U.A., Zamani, R., Gorsse, S., Li, W., Shavel, A., López, A.M., Morante, J.R., Arbiol, J. and Cabot, A. (2013) 'Colloidal synthesis and thermoelectric properties of Cu_2SnSe_3 nanocrystals', *J. Mater. Chem. A*, Vol. 1, pp.1421–1426.

11 Cadavid, D., Ibáñez, M., Gorsse, S., López, A.M., Cirera, A., Morante, J.R. and Cabot, A. (2012) 'Bottom-up processing of thermoelectric nanocomposites from colloidal nanocrystal building blocks: the case of Ag_2Te-PbTe', *J. Nanopart. Res.*, Vol. 14, pp.1–10.

12 Carrete, A., Shavel, A., Fontané, X., Montserrat, J., Fan, J., Ibáñez, M., Saucedo, E., Pérez-Rodríguez, A. and Cabot, A. (2013) 'Antimony-based ligand exchange to promote crystallization in spray-deposited $Cu_2ZnSnSe_4$ solar cells', *J. Am. Chem. Soc.*, Vol. 135, pp.15982–15986.

13 Talapin, D.V., Shevchenko, E.V., Bodnarchuk, M.I., Ye, X., Chen, J. and Murray, C.B. (2009) 'Quasicrystalline order in self-assembled binary nanoparticle superlattices', *Nature*, Vol. 461, pp.964–967.

14 Urban, J.J., Talapin, D.V., Shevchenko, E.V., Kagan, C.R. and Murray, C.R. (2007) 'Synergism in binary nanocrystal superlattices leads to enhanced p-type conductivity in self-assembled PbTe/Ag_2Te thin films', *Nat. Mater.*, Vol. 6, pp.115–121.

15 Nafria, R., Ramírez de la Piscina, P., Homs, N., Morante, J.R., Cabot, A., Diaz, U. and Corma, A. (2013) 'Embedding catalytic nanoparticles inside mesoporous structures with controlled porosity: Au@TiO_2',*J. Mater. Chem. A*, Vol. 1, pp.14170–14176.

16 Li, W., Ibáñez, M., Zamani, R., Garcia-Castello, N., Gorsse, S., Cadavid, D., Prades, J.D., Arbiol, J. and Cabot, A. (2013) '$Cu_2HgSnSe_4$ nanoparticles: synthesis and thermoelectric properties', *Cryst. Eng. Commun.*, Vol. 135, pp.8966–8971.

Bottom-up processing of PbTe-PbS thermoelectric nanocomposites 969

17 Shavel, A., Arbiol, J. and Cabot, A. (2010) 'Synthesis of quaternary chalcogenide nanocrystals: stannite $Cu_2Zn_xSn_ySe_{1+x+2y}$', *J. Am. Chem. Soc.*, Vol. 132, No. 13, pp.4514–4515.

18 Ibáñez, M. and Cabot, A. (2013) 'All change for nanocrystals', *Science*, Vol. 340, No. 6135, pp.935–936.

19 Li, W., Zamani, R., Ibáñez, M., Cadavid, D., Shavel, A., Morante, J.R., Arbiol, J. and Cabot, A. (2013) 'Metal ions to control the morphology of semiconductor nanoparticles: copper selenide nanocubes', *J. Am. Chem. Soc.*, Vol. 135, No. 12, pp.4664–4667.

20 Li, W., Zamani, R., Rivera-Gil, P., Pelaz, B., Ibáñez, M., Cadavid, D., Shavel, A., Alvarez-Puebla, R.A., Parak, W.J., Arbiol, J. and Cabot, A. (2013) 'CuTe nanocrystals: shape and size control, plasmonic properties, and use as SERS probes and photothermal agents', *J. Am. Chem. Soc.*, Vol. 135, pp.7098–7101.

21 Shavel, A., Cadavid, D., Ibáñez, M., Carrete, A. and Cabot, A. (2012) 'Continuous production of Cu_2ZnSnS_4 nanocrystals in a flow reactor', *J. Am. Chem. Soc.*, Vol. 134, pp.1438–1441.

22 Ibáñez, M., Zamani, R., Li, W., Shavel, A., Arbiol, J., Morante, J.R. and Cabot, A. (2012) 'Extending the nanocrystal synthesis control to quaternary compositions', *Cryst. Growth Des.*, Vol. 12, No. 3, pp.1085–1090.

23 Ibáñez, M., Fan, J., Li, W., Cadavid, D., Nafria, R., Carrete, A. and Cabot, A. (2011) 'Means and limits of control of the shell parameters in hollow nanoparticles obtained by the Kirkendall effect', *Chem. Mater.*, Vol. 23, pp.3095–3104.

24 Ibáñez, M., Guardia, P., Shavel, A., Cadavid, D., Arbiol, J., Morante, J.R. and Cabot, A. (2011) 'Growth kinetics of asymmetric Bi_2S_3 nanocrystals: size distribution focusing in nanorods', *J. Phys. Chem. C*, Vol. 115, No. 16, p.7947.

25 Li, W.H., Shavel, A., Guzman, R., Rubio-Garcia, J., Flox, C., Fan, J.D., Cadavid, D., Ibáñez, M., Arbiol, J., Morante, J.R. and Cabot, A. (2011) 'Morphology evolution of $Cu_{2-x}S$ nanoparticles: from spheres to dodecahedrons', *Chem. Comm.*, Vol. 47, No. 37, p.10332.

26 Cabot, A., Ibáñez, M., Guardia, P. and Alivisatos, A.P. (2009) 'Reaction regimes on the synthesis of hollow particles by the Kirkendall effect', *J. Am. Chem. Soc.*, Vol. 131, No. 32, pp.11326–11328.

27 Fan, J., Güell, F., Fábrega, C., Shavel, A., Carrete, A., Andreu, T., Morante, J.R. and Cabot, A. (2011) 'Enhancement of the photoelectrochemical properties of ZnO nanowires by tuning their coaxial doping profile', *Appl. Phys. Lett.* Vol. 99, p.262102.

28 Fan, J., Fábrega, C., Zamani, R., Hao, Y., Parra, A., Andreu, T., Arbiol, J., Boschloo, G., Hagfeldt, A., Morante, J.R. and Cabot, A. (2013) 'Enhanced photovoltaic performance of nanowire dye-sensitized solar cells based on coaxial $TiO_2@TiO$ heterostructures with a cobalt (II/III) redox electrolyte', *ACS Appl. Mater. Interfaces*, Vol. 5, pp.9872–9877.

29 Fan, J., Fábrega, C., Zamani, R., Shavel, A., Güell, F., Carrete, A., Andreu, T., Lopez, A.M., Morante, J.R., Arbiol, J. and Cabot, A. (2013) 'Solution-growth and optoelectronic properties of ZnO:Cl@ZnS core-shell nanowires with tunable shell thickness'. *J. Alloys Compd.*, Vol. 555, pp.213–218.

30 Fan, J., Zamani, R., Fábrega, C., Shavel, A., Flox, C., Ibáñez, M., Andreu, T., López, A.M., Arbiol, J., Morante, J.R. and Cabot, A. (2012) 'Solution-growth and optoelectronic performance of ZnO: Cl/TiO_2 and ZnO: Cl/Zn_xTiO_y/TiO_2 core–shell nanowires with tunable shell thickness', *J. Phys. D: Appl. Phys.*, Vol. 45, pp.415301.

31 Fan, J., Shavel, A., Zamani, R., Fábrega, C., Rousset, J., Haller, S., Güell, F., Carrete, A., Andreu, T., Arbiol, J., Morante, J.R. and Cabot, A. (2011) 'Control of the doping concentration, morphology and optoelectronic properties of vertically aligned chlorine-doped ZnO nanowires', *Acta Mater.*, Vol. 59, pp.6790–6800.

32 Fan, J., Hao, Y., Hernández, M.G., Munuera, C., Güell, F., Johansson, E.M.J., Boschloo, G., Hagfeldt, A. and Cabot, A. (2013) 'Influence of the annealing atmosphere on the performance of ZnO nanowires-based dye-sensitized solar cells', *J. Phys. Chem. C*, Vol. 117, pp.16349−16356.

33 Fan, J., Güell, F., Fábrega, C., Fairbrother, A., Andreu, T., López, A.M., Morante, J.R. and Cabot, A. (2012) 'Visible photoluminescence components of solution-grown ZnO nanowires: influence of the surface depletion layer', *J. Phys. Chem. C*, Vol. 116, pp.19496–19502.

34 Fan, J., Hao, Y., Cabot, A., Johansson, E.M.J., Boschlo, G. and Hagfeldt, A. (2013) 'Cobalt(II/III) redox electrolyte in ZnO nanowire-based dye-sensitized solar cells', *ACS Appl. Mater. Interfaces*, Vol. 5, pp.1902–1906.

35 Hines, M.A. and Scholes, G.D. (2003) 'Colloidal PbS nanocrystals with size-tunable near-infrared emission: observation of post-synthesis self-narrowing of the particle size distribution', *Adv. Mater.*, Vol. 15, pp.1844–1849.

36 Murphy, J.E., Beard, M.C., Norman, A.G., Ahrenkiel, S.P., Johnson, J.C., Yu, P., Mićić, O.I., Ellingson, R.J. and Nozik, A.J. (2006) 'PbTe colloidal nanocrystals: synthesis, characterization and multiple exciton generation', *J. Am. Chem Soc.*, Vol. 128, pp.3241–3247.

37 Cadavid, D., Ibáñez, M., Shavel, A., Durá, O.J., López, M.A. and Cabot, A. (2013) 'Organic ligand displacement by metal salts to enhance nanoparticle functionality: thermoelectric properties of Ag_2Te', *J. Mater. Chem. A*, Vol. 1, p.4864.

38 Huynh, W.U., Dittmer, J.J. and Alivisatos, A.P. (2002) 'Hybrid nanorod-polymer solar cells', *Science*, Vol. 295, pp.2425–2427.

39 Kovalenko, M.V., Scheele, M. and Talapin, D.V. (2009) 'Colloidal nanocrystals with molecular metal chalcogenide surface ligands', *Science*, Vol. 324, pp.1417–1420.

40 Zhang, H., Hu, B., Sun, L., Hovden, R., Wise, F.W., Muller, D.A. and Robinson, R.D. (2011) 'Surfactant ligand removal and rational fabrication of inorganically connected quantum dots', *Nano Lett.*, Vol. 11, pp.5356–5361.

41 Nag, A., Kovalenko, M.V., Lee, J-S., Liu, W., Spokoyny, B. and Talapin, D.V. (2011) 'Metal-free inorganic ligands for colloidal nanocrystals: S^{2-}, HS^-, Se^{2-}, HSe^-, Te^{2-}, HTe^-, TeS_3^{2-}, OH^-, and NH_2^- as surface ligands', *J. Am. Chem. Soc.*, Vol. 133, pp.10612–10620.

42 Nag, A., Chung, D.S., Dolzhnikov, D.S., Dimitrijevic, N.M., Chattopadhyay, S., Shibata, T. and Talapin, D.V. (2012) 'Effect of metal ions on photoluminescence, charge transport, magnetic and catalytic properties of all-inorganic colloidal nanodrystals and nanocrystal solids', *J. Am. Chem. Soc.*, Vol. 134, pp.13604–13615.

J|A|C|S

JOURNAL OF THE AMERICAN CHEMICAL SOCIETY

Electron Doping in Bottom-Up Engineered Thermoelectric Nanomaterials through HCl-Mediated Ligand Displacement

Maria Ibáñez,[†] Rachel J. Korkosz,[‡] Zhishan Luo,[†] Pau Riba,[†] Doris Cadavid,[†] Silvia Ortega,[†] Andreu Cabot,*,[†,§] and Mercouri G. Kanatzidis*,[‡]

[†]Catalonia Energy Research Institute—IREC, Sant Adria del Besos, 08930 Barcelona, Spain
[‡]Department of Chemistry, Northwestern University, Evanston, Illinois 60208, United States
[§]Institució Catalana de Recerca i Estudis Avançats—ICREA, 08010 Barcelona, Spain

⑤ Supporting Information

ABSTRACT: A simple and effective method to introduce precise amounts of doping in nanomaterials produced from the bottom-up assembly of colloidal nanoparticles (NPs) is described. The procedure takes advantage of a ligand displacement step to incorporate controlled concentrations of halide ions while removing carboxylic acids from the NP surface. Upon consolidation of the NPs into dense pellets, halide ions diffuse within the crystal structure, doping the anion sublattice and achieving n-type electrical doping. Through the characterization of the thermoelectric properties of nanocrystalline PbS, we demonstrate this strategy to be effective to control charge transport properties on thermoelectric nanomaterials assembled from NP building blocks. This approach is subsequently extended to $PbTe_xSe_{1-x}@PbS$ core–shell NPs, where a significant enhancement of the thermoelectric figure of merit is achieved.

The PbTe/Se-PbS bulk nanostructured systems are some of the most important thermoelectric materials under investigation.[1] Their high performance arises from their very low thermal conductivity and high power factor, translating into high thermoelectric figures of merit, $ZT = ((\sigma S^2)/\kappa)T$, where σ is the electrical conductivity, S is the thermopower, or Seebeck coefficient, κ is the thermal conductivity, and T is the temperature. These bulk materials are essentially biphasic where a second phase, e.g., PbS is on the nanoscale and embedded in a coherent (endotaxial) manner in the matrix phase, e.g., PbTe. This type of nanostructuring emerges from the nucleation and growth of one phase inside another in the solid state. Another type of nanostructuring can be envisioned in which colloidal nanocrystals of lead chalcogenides can be assembled and consolidated into bulk specimens. Colloidal NPs with tuned size, shape, crystal phase, and composition offer an exceptional platform for the precise and cost-effective engineering of functional bulk nanomaterials and thin films.[2] However, the presence of organic ligands at the NP surface and the extremely challenging introduction of controlled amounts of electrical dopants remain as the two main drawbacks of bottom-up assembled nanomaterials in technological applications.[3] While organic ligands limit charge transfer between NPs and between NPs and the media, the difficult control of the charge carrier concentration prevents the optimization of the material electronic and thermoelectric performance.

The exchange or displacement of surface organic ligands by short inorganic molecules represented a major step toward improving the charge transfer and transport properties in bottom-up assembled nanomaterials.[4] While inorganic ligands may volatilize or decompose upon thermal consolidation or stabilization,[5] frequently foreign ions incorporate to the NP lattice partially changing its composition and therefore its functional properties.[6] At first view, this is a drawback of inorganic ligand exchange strategies. However, when controlled, it can offer an excellent opportunity to dope and change the charge transport properties of the nanomaterials obtained from the bottom-up assembly of colloidal NPs.[7]

Herein, using thermoelectrically relevant PbQ (Q = S, Se, Te) NPs, we describe a surface treatment designed to both remove carboxylic acid ligands from NP surface and introduce controlled amounts of dopant thereby controlling their electrical properties. We demonstrate the suitability of the procedure by characterizing the thermoelectric properties of nanocrystalline PbS doped with controlled amounts of chlorine ions, which act as n-type dopants. We further demonstrate the potential of this process by preparing Cl-doped $PbTe_xSe_yS_{1-x-y}$ nanocomposites with high thermoelectric performance from the assembly and consolidation of $PbTe_xSe_{1-x}@PbS$ core–shell NPs.

PbS NPs were prepared by reacting lead oleate with elemental sulfur dissolved in oleylamine (Supporting Information, SI). Figure 1 displays a representative transmission electron microscopy (TEM) image of the 14 ± 1 nm, cube-shaped PbS NPs obtained by the above detailed procedure. Thermogravimetric analysis showed that even after purification by multiple precipitation/redispersion steps, significant amounts of organics (~6.7% in weight) remained at the NP surface (Figure SI1). We refer to the purified but untreated NPs as PbS-OA.

HCl was used to partially remove the OA from the NP surface and because chlorine is a commonly used n-type dopant in bulk PbS, usually introduced as $PbCl_2$.[8] Our hypothesis was that Cl^- would remain at the PbS NP surface and from there it would incorporate to the PbS anion sublattice during the bulk consolidation step. The displacement of OA by HCl was carried out by injecting controlled amounts of a 1.25 M HCl ethanol
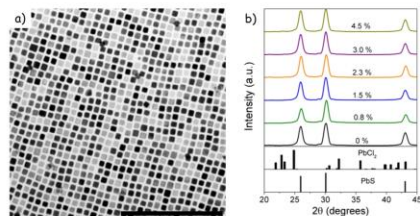
4046

Figure 1. (a) TEM micrograph of 14 ± 1 nm, cube-shaped PbS NPs (scale bar = 100 nm). (b) XRD patterns of PbS NPs after ligand displacement with several HCl concentrations as noted.

Figure 2. Electrical conductivity (a) and Seebeck coefficient (b) of nanocrystalline PbS obtained from the bottom-up assembly of PbS-OA NPs and PbS-x% NPs with $0\% < x < 9\%$ as noted in the legend. (c) Scheme of the HCl-based doping strategy.

solution in 1 g of PbS NPs dissolved in chloroform. The mixture was stirred at room temperature and in an argon filled glovebox for 1 h before purification by multiple precipitation/redispersion steps using anhydrous chloroform/methanol as a solvent/nonsolvent. We will refer to the samples obtained after this process as PbS-x%, x being the atomic concentration of Cl introduced. For HCl amounts up to 4.5%, PbS NPs remained soluble in relatively nonpolar solvents. Thermogravimetric analysis (Figure SI1) of the PbS-x% NPs treated with different HCl amounts clearly demonstrated the effectiveness of the HCl treatment to displace OA from the NP surface. It is important to highlight that all HCl concentrations presented in this work were calculated considering a 1.25 M solution of HCl in ethanol. Therefore, these numbers represent an upper limit on the HCl concentration, as HCl is highly volatile. In any case, no evidence of lead chloride was observed in the initial PbS-x% NPs from XRD analysis (Figure 1b).

As a reference, a PbS-0% sample, where all OA was displaced using NH$_4$SCN, was also produced. This sample was obtained by mixing 6 mL of a 130 mM NH$_4$SCN solution in methanol with 1 g of PbS NPs suspended in anhydrous chloroform.[5a] NPs were then purified using chloroform and methanol to remove free carboxylic acid and excess NH$_4$SCN, respectively.

Untreated and HCl- and NH$_4$SCN-treated PbS NPs were dried and annealed under Ar flow at 400 °C for 1 h to remove the remaining organic surfactants and to promote the insertion of Cl$^-$ ions into the anion sublattice of the bulk nanocomposite. The obtained nanopowders were subsequently consolidated in a hot press system (SI) into 10 mm in diameter and ~1 mm thick disk-shaped pellets at 40 MPa and 400 °C in an inert atmosphere. PbS-OA and PbS-x% pellets with relative densities of 85% and above 90%, respectively, were finally obtained. During these two thermal processes, crystal domains grew from the initial 14 nm to ~50 nm for the PbS-OA and ~55 nm for PbS-x% as calculated from the fitting of the XRD patterns using Scherrer eq (Figure SI2). Moreover, in the PbS-9.0% sample, peaks corresponding to the PbCl$_2$ phase were identified in the XRD patterns obtained after the annealing processes (Figure SI2).

Figure 2 shows the electrical conductivity and Seebeck coefficient of the consolidated nanocrystalline PbS pellets obtained from PbS-OA NPs and PbS-x% NPs with $0\% \leq x \leq$ 4.5%. PbS-OA samples (undoped) were characterized by relatively low electrical conductivities with a characteristic step increase of the conductivity above 450 K. This step change of the electrical conductivity was accompanied by a simultaneous step change of the Seebeck coefficient that included a sign inversion at around 450 K, from positive to negative values. The low electrical
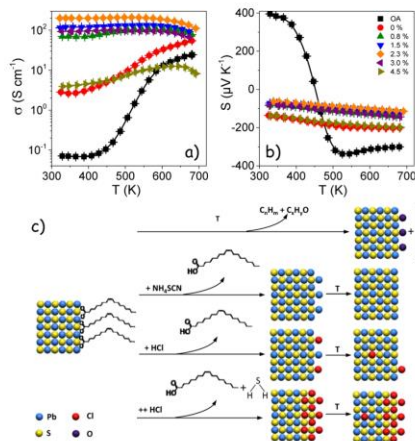
conductivity at low temperature and the electrical conductivity and Seebeck coefficient step changes above 400 K, suggesting a low concentration of charge carriers at room temperature and a thermal activation of a relatively large concentration of negative charge carriers above 400 K.

The removal of organic ligands using NH$_4$SCN, PbS-0%, resulted in a strong increase of the electrical conductivity in the low temperature range (Figure 2a). The step change at 450 K observed in PbS-OA was preserved, and a monotonous increase of the electrical conductivity was measured up to 700 K. However, a negative Seebeck coefficient, but smaller in absolute value to that obtained for PbS-OA, was measured in the whole temperature range evaluated (Figure 2b). These results confirm the n-type doping as a result of the NH$_4$SCN treatment. We associate this increase of the electrical conductivity and the shift toward negative Seebeck coefficients with the removal of S from PbS NPs during the thermal treatment. This was not observed in the PbS-OA samples because of the protection given by the surface organic/carbon layer toward S removal and by a possible surface oxide layer formed from the decomposition of the OA carboxylic group during annealing.[9] Nevertheless, no PbO phase was identified from XRD analysis.

Pellets produced from HCl-treated NPs were characterized by significantly higher electrical conductivities. Moreover, the electrical conductivities increased with the amount of Cl introduced, up to 2.3%. Above this concentration, a decrease of electrical conductivity, associated with the formation of a PbCl$_2$ secondary phase (Figure SI2), was observed. All PbS-x% nanomaterial samples showed negative Seebeck coefficients with monotonically decreasing absolute values as expected for increasing degree of n-type doping (Figure 2b). However, the Seebeck coefficient absolute values obtained for the PbS-x% ($x > 0$) samples were significantly lower than those obtained for PbS-OA and PbS-0%, which indicates a higher carrier concentration due to successful doping with the Cl anions.

4047

From these results, we conclude that HCl is able to displace oleic acid by breaking the lead oleate Pb−O bonds stabilizing the PbS NP surface. As a result of this reaction, free OA is released to the solution and chlorine ions react with surface Pb cations to form $PbCl_2$. Additionally, small amounts of sulfide ions may be removed by the formation of H_2S (Figure 2c). The data clearly indicate that during the thermal treatment, the chloride ions diffuse within PbS and incorporate to the anion sublattice, acting as electron donors.

We note that the thermal treatments also introduce a small stoichiometry imbalance in PbS-x% due to partial sulfide removal. However, electrical conductivities obtained with the HCl treatment were much higher than with the NH_4SCN treatment, pointing toward a much stronger doping influence of the chlorine ion. Furthermore, the doping level could be controlled by adjusting the amount of HCl introduced.

To further differentiate the influence of the two treatments, a second set of HCl-treated samples was produced by subsequently treating the samples first with the appropriate amount of HCl and subsequently with an excess of NH_4SCN to remove all remaining OA. The thermoelectric properties of this second set of samples did not substantially differ from those obtained from materials treated just with HCl (Figure SI3).

These results overall demonstrate the strong influence of the surface treatment with hydrogen halides on the transport properties of PbS nanocrystalline materials and suggests a key role of such introduced halide ions as n-type dopants (Figure 2c). While PbS provided us with a simple system to demonstrate the potential of the developed procedure to introduce controlled amounts of dopants, in order to prove the potential of this strategy for achieving a high thermoelectric figure of merit for the bottom-up assembled nanocrystalline materials, we prepared new nanomaterial based on $PbTe_xSe_{1−x}@PbS$ core−shell NPs and applied the same doping strategy.

$PbTe_xSe_{1−x}@PbS$ core−shell NPs were produced by consecutive reactions of lead oleate with chalcogens following a combination of the methods developed by Quan et al.[10] to produce $PbTe_xSe_{1−x}$ cores and ourselves to produce PbTe@PbS core−shell NPs (SI).[11] Figure 3 displays representative TEM micrographs of the cube-shaped $PbTe_xSe_{1−x}$ cores and the final $PbTe_xSe_{1−x}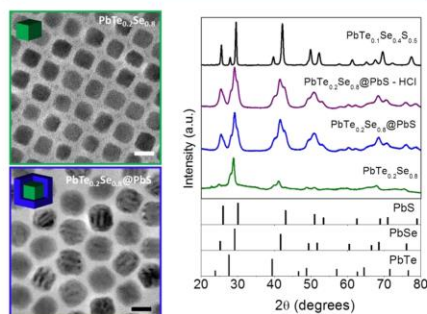@PbS$ core−shell NPs produced. The average size of the cores and core−shell NPs was 9 ± 1 and 14 ± 1 nm, respectively. The composition of the core−shell NPs further used in this work was $(PbTe_{0.2}Se_{0.8})_{0.47}@(PbS)_{0.53}$. Following the same procedure described above, chlorine was introduced within the lead chalcogenide lattice using HCl to displace OA from the surface of the NPs. After the HCl treatment, the $PbTe_{0.2}Se_{0.8}@PbS$ NPs were purified, dried, and annealed at 400 °C for 1 h. The obtained nanopowder was consolidated into 10 mm pellets at 40 MPa and 450 °C using spark plasma sintering (SPS). Densities around 85% and 93% were systematically obtained for $PbTe_{0.1}Se_{0.4}S_{0.5}$-OA and $PbTe_{0.1}Se_{0.4}S_{0.5}$-Cl pellets, respectively.

Figure 3 displays the XRD pattern of the initial $PbTe_{0.2}Se_{0.8}$ cores, the $(PbTe_{0.2}Se_{0.8})_{0.47}@(PbS)_{0.53}$ core−shell NPs, and the $PbTe_{0.1}Se_{0.4}S_{0.5}$ bulk nanomaterial obtained after SPS. XRD analysis shows the initial $PbTe_{0.2}Se_{0.8}$ cores to be probably a core−shell NP in themselves. After SPS processing a PbTe phase was clearly identified from the XRD pattern. However, the PbSe from the core was found forming a PbSeS alloy with the PbS from the shell.

Figure 4 shows the electrical conductivity, Seebeck coefficient, thermal conductivity, and final figure of merit of two
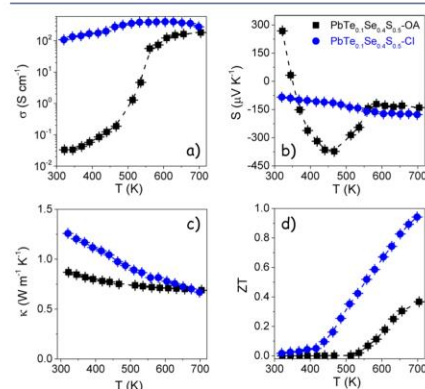

Figure 4. Electrical conductivity (a), Seebeck coefficient (b), thermal conductivity (c), and thermoelectric figure of merit (d) of nanocrystalline $PbTe_xSe_yS_{1−x−y}$ obtained from the bottom-up assembly of $PbTe_xSe_{1−x}@PbS$ core−shell NPs with and without 2.3% HCl addition.

$PbTe_{0.1}Se_{0.4}S_{0.5}$ bulk nanocrystalline materials obtained from the bottom-up assembly of $(PbTe_{0.2}Se_{0.8})_{0.47}@(PbS)_{0.53}$ core−shell NPs with and without HCl treatment (2.3%). A dependence of the electrical conductivity and the Seebeck coefficient with the temperature similar to that observed for PbS, including a step change of electrical conductivity at around 500 K, was obtained. A sign inversion of the Seebeck coefficient at around 350 K, was observed for the $PbTe_{0.1}Se_{0.4}S_{0.5}$-OA sample. Upon organic removal with 2.3% HCl, close to 4 orders of magnitude higher electrical conductivities were obtained, Figure 4a. The absolute value of the negative Seebeck coefficient obtained for the $PbTe_{0.1}Se_{0.4}S_{0.5}$-Cl sample increased with temperature, reaching similar values as those obtained from $PbTe_{0.1}Se_{0.4}S_{0.5}$-OA, up to ∼180 μV K$^{−1}$, Figure 4b.

Figure 3. TEM micrographs of $PbTe_{0.2}Se_{0.8}$ and $PbTe_{0.2}Se_{0.8}@PbS$ NPs (scale bar = 10 nm) and XRD patterns of $PbTe_{0.2}Se_{0.8}$ NPs, $PbTe_{0.2}Se_{0.8}@PbS$ NPs before and after HCl ligand exchange, and $PbTe_{0.1}Se_{0.4}S_{0.5}$ nanomaterial obtained after SPS.

Relatively low thermal conductivities were obtained for both types of nanocrystalline materials, Figure 4c. The low thermal conductivities ($\sim$0.7 W/mK) indicate an efficient scattering of phonons at the large density of point defects and interfaces in these nanocrystalline alloy composites. Lower thermal conductivities were measured for the $PbTe_{0.1}Se_{0.4}S_{0.5}$-OA sample, which may be related to residual carbon at the grain boundaries provided from the decomposition of OA and to the slightly smaller crystal domains when compared with $PbTe_{0.1}Se_{0.4}S_{0.5}$-Cl.

Finally, a 2.6-fold increase in the thermoelectric figure of merit, up to $ZT = 0.94$, was obtained for the $PbTe_{0.1}Se_{0.4}S_{0.5}$-Cl nanocrystalline material compared with the $PbTe_{0.1}Se_{0.4}S_{0.5}$-OA sample, Figure 4d. The high ZT values obtained are comparable to the best figures of merit measured for bulk PbSe-PbS systems obtained by using long thermal processes ($t > 60$ h) at high temperatures ($T \approx 1150$ °C).[12]

In summary, we detailed a NP surface treatment procedure both to displace organic ligands and to introduce controlled amounts of halide ions as n-type doping elements. The convenience of the process was established with PbS, and the potential of the procedure was demonstrated with $PbTe_xSe_{1-x}$@PbS core−shell NPs, which possess ZTs comparable to bulk n-type PbTe. We believe this strategy to be generally applicable to all NPs stabilized with carboxylic acids and being potentially dopable by halide anions.

■ ASSOCIATED CONTENT

ⓢ Supporting Information

Additional experimental and material characterization details. This material is available free of charge via the Internet at http://pubs.acs.org.

■ AUTHOR INFORMATION

Corresponding Authors

*acabot@irec.cat

*m-kanatzidis@northwestern.edu

Notes

The authors declare no competing financial interest.

■ ACKNOWLEDGMENTS

■ REFERENCES

(1) (a) Wu, H. J.; Zhao, L. D.; Zheng, F. S.; Wu, D.; Pei, Y. L.; Tong, X.; Kanatzidis, M. G.; He, J. Q. *Nat. Commun.* **2014**, *5*, 4515. (b) Girard, S. N.; He, J.; Zhou, X.; Shoemaker, D.; Jaworski, C. M.; Uher, C.; Dravid, V. P.; Heremans, J. P.; Kanatzidis, M. G. *J. Am. Chem. Soc.* **2011**, *133*, 16588−16597. (c) Heremans, J. P.; Jovovic, V.; Toberer, E. S.; Saramat, A.; Kurosaki, K.; Charoenphakdee, A.; Yamanaka, S.; Snyder, G. J. *Science* **2008**, *321*, 554−557. (d) Aminorroaya Yamini, S.; Wang, H.; Gibbs, Z. M.; Pei, Y.; Mitchell, D. R. G.; Dou, S. X.; Snyder, G. J. *Acta Mater.* **2014**, *80*, 365−372.

(2) (a) Ibáñez, M.; Cabot, A. *Science* **2013**, *340*, 935−936. (b) Talapin, D. V.; Lee, J.-S.; Kovalenko, M. V.; Shevchenko, E. V. *Chem. Rev.* **2010**, *110*, 389−458. (c) Yin, Y.; Alivisatos, A. P. *Nature* **2005**, *437*, 664−670.

(3) (a) Mocatta, D.; Cohen, G.; Schattner, J.; Millo, O.; Rabani, E.; Banin, U. *Science* **2011**, *332*, 77−81. (b) Erwin, S. C.; Zu, L.; Haftel, M. I.; Efros, A. L.; Kennedy, T. A.; Norris, D. J. *Nature* **2005**, *436*, 91−94.

(4) (a) Kovalenko, M. V.; Scheele, M.; Talapin, D. V. *Science* **2009**, *324*, 1417−1420. (b) Dong, A.; Ye, X.; Chen, J.; Kang, Y.; Gordon, T.; Kikkawa, J. M.; Murray, C. B. *J. Am. Chem. Soc.* **2010**, *133*, 998−1006.

(5) (a) Fafarman, A. T.; Koh, W.-k.; Diroll, B. T.; Kim, D. K.; Ko, D.-K.; Oh, S. J.; Ye, X.; Doan-Nguyen, V.; Crump, M. R.; Reifsnyder, D. C.; Murray, C. B.; Kagan, C. R. *J. Am. Chem. Soc.* **2011**, *133*, 15753−15761. (b) Carrete, A.; Shavel, A.; Fontané, X.; Montserrat, J.; Fan, J.; Ibáñez, M.; Saucedo, E.; Pérez-Rodríguez, A.; Cabot, A. *J. Am. Chem. Soc.* **2013**, *135*, 15982−15985.

(6) Kovalenko, M. V.; Spokoyny, B.; Lee, J.-S.; Scheele, M.; Weber, A.; Perera, S.; Landry, D.; Talapin, D. V. *J. Am. Chem. Soc.* **2010**, *132*, 6686−6695.

(7) (a) Buonsanti, R.; Milliron, D. J. *Chem. Mater.* **2013**, *25*, 1305−1317. (b) Yakunin, S.; Dirin, D. N.; Protesescu, L.; Sytnyk, M.; Tollabimazraehno, S.; Humer, M.; Hackl, F.; Fromherz, T.; Bodnarchuk, M. I.; Kovalenko, M. V.; Heiss, W. *ACS Nano* **2014**, *8*, 12883−12894.

(8) (a) Androulakis, J.; Chung, D.-Y.; Su, X.; Zhang, L.; Uher, C.; Hasapis, T.; Hatzikraniotis, E.; Paraskevopoulos, K.; Kanatzidis, M. *Phys. Rev. B* **2011**, *84*, 155207. (b) Zhao, L.-D.; Lo, S.-H.; He, J.; Li, H.; Biswas, K.; Androulakis, J.; Wu, C.-I.; Hogan, T. P.; Chung, D.-Y.; Dravid, V. P.; Kanatzidis, M. G. *J. Am. Chem. Soc.* **2011**, *133*, 20476−20487.

(9) (a) Marks, B. M.; Howard, H. C. *J. Phys. Chem.* **1927**, *32*, 1040−1048. (b) Zherebetskyy, D.; Scheele, M.; Zhang, Y.; Bronstein, N.; Thompson, C.; Britt, D.; Salmeron, M.; Alivisatos, P.; Wang, L.-W. *Science* **2014**, *344*, 1380−1384. (c) Hyeon, T. *Chemm. Comm.* **2003**, 927−934.

(10) Quan, Z.; Luo, Z.; Loc, W. S.; Zhang, J.; Wang, Y.; Yang, K.; Porter, N.; Lin, J.; Wang, H.; Fang, J. *J. Am. Chem. Soc.* **2011**, *133*, 17590−17593.

(11) Ibáñez, M.; Zamani, R.; Gorsse, S.; Fan, J.; Ortega, S.; Cadavid, D.; Morante, J. R.; Arbiol, J.; Cabot, A. *ACS Nano* **2013**, *7*, 2573−2586.

(12) Androulakis, J.; Todorov, I.; He, J.; Chung, D.-Y.; Dravid, V.; Kanatzidis, M. *J. Am. Chem. Soc.* **2011**, *133*, 10920−10927.

Electron doping in bottom-up engineered thermoelectric nano-materials through HCl-mediated ligand displacement

Supporting Information

Maria Ibáñez,[†] Rachel Korkosz,[¥] Zhishan Luo,[†] Pau Riba,[†] Doris Cadavid,[†] Silvia Ortega,[†] Andreu Cabot[†,‡,]* and Mercouri G. Kanatzidis[¥,]*

† Catalonia Energy Research Institute - IREC, Sant Adria del Besos, 08930 Barcelona, Spain
¥ Department of Chemistry, Northwestern University, Evanston, Illinois 60208, United States
‡ Institució Catalana de Recerca i Estudis Avançats - ICREA, 08010 Barcelona, Spain

S1

Contents

1- Chemicals

Lead (II) Oxide (99.9%), oleic acid (OA, tech. 90%), 1-octadecene (ODE, 90%), anhydrous thioacetamide (ACS reagent≥99.0%), Oleylamine (OLA, tech. 70%), elemental sulfur (99.98 %), tributylphosphine (TBP, 97%), N,N-Dimethylformamide (DMF, ≥99%), Hydrogen chloride – ethanol solution (1.25M), were purchased from Aldrich. Tri-*n*-octylphosphine (TOP, 97%) was purchased from Strem. Anhydrous hexane, chloroform, and methanol were obtained from various sources. All chemicals, except OLA were used as received without further purification. OLA was distillated to remove impurities. All syntheses were carried out using standard airless techniques: a vacuum/dry argon gas Schlenk line was used for the synthesis and a argon glove-box for storing and handling air and moisture-sensitive chemicals.

Important note: HCl is a highly volatile compound. All the concentrations reported on the paper were calculated considering we have exactly 1.25 M solution. However, we believe that the numbers we provide must be consider as an upper limit. In order to be systematic on the experimental procedures, sets of experiments were done the same day the bottle was opened and all the different mixtures of NPs and HCl solution were done with a few seconds of difference.

2- Synthesis of PbS NPs

In a typical synthesis, PbO (4.64 g, 20 mmol) and oleic acid (OA, 50 ml, 0.158 mol) were mixed with 100 ml of octadecene (ODE). This mixture was degassed at RT and 100 ºC for 0.5 h each to form the lead oleate complex. Then the solution was flushed with Ar, and the temperature was raised to 210 ºC. At this temperature, a sulfur precursor, prepared by dissolving elemental sulfur (0.64 g, 20 mmol) in distilled oleylamine (OLA, 20 ml, 0.061 mol), was rapidly injected. The reaction mixture was maintained between 195 and 210 ºC for 5 min and then quickly cooled down to room temperature using a water bath. PbS NPs were thoroughly washed by multiple precipitation/re-dispersion steps using ethanol as a non-solvent and hexane as solvent. Washed NPs were dried out under vacuum and stored for further use.

3- Synthesis of PbTe$_x$Se$_{1-x}$@PbS core-shell NPs

PbTe$_x$Se$_{1-x}$@PbS core-shell NPs were produced by consecutive reactions of lead oleate with chalcogens following a combination of the methods developed by Quan et al.[1] and ourselves (SI).[2] Core PbTe$_x$Se$_{1-x}$ NPs were produced using a modified approach of that reported by Quan et al.[1] PbTe$_x$Se$_{1-x}$@PbS NPs

S3

were subsequently obtained following the procedure we previously reported to produce PbTe@PbS core-shell NPs. In a typical synthesis, lead (II) oxide (4.5 g, 20 mM) and oleic acid (22.24 g, 80 mM) were dissolved in 130 ml ODE. This mixture was degassed at RT and 100 °C for 0.5 h each to form a lead oleate complex. Afterwards, the clear transparent solution was flashed with argon and heated up to the reaction temperature (175 °C). At this temperature, 16 mL of a 1M TBP:Se solution were rapidly injected under argon gas flow. After 1 min, 1 mL of TOP:Te was rapidly added to the reaction. The reaction mixture was kept for 4 more minutes and then quickly cooled down to room temperature using a water bath. Once the crude solution was at room temperature, 189 mg of thioacetamide dissolved in 10 mL of dimethylformamide was injected into the flask. NPs solution containing the sulfur precursor was heated up to 80 °C at 1.7°C/min and kept at this temperature for an additional 60 min. NPs were washed by the several precipitation/redispersion steps. The core composition could be tuned by introducing different relative amount of Se and Te precursors or controlling the nucleation time of PbSe initial NPs. The overall composition of the core-shell NP could be adjusted by tuning the initial core size following a similar approach of that we previously reported for PbTe@PbS NPs.[2]

4- Thermogravimetric analysis (TGAs)

TGA was used to estimate the amount of organic ligand present in the as-synthesized and HCl treated NPs. TGAs were done using Perkin-Elmer TGA 4000 equipment between 30 °C and 400 °C degree with a heating rate of 10 °C/min under nitrogern atmosphere.
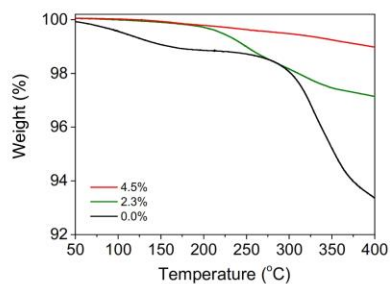

Figure SI1. Thermogravimetric profile of PbS-OA, PbS-X% nanoparticles

5- Sulfur removal during HCl-mediated ligand exchange

Sulfur removal is a part of the mechanism of the HCl-mediated ligand exchange. We believe the reaction with HCl involves the formation of $PbCl_2$ at the nanoparticle surface and the parallel reaction of 2 H+ with S^{2-} which leaves the material in the form of H_2S gas. When large amounts of HCl are used, $PbCl_2$ domains are formed. However, when small contents of HCl are used, Cl^- ion at the nanoparticle surface diffuse and randomly incorporate within the PbS anion sub-lattice during the thermal treatment and consolidation process. The main experimental evidence demonstrating the formation of Pb-Cl bonds is obtained when using high concentrations of HCl when $PbCl_2$ crsystalline domains are formed and can be observed by x-ray diffraction. XRD patterns obtained after consolidation of PbS nanoparticles treated with increasingly higher amounts of HCl are shown in figure SI5. Peaks corresponding to $PbCl_2$ where detected for large concentrations of HCl. Howeber, $PbCl_2$ could be also observed in as treated nanoaprticles when large excess of HCl as used. We could even be able to completely convert the PbS nanoparticles to pure $PbCl_2$ powder. In figure SI2 we present a picture of the PbS NPs compared and the white precipitated obtained after the HCl treatment. Additionally in figure SI3 we show the XRD pattern of the white precipitated which allows us to indemnify it as $PbCl_2$.
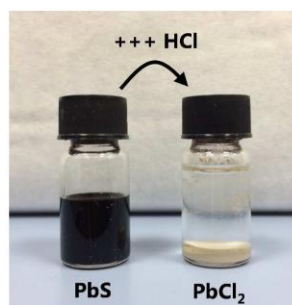

Figure SI2. Picture of PbS NPs dissolve in chloroform and the $PbCl_2$ powder obtained after treating the NPs with large excess of HCl.
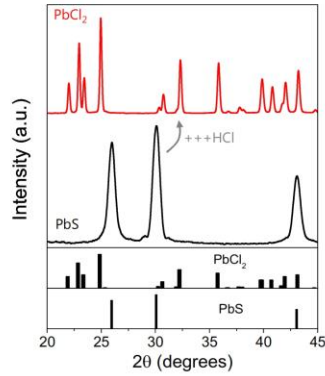
S5

Figure SI3. XRD patterns of the PbS NPs (black) and $PbCl_2$ crystalline powder (red) obtained after treating PbS NPs with a large amount of HCl.

6- Pellet Fabrication

In all cases HCl treated and non-treated NPs were dried out from solution under vacuum. Afterward, NPs were heated to 400 °C for 1 hour under an Ar flow.

PbS NPs powders were pressed using a custom-made hot press. In this system, the heat is provided by an induction coil operated in the RF range applied directly to a graphite die acting as a susceptor. This set up configuration allows increasing temperature at a similar rate than Spark Plasma Sintering (SPS). Inside a glovebox powders were ground into fine powder and loaded into a 10 mm diameter graphite die lined with 0.13 mm thick graphite paper. The filled die was place in the hot press system. The densitfication profile applied an axial pressure of 40 MPa before heating the die to 400 °C. The temperature was hold between 400-420 °C for 5 minutes. The pressure was then removed and the die cooled to room temperature. The resulting pellets were >85% dense, ~1 mm thick, 10 mm in diameter, and air stable. The density of the pressed pellets was measured by weight/volume.

$(PbTe_{0.2}Se_{0.8})_{0.47}@(PbS)_{0.53}$ core-shell NP powders were pressed into dense pellets with an FDC Dr. Sinter Lab Jr SPS-211LX. Inside the glovebox, the powders were ground and loaded into a 10 mm diameter graphite die lined with 0.2 mm thick graphite paper. The filled die was rapidly placed inside the SPS

system, and the chamber was immediately closed and placed under vacuum. The chamber was evacuated for at least 3 minutes before pressing. The densification profile applied an axial pressure of 40 MPa before heating the die with pulsed electric current to 400 °C over 5 minutes, then to 450 °C over 1 minute, and holding at 450 °C for 5 minutes. The pressure was then removed and the die cooled, still under vacuum to ~100 °C and then cooled in air to room temperature. The resulting pellets were >85% dense, ~2 mm thick, 10 mm in diameter, and air stable. The experimental density was measured with a Micromeritics Accu-pyc 1340 gas pycnometer.

7- Note on thermal treatment

Thermal treatments (annealing and consolidation) were required to thermally decompose the remaining organic ligand at the nanoparticles surface and to compact the material into a dense pellet.

Therefore, temperature and time of the thermal treatment before powder consolidation were chosen based on the required temperature to decompose the organic surfactant present in the nanoparticles surface. This was evaluated using thermogravimetry analysis (figure SI1). Pellet consolidation conditions were selected in order to minimize pellet fragility and optimize density. Pellets with the highest densities and proper crystallographic phases were obtained for the conditions reported.

The temperature and time window for this treatments is very narrow as too low temperatures do not allow decomposing the residual organics thus resulting in very low electrical conductivities and too high thermal treatments resulted both in very large crystal domains which were chalcogen-poor as the chalcogen tends to leave the material at relatively high temperatures if the material is annealed in an open tub furnace. In this case, after nanopowder consolidation, XRD pattern present reflections corresponding to metallic lead (figure SI4). Annealing in a close reactor, while may prevent the chalcogen leave, does not allow appropriately removing the organics and increasing significantly the amount of residual carbon in the final nanomaterial. Conveniently, as a side effect, these absolutely necessary thermal treatments promote the insertion of Cl^- ions into the anion sub-lattice.

S7

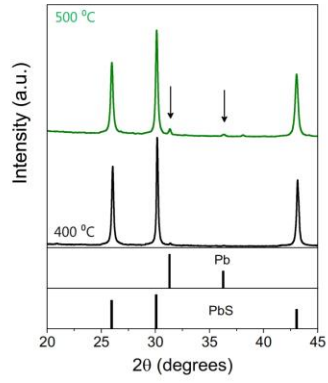**Figure SI4.** XRD patterns of the PbS nanomaterials after annealed at 400 $^{\circ}$C (black) and 500 $^{\circ}$C (green) and pressed at 400-420 $^{\circ}$C. Arrows point out at the presence of Pb in the sample annealed at 500 $^{\circ}$C un-der an Ar flow.

8- XRD characterization of PbS-x% pellets

XRD analyses were collected directly on the as-synthesized NPs and final pellets on a Bruker AXS D8
Advance X-ray diffractometer with Ni-filtered (2 μm thickness) Cu K$_\lambda$ radiation ($\lambda = 1.5406$ Å) operat-
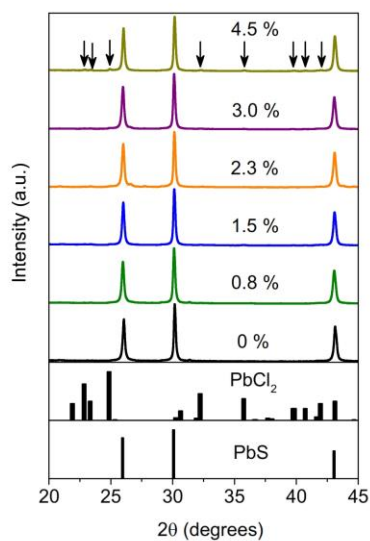ing at 40kV and 40mA. A LynxEye linear position-sensitive detector was used in reflection geometry.

Figure SI5. XRD patterns of the PbS nanomaterials after hot press. Arrows point out at the presence of
PbCl$_2$ in the sample with a 9% of Cl.

S9

9- Thermoelectric characterization

Seebeck coefficient was measured by using a static DC method. Electrical resistivity data were obtained by a standard four-probe method. Both the Seebeck coefficient and the electrical resistivity were measured simultaneously in a LSR-3 LINSEIS system in the range between room temperature and 673 K, under helium atmosphere.

XFA 600 Xenon Flash Apparatus was used to determine the thermal diffusivities of samples. The thermal conductivity Thermal conductivity was calculated The thermal conductivity (κ) was calculated using the relation $\kappa = DC_p\rho$, where D is the thermal diffusivity, C_p is the heat capacity, and ρ is the mass density of the specimen. The ρ values used here were calculated using the Archimedes method. The specific heats (Cp) of the samples were estimated using established literature values. In the case of PbS we used the values reported in reference 5 in the supporting information document. For $PbTe_{0.1}Se_{0.4}S_{0.5}$ nanocomposites we estimated heat capacity using the Dulong-Petit approximation. We considered the values for PbTe, PbSe and PbS and their content to final in the nanocomposite to calculate the nanocomposite heat capacity. Used numbers are presented in the following table.

Compound	Heat Capacity (Dulong-Petit approximation) $(J \cdot g^{-1} K^{-1})$
PbS	0.208
PbSe	0.174
PbTe	0.149
$PbTe_{0.1}Se_{0.4}S_{0.5}$	0.189

S10

10- PbS-OA Nanoparticles

During the thermal treatment, OA at the PbS surface is decomposed to various carbon containing species. However, we speculate the decomposition of the carboxylic groups bonded to surface Pb atoms result in the formation of a monotoatomic PbO surface layer in the same way as the decomposition of metal oleates in air free conditions result in the formation of oxides(Chem. Commun. 2003, 927-934). Thus, after decomposition, at the grain boundaries a very thin PbO layer and a slightly thicker carbon layer remain. These certainly introduce a barrier for charge carriers to move across the polycrystalline material. It also blocks grain growth and results in relatively lower thermal conductivities at low temperatures.

11- Note on the sign inversion of Seebeck coefficient

The sign inversion is a clear evidence of a relatively low charge carrier concentration in undoped PbS nanomaterials. Pure PbS nanomaterials were characterized by relatively low electrical conductivities at room temperature which strongly increased with temperature due to band to band charge carrier thermal excitation. This increase in electrical conductivity was accompanied by a sign inversion of the Seebeck coefficient, indicating the higher electron-to-hole mobility ratio as the temperature increase.
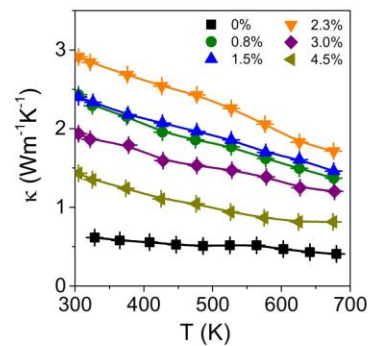
12- Thermal conductivity of PbS

Figure SI6. Thermal conductivity for PbS-OA NPs (black squares) and PbS-X% NPs with 0.8 % < X < 4.5 % as noted in the legend.
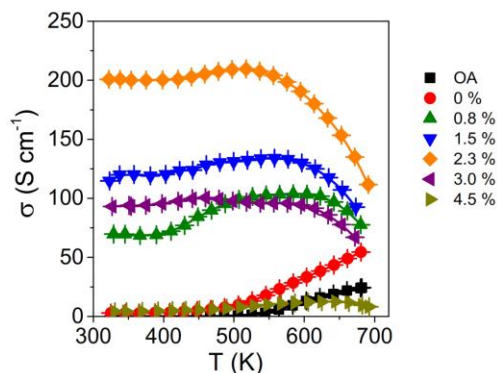
S11

13- Doped PbS metallic behaviour

Figure SI7. Electrical conductivity (σ) of nanocrystalline PbS obtained from the bottom-up assembly of PbS-OA NPs and PbS-X% NPs with 0 % < X < 4.5 % as noted in the legend.

Electric performance of our nanocrystalline materials is quite different than the performance of a bulk crystal with endotaxial nanograin embedded. As expected for heavily doped semiconductors (metallic behavior) electricalconductivity should decrease with temperature. However, at low temperatures we do not see this behavior for any (doped and undoped) of our nanomaterials. Instead electrical conductivity either increases or remains constant at low temperatures. We associate this behavior to the presence of energy barriers in the nanomaterial and the band to band charge carrier thermal excitation. However, at high temperatures electrical conductivity clearly drops due to the scattering induced by the ionized impurities which reduce electron mobility and hence the electrical conductivity, as it is expected for a highly degenerated semiconductor.

14- Porosity correction

In order to be able to estimate properly the contribution of the lattice on the final thermal conductivity we need to subtract the possible contribution added due to the sample porosity. An estimation of the electrical and thermal conductivity that would be measured from a 100% dense sample can be obtained using a Maxwell-Eucken expression [2-3]:

S12

$$X_{100} = X_P \frac{1 + \beta P}{1 - P}$$

Where X_{100} is the electrical or thermal conductivity in the 100 % dense medium, P is the porosity degree in the range between 0 and 1, and β is an empirical parameter related to the pore geometry, which we fixed to 2 [3b]. It is important to notice that the thermoelectric figure of merit ZT is not modified by this correction because the porosity effect on the electrical and thermal conductivities compensates each other.

The Maxwell-Eucken model is one of the most widely used methods to estimate the reduction in conductivity due to porosity. This model is based on randomly distributed spherical pores. The model considers a low concentration of isolated spherical pores. Additionally, the thermal conductivity through the porous is considered negligible when compared to that of the solid material. The factor β allows correcting for pores with a different geometry. If the pores are resembled to a sphere the β value is between 1 and 3. Due to the random distribution of pores in our nanomaterials, we estimated a β value equal to 2.[4]

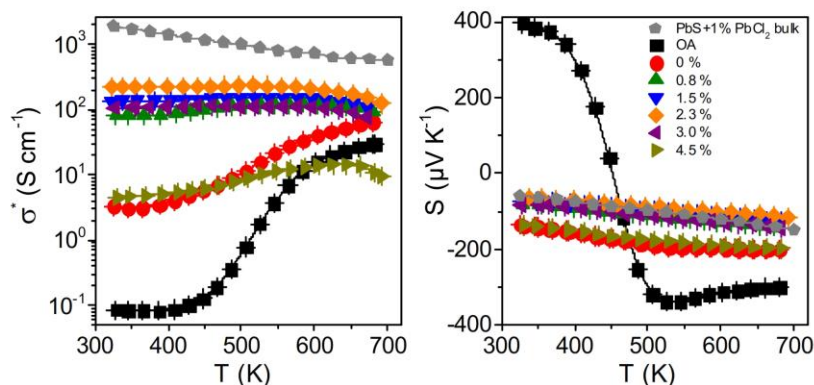**15- Comparison with bulk PbS 1% PbCl₂ doped**

Figure SI8. Porosity corrected electrical conductivity (σ^*) and Seebeck coefficient (S) of nanocrystalline PbS obtained from the bottom-up assembly of PbS-OA NPs and PbS-X% NPs with 0 % < X < 4.5

S13

% as noted in the legend compared with a reported value for PbS doped with 1% PbCl$_2$ taken from reference 5.

16- Thermal conductivity study for the PbTe$_{0.1}$Se$_{0.4}$S$_{0.5}$ system

Considering PbTe$_{0.1}$Se$_{0.4}$S$_{0.5}$-OA relative density 85% and PbTe$_{0.1}$Se$_{0.4}$S$_{0.5}$-Cl relative density 93%, figure SI4 shows thermal conductivities with porosity correction (*) and without.
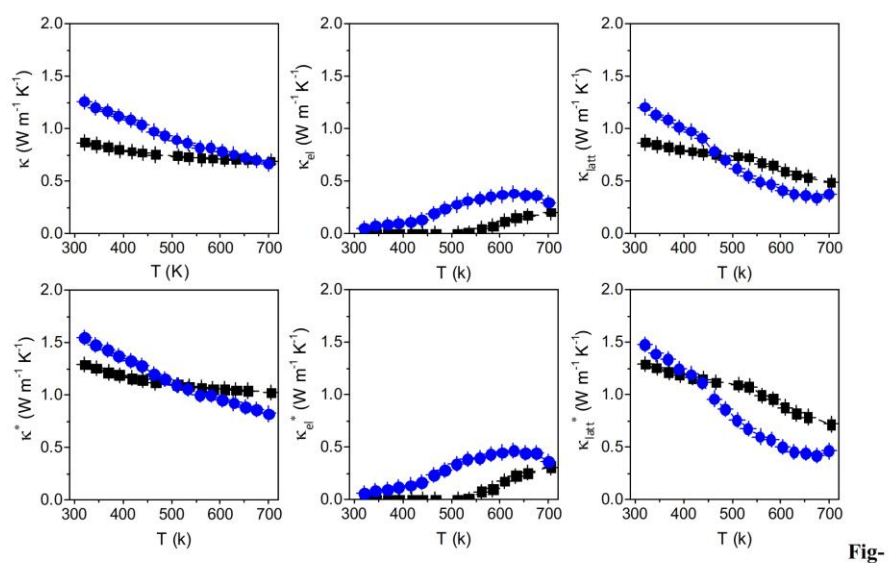

Fig-

Figure SI9. Thermal conductivity (κ), electronic thermal conductivity (κ_{el}) and lattice thermal conductivity (κ_{latt}). Porosity corrected data is market with the superscript *.

S14

17- Thermoelectric properties of NPs treated with HCl and NH₄SCN.

Figure SI10. Electrical conductivity (a) and Seebeck coefficient (b) of nanocrystalline PbS obtained from the bottom-up assembly of PbS-OA NPs and PbS-X% NPs with 0 % < X < 3 % as noted in the legend. PbS NPs were initially treated with different amounts of HCl and later with an excess of NH₄SCN.

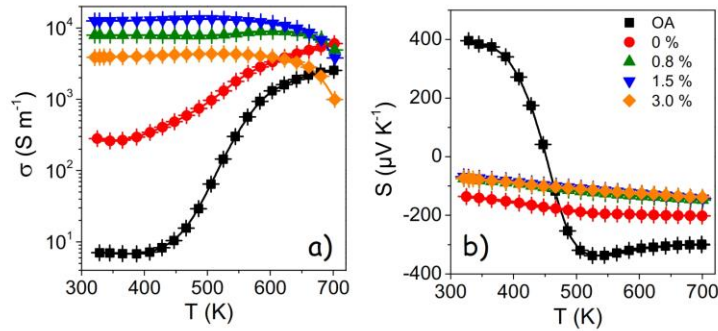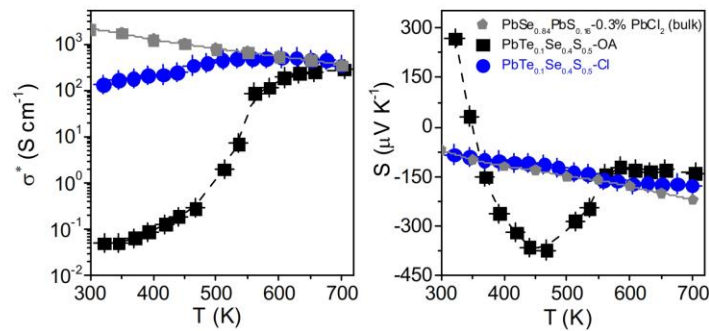**18- Comparison with bulk PbSe₀.₈₄PbS₀.₁₆ doped with 0.3% PbCl₂**

Figure SI11. Electrical conductivity (σ) and Seebeck coefficient (S) of nanocrystalline PbTe₀.₁Se₀.₄S₀.₅ obtained from the bottom-up assembly of PbTe₀.₁Se₀.₄S₀.₅-OA and PbTe₀.₁Se₀.₄S₀.₅-Cl as noted in the legend compared with a PbSe₀.₈₄PbS₀.₁₆-0.3% PbCl₂ doped taken from reference 12.

S15

19- State-of-the-art values for lead chalcogenide compounds

System	σ (S cm^{-1})	S (μV K^{-1})	PF (μW cm^{-1} K^{-2})	κ (W m^{-1} K^{-1})	ZT (700K)	ZT$_{max}$ T(K)	Ref.
$Pb_{0.975}Na_{0.025}S$ + 3.0% CdS	142	280	11.1	0.79	0.65	1.3 (923 K)	5
PbS + 1% Bi_2S_3 + 1% $PbCl_2$	275	-220	13.31	1.1	0.51	1.1 (923 K)	6
PbS + 3% SrS + 2.5% Na	109	290	9.1	0.70	0.62	1.2 (923 K)	7
PbTe-PbS12% + 2% Na	390	252	24	1.1	1.3	1.8 (800 K)	8
$PbTe_{0.7}S_{0.3}$ + 2.5% K	170	294	14.7	0.65	1.9	2.0 (923 K)	9
PbTe + 4% SrTe + 2% Na	285	290	23.9	1.0	1.6	2.2 (923 K)	10
$PbTe_{0.86}PbSe_{0.07}PbS_{0.07}$ + 2% Na	375	270	27.4	1.1	1.8	2.0 (825 K)	11
$(PbSe)_{0.88}(PbS)_{0.12}$ + 0.3% $PbCl_2$	220	260	14	1.1	1.0	1.2 (900 K)	12
$PbTe_{0.1}Se_{0.4}S_{0.5}$-Cl	280	-180	9.1	0.68	0.94	0.94 (700 K)	This work

20-References:

1.   Quan, Z.; Luo, Z.; Loc, W. S.; Zhang, J.; Wang, Y.; Yang, K.; Porter, N.; Lin, J.; Wang, H.; Fang, J., Synthesis of PbSeTe Single Ternary Alloy and Core/Shell Heterostructured Nanocubes. *J. Am. Chem. Soc.* **2011,** *133* (44), 17590-17593.

2.   Ibáñez, M.; Zamani, R.; Gorsse, S.; Fan, J.; Ortega, S.; Cadavid, D.; Morante, J. R.; Arbiol, J.; Cabot, A., Core–Shell Nanoparticles As Building Blocks for the Bottom-Up Production of Functional Nanocomposites: PbTe–PbS Thermoelectric Properties. *ACS Nano* **2013,** *7* (3), 2573-2586.

3.   (a) Yang, L.; Wu, J. S.; Zhang, L. T., Synthesis of filled skutterudite compound La0.75Fe3CoSb12 by spark plasma sintering and effect of porosity on thermoelectric properties. *J. Alloys Compd.* **2004,** *364* (1–2), 83-88; (b) Adachi, J.; Kurosaki, K.; Uno, M.; Yamanaka, S., Effect of porosity on thermal and electrical properties of polycrystalline bulk ZrN prepared by spark plasma sintering. *J. Alloys Compd.* **2007,** *432* (1–2), 7-10.

4.   (a) Carson, J. K.; Lovatt, S. J.; Tanner, D. J.; Cleland, A. C., Thermal conductivity bounds for isotropic, porous materials. *Int. J. Heat Mass Transfer* **2005,** *48* (11), 2150-2158; (b) Ondracek, G.; Schulz, B., The porosity dependence of the thermal conductivity for nuclear fuels. *J. Nucl. Mater.* **1973,** *46* (3), 253-258.

5.   Zhao, L.-D.; He, J.; Hao, S.; Wu, C.-I.; Hogan, T. P.; Wolverton, C.; Dravid, V. P.; Kanatzidis, M. G., Raising the Thermoelectric Performance of p-Type PbS with Endotaxial Nanostructuring and Valence-Band Offset Engineering Using CdS and ZnS. *J. Am. Chem. Soc.* **2012,** *134* (39), 16327-16336.

6.   Zhao, L.-D.; Lo, S.-H.; He, J.; Li, H.; Biswas, K.; Androulakis, J.; Wu, C.-I.; Hogan, T. P.; Chung, D.-Y.; Dravid, V. P.; Kanatzidis, M. G., High Performance Thermoelectrics from Earth-Abundant Materials: Enhanced Figure of Merit in PbS by Second Phase Nanostructures. *J. Am. Chem. Soc.* **2011,** *133* (50), 20476-20487.

7.   Zhao, L.-D.; He, J.; Wu, C.-I.; Hogan, T. P.; Zhou, X.; Uher, C.; Dravid, V. P.; Kanatzidis, M. G., Thermoelectrics with Earth Abundant Elements: High Performance p-type PbS Nanostructured with SrS and CaS. *J. Am. Chem. Soc.* **2012,** *134* (18), 7902-7912.

8.   Girard, S. N.; He, J.; Zhou, X.; Shoemaker, D.; Jaworski, C. M.; Uher, C.; Dravid, V. P.; Heremans, J. P.; Kanatzidis, M. G., High Performance Na-doped PbTe–PbS Thermoelectric Materials: Electronic Density of States Modification and Shape-Controlled Nanostructures. *J. Am. Chem. Soc.* **2011,** *133* (41), 16588-16597.

9.   Wu, H. J.; Zhao, L. D.; Zheng, F. S.; Wu, D.; Pei, Y. L.; Tong, X.; Kanatzidis, M. G.; He, J. Q., Broad temperature plateau for thermoelectric figure of merit ZT>2 in phase-separated PbTe0.7S0.3. *Nat. Commun.* **2014,** *5*, 4515.

10.   Biswas, K.; He, J.; Blum, I. D.; Wu, C.-I.; Hogan, T. P.; Seidman, D. N.; Dravid, V. P.; Kanatzidis, M. G., High-performance bulk thermoelectrics with all-scale hierarchical architectures. *Nature* **2012,** *489* (7416), 414-418.

11.   Korkosz, R. J.; Chasapis, T. C.; Lo, S.-h.; Doak, J. W.; Kim, Y. J.; Wu, C.-I.; Hatzikraniotis, E.; Hogan, T. P.; Seidman, D. N.; Wolverton, C.; Dravid, V. P.; Kanatzidis, M. G., High ZT in p-Type $(PbTe)_{1–2x}(PbSe)_x(PbS)_x$ Thermoelectric Materials. *J. Am. Chem. Soc.* **2014,** *136* (8), 3225-3237.

12.   Androulakis, J.; Todorov, I.; He, J.; Chung, D.-Y.; Dravid, V.; Kanatzidis, M., Thermoelectrics from Abundant Chemical Elements: High-Performance Nanostructured PbSe–PbS. *J. Am. Chem. Soc.* **2011,** *133* (28), 10920-10927.
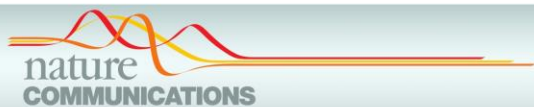
Solution processing and engineering of thermoelectric nanomaterials

ARTICLE

High-performance thermoelectric nanocomposites from nanocrystal building blocks

Maria Ibáñez[1,2,3], Zhishan Luo[3], Aziz Genç[4], Laura Piveteau[1,2], Silvia Ortega[3], Doris Cadavid[3], Oleksandr Dobrozhan[3], Yu Liu[3], Maarten Nachtegaal[5], Mona Zebarjadi[6], Jordi Arbiol[4,7], Maksym V. Kovalenko[1,2] & Andreu Cabot[3,7]

The efficient conversion between thermal and electrical energy by means of durable, silent and scalable solid-state thermoelectric devices has been a long standing goal. While nanocrystalline materials have already led to substantially higher thermoelectric efficiencies, further improvements are expected to arise from precise chemical engineering of nanoscale building blocks and interfaces. Here we present a simple and versatile bottom–up strategy based on the assembly of colloidal nanocrystals to produce consolidated yet nanostructured thermoelectric materials. In the case study on the PbS–Ag system, Ag nanodomains not only contribute to block phonon propagation, but also provide electrons to the PbS host semiconductor and reduce the PbS intergrain energy barriers for charge transport. Thus, PbS–Ag nanocomposites exhibit reduced thermal conductivities and higher charge carrier concentrations and mobilities than PbS nanomaterial. Such improvements of the material transport properties provide thermoelectric figures of merit up to 1.7 at 850 K.

[1] Department of Chemistry and Applied Biosciences, Institute of Inorganic Chemistry, ETH Zürich, Vladimir Prelog Weg 1, CH-8093 Zurich, Switzerland. [2] Laboratory for Thin Films and Photovoltaics, Empa-Swiss Federal Laboratories for Materials Science and Technology, Dübendorf, Überlandstrasse 129, CH-8600 Dübendorf, Switzerland. [3] Advanced Materials Department, Catalonia Energy Research Institute - IREC, Sant Adria de Besos, Jardins de les Dones de Negre n.1, Pl. 2, 08930 Barcelona, Spain. [4] Department of Advanced Electron Nanoscopy, Catalan Institute of Nanoscience and Nanotechnology (ICN2), CSIC and The Barcelona Institute of Science and Technology, Campus UAB, Bellaterra, 08193 Barcelona, Spain. [5] Paul Scherrer Institute, 5232 Villigen PSI, Switzerland. [6] Department of Mechanical and Aerospace Engineering, Rutgers University, 98 Brett Rd, Piscataway, New Jersey 08854-8058, USA. [7] Institució Catalana de Recerca i Estudis Avançats, ICREA, Passeig de Lluís Companys, 23 08010 Barcelona, Spain. Correspondence and requests for materials should be addressed to A.C. (email: acabot@irec.cat).

Thermoelectric devices allow direct conversion of heat into electricity and *vice versa*, holding great potential for heat management, precise temperature control and energy harvesting from ubiquitous temperature gradients. The efficiency of thermoelectric devices is primarily governed by three interrelated material parameters: the electrical conductivity, σ, the Seebeck coefficient or thermopower, S, and the thermal conductivity, κ. These parameters are grouped into a dimensionless figure of merit, ZT, defined as $ZT = \sigma S^2 T \kappa^{-1}$ where T is the absolute temperature. While there is no known limitation to the maximum thermoelectric energy conversion efficiency other than the Carnot limit, current thermoelectric materials struggle to simultaneously display high σ and S, and low κ, which prevents their widespread implementation[1].

Control of the chemical composition and crystallinity of thermoelectric materials at the nanoscale via engineering of multicomponent nanomaterials (nanocomposites) has proven to be effective for the reduction of thermal conductivity by promoting phonon scattering at grain boundaries[2–7]. The remaining major challenge facing the next generation of high-efficiency thermoelectric materials is the enhancement of the thermoelectric power factor (PF $= S^2 \sigma$) while keeping a low thermal conductivity. Strategies to accomplish this goal have focused on increasing the average energy per carrier through energy filtering[8], carrier localization in narrow bands in quantum confined structures[9], or the introduction of resonant levels[10]. At the same time, the electrical conductivity must be optimized by properly adjusting the concentration of charge carriers and maximizing their mobility.

These improvements of thermoelectric properties have been mainly demonstrated at the thin-film level, oftentimes using precise but expensive vacuum-based materials growth techniques[11]. However, practical applications of thermoelectric materials demand inexpensive and, for withstanding relatively high temperature gradients, macroscopic devices. In this regard, current approaches to produce bulk nanocomposites, such as ball-milling or the precipitation of secondary phases from metastable solid solutions, lack precision control over the distribution of phases and/or are limited in compositional versatility. Thus, novel cost-effective and general strategies to produce bulk nanocomposites with high accuracy and versatility need to be developed.

Here we demonstrate that a simple route to engineering nanocomposites by the assembly of precisely designed nanocrystal building blocks is able to reach high thermoelectric efficiencies. We propose to blend semiconductor nanocrystals with metallic nanocrystals forming Ohmic contact with the host semiconductor. In such nanocomposites, metallic nanocrystals control charge carrier concentration through charge spill over to the host semiconductor. The goal of this configuration is to reach large charge carrier concentrations without deteriorating the mobility of charge carriers[12–16]. In this three-dimensional (3D) modulation doping strategy[17–20], composition, size and distribution of semiconductor and metal nanodomains control the nanocomposite transport properties. Consider a slab of a semiconductor sandwiched between two metallic plates. Transfer of charges at the interfaces will cause band bending, extending over charge-screening length. If the width of a semiconductor slab is on the order of this screening length, there will be an overlap of the bended bands and therefore carriers will not be confined to the interfaces, but they will be able to travel through the bulk of a semiconducting region. Similarly, in the 3D case, the size of the semiconducting nanocrystals should be on the order of the screening length, enabling charge transport with minimum scattering. The position of the quasi Fermi level relative to the conduction band of the semiconductor at the

metal–semiconductor interface should be adjusted to align the bands and minimize scattering rates. This can be done by selecting metallic nanocrystals of the appropriate material and size and adjusting their volume fraction. The bottom-up approach presented in this work (Fig. 1) offers sufficient materials versatility to harness the key benefits of such 3D modulation doping by selecting materials with appropriate Fermi levels and allowing a facile control of nanocrystals size and volume fraction. For this study, PbS was selected as inexpensive host semiconductor that comprises Earth-abundant elements (that is, contrary to tellurides), and holds great potential for reaching high thermoelectric efficiencies; with reported ZT values of up to 1.3 at 923 K in PbS–CdS[21]. Silver is chosen as a nanoscopic metallic dopant owing to its low work function (4.26–4.9 eV) (refs 22–24) needed for efficient injection of electrons into the PbS conduction band. The PbS–Ag nanocomposites derived from colloidal PbS and Ag nanocrystals exhibit high electrical conductivities due to (i) injection of electrons from Ag nanoinclusions to the host PbS and (ii) improved charge carrier mobility. The simultaneous combination of high electrical conductivity, relatively large Seebeck coefficients, and reduced thermal conductivities provides thermoelectric figures of merit up to 1.7 at 850 K.

Results

PbS–Ag nanocomposites. PbS–Ag nanocomposites were produced by combining cubic PbS nanocrystals (*ca.* 11 nm, Fig. 2a) and spherical Ag nanocrystals (*ca.* 3 nm Fig. 2b), followed by the evaporation of a solvent. Thereby obtained powdered nanocrystal blend was annealed to remove residual organic compounds and then hot-pressed into pellets. This simple procedure yielded nanocomposites with a highly homogeneous distribution of metallic Ag nanodomains at the interfaces of PbS grains, as evidenced by high-resolution transmission electron microscopy (HRTEM), high-angle annular dark field scanning transmission electron microscopy and energy-dispersive X-ray spectroscopy (Fig. 2c,d). Further atomistic insights into bonding and chemical identities of constituents were obtained by X-ray absorption
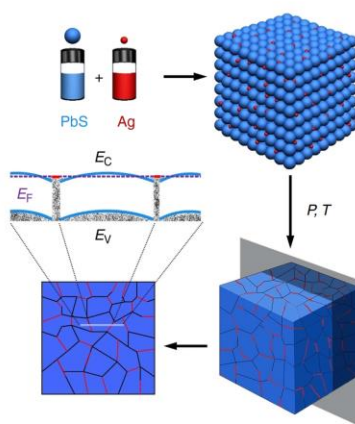

Figure 1 | Bottom-up Design. Bottom-up assembly process to produce PbS-Ag TE nanocomposites from the assembly of PbS (blue) and Ag (red) NCs, and the corresponding band alignment of the resulting nanocomposite.
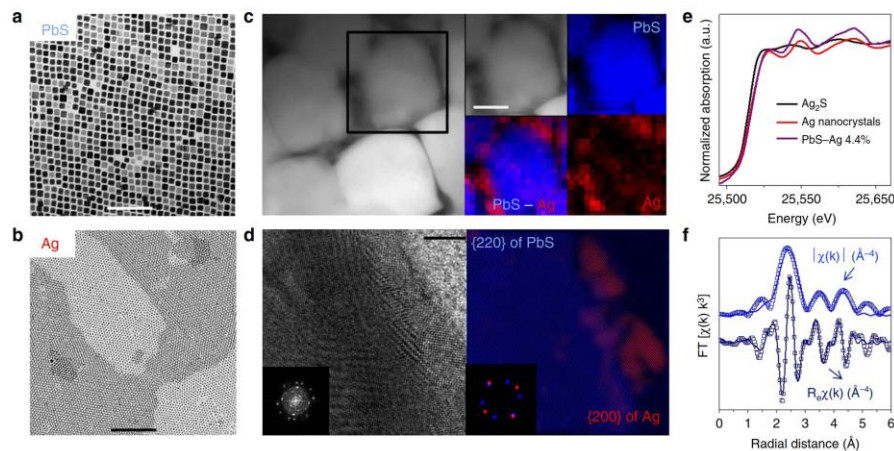
ARTICLE

Figure 2 | Structural and compositional characterization of initial NCs and resulting PbS-Ag 4.4 mol% nanocomposite. TEM micrographs of
(**a**) PbS and (**b**) Ag NCs; (**c**) HAADF-STEM micrograph and elemental EDX maps; and (**d**) HRTEM micrograph of the PbS-Ag interface with the
corresponding power spectrum (inset) and filtered colourful composite image for the {220} family of planes of PbS (blue) and {200} family of planes
of Ag (red). In the filtered images, PbS and Ag are visualized along their [111] and [001] zone axes, respectively (Supplementary Note 1); (**e**) Ag K-edge
XANES spectra of Ag_2S reference (black), Ag NCs (red) and PbS-Ag 4.4 mol% nanocomposite (purple); (**f**) Fourier transform magnitude, $|\chi_{(k)}|$,
and real part, $_{Re}\chi_{(k)}$, of the Pb L_3-edge EXAFS spectrum, the experimental data are given by the dotted line, the best fit by the solid line. Scale bars, 100 nm
(**a**), 100 nm (**b**), 50 nm (**c**), 5 nm (**d**).

spectroscopy (XAS) at the Ag K edge (25515 eV) and Pb L_3 edge
(13035 eV), respectively. Linear combination fitting of the X-ray
absorption near edge structure (XANES) around the Ag absorp-
tion K edge, using references of Ag_2S and Ag metal, confirmed
that at least 97% of Ag retained its metallic state (Fig. 2e,
Supplementary Fig. 1 and Table 1). Only a small percentage of Ag
may have diffused as Ag^+ within the PbS matrix. In addition,
fitting of the Pb L_3 edge extended X-ray absorption fine structure
spectra indicated interatomic distances and coordination num-
bers characteristics of PbS[25] (Fig. 2f). Metallic lead, lead oxide or
lead sulfate species did not noticeably contribute to the spectra,
suggesting that the presence of these phases can be disregarded
(Supplementary Table 2).

Thermoelectric properties. To determine the effect of the
Ag content on thermoelectric performance, a series of nano-
composites with Ag concentrations up to 5 mol% were prepared
and analysed. Ag-free PbS nanomaterials exhibited relatively
low electrical conductivities, which greatly increased from
0.07 S cm^{-1} at room temperature (RT) up to 46 S cm^{-1} at 850 K
due to band to band charge carrier thermal excitation (Fig. 3a).
This increase was accompanied by a sign inversion of the Seebeck
coefficient from positive to negative at around 470 K (Fig. 3b). On
the contrary, PbS-Ag nanocomposites possess significantly
higher, Ag concentration-dependent, electrical conductivities. At
RT, electrical conductivities of up to 660 S cm^{-1} were measured
for Ag concentrations above 4 mol% (Fig. 3a). Furthermore, over
the whole studied temperature range of 300-850 K, PbS-Ag
nanocomposites exhibit negative Seebeck coefficients. Unlike
to electrical conductivity, Seebeck coefficient decreases with
increasing Ag content. Hence an optimal concentration of ca.
4.4-4.6 mol% Ag nanocrystals was established for maximizing the
PF (Fig. 3c). Overall, around 20 PbS-Ag pellets were produced, all
showing PFs above 1 mW m^{-1} K^{-2} at 850 K, with a champion
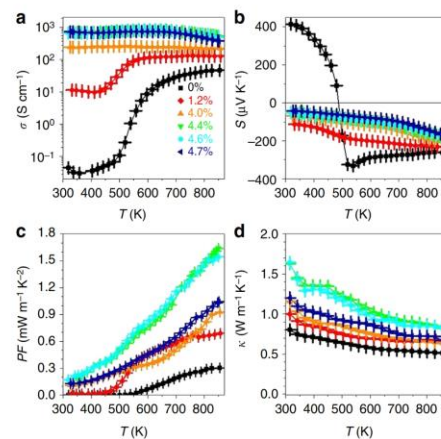
Figure 3 | Thermoelectric characterization of PbS-Ag nanocomposites.
Temperature dependence of the (**a**) electrical conductivity, σ; (**b**) Seebeck
coefficient, S; (**c**) thermal conductivity, κ; and (**d**) power factor, PF. Error
bars were estimated from the repeatability of the experimental result;
3-5 measurements were carried out for each material.

value of 1.68 mW m^{-1} K^{-2} at 850 K for a PbS-Ag 4.4 mol%.
This is a sixfold increase over identically prepared Ag-free
samples, and a significant improvement by 23-47% over
previously reported PbS-based nanocomposites[21,26].

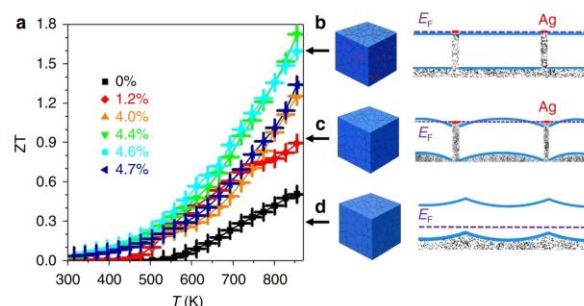**Figure 4 | Figure of merit and schematic representation of the electron energy band alignment.** (**a**) Figure of merit, ZT, of PbS and PbS–Ag pellets; (**b**) band alignment in PbS–Ag nanocomposite with a larger amount of Ag and flat bands across the whole PbS domains; (**c**) band aligment in PbS–Ag nanocomposite with a low Ag volume fraction, showing electron energy wells in between PbS domains; (**d**) band alignment in bare PbS with an upward band-bending at the PbS intergrains. Error bars were estimated from the repeatability of the experimental result; 3–5 measurements were carried out for each material.

The thermal conductivities of the PbS–Ag nanocomposites monotonically increased with the Ag content (Fig. 3d) due to the increase of the electronic contribution (Supplementary Fig. 2 and Methods), yet not exceeding in the high-temperature range the values reported for PbS-based nanocomposites produced by co-precipitation of secondary phases[21,26,27]. Thus, beyond injecting charge carriers and facilitating charge transport between PbS nanocrystals, Ag nanodomains also assisted in blocking phonon propagation. The relatively low thermal conductivities may also in part result from phonon scattering at nanodomains within the large PbS grains as observed by extensive HRTEM analysis (Supplementary Figs 3 and 4 and Note 2).

Overall, the outstanding electrical properties along with low thermal conductivities of PbS–Ag samples resulted in thermoelectric figures of merit of up to ZT = 1.7 at 850 K (Fig. 4a). This value corresponds to a 30% increase over the highest figure of merit obtained for PbS to date (ZT = 1.3, $Pb_{0.975}Na_{0.025}S + 3\%$ CdS)[21] and is comparable to the highest thermoelectric figures of merit reported for other lead chalcogenide materials (Supplementary Table 3)[3,21,26–30].

Discussion

The high PFs displayed by PbS–Ag nanocomposites are at the origin of their outstanding thermoelectric figures of merit. Such high PFs could not be explained by a simple weighed sum of the properties of two randomly distributed compounds (Supplementary Table 4 and Supplementary Discussion). Neither can we explain the high electrical conductivity by percolation transport through Ag domains, as much lower Seebeck coefficients would be expected for a metallic conductor. It must be also pointed out that doping of PbS with Ag^+ ions cannot explain these transport properties either, since previous studies have demonstrated Ag^+ to be a p-type dopant for PbS[31–34]. Simultaneous combination of high electrical conductivity and relatively large Seebeck coefficients can be explained by an efficient injection of electrons from the metal to the conduction band of the semiconductor (Fig. 4b–d). In this regard, RT Hall charge carrier concentration measurements evidenced an increase in concentration of majority charge carriers from $p = 1 \times 10^{16}$ in the bare PbS nanomaterial to $n = 3 \times 10^{19}$ in PbS–Ag 4.4 mol% samples (Fig. 5 and Supplementary Table 5). This is consistent with the initial Ag Fermi level above that of the intrinsic PbS.

What is surprising is that the obtained charge carrier mobilities also increased with the Ag introduction, from $20 \, cm^2 \, V^{-1} \, s^{-1}$ for bare PbS to $90 \, cm^2 \, V^{-1} \, s^{-1}$ for PbS–Ag 4.4 mol% (Supplementary Table 5). In a simple modulation doping scenario, one would expect the injection of charge carriers from Ag nanodomains into PbS to have little negative impact on the charge carrier mobility. However, in PbS–Ag nanocomposites, the actual effect of Ag was found to facilitate charge transport through the material. We attribute this to a reduction of the energy barriers between PbS crystal domains (Fig. 4b–d). To determine the band alignment, we used the Anderson model to align the vacuum levels of Ag and PbS and then solve the Poisson equation self consistently assuming a parabolic two-band model for PbS (Fig. 5a). We used the Ag work function, which depends on its crystallographic surface and domain size, as a fitting parameter to fit the experimentally measured Hall data (Fig. 5b). The obtained fitted parameter was 4.4 eV, which is in the correct range (4.26–4.9 eV) (refs 22,23).

At a bulk metal–semiconductor junction, the Fermi level is pinned by the metallic layer due to the large carrier density in the metallic layer (Fig. 5a). However, for small nanocrystals, the number of electrons is limited and at low metal concentrations it may be not enough to completely pin the Fermi level. To simulate charge transfer from Ag nanocrystals to PbS, we assumed Ag nanocrystals were spheres of radius 1.5 nm (to replicate the 3-nm size of Ag nanodomains observed) embedded within another sphere made out of PbS. The radius of PbS sphere was determined by the volume fraction of each sample (Fig. 5b, inset). Figure 5c shows the Fermi level with respect to the bottom of the conduction band. This is an indicator for the effective well depth for the electrons as marked in Fig. 5a. As can be seen in Fig. 5c, when the Ag fraction increases, the Fermi level also increases, lowering the effective well depth in between PbS grains, which reaches zero at around a 0.5 % Ag volume fraction, that is, 1.5 mol%. At this point and beyond, there is no effective well in the path of the electrons (Fig. 4b). Therefore, as the Ag fraction increases, the electron-nanocrystal scattering decreases, which is consistent with the observed enhancement in electron mobility.

Note that the high PFs found in PbS–Ag nanocomposites cannot be obtained by a conventional doping strategy, where the introduction of ionic impurities would lead to increased scattering of charge carriers. This is shown in Fig. 6a,b, where the thermoelectric properties of PbS nanomaterials with different
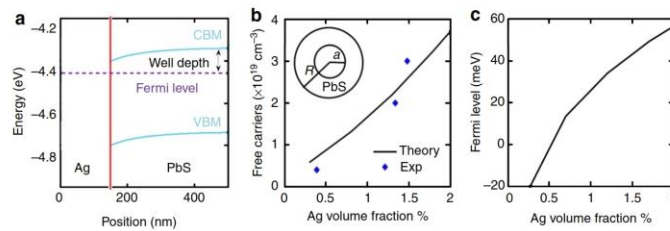
ARTICLE

Figure 5 | Theoretical calculations. (a) Band alignment at the Ag-PbS interface considering bulk Ag and bulk PbS at 300 K. The Fermi level is pinned at $-4.4\,eV$ (silver work function). Electrons in PbS experience a well, as marked, when going to the silver side. **(b)** Carrier concentration versus silver volume fraction. Experimentally measured Hall data are shown by blue dots. Free carrier concentration, calculated using Anderson model and Poisson solver for the geometry shown in the inset of the figure, is shown by solid line. The inner sphere represents a silver NC ($a = 1.5\,nm$) and the outer sphere represent PbS host matrix with radius R (silver volume fraction $= (a/R)^3$. **(c)** Fermi level plotted with respect to the conduction band minimum of PbS (far away from the interface). When negative, this value corresponds to the well depth experienced by electrons when moving between PbS grains.
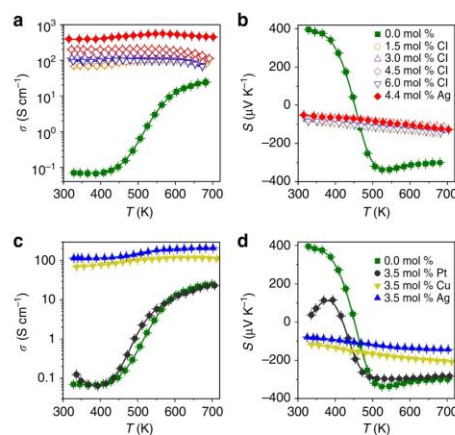

Figure 6 | Electrical properties of PbS nanomaterials with different doping strategies. (a) σ and **(b)** S of x mol% PbS ($x = 1.5$, 3.0, 4.5 and 6.0) doped with Cl (open symbols) compared with pure PbS (0.0 mol %) and PbS–Ag (4.4 mol%). **(c)** σ and **(d)** S of PbS (0.0 mol%) and PbS–X (3.5 mol%) with X = Pt, Cu and Ag.

chlorine concentrations are presented. By introducing Cl^- ions, a common dopant used in n-type PbS, the electron density can be increased, which translates into an enhancement of the electrical conductivity[35]. However, the highest electrical conductivities reached by halide doping remained below the values obtained for PbS–Ag nanocomposites. Thus, despite that PbS:Cl (4.5 mol%) nanomaterials had charge carrier concentrations in the same order of magnitude and similar Seebeck coefficients as the PbS–Ag (4.4 mol%) nanocomposites, the later showed significantly higher electrical conductivities and, therefore, higher PFs.

Besides PbS–Ag nanocomposites, a variety of other compositions were accomplished from colloidal nanocrystal building blocks, often showing similar synergistic effects on charge transport. For instance, we have carefully examined composites of PbS with nanoscopic Cu (Supplementary Fig. 5) and Pt (Supplementary Fig. 6). Like Ag, Cu has a low work function and hence is able to inject charges into the conduction band of PbS.

On the contrary, Pt has a much higher work function and does not exhibit efficient charge transfer (Fig. 6c,d).

Colloidal nanocrystals can be prepared with unmatched control over size, composition, shape, crystal phase and surface chemistry and benefit from facile handling and mixing in stable dispersions[36]. The current availability of a rich palette of such building blocks lends the opportunity to create a plethora of different nanocomposites by simply blending nanocrystals of various materials in the appropriate proportions and, afterward, consolidating them into arbitrarily shaped composites. Thus the facile bottom–up approach used here allows engineering a nearly endless variety of nanocomposites, which will allow a high-throughput screening of materials in the effort to maximize the thermoelectric energy conversion efficiency of durable, silent and scalable thermoelectric devices.

Methods

Nanocomposite preparation. *Chemicals.* Lead(II) oxide (PbO, 99.9%), copper(I) acetate (CuOAc, 97%), silver nitrate (AgNO$_3$, ≥ 99.8%), iron(III) nitrate nonahydrate (Fe(NO$_3$)$_3 \cdot 9$H$_2$O, 99.99%), platinum acetylacetonate (Pt(acac)$_2$, 97%), manganese(0) carbonyl (Mn$_2$(CO)$_{10}$, 98%), elemental sulfur (99.998%), oleic acid (OA, tech. 90%), 1-octadecene (ODE, 90%), oleylamine (OLA, tech. 70%) and benzyl ether (BE, 98%) were purchased from Aldrich. Tri-n-octylamine (TOA, 97%) was purchased from Across. Tetradecylphosphonic acid (TDPA, 97%) was purchased from PlasmaChem. Hexane, toluene, ethanol, anhydrous chloroform and anhydrous methanol were obtained from various sources. All chemicals, except OLA, were used as received without further purification. OLA was distilled to remove impurities.

Synthesis of nanocrystals. All syntheses were carried out using standard air-free techniques; a vacuum/dry argon Schlenk line was used for synthesis and an argonfilled glove box for storing and handling air and moisture-sensitive chemicals.

PbS nanocrystals with a mean edge size of 11 nm were prepared similarly to previously reported procedures[35]. In a typical synthesis, PbO (4.46 g, 20 mmol) and OA (50 ml, 0.158 mol) were mixed with 100 ml of ODE. This mixture was degassed at RT and 100 °C for 0.5 h each to form the lead oleate complex. Then the solution was flushed with Ar, and the temperature was raised to 210 °C. At this temperature, a sulfur precursor, prepared by dissolving elemental sulfur (0.64 g, 20 mmol) in distilled OLA (20 ml, 0.061 mol), was rapidly injected. The reaction mixture was maintained between 195 °C and 210 °C for 5 min and then quickly cooled down to RT using a water bath. Ag nanocrystals with an average diameter of 2–3 nm were produced using a modified approach of that reported by Wang *et al.*[37] In a typical reaction, AgNO$_3$ (0.17 g, 1 mmol), Fe(NO$_3$)$_3 \cdot 9$H$_2$O (0.04 g, 0.01 mmol), OA (10 ml, 0.0316 mol) and OLA (10 ml, 0.0305 mol) were mixed and placed under Ar at RT for 30 min. Afterwards the reaction mixture was heated to 120 °C at the rate of 5 °C min^{-1} and kept at this temperature for an additional 60 min. Cu nanocrystals with an average diameter of 5–6 nm were prepared following the approach developed by Yang *et al.*[38] In a typical synthesis, TOA (50 ml, 0.114 mol) was heated in a 100 ml three-neck flask to 130 °C for 30 min under Ar atmosphere. After cooling to RT, CuOAc (613 mg, 5 mmol) and TDPA (696 mg, 2.5 mmol) were added to the flask. The mixture was heated to 180 °C and maintained at this temperature for 30 min. Then, the reaction temperature was further increased to 270 °C and held for another 30 min. Cu nanocrystals are highly air sensitive and easily oxidized. To avoid any possible oxidation, the nanocrystals were purified in

an Ar filled glove box. Pt nanocrystals with an average diameter of 6 nm were prepared using the method developed by Murray et al.[39] In a typical synthesis, Pt(acac)$_2$ (80 mg, 0.20 mmol) was dissolved in BE (10 ml, 52.6 mmol), OLA (7.36 ml, 22.37 mmol) and OA (1.25 ml, 3.94 mmol) under Ar atmosphere for 30 min at 60 °C. The precursor mixture was heated to 160 °C and a solution of 80 mg Mn$_2$(CO)$_{10}$ in 1 ml of chloroform was rapidly injected. Afterwards, the temperature was heated to 200 °C and held for an additional 30 min at this reaction temperature. Finally, the crude solution was cooled to RT.

Blending of nanocrystals. In this work we prepared PbS-metal semiconductor nanocomposites with different metal concentrations. The blending of nanocrystals was performed by wetting 1 g of dried PbS nanocrystals (a powder) with different amounts of a 0.093 M solution of metallic nanocrystals in anhydrous chloroform. Subsequently, the solvent was allowed to evaporate under Ar atmosphere. The concentration of metallic nanocrystals in chloroform was initially estimated by mass (considering a 30% of organic ligand) and later verified by inductively coupled plasma (ICP) spectroscopy. The values were found to differ slightly between the estimation from the weight and from ICP. The final quantities reported in this work correspond to the values obtained from ICP measurements.

Pellet fabrication. Before powder consolidation in a hot press, the nanocrystal powders were treated thermally to decompose the remaining organic ligands present at the nanocrystal surface. All nanocrystal powders were heated to 450 °C at 10 °C min^{-1} and held at this temperature for 1 h under an Ar flow. After cooling to RT, the nanocrystal powders were pressed using a custom-made hot press. In this system, heat is provided by an induction coil operated in the RF range and applied directly to a graphite die acting as a susceptor. Before hot pressing, coarse powders were ground into fine powder using a mortar inside the glove box and then loaded into a 10-mm diameter graphite die lined with 0.13-mm thick graphite paper. The filled die was placed in the hot press system. The densification profile applied an axial pressure of 45 MPa before heating the die to between 420 and 440 °C. The temperature was held between 420 and 440 °C for 4 min. The pressure was then removed and the die cooled to RT. The resulting pellets were >85% dense with theoretical maximum into air-stable monoliths measuring ~1-mm thick by 10 mm in diameter. The density of the pressed pellets was measured by the Archimedes method.

Structural characterization. The size and shape of the initial nanocrystals were examined by TEM using a ZEISS LIBRA 120 instrument, operating at 120 kV. Structural and compositional characterizations of the nanocomposites were examined after thermoelectrical characterization. TEM Samples were mechanically thinned to 20–30 μm and further thinned to electron transparency by Ar$^+$ polishing using a Gatan Precision Ion Polishing System. HRTEM and scanning transmission electron microscopy studies were conducted by using a FEI Tecnai F20 field emission gun microscope operated at 200 kV, which is equipped high-angle annular dark field and energy-dispersive X-ray spectroscopy detectors. ICP atomic emission spectrometry was used for elemental analysis of the nanocomposites, especially to determine the ratio between Pb and Ag, Pt or Cu. ICP atomic emission spectrometry measurements were carried out using Perkin-Elmer Optima instrument, model 3200RL, under standard operating conditions. Samples were prepared by microwave-assisted digestion of the dried materials in a mixture of HNO$_3$ and H$_2$O$_2$ in a closed container. X-ray powder diffraction analyses were collected directly on the as-synthesized nanocrystals and final pellets using a Bruker AXS D8 Advance X-ray diffractometer with Ni-filtered (2 μm thickness) Cu K$_\alpha$ radiation ($\lambda = 1.5406$ Å) operating at 40 kV and 40 mA (Supplementary Fig. 7). A LynxEye linear position-sensitive detector was used in reflection geometry. XAS measurements were carried out at the X10DA (SuperXAS) beamline at the Swiss Light Source, Villigen, Switzerland, which operated with a ring current of ~400 mA in top-up mode. The polychromatic radiation from the superbend magnet, with a magnetic field of 2.9 T and critical energy of 11.9 keV, was monochromatized using a channel cut Si(311) crystal monochromator. Spectra were collected on pressed pellets optimized to 1 absorption length at the Ag K edge (25515 eV) and Pb L$_3$ edge (13035 eV) in transmission mode. XAS data were treated with the Demeter software suite[40]. For all samples, three spectra were acquired and merged. These averaged XAS data were background-subtracted and normalized. Linear combination fitting of the Ag K edge X-ray absorption near edge structure spectra was performed over the energy range from 25,498 to 25,598 eV. The goal was to determine composition of Ag-species present in the PbS–Ag sample. For this, reference spectra of metallic Ag NPs and Ag$_2$S were combined linearly. Fourier transformation of the Pb L$_3$ edge extended X-ray absorption fine structure spectra was performed over the k range of 3 – 9 Å^{-1} yielding a pseudo radial structure function. The R-range from 1 to 4.8 Å was fitted using theoretical single scattering paths of bulk PbS (S6)[25] based on crystallographic data.

Thermoelectric characterization. *Electric properties.* The pressed samples were polished, maintaining the disk-shape morphology. Final pellets had a 10-mm diameter and were ~1 mm thick. The Seebeck coefficient was measured using a static DC method. Electrical resistivity data were obtained by a standard four-probe method. Both the Seebeck coefficient and the electrical resistivity were simultaneously measured with accuracies better than 1% in a LSR-3 LINSEIS system from RT to 850 K, under helium atmosphere. Samples were held between two alumel

electrodes and two probe thermocouples with spring-loaded pressure contacts. A resistive heater on the lower electrode created temperature differentials in the sample to determine the Seebeck coefficient. Samples measured up to 850 K were spray coated with boron nitride to minimize out-degassing except where needed for electrical contact with the thermocouples, heater and voltage probes. In addition, before high-temperature measurements, samples were heated within the LINSEIS system in a He atmosphere up to 850 K at 3 K min^{-1} and hold at this temperature for 10 min with the boron nitride coating. Such preliminary treatment warrants sample stability for all the cycles tested (Supplementary Figs 8 and 9 and Discussion). Carrier concentration and mobility were estimated from Hall Effect measurements, which were performed at RT using an Ecopia HMS-3000 set-up with golden spring-loaded contacts positioned at the edges of plates in the Van der Pauw configuration.

Thermal properties. An XFA 600 Xenon Flash Apparatus was used to determine the thermal diffusivities of all samples with an accuracy of ca. 6%. Total thermal conductivity (κ) was calculated using the relation κ = $DC_p\rho$, where D is the thermal diffusivity, C_p is the heat capacity and ρ is the mass density of the pellet. The ρ values were calculated using the Archimedes method. The specific heat (C_p) of the samples was measured using a Differential Scanning Calorimeter DSC 204 F1 Phoenix from NETZSCH (Supplementary Fig. 10). The electronic contribution of the thermal conductivity was calculated using the Wiedemann–Franz law (Supplementary Fig. 11 and Methods).

References

1. Bell, L. E. Cooling, heating, generating power, and recovering waste heat with thermoelectric systems. *Science* **321,** 1457–1461 (2008).
2. Vineis, C. J., Shakouri, A., Majumdar, A. & Kanatzidis, M. G. Nanostructured thermoelectrics: big efficiency gains from small features. *Adv. Mater.* **22,** 3970–3980 (2010).
3. Biswas, K. *et al.* High-performance bulk thermoelectrics with all-scale hierarchical architectures. *Nature* **489,** 414–418 (2012).
4. Ibáñez, M. *et al.* Core-shell nanoparticles as building blocks for the bottom-up production of functional nanocomposites: PbTe-PbS thermoelectric properties. *ACS Nano* **7,** 2573–2586 (2013).
5. Hsu, K. F. *et al.* Cubic AgPb$_m$SbTe$_{2 + m}$: bulk thermoelectric materials with high figure of merit. *Science* **303,** 818–821 (2004).
6. Kim, S. I. *et al.* Dense dislocation arrays embedded in grain boundaries for high-performance bulk thermoelectrics. *Science* **348,** 109–114 (2015).
7. Ibáñez, M. *et al.* Crystallographic control at the nanoscale to enhance functionality: polytypic Cu$_2$GeSe$_3$ nanoparticles as thermoelectric materials. *Chem. Mater.* **24,** 4615–4622 (2012).
8. Bahk, J.-H., Bian, Z. & Shakouri, A. Electron energy filtering by a nonplanar potential to enhance the thermoelectric power factor in bulk materials. *Phys. Rev. B* **87,** 075204 (2013).
9. Ohta, H. *et al.* Giant thermoelectric Seebeck coefficient of a two-dimensional electron gas in SrTiO3. *Nat. Mater.* **6,** 129–134 (2007).
10. Heremans, J. P. *et al.* Enhancement of thermoelectric efficiency in PbTe by distortion of the electronic density of states. *Science* **321,** 554–557 (2008).
11. Harman, T. C., Taylor, P. J., Walsh, M. P. & LaForge, B. E. Quantum dot superlattice thermoelectric materials and devices. *Science* **297,** 2229–2232 (2002).
12. García de Arquer, F. P., Lasanta, T., Bernechea, M. & Konstantatos, G. Tailoring the electronic properties of colloidal quantum dots in metal–semiconductor nanocomposites for high performance photodetectors. *Small* **11,** 2636–2641 (2015).
13. Zebarjadi, M., Esfarjani, K., Dresselhaus, M. S., Ren, Z. F. & Chen, G. Perspectives on thermoelectrics: from fundamentals to device applications. *Energ. Environ. Sci.* **5,** 5147–5162 (2012).
14. Dingle, R., Störmer, H. L., Gossard, A. C. & Wiegmann, W. Electron mobilities in modulation-doped semiconductor heterojunction superlattices. *Appl. Phys. Lett.* **33,** 665–667 (1978).
15. Hicks, L. D. & Dresselhaus, M. S. Thermoelectric figure of merit of a one-dimensional conductor. *Phys. Rev. B* **47,** 16631–16634 (1993).
16. Moon, J., Kim, J.-H., Chen, Z. C. Y., Xiang, J. & Chen, R. Gate-modulated thermoelectric power factor of hole gas in Ge–Si core–shell nanowires. *Nano Lett.* **13,** 1196–1202 (2013).
17. Zebarjadi, M. *et al.* Power factor enhancement by modulation doping in bulk nanocomposites. *Nano Lett.* **11,** 2225–2230 (2011).
18. Yu, B. *et al.* Enhancement of thermoelectric properties by modulation-doping in silicon germanium alloy nanocomposites. *Nano Lett.* **12,** 2077–2082 (2012).
19. Pei, Y.-L., Wu, H., Wu, D., Zheng, F. & He, J. High thermoelectric performance realized in a BiCuSeO system by improving carrier mobility through 3D modulation doping. *J. Am. Chem. Soc.* **136,** 13902–13908 (2014).
20. Wu, D. *et al.* Significantly enhanced thermoelectric performance in n-type heterogeneous BiAgSeS composites. *Adv. Funct. Mater.* **24,** 7763–7771 (2014).
21. Zhao, L.-D. *et al.* Raising the thermoelectric performance of p-type PbS with endotaxial nanostructuring and valence-band offset engineering using CdS and ZnS. *J. Am. Chem. Soc.* **134,** 16327–16336 (2012).
22. Chelvayohan, M. & Mee, C. H. B. Work function measurements on (110), (100) and (111) surfaces of silver. *J. Phys. C* **15,** 2305 (1982).

ARTICLE

23. Dweydari, A. W. & Mee, C. H. B. Work function measurements on (100) and (110) surfaces of silver. *Phys. Status Solidi A* **27**, 223–230 (1975).

24. Knapp, R. A. Photoelectric Properties of Lead Sulfide in the Near and Vacuum Ultraviolet. *Phys. Rev.* **132**, 1891–1897 (1963).

25. Noda, Y., Ohba, S., Sato, S. & Saito, Y. Charge distribution and atomic thermal vibration in lead chalcogenide crystals. *Acta Crystallogr. Sect. B* **39**, 312–317 (1983).

26. Zhao, L.-D. *et al.* High performance thermoelectrics from earth-abundant materials: enhanced figure of merit in PbS by second phase nanostructures. *J. Am. Chem. Soc.* **133**, 20476–20487 (2011).

27. Zhao, L.-D. *et al.* Thermoelectrics with earth abundant elements: high performance p-type PbS nanostructured with SrS and CaS. *J. Am. Chem. Soc.* **134**, 7902–7912 (2012).

28. Wu, H. J. *et al.* Broad temperature plateau for thermoelectric figure of merit $ZT > 2$ in phase-separated $PbTe_{0.7}S_{0.3}$. *Nat. Commun.* **5**, 4515 (2014).

29. Korkosz, R. J. *et al.* High ZT in p-Type (PbTe)1–2x(PbSe)x(PbS)x thermoelectric materials. *J. Am. Chem. Soc.* **136**, 3225–3237 (2014).

30. Girard, S. N. *et al.* High performance Na-doped PbTe–PbS thermoelectric materials: electronic density of states modification and shape-controlled nanostructures. *J. Am. Chem. Soc.* **133**, 16588–16597 (2011).

31. Yun, Z. *et al.* Thermoelectric transport properties of p-type silver-doped PbS with in situ Ag 2 S nanoprecipitates. *J. Phys. D Appl. Phys* **47**, 115303 (2014).

32. Shanyu, W. *et al.* Exploring the doping effects of Ag in p-type PbSe compounds with enhanced thermoelectric performance. *J. of Phys. D Appl. Phys* **44**, 475304 (2011).

33. Dow, H. S. *et al.* Effect of Ag or Sb addition on the thermoelectric properties of PbTe. *J. Appl. Phys.* **108**, 113709 (2010).

34. Ryu, B. *et al.* Defects responsible for abnormal n-type conductivity in Ag-excess doped PbTe thermoelectrics. *J. Appl. Phys.* **118**, 015705 (2015).

35. Ibáñez, M. *et al.* Electron doping in bottom-up engineered thermoelectric nanomaterials through HCl-mediated ligand displacement. *J. Am. Chem. Soc.* **137**, 4046–4049 (2015).

36. Kovalenko, M. V. *et al.* Prospects of nanoscience with nanocrystals. *ACS Nano* **9**, 1012–1057 (2015).

37. Li, L., Hu, F., Xu, D., Shen, S. & Wang, Q. Metal ion redox potential plays an important role in high-yield synthesis of monodisperse silver nanoparticles. *Chem. Commun.* **48**, 4728–4730 (2012).

38. Hung, L.-I., Tsung, C.-K., Huang, W. & Yang, P. Room-temperature formation of hollow Cu2O nanoparticles. *Adv. Mater.* **22**, 1910–1914 (2010).

39. Kang, Y. *et al.* Shape-controlled synthesis of Pt nanocrystals: the role of metal carbonyls. *ACS Nano* **7**, 645–653 (2012).

40. Ravel, B. & Newville, M. ATHENA, ARTEMIS, HEPHAESTUS: data analysis for X-ray absorption spectroscopy using IFEFFIT. *J. Synchrotron Radiat.* **12**, 537–541 (2005).

Author contributions

The manuscript was prepared through the contribution of all authors. M.I., Z.L., S.O., O.D. and D.C. produced the nanocomposite and performed the thermoelectric characterization. A.G., J.A., L.P. and M.N. performed structural nanocomposite characterization. M.Z. performed band alignment calculations. M.I., M.K. and A.C. planned and supervised the work and had major input in the writing of the manuscript.

Additional information

Supplementary Figure 1. Linear combination fit of 4.4% Ag-PbS with the weighted components and the residual error.
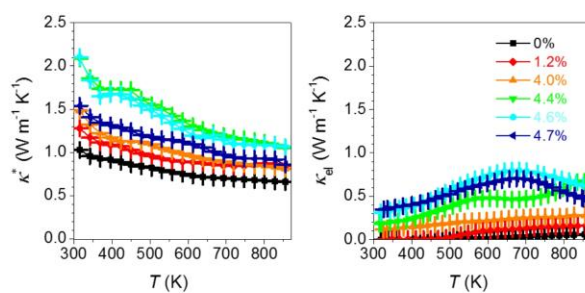
Supplementary Figure 2. Temperature dependence of the porosity corrected thermal conductivity (κ^*) and the electronic contribution (κ_e) for x mol% PbS-Ag with x=0 (black squares), 1.2 (red diamonds), 4.0 (orange triangles up), 4.4 (green triangles down), 4.6 (cyan cercles) and 4.7 (blue triangles left) up to 850 K.
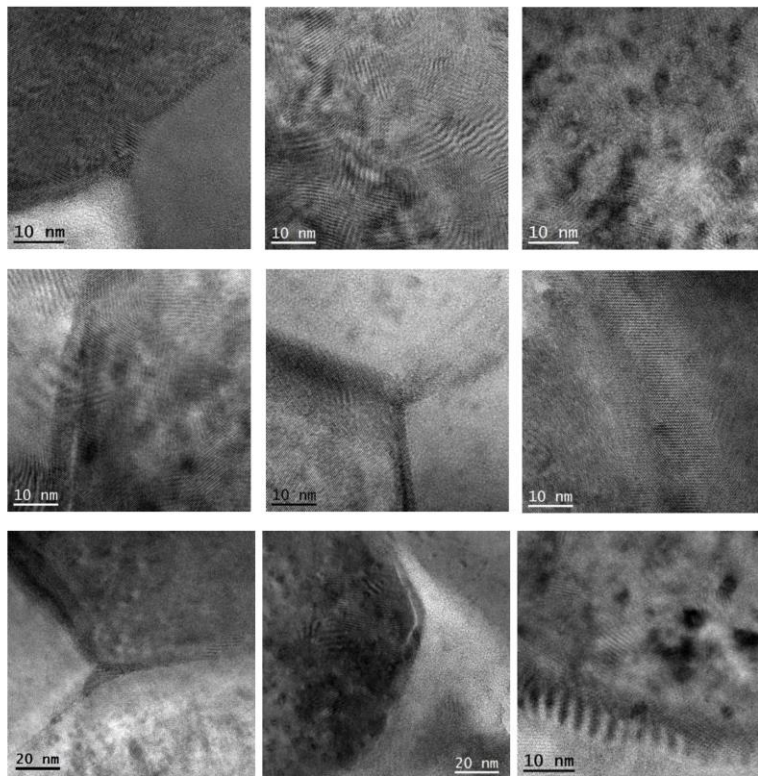
Supplementary Figure 3. Selection of HRTEM images showing regions with different crystallographic phases along the grain boundaries and inclusions inside the grains.

2
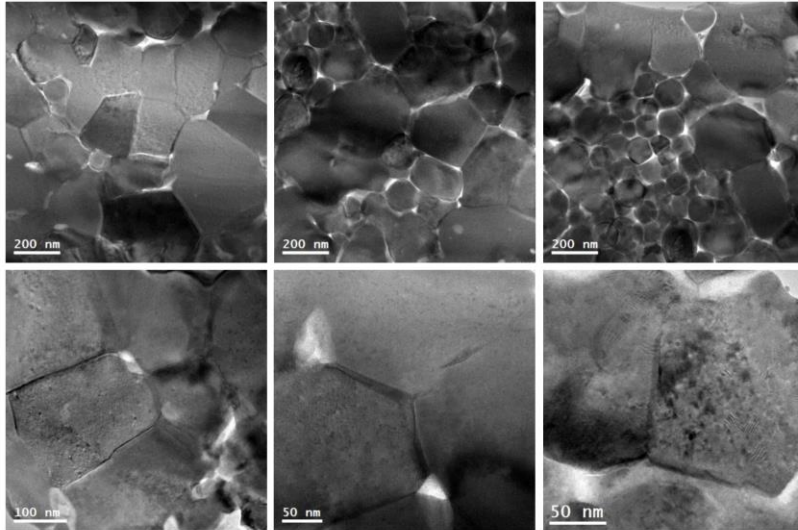
Supplementary Figure 4. Selection of TEM images showing the microstructure of the PbS bulk sample in different directions.
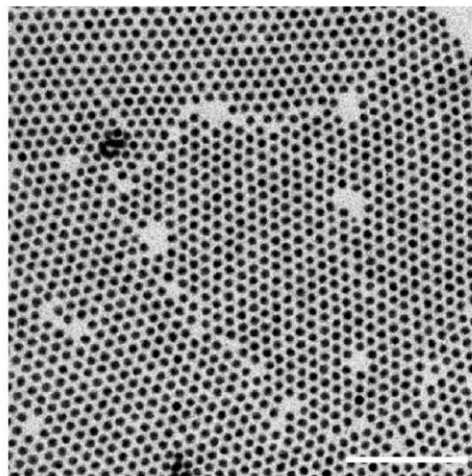
Supplementary Figure 5. TEM image of Cu nanocrystals. Scale bar is 100 nm.

3
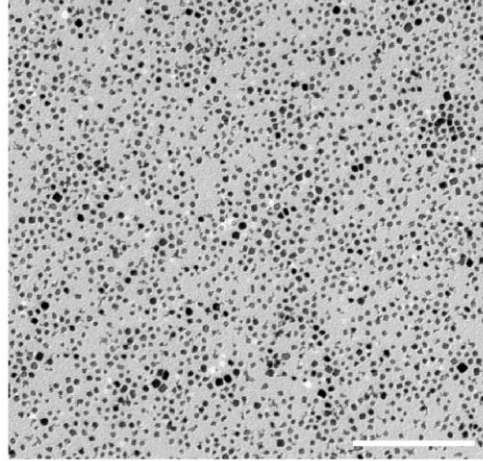
Supplementary Figure 6. TEM image of Pt nanocrystals. Scale bar is 100 nm.
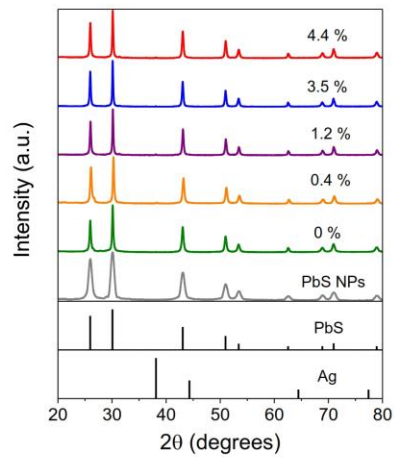
Supplementary Figure 7. XRD patterns of PbS NCs (grey) and x mol% PbS-Ag nanocomposites with x=0 (green), 0.4 (orange), 1.2 (purple), 3.5 (blue), 4.4 (red). The reference patterns for PbS (galena) and Ag are shown as black lines.

4
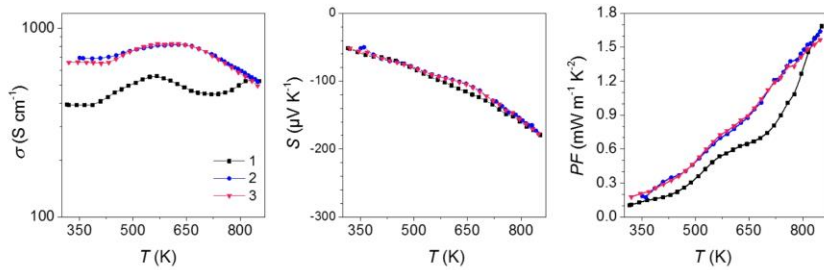
Supplementary Figure 8. Temperature dependence of the electrical conductivity, Seebeck coefficient and power factor of a 4.4 mol% PbS-Ag nanocomposite measured 3 consecutive times during heating up to 850 K. No pre-stabilization treatment was carried out before the first measurement.
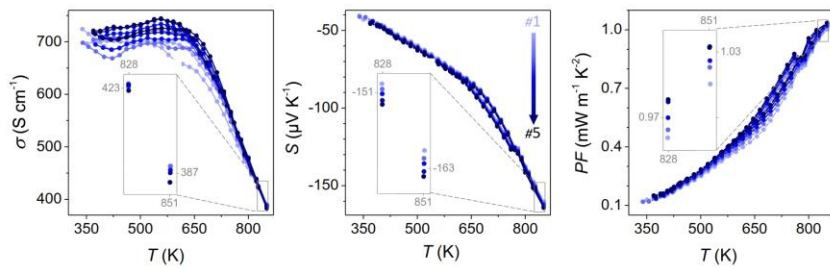
Supplementary Figure 9. Temperature dependence of the electrical conductivity, Seebeck coefficient and power factor of a 4.7 mol% PbS-Ag nanocomposite measured for 5 consecutive temperature cycles up to 850 K.
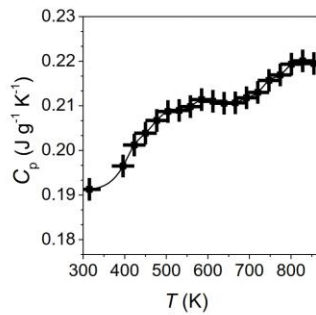
Supplementary Figure 10. C_p of the PbS nanomaterial measured using DSC

5
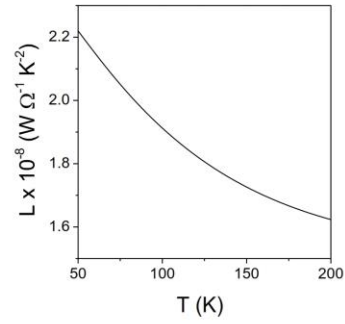
Supplementary Figure 11. The Lorentz number estimation based on the Seebeck coefficient measurements and assuming scattering from acoustic phonons, following Fermi-Dirac statistics.

6

Supplementary Table 1. Linear combination fit results for 4.4% Ag-PbS. Summary of the results of the linear combination fit for 4.4 mol% Ag-PbS nanocomposite. The remaining deviation can be explained by the oxidation of silver during sample preparation in air for the XAS measurements. R-factor: 0.0018; Reduced chi-square: 0.00025.

Reference spectrum	Weight	E_0 shift (eV)
Ag NPs	0.100	0.772
Ag_2S	0.027	25.068

Supplementary Table 2: Best fit parameters for 4.4% Ag-PbS. CNs were set to the bulk values when performing the fit. The first shell consisting of S atoms was fitted first using a range from 1 to 3.1 Å assuming the coordination number (*CN*) to be the same as in the bulk [24]. The fitted parameters for the first shell (amplitude reduction factor, S_0^2, energy shift, ΔE_0, bond distance difference, ΔR, and Debye-Waller factor, σ^2) were maintained constant when fitting the second shell while extending the range to 4.8 Å. The *CN* of the second shell was set to 12 and ΔE_0 was assumed to be the same for both shells. Reduced chi-square: 476; R-factor: 0.0214 (The reduced chi-square and the *R* factor are defined according to the FEFFIT conventions (ref: http://cars9.uchicago.edu/ifeffit/Documentation).

Scattering Path	CN	$S0^2$	ΔE_0 [eV]	R [Å]	σ^2 [Å²]
Pb-S	6.0	0.63 ± 0.09	2.8 ± 1.1	2.95 ± 0.02	0.021 ± 0.003
Pb-Pb	12.0	0.62 ± 0.12	2.8 ± 1.1	4.20 ± 0.01	0.020 ± 0.004

7

Supplementary Table 3. Table with the thermoelectric properties and corresponding figures of merit of state of the art lead chalcogenides.

System	σ (S cm^{-1})	S (μV K^{-1})	PF (μW cm^{-1}K^{-2})	κ (W m^{-1}K^{-1})	ZT_{max}	T_{ZTmax} (K)	Ref.
$Pb_{0.975}Na_{0.025}S$ + 3.0% CdS	142	280	11.1	0.79	1.3	923 K	[12]
$PbS + 1\% Bi_2S_3$ + 1% $PbCl_2$	275	-220	13.31	1.1	1.1	923 K	[13]
PbS + 3% SrS + 2.5% Na	109	290	9.1	0.70	1.2	923 K	[14]
PbS-Ag 4.4%	**530**	**-177**	**1.66**	**0.82**	**1.7**	**854 K**	**This work**
PbTe-PbS12% + 2% Na	390	252	24	1.1	1.8	800 K	[15]
$PbTe_{0.7}S_{0.3}$ + 2.5% K	170	294	14.7	0.65	2.0	923 K	[16]
PbTe + 4% SrTe + 2% Na	285	290	23.9	1.0	2.2	923 K	[17]
$PbTe_{0.86}PbSe_{0.07}PbS_{0.07}$ + 2% Na	375	270	27.4	1.1	2.0	825 K	[18]
$(PbSe)_{0.88}(PbS)_{0.12}$ + 0.3% $PbCl_2$	220	260	14	1.1	1.2	900 K	[19]
$PbTe_{0.1}Se_{0.4}S_{0.5}$-Cl	280	-180	9.1	0.68	0.94	700 K	[20]

8

Supplementary Table 4. Electrical conductivity and Seebeck coefficient of PbS-Ag (4.5 mol%) nanocomposite taking into account a weighted sum of properties of the two components.

γ_{PbS}	0.955
γ_{Ag}	0.045
σ_{PbS} (S cm^{-1})	0.1
σ_{Ag} (S cm^{-1})	6.3 x 10^5
S_{PbS} (μV K^{-1})	200
S_{Ag} (μV K^{-1})	6.5
k_{PbS} (W m^{-1} K^{-1})	1
k_{Ag} (W m^{-1} K^{-1})	429
σ_{PbS-Ag} (S cm^{-1})	0.1
S_{PbS-Ag} (μV K^{-1})	200

Supplementary Table 5. Hall charge carrier concentration and mobility measured at ambient temperature.

Ag content (mol %)	Carrier concentration (cm^{-3})	Carrier Mobility (cm^2 V^{-1} s^{-1})
0	$p = 1 \times 10^{16}$	20
1.2	$n = 4 \times 10^{18}$	20
4.0	$n = 2 \times 10^{19}$	75
4.4	$n = 3 \times 10^{19}$	90

9

Supplementary Note 1

Extensive TEM and HRTEM analysis of the nanocomposites was performed. Two main conclusions can be outlined from this analysis:

- Nanocomposites exhibit a highly homogeneous and isotropic microstructure. All regions analyzed showed the same characteristics in all orientations.
- Three distinct crystal phases were observed: 1) relatively large PbS crystal domains; 2) a high density of small nanodomains within the PbS grains and which phase could not be unequivocally identified; 3) elongated nanodomains in between PbS grains identified as *fcc* Ag. The different phases were observed to be homogeneously distributed throughout the nanocomposite.

Supplementary Note 2. Note on figure 2f HRTEM image. When the power spectrum (FFT) for the HRTEM images was obtained, contributions from the Moiré fringes and/or other inclusions that may be present in the sample were included. Therefore the identification of the various phases by inspecting the overall power spectrum was extremely difficult. Since almost all of the observed grains contained many Moiré fringes and some other inclusions, we applied an alternative approach to identify the crystallographic phases. In the image presented in the main text, we filtered the "known" diffraction spots of both *fcc* PbS and *fcc* Ag from the fast Fourier transform (FFT) obtained from the TEM micrograph showing a grain with a ~ 3-4 nm shell-like feature (main text, Fig. 2F). When the "known" diffraction spots of both the *fcc* PbS and *fcc* Ag phases were filtered, it was revealed that the grain consisted of the *fcc* PbS phase covered by a ~3-4 nm Ag shell. These findings are perfectly consistent with the EDX maps obtained from the same sample and the results of the linear combination fits of the XAS data.

10

Supplementary Discussion

Weighted sum of the properties of two randomly distributed compounds. The electrical conductivity and Seebeck coefficient of a nanocomposite with a random distribution of phases A and B is given by the following equations[6,7]:

$$\text{(Eq. 1)} \qquad \frac{1}{\sigma_{AB}} = \frac{\gamma_A}{\sigma_A} + \frac{\gamma_B}{\sigma_B}$$

$$\text{(Eq. 2)} \qquad S_{AB} = \frac{\frac{S_A \gamma_A}{k_A} + \frac{S_B \gamma_B}{k_B}}{\frac{\gamma_A}{k_A} + \frac{\gamma_B}{k_B}}$$

In eq. 1 and 2, e is the electron charge, γ_A and γ_B are the volume fractions of compounds A and B, respectively.

In the case of PbS-Ag 4.5 mol%, considering a simple weighted sum of the properties, we should obtain nanocomposites with much higher Seebeck coefficients and much lower electrical conductivities as shown in supplementary table 4.

Stability considerations. To ensure thermal stability of the nanocomposites when measured at high temperatures, samples were heated within the LINSEIS system in a He atmosphere up to 850 K at 3 K/min and hold at this temperature for 10 minutes with the boron nitride coating. Such preliminary treatment warranty sample stability for all the cycles tested.

Figure S13 shows the measurements obtained during 3 cycles, including measurements during the stabilization cycle. Notice how measurements obtained during the first temperature ramp are significantly different from the ones obtained in posterior cycles, especially at low temperatures. However, after the first cycle measurements are very repetitive.

To further demonstrate the stability of the material after the first ramp, figure S14 displays the thermoelectric properties of a nanocomposite measured for 5 consecutive up-down cycles between room temperature and up to 850K (after the initial heating up stabilization ramp).

In the low temperature range of the measurement, we observed a slight increase in electrical conductivity with the cycle number and no appreciable variation of the Seebeck coefficient. In the high temperature range of the measurement, a minor decrease of the electrical conductivity with the cycle number (*ca.* -2% after 5 cycles) and an increase of the absolute Seebeck coefficient values (*ca.* +3% after 5 cycles) were obtained. These variations translated in an overall slight increase of the power factor (*ca.* +3% after 5 cycles). Overall we conclude the nanocomposite to have a relatively good stability.

11

Supplementary methods

Electronic contribution to the thermal conductivity. The electronic contribution to the thermal conductivity (k_{el}) was calculated using the Wiedemann-Franz relation, $k_{el}=LT\sigma$, where L is the Lorentz number, T is the temperature, and σ is the electrical conductivity. Usually the Lorentz number is between two limiting values. For metals and highly degenerate electron gases it is $2.45\cdot10^{-8}$ Ω W K^{-2}, while the non-degenerate limit is $1.49\cdot10^{-8}$ Ω W K^{-2}. A better temperature dependence estimation can be done. The Lorentz number can be estimated based on the Seebeck coefficient measurements and assuming scattering from acoustic phonons, following Fermi-Dirac statistics:

$$S = \pm\frac{k_B}{e}\left[\frac{2F_1(\eta)}{F_0(\eta)} - \eta\right]$$

$$L = \left(\frac{k_B}{e}\right)^2\left[\frac{3F_0(\eta)F_2(\eta) - 4F_1^2(\eta)}{F_0^2(\eta)}\right]$$

$$F_i(\eta) = \int_0^\infty \frac{x^i}{1+\exp(x-\eta)}dx$$

$$\eta = \frac{E_F}{k_B T}$$

Here, $F_i(\eta)$ are the Fermi-Dirac integrals and k_B is the Boltzmann constant. The values obtained for the Lorentz number are plotted in Supplementary Fig. 8. However, the value used for the calculation of k_{el} and k_{latt} was the non-degenerate limit, due to the special distribution of charge carriers in our nanocomposite.

Porosity correction. In order to study the different contributions to the thermal conductivity, it is necessary to correct thermal and electronic conductivity values for the effects due to porosity of the pellets. An estimation of the electrical and thermal conductivity that would be measured from a 100% dense sample can be obtained using a Maxwell-Eucken expression[1-3]:

$$X_{100} = X_P\frac{1+\beta P}{1-P}$$

Here, X_{100} is the electrical or thermal conductivity in the 100% density medium, P is the porosity degree in the range between 0 and 1, and β is an empirical parameter related to the pore geometry, which we fixed to 2[3]. Notice that the thermoelectric figure of merit ZT is not modified by this correction because the porosity effects on the electrical and thermal conductivities compensate for each other.

12

The Maxwell-Eucken model is one of the most widely used methods to estimate the reduction in conductivity due to porosity. This model is based on randomly distributed spherical pores. The model considers a low concentration of isolated spherical pores. Additionally, the thermal conductivity through the porous medium is considered negligible when compared to that of the solid material. The factor β allows for correction due to pores with a different geometry. If the pores resemble a sphere, the β value is between 1 and 3. Due to the random distribution of pores in our nanomaterials, we estimated a β value of $2^{4,5}$.

13

Supplementary References

1   Ibáñez, M. *et al.* Core–Shell Nanoparticles As Building Blocks for the Bottom-Up Production of Functional Nanocomposites: PbTe–PbS Thermoelectric Properties. *ACS Nano* **7**, 2573-2586, (2013).

2   Yang, L., Wu, J. S. & Zhang, L. T. Synthesis of Filled Skutterudite Compound $La_{0.75}Fe_3CoSb_{12}$ by Spark Plasma Sintering and Effect of Porosity on Thermoelectric Properties. *J. Alloys Compd.* **364**, 83-88, (2004).

3   Adachi, J., Kurosaki, K., Uno, M. & Yamanaka, S. Effect of Porosity on Thermal and Electrical Properties of Polycrystalline Bulk ZrN Prepared by Spark Plasma Sintering. *J. Alloys Compd.* **432**, 7-10, (2007).

4   Carson, J. K., Lovatt, S. J., Tanner, D. J. & Cleland, A. C. Thermal Conductivity Bounds for Isotropic, Porous Materials. *Int. J. Heat Mass Transfer* **48**, 2150-2158, (2005).

5   Ondracek, G. & Schulz, B. The porosity dependence of the thermal conductivity for nuclear fuels. *J. Nucl. Mater.* **46**, 253-258, (1973).

6   Yu, B. *et al.* Enhancement of Thermoelectric Properties by Modulation-Doping in Silicon Germanium Alloy Nanocomposites. *Nano Lett.* **12**, 2077-2082, (2012).

7   Zebarjadi, M. *et al.* Power Factor Enhancement by Modulation Doping in Bulk Nanocomposites. *Nano Lett.* **11**, 2225-2230, (2011).

8   Razeghi, M. *Fundamentals of Solid State Engineering*. (Springer US, 2009).

9   Knapp, R. A. Photoelectric Properties of Lead Sulfide in the Near and Vacuum Ultraviolet. *Phys. Rev.* **132**, 1891-1897, (1963).

10   Chelvayohan, M. & Mee, C. H. B. Work function measurements on (110), (100) and (111) surfaces of silver. *J. Phys. C: Solid State Phys.* **15**, 2305, (1982).

11   Dweydari, A. W. & Mee, C. H. B. Work function measurements on (100) and (110) surfaces of silver. *Phys. Status Solidi A* **27**, 223-230, (1975).

12   Zhao, L.-D. *et al.* Raising the Thermoelectric Performance of p-Type PbS with Endotaxial Nanostructuring and Valence-Band Offset Engineering Using CdS and ZnS. *J. Am. Chem. Soc.* **134**, 16327-16336, (2012).

13   Zhao, L.-D. *et al.* High Performance Thermoelectrics from Earth-Abundant Materials: Enhanced Figure of Merit in PbS by Second Phase Nanostructures. *J. Am. Chem. Soc.* **133**, 20476-20487, (2011).

14   Zhao, L.-D. *et al.* Thermoelectrics with Earth Abundant Elements: High Performance p-type PbS Nanostructured with SrS and CaS. *J. Am. Chem. Soc.* **134**, 7902-7912, (2012).

15   Girard, S. N. *et al.* High Performance Na-doped PbTe–PbS Thermoelectric Materials: Electronic Density of States Modification and Shape-Controlled Nanostructures. *J. Am. Chem. Soc.* **133**, 16588-16597, (2011).

16   Wu, H. J. *et al.* Broad temperature plateau for thermoelectric figure of merit ZT>2 in phase-separated $PbTe_{0.7}S_{0.3}$. *Nat. Commun.* **5**, 4515, (2014).

17   Biswas, K. *et al.* High-performance bulk thermoelectrics with all-scale hierarchical architectures. *Nature* **489**, 414-418, (2012).

18   Korkosz, R. J. *et al.* High ZT in p-Type $(PbTe)_{1-2x}(PbSe)_x(PbS)_x$ Thermoelectric Materials. *J. Am. Chem. Soc.* **136**, 3225-3237, (2014).

19   Androulakis, J. *et al.* Thermoelectrics from Abundant Chemical Elements: High-Performance Nanostructured PbSe–PbS. *J. Am. Chem. Soc.* **133**, 10920-10927, (2011).

20   Ibáñez, M. *et al.* Electron Doping in Bottom-Up Engineered Thermoelectric Nanomaterials through HCl-Mediated Ligand Displacement. *J. Am. Chem. Soc.* **137**, 4046-4049, (2015).

14

Solution processing and engineering of thermoelectric nanomaterials

Chapter 3   From nanomaterials to devices
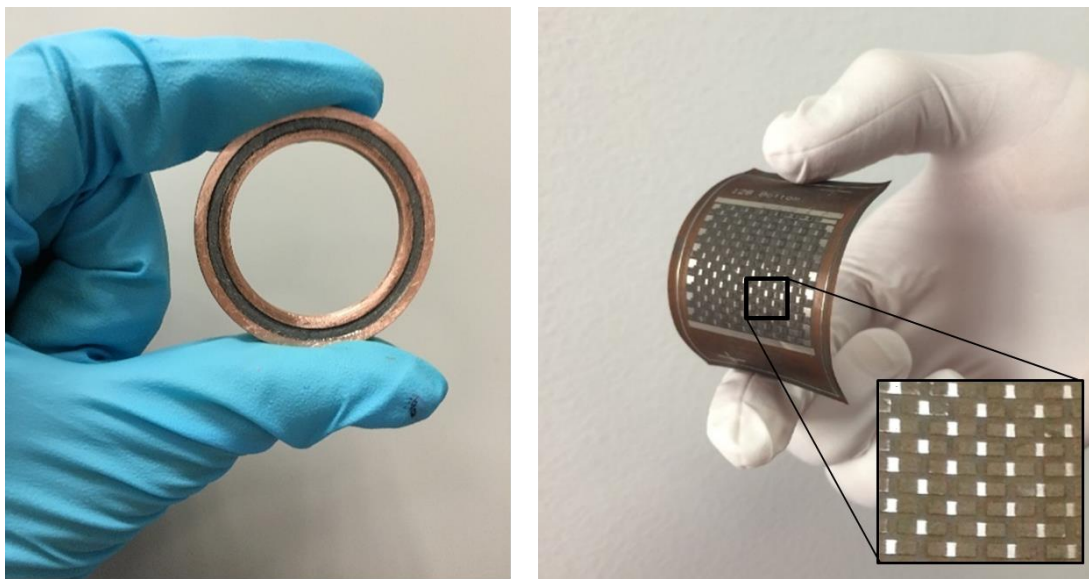
First two objectives of this thesis were i) the development of efficient TE materials from the engineering of colloidal nanomaterials and ii) to control the TE properties at the three different synthesis steps. Once having accomplished both, it is time to move forward to the device fabrication.

Taking advantage of the versatility that bottom-up solution-processed synthesis techniques offer, it is possible to design new TE modules in a wide range of sizes and shapes and over different kinds of substrates than the usual ceramic plates. The idea is to maximize the thermal contact with the surface that has to be cooled down or from which the heat has to be harvested.[63] A full list of TE devices from solution-processed techniques has been presented in Chapter 1.

In the present case, the fabrication of a simple model of ring-shaped TE device is proposed. This shape is perfect to be used in pipes or tubes transporting hot

fluids for the energy efficiency improvement of different applications or for the temperature control of such fluids.[107, 108] Originally, the intention when designing this ring shape was for its installation in automobile exhaust tubes, where a lot of energy is lost in the form of heat as introduced in Chapter 0.[10]

The rings are formed by two concentric Cu rings with the TE material between them. Since there were no commercially available dies to densify a structure like this, this configuration required the previous design of a custom die able to hold together the components. At the same time, it should resist the pressure needed for the compaction of the material in the hot press system, while allowing an easy dismantling that does not affect the newborn ring. In addition, a custom-made test bench was also fabricated to measure the outcoming power generated by the ring when applying a temperature difference. Rings were able to reach temperatures as high as 250 °C in their inner Cu ring while the outer one was maintained at 60 °C thus effectively creating a temperature gradient, monitored with two thermocouples, and a voltage between the two Cu rings.

In the work presented in this chapter, PbSe is used as the model material, taking into account its suitability for the mid-range temperature applications. The TE properties of different nanomaterials produced with PbSe NPs with different surface modifications were studied. The best results were obtained for the ones treated with sodium amide salts. This system was then up-scaled to fabricate the TE ring, which requires around 3 g of material.

An electrical model was further developed for this architecture to evaluate its potential. From calculations of the maximum electrical power that a ring-shaped TE leg can supply, it is envisaged the possibilities that this approach presents. This, together with the efficiency enhancements that can be done in solution-processed nanomaterials shown in the previous chapters, position the results of this work as a firm strategy for the progress of new TE devices.

Influence of the ligand striping on the transport properties of nanoparticle-based PbSe bulk nanomaterials

Doris Cadavid,[a,‡] Silvia Ortega,[a,b,‡] Sergio Illera,[c] Yu Liu,[a] Oscar Juan Durá,[d] Maria Ibáñez,[e,f] Alexey Shavel,[a] Yu Zhang,[a] Antonio M. López,[g] M. A. López de la Torre,[d] Joan Daniel Prades,[c] Germán Noriega,[b] Maksym Kovalenko[e,f] and Andreu Cabot*[a,h]

[a] Catalonia Institute for Energy Research - IREC, 08930 Sant Adrià de Besòs, Barcelona, Spain. E-mail: acabot@irec.cat

[b] Cidete Ingenieros S.L., Anselm Clavé 98, 08800 Vilanova i la Geltrú, Barcelona, Spain

[c] Departament d'Electrònica, Universitat de Barcelona, C. Martí i Franquès 1, 08028 Barcelona, Spain

[d] Departamento de Física Aplicada, Universidad de Castilla-La Mancha, Avd. Camilo José Cela, Edificio Politécnico, ETSII, 13071 Ciudad Real, Spain

[e] Institute of Inorganic Chemistry, Department of Chemistry and Applied Biosciences, ETH Zürich, CH-8093, Switzerland

[f] Empa-Swiss Federal Laboratories for Materials Science and Technology, Dübendorf, CH-8600, Switzerland

[g] Departament d'Enginyeria Electrònica, Universitat Politècnica de Catalunya, EPSEVG, 08800 Vilanova i la Geltrú, Barcelona, Spain

[h] ICREA, Pg. Lluís Companys 23, 08010 Barcelona, Spain

[‡] These authors contributed equally to this work

Abstract

Nanomaterials produced from the bottom-up assembly of nanocrystals incorporate $\sim 10^{20} - 10^{21}$ cm^{-3} surface atoms which may be not fully coordinated, thus $\sim 10^{20} - 10^{21}$ cm^{-3} potential donor or acceptor states that can strongly affect the nanomaterial transport properties. Thus, to exploit the full potential of nanocrystal building blocks to produce functional bulk nanomaterials and thin films, a proper control of their surface chemistry is required. We analyze here how the ligand stripping procedure influences the charge and heat transport properties of PbSe bulk nanomaterials produced from the bottom-up assembly of colloidal PbSe nanocrystals produced in the presence of oleic acid. The removal of the native organic ligands by thermal decomposition in an inert atmosphere leaves relatively large amounts of carbon at the crystal interfaces. This carbon blocks crystal growth during consolidation of the nanocrystals into bulk nanomaterials. Additionally, ligand removal by thermal decomposition results in materials with low electrical and thermal conductivities. Striping X-type ligands from the nanocrystal surface before their consolidation provides nanomaterials with larger crystal domains, lower porosity and higher charge carrier concentrations, thus resulting in higher electrical and thermal conductivities. In addition, the ligand displacement leaves the nanocrystal surface unprotected, facilitating its oxidation or the chalcogen evaporation. The influence of the ligand displacement on the nanomaterial charge transport properties is rationalized here using a two band model based on the standard Boltzmann transport equation with the relaxation time approximation. Additionally, we demonstrate the suitability of the produced functional nanomaterials by fabricating and testing a simple PbSe-based thermoelectric device with a ring geometry.

1

1. Introduction

The use of colloidal nanocrystals (NCs) building blocks, with controlled size, shape, crystal phase and composition, provides a huge flexibility to engineer a wide range of functional nanomaterials.[1,2] At the same time, bottom-up solution-processing technologies not only provide the means to produce functional materials by design with an unprecedented control over material parameters at the nanometer scale, but they also allows to do so in a cost-effective manner.

Nevertheless, to exploit the full potential of NC-based bottom-up assembly technologies to produce functional nanomaterials, some limitations remain to be overcome. One first challenge is the presence of the electrically insulating organic surfactants used to control NCs growth, e.g. long chain alkanes and alkenes with functional groups such as carboxylic and phosphonic acids, thiols, or amines. These surface organic ligands block charge transport, injection and extraction between NCs and between NCs and the media, thus constraining the performance of bottom-up nanomaterials in all fields where charge transport is involved, e.g. electronics, optoelectronics, catalysis or thermoelectricity. To remove surface organic ligands, several displacement and exchange procedures, based on the use of substituting shorter-surface species, have been proposed: pyridine,[3] hydrazine-based metal chalcogenides complexes,[4–8] nitrosonium, diazonium[9] and trialkyl oxonium tetrafluoroborates;[10] tetrafluoroborate acids (HBF$_4$, HPF$_6$);[11] ammonium thiocianate (NH$_4$SCN);[12,13] sulphides such as Na$_2$S, NH$_4$S, and K$_2$S;[11,14,15] or halide anions like Cl$^-$, Br$^-$ and I$^-$.[16–18] tretrabutylammonium iodide, 1,2-ethanedithiol.[19]

A second main challenge to optimize the performance of bulk nanomaterials obtained from the bottom-up assembly of colloidal NCs is to tune their charge carrier concentration. The introduction of controlled amounts of external elements within the NC lattice, as done to dope conventional bulk or thin film semiconductors, has seen important progresses in recent years, but it remains as an important limitation.[20–25] A second main limitation in this direction is the control of the NC surface composition. Interfaces have a very strong impact on the electronic transport of nanocrystalline materials. This impact has two main origins: i) charge carrier scattering at the potential barriers created in the grain-boundaries, which controls charge carrier mobility;[26] and ii) acceptor and donor states associated with non-fully coordinated ions at the interfaces, which control charge carrier concentration.[27], which dominates charge transport properties of the final bulk or thin film nanomaterial. Even stoichiometric and pure nanomaterials obtained from the bottom up assembly of 10 nm NCs incorporate $10^{20} - 10^{21}$ cm^{-3} interface atoms potentially not fully coordinated, thus introducing $10^{20} - 10^{21}$ cm^{-3} potential donor or acceptor states. This large density of interface states may translate in very large charge carrier concentrations and charge transport barriers at crystal interfaces which strongly influence charge carrier transport in the nanomaterial.

To solve these two challenges is a topic of major interest within the research and development communities using nanoparticle-based bottom up technologies to produce thin film or bulk nanomaterials devices, such as quantum dot solar cells, catalysts or thermoelectrics. Nevertheless, most studies have focus on the study of ligand exchange strategies to passivate an even introduce controlled amounts of dopants in non-sintered nanoparticle arrays. In spite of the extraordinary progress in this direction, nanomaterials obtained by this strategy still suffer of low charge carrier mobilities and relatively poor performances compared with competing technologies.

In this work, we investigated the effect of the ligand displacement (LD) procedure on the thermoelectric properties of nanomaterials obtained from by bottom-up strategies. The influence of the ligand exchange

2

procedure on the nanomaterial transport properties is discussed in the framework of a charge transport model based on the standard Boltzmann transport equation[28] with the relaxation time approximation and developed to fit our experimental data. We used PbSe as the model material owing to its easy synthesis with exceptional size and shape control at the gram scale and its excellent thermoelectric properties. In this regards, while PbSe has attracted less attention than PbTe, heavily doped PbSe has been predicted to reach thermoelectric figures of merit, ZT up to 2,[29] and experimental ZT values up to 1.3 has been obtained for PbSe:Al at 850 K and up to 1.2 for $Pb_{1-x}Na_xSe$ at 850 K.[30–33] Additionally, with the optimized material, and taking advantage of the versatility that bottom-up solution-processed nanomaterials offer, we made a step forward on the development of a TE generator. While current commercially available TE devices show the conventional planar architecture and cannot fit the huge variety of surfaces to optimize the thermal energy transfer, solution-processed TE devices could be constructed with potentially any shape and size and here we demonstrate it by the construction of a simple shape-adapted TE ring generator.

2. Experimental

Materials. Selenium pieces (99.999 %), lead acetate trihydrate (99.9%), lead nitrate (99.0 %), 1-octadecene (ODE, technical grade 90 %), oleic acid (OA, technical grade 90 %), sodium amide (95 %), ammonium nitrate (98 %), anhydrous methanol, anhydrous chloroform, formamide (FA >99.5%) and dimethylformamide (DMF 99.8%) were purchased from Aldrich. Triocthiylphosphine (TOP, 97 %) was purchased from Strem Chemicals. Analytical grade ethanol, hexane and chloroform were purchased from Panreac. All chemicals were used without further purification. A stock solution of TOPSe (1 M) was prepared dissolving 7.89 g of selenium pieces in 100 ml of TOP. All NC preparations were carried out using standard airless techniques: a vacuum/dry Ar Schlenk line was used for the synthesis and an Ar-filled glovebox for storing and handling oxygen- and moisture-sensitive chemicals

PbSe NCs. A modified approach to the developed by J. J. Urban et al.[34] was used to synthesize PbSe NCs. In a typical procedure, 7 mmol (2.8 g) of lead acetate trihydrate and 23 mmol (6.6 g) of OA were dissolved in 50 ml of ODE. The mixture was heated up to 130 °C under vacuum for 1.5 h. afterward, the solution was flushed with Ar and heated up to 190 °C. At this temperature, 12 ml of the TOPSe stock solution was quickly injected. After injection, the reaction temperature was maintained between 180 °C and 190 °C for 10 minutes. Then the solution was cooled using a water bath. PbSe NCs were precipitated and redispersed several times using ethanol and hexane. Finally, PbSe NCs were dispersed in chloroform and stored in the glovebox.

Organic ligand replacement. Several salts were used to displace organic ligands from the PbSe NCs surface. In a typical procedure, and using $NaNH_2$ as example, PbSe NCs (250 mg) were dispersed in 10 ml of chloroform and mixed at room temperature with 5 ml of $NaNH_2$ solution (0.01 M) in methanol. The solution was shacked during 1-2 minute to displace the OLs attached to the NCs surface. Afterward, NCs were precipitated by centrifugation and they were thoroughly purified using chloroform/methanol to remove the remaining organic species. Finally, PbSe NCs were precipitated and dried under vacuum or redispersed in polar solvents like FA, DMF or ethanol for further analysis. To avoid the oxidation of the chalcogenide NCs, the OL replacement was conducted inside the Ar-filled glovebox.

PbSe bulk nanomaterial. To produce PbSe bulk nanostructured materials, NCs were dried under vacuum, annealed at 450 °C for 1 h and compacted at 350 °C for 2 minutes into disk-shaped pellets of 10 mm of diameter and 1 mm of thickness under 40 MPa of pressure. For pellet preparation, we used graphite dies and a custom-made hot-press (HP) consisting in an induction heater coupled to a hydraulic press kept inside the Ar-filled glove box.

3

Ring thermoelectric generator. TE rings (39 mm and 28 mm, outer and inner diameter respectively, 2 mm thick) were built by filling two Cu concentric rings with dried PbSe NCs followed by uniaxial pressing at 350 °C and 20 MPa during 5 minutes. Rings were pressed using a custom-made die in the hot press system previously described.

Structural and chemical characterization. X-ray power diffraction (XRD) analyses were carried out on a Bruker AXS D8 ADVANCE X-ray diffractometer with Cu Kα1 radiation (λ = 1.5406 Å). Size and shape of the nanoparticles were examined by transmission electron microscopy (TEM) using a ZEISS LIBRA 120, operating at 120 keV accelerating voltage. Scanning electron microscopy (SEM) was performed using a ZEISS Auriga microscope with an energy dispersive X-ray spectroscopy (EDX) detector to study the material´s composition. Nuclear magnetic resonance (NMR) spectra (1H-NMR) were acquired using a Bruker DRX 500 spectrometer equipped with an 11.7 Tesla magnet and an Avance III console. The spectral frequency was set at 500 MHz for ^{1}H, 125.7 MHz for ^{13}C and 202.4 MHz for ^{31}P. ^{1}H and ^{13}C NMR spectra were referenced externally to tetramethyl silane (SiMe$_4$) and ^{31}P NMR to 85% phosphoric acid (H$_3$PO$_4$). Spectra were acquired on a 2.5mm MAS probe head using 20 kHz MAS frequency at room temperature. Thermal gravimetric analyses (TGA) were done using Perkin-Elmer TGA 4000 equipment. The dried PbSe nanopowders were heated up to 500 °C under a nitrogen flow and a heating ramp of 5 °C/min. Fourier-transform infrared (FTIR) spectra were acquired using an Alpha Bruker FTIR spectrometer with the platinum attenuated total reflectance (ATR) single reflection module, FTIR data were typically averaged over 64 scans.

Thermoelectric characterization. Seebeck coefficients and electrical resistivities were measured simultaneously using a Linseis - LSR 3 system under helium atmosphere. The Seebeck coefficient was obtained using a static DC method and the electrical resistivity was measured by means of a standard four probe technique in the temperature range from 300 K to 600 K. Thermal conductivity data were obtained from flash diffusivity measurements (Linseis LFA 1000) as a function of temperature. The thermal conductivity was calculated as κ = DC$_p$d, where D is the thermal diffusivity, C$_p$ is the heat capacity, and d is the density. C$_p$ was approximated by the formula 0.171+(2.65x10^{-5})T, where T is absolute temperature. [31,35,36] At T>T$_D$ (where T$_D$ is the Debye temperature), this equation is consistent with the higher C$_p$ values reported for nanostructured materials, as compared with values obtained by the Dulong-Petit approximation.[37] These alterations of C$_p$ values are caused probably by the high surface to volume ratio in nanostructured materials. Room temperature measurements of the Hall charge carrier concentration and mobility were performed in a four-probe configuration using an electromagnet that generated a magnetic field up to 1.2 T. Current was passed through the sample while the field was varied between 0.1 to 1 T in increments of 0.1 T with an inversion of the field to eliminated voltage probe misalignment effects.

Device Test. Ring TE generators were tested in a custom-made test bench. The inner part of the rings was heated fitting a metal block containing a heating cartridge, while the outer part was maintained cold by means of commercial TE modules attached. Starting from a 10 °C thermal gradient at room temperature, it increased gradually until reaching the highest temperature at the hot side at 250 °C, while the cold side was kept at 60 °C at the same time, thus generating a maximum temperature gradient of 190 °C. Temperature was monitored with two thermocouples attached to the cold and hot sides of the ring respectively and the open circuit voltage generated between the two Cu electrodes was measured using a Keithley 2400 multimeter.

3. Results and discussion

PbSe NCs were synthesized by reacting lead acetate with TOPSe at 190 °C. The presence of OA in the reacting mixture was essential to limit the PbSe NC growth during their synthesis and to keep them in solution. As-

4

produced PbSe NCs, henceforth referred to as PbSe-OL, had an average size of 16 ± 2 nm with a ~10 % size dispersion, cubic shape (Figure 1a) and face centered cubic crystallographic phase (fcc, JCPDS 1-78-1903, Figure 1b).
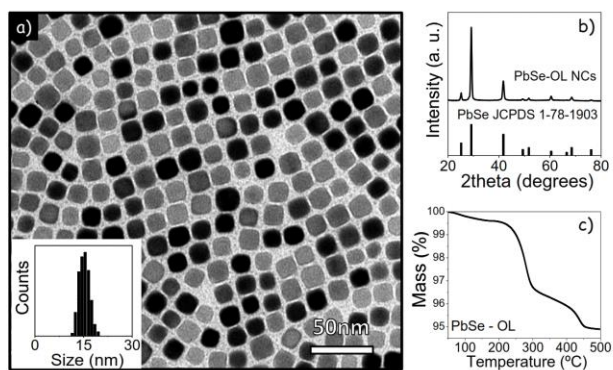

Figure 1. TEM micrograph (a) and histogram of the particle size distribution (a, inset); XRD pattern (b) and thermogravimetric profile (c) of 16±2 nm cube-shaped PbSe-OL NCs used as building blocks to produce bulk nanocrystalline PbSe.

Thermogravimetric (TG) analysis (Figure 1c) allowed us to quantify the amount of surface ligands at the surface of PbSe NCs purified by 3 precipitation and redispersion steps at ~6 % of the total mass. To determine the NC surface composition, NMR analysis of the PbSe-OL NCs in chloroform was performed. ^{1}H-NMR spectra displayed the characteristic $CH_3(CH_2)_x$ peaks present both in OA and TOP (figure S3). ^{13}C NMR spectrum displayed the characteristic C=C peak and the COOH band associated to OA. Additionally, the ^{31}P NMR spectrum (figure S2) of PbSe-OL NCs did not show any evidence of the presence of TOP. We therefore concluded OA to be the only ligand present at the PbSe NC surface. Taking into account the organic amount measured by TG, a ligand surface concentration of ~1.4 nm^{-2} was estimated.

The presence of organic ligands at the NC surface is anticipated to strongly limit the performance of any PbSe NC-based application involving charge transport/transfer between/from/to NCs, e.g. photovoltaics, electroluminescent light emitting diodes, thermoelectrics and catalysis. To take full advantage of the convenient processability of colloidal NCs, organic ligands can be chemically or thermally removed after their deposition/assembly. In dense bulk nanomaterials and relatively thick film, chemical processes are not effective and thermal decomposition becomes the only viable procedure. Alternatively, native organic ligands can be exchanged by smaller organic or inorganic species able to colloidally stabilize the NCs, typically electrostatically in polar solvent, but having no detrimental effect on the nanomaterial transport properties. Among the potential candidates to displace organic ligands from the PbSe-OL NC surface, hydrazine was discarded due to its toxicity and dangerous manipulation, and sulfur-based compounds were not considered due to their potential to sulfurize the selenide NCs. Alternative inorganic salts were tested, e.g. $NaNH_2$, $Pb(NO_3)_2$, NH_4NO_3, focusing our efforts on $NaNH_2$.

To displace OA using such salts, PbSe-OL NCs dispersed in chloroform were mixed with a 0.01 M solution of the salt in methanol. The resulting mixture was vigorously shaken at room temperature for a few minutes. During this process, the OL was stripped from the PbSe-OL NC surface and the resulting charge-stabilized PbSe NCs moved to the methanol phase. The obtained PbSe NCs, henceforth referred to as PbSe-LD, were thoroughly washed with chloroform to remove the remaining organic species and they were finally

5

precipitated and dried under vacuum to a nanocrystalline powder. All these processes were carried out inside an Ar-filled glovebox to avoid oxidation. PbSe-LD NCs preserved the shape and size distributions of the original PbSe-OL NCs (see figure S1) and were dispersable in polar solvents like FA, DMF or alcohols for a limited amount of time.
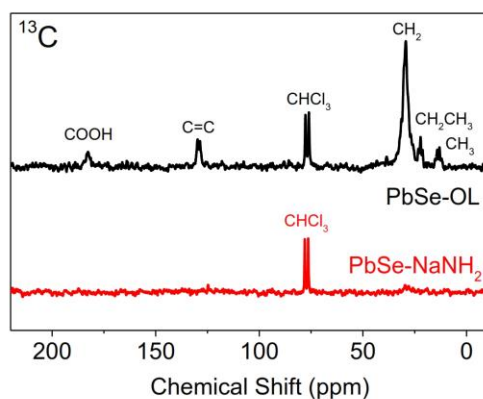

Figure 2. ^{13}C NMR spectra of PbSe-OL (black spectra) dissolved in CHCl$_3$ these peaks correspond to the OA fingerprints. ^{13}C NMR spectra of PbSe-NaNH$_2$ showing that after ligand displacement it is possible to obtain naked PbSe NCs.

^{13}C and ^{1}H NMR analysis of the PbSe NCs treated with NaNH$_2$, henceforth referred to as PbSe-NaNH$_2$, showed the OA fingerprints to vanish after the ligand displacement process (Figure 2). While a previous work identified NH$_2^-$ as the species remaining at the surface of CdSe NCs,[11] no evidence of NH$_2^-$ fingerprints in the ^{1}H-NMR spectrum of PbSe-NaNH$_2$ NCs could be found. We associate this fact to the facile decomposition of the amide group. It should be also mentioned in this regard that the ligand displacement procedure was carried out in a glove-box, but for NMR characterization NCs were exposed to air, which may have modified their surface chemistry, especially taking into account the high reactivity of the amide group.

To produce bulk nanostructured PbSe, ~1 g of PbSe NCs were thoroughly cleaned, dried and annealed at 450 °C for 1h in argon. The annealed material was afterward compacted at 350 °C under 40 MPa of pressure using a hot press. The relative densities of the final PbSe-OL pellets were around 85 %. Those of the PbSe-LD pellets were systematically higher, above 90 %. The annealing of PbSe-OL under inert atmosphere caused the thermal decomposition of the surface OLs. This decomposition left a relatively large amount of carbon, which was quantified by elemental analysis at around 2 %. On the other hand, the residual carbon within the final PbSe-LD nanocrystalline powders was within the limit of detection of our system, ~0.1 %. Further EDX and ICP analysis of PbSe-NaNH$_2$ showed no evidence of the presence of Na, pointing out the inefficiency of doping PbSe with Na by this simple procedure. [30,31,36,38]

During the thermal treatments the average PbSe-OL crystal size increased from the initial ~ 16 nm to ~ 20 nm (Figure 3). The average crystal domain size of the thermal treated PbSe-LD materials was systematically larger, what we associate to the lack of a carbon layer hindering the crystal growth. For the PbSe-NaNH$_2$ sample, the crystal size domain increased from 16 nm to 25-30 nm with the two thermal treatments (Figure 3).
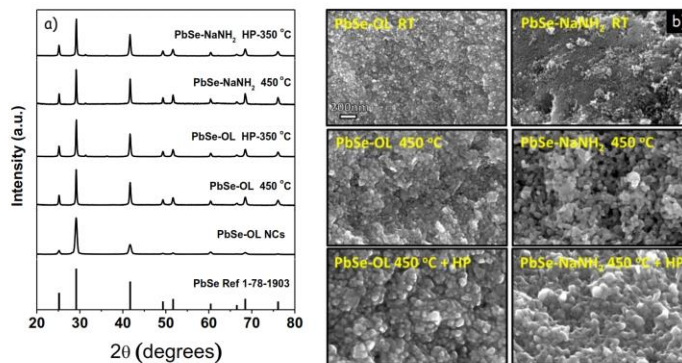
6

Figure 3. XRD patterns and SEM images of PbSe initial NCs (PbSe-OL), the nanocomposites after OL displacement (PbSe-LD) and heat treatment at 450 °C, and the final samples after densification with HP at 350 °C and 4 MPa for 2 min.

Figure 4 displays the electrical conductivity (σ), Seebeck coefficient (S), thermal conductivity (κ), power factor (PF) and thermoelectric figure of merit (ZT) of the nanocrystalline PbSe-OL and PbSe-LD samples in the temperature range from 300 to 600 K. Electrical conductivities of the PbSe-OL samples were relatively low, below 10^4 S m^{-1}. The temperature dependence of the electrical conductivities displayed a step increase in the range from 400 to 500 K. This step was accompanied by a parallel step change of the Seebeck coefficient, which included a sign inversion at around 400 K, from positive to negative values. Such related step changes and the sign inversion of the Seebeck coefficient suggested the thermal activation of a large concentration of negative charge carriers above 400 K.

The stripping of the organic ligands before consolidation resulted in a strong rise, up to two orders of magnitude, of the electrical conductivity when compared with PbSe-OL samples (Figure 4a). For PbSe-NaNH$_2$, a slight decrease of the electrical conductivity with temperature was observed, denoting a degenerated semiconductor behavior. On the other hand, negative Seebeck coefficients with monotonically increasing absolute values were measured for all the PbSe-LD materials in the entire temperature range tested (Figure 4b). The absolute values of the Seebeck coefficient of the PbSe-LD materials were lower than those of PbSe-OL, what denoted higher charge carrier concentrations. Other inorganic ligand displacement agents resulted in similar transport properties. However, NaNH$_2$ was the salt resulting in a larger electrical conductivity increase, which we associated to the ease decomposition of the amide group during the NC consolidation.

We believe the strong differences observed in the temperature evolution of the electrical conductivity and Seebeck coefficient, in large part related to significant variations of the charge carrier concentration, were related to dissimilarities in the material composition associated by the different organic ligands removal strategies. Initial colloidal nanoparticles were uncharged and oleic acid molecules compensate for the surface dangling bonds. The thermal decomposition of oleic acid bond to the Pb ions at the PbSe surface leaves oxygen ion behind [39,40] that can compensate the charge of the PbSe surface ions. We experimentally see that there is a surprisingly good compensation of charges, from the 10^{20}-10^{21} dangling bonds to less than 10^{16} electronically active species. On the other hand, the stripping of the oleic acid molecules with NaNH$_2$ results in NCs with Pb-rich surfaces and overall off-stoichiometric compositions which are not compensated by any additional ion. Thus, high concentrations of free electrons are measured. In addition, during the thermal

7

treatments some amount of Se can leave the NCs intensifying the stoichiometry unbalance. This effect may be insignificant in PbSe-OL samples as the carbon left after the organic thermal decomposition may protect them from this lost.
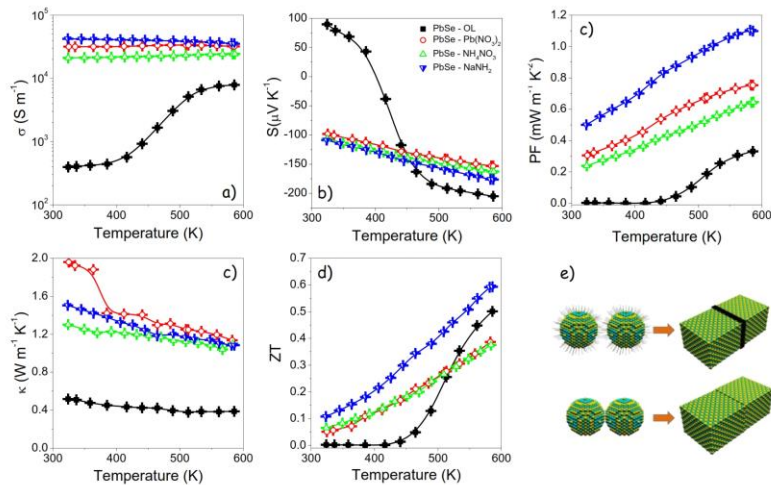

Figure 4. Electrical conductivity (a), Seebeck coefficient (b), power factor (c), thermal conductivity (c) and thermoelectric figure of merit (d) of nanocrystalline PbSe obtained from the bottom-up assembly of PbSe-OL and PbSe-LE NCs. e) Scheme of the nanomaterial obtained with and without ligand displacement.

To further understand the electrical conductivity and Seebeck coefficient evolution with temperature, a charge transport model based on the standard Boltzmann transport equation[28] with the relaxation time approximation (RTA) was used (see supporting information). The electrical conductivity and the Seebeck coefficient of the PbSe-OL and PbSe-LD nanomaterials were fitted using this two band model in the temperature range from 300 K to 600 K. The parameters that describe the phonon scattering processes were fixed for all materials and were not allowed to change with temperature (Table S1). Using the bulk material parameters of table S1, to reproduce the experimental values was not possible. Thus we included interface scattering as an infinite series of potential barriers to describe nanostructured materials reflecting the material discontinuity between NC reducing the conductivity of the sample respect to the bulk case. Interface scattering parameters were adjusted for each sample to simultaneously fit both, the electrical conductivity and Seebeck coefficient tendencies (Figure 5).
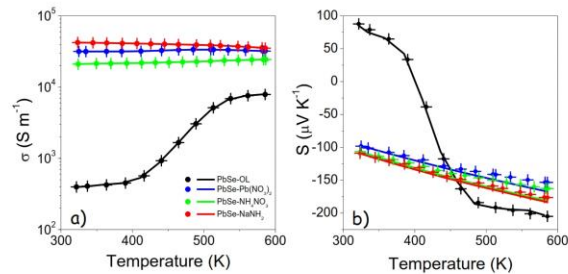
8

Figure 5. (a) Electrical conductivity, and (b) Seebeck coefficient as a function of temperature (symbols) and the calculated values from the two band model (continuous line).

Including interface scattering, the two band model successfully reproduced the complex temperature evolution of the electrical conductivity and Seebeck coefficient of the PbSe-OL sample (Figure 5). The electrical conductivity increase with temperature and the complex Seebeck trend reflected an intrinsic semiconductor behavior. The sign change in the Seebeck coefficient and the different slopes in the conductivity showed two different regimes in which each type of carrier dominated. In the low temperature region (300 K < T < 420 K), the electrical conductivity remained approximately constant and the Seebeck coefficient was positive, thus holes dominated transport. In the intermediate temperature region (420 K < T < 520 K), when the temperature increased, the Seebeck coefficient strongly decreased to zero, reflecting a similar electron and hole contribution. In the highest temperature range (520 K < T < 600 K) electrons dominated the conduction as reflected in the negative Seebeck coefficients obtained. We used the parameters of table S1 to describe the phonon scatterings. We additionally included the interface scattering in the scattering rates of both electrons and holes. The height and the width of the barrier were used as fitting parameters whereas the grain size was L=25nm as we inferred from the XRD measurements. The height of the barrier for each carrier was assumed independent of each other but temperature dependent. The initial hole concentration that best fitted the experimental results was p = 5 x 10^{15} cm^{-3} and the best energy barrier was 0.1 eV.

On the other hand, for the PbSe-NaNH$_2$ sample, the increase of the Seebeck coefficient with temperature and the decrease of the electrical conductivity denoted the sample to be completely degenerated in the whole temperature range. Thus, it could be well explained using only the majority carriers, electrons in this case. We assumed the electron concentration to remain constant in the whole temperature range at n=Nd (where Nd is the doping concentration with all the impurities being ionized), while scattering times decreased with temperature. To determine n, the Hall charge carrier concentration at room temperature was measured obtaining n$_e$ = 2x10^{19} cm^{-3} for PbSe-LD. Thus, the doping concentration was set to Nd = 2x10^{19} cm^{-3}. This high charge carrier concentration was associated to a stoichiometry unbalance with the OA removal and/or a small selenium evaporation during the thermal treatments in the PbSe-LD samples. The carbon remaining after temperature treatments better protected the PbSe-OL toward Se evaporation. We used the same parameters as in the previous case to describe the phonon scatterings. To describe the interface scattering, we used a fixed barrier width w = 3nm and a grain size L=30 nm, as given from XRD results. The barrier height was used as a fitting parameter. With the introduction of interface scattering, the experimental conductivity and Seebeck coefficients were well reproduced by the two band model when considering a lineal temperature dependence of the chemical potential $\mu = 3.4164x10^{-4}T + 0.2879$, measured from the top of the valence band. This result was consistent with a completely degenerated semiconductor since the chemical

9

potential was always inside the conduction band in all the temperature range. Concerning the interface scattering, the barrier height was temperature dependent, following a lineal trend described by $E_b = 0.26699 - 2.2495 \times 10^{-4}T$, which results in effective barriers slightly above those of PbSe-OL.

Figure 4d displays the thermal conductivity (κ) of the different PbSe materials in the temperature range 300-600 K. Thermal conductivities monotonously decreased with temperature for all nanomaterials. PbSe-OL was characterized by up to 3 fold lower thermal conductivities than PbSe-LD. These experimental results prove that the products from the decomposition of the OLs not only block crystal domain growth, charge carrier transport and possibly Se evaporation, but also phonon propagation. The lower thermal conductivities obtained for PbSe-OL have an origin on the carbon present in between NCs in the nanocrystalline from the decomposition of the OLs, the slightly larger interface density of PbSe-OL related with its smaller crystal domains and the higher porosity of the PbSe-OL when compared to PbSe-LD.

Finally, the thermoelectric figure of merit, $ZT=TS^2\sigma/\kappa$, increased with temperature for all materials, reaching values up to 0.5 for PbSe-OL and 0.6 for PbSe-NaNH$_2$ (figure 4e). These values were significantly higher than those of undoped bulk PbSe and comparable with those obtained from bulk PbSe doped with Ag or Na at 600 K.[31, 38]

To demonstrate the suitability of this strategy to produce functional materials and devices, PbSe-NaNH$_2$ nanomaterials were employed to build ring-shaped TE generators. [41, 42] While most of the commercially available TE devices are plate-shaped, TE devices build on a ring configuration are very convenient and appealing when the thermal power to be harvested or delivered is in the radial direction, *e.g.*. in pipe transporting a hot fluid. [42] The assembly of several n- and p-type TE rings connected thermally in parallel and electrically in series results in a cylindrical-tube TE generator with improved thermal contact between the hot surface and the device, maximizing the thermal power collected or delivered.
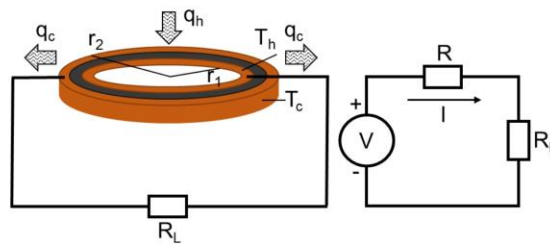
Figure 7. Basic electrical model of a ring TE generator.

The electrical power generated by a thermoelectric device can be generally expressed as: [43]

$$P_{gen} = q_h - q_c$$

Where q_h and q_c are the incoming and outgoing power in the hot and cold side of the thermoelectric generator respectively. Assuming mean values for S, σ and λ, considering I as the generated electrical current that flows through the closed loop circuit, R as the electrical resistance of solely the TE material, and T_h and T_c as the temperatures in the hot and cold sides respectively,

10

$$q_h = SIT_h - \frac{1}{2}I^2R + \lambda\Delta T$$

$$q_c = SIT_c + \frac{1}{2}I^2R + \lambda\Delta T$$

in the load resistance, the electrical power can be redefined as:

$$P_{gen} = SI\Delta T - I^2R$$

Therefore, the maximum electrical power P_{max} is obtained when the load R_L has the same value of the internal resistance R:

$$\frac{\partial P_{gen}}{\partial I} = 0 = S\Delta T - 2IR \quad \rightarrow \quad I_{max} = \frac{S\Delta T}{2R}$$

Considering that the resistivity of a single ring is found by:[44]

$$R = \frac{1}{2\pi t\sigma}\int_{r_1}^{r_2}\frac{1}{r} = \frac{1}{2\pi t\sigma}\ln\frac{r_2}{r_1}$$

where t is the thickness of the TE material. Then, the maximum electrical power of one TE ring generator can be expressed as a combination of material parameters:

$$P_{max} = \frac{(S\Delta T)^2}{4R} = \frac{\pi t\sigma(S\Delta T)^2}{\ln\frac{r_2}{r_1}}$$

Figure 8. (a) Open circuit voltage (black squares) obtained from a single PbSe ring as a function of the temperature gradient generated by increasing the temperature at the hot side (internal part of the ring) and S (red open circles). (b) Power output of the PbSe ring as a function of the thermal gradient. Red squares represent the experimental data collection and the solid black line the theoretical calculated values taking into account experimental values for S and σ from the starting surface-engineered PbSe bulk nanomaterial.

A single n-type ring was fabricated and tested in a custom-made test bench in which the TE ring, 38 mm complete external diameter and 29 mm internal hole diameter, was fitted between two electrically isolated metal blocks. The inner block contains a heat cartridge and provides the heat to the internal part of the ring, while the metal block around the ring was kept cool by means of commercial TE modules attached. Thus, a thermal gradient was applied to the ring generator, fabricated by filling with dried surface-engineered PbSe NCs the 1.5 mm empty space between two concentric Cu rings and hot pressed at 350 °C, while measuring

11

the open circuit voltage produced until reaching 250 °C at the hot side (Fig. 8a). Voltage generated, around 30 mV at 190 °C thermal gradient, is in good agreement with the previous measurements of the S of the PbSe bulk nanomaterial (Fig. 4b). As shown in Fig. 2b, and showing the ring an electrical resistance of 1.75 mΩ, the power output generated is around 500 mW at the maximum temperature difference reached at the test bench. These values were higher than those previously reported with a similar geometry [44] due to the larger size of the present ring and the higher Seebeck coefficient of the materials here used and the higher temperature difference tested in the present work. Power experimental values agree partially with the theoretical calculated ones, which were more optimistic probably due to the non-consideration of the contact resistance in the development of the electrical model. Nevertheless, these results indicate the real potential of, not only the ring configuration for a TE module, but also for bottom-up engineered solution-processed nanoparticle building blocks for the production of TE materials and shape-adaptable devices.

5. Conclusions

In summary, nanocrystalline PbSe nanomaterials were produced from the bottom-up assembly of PbSe colloidal NCs produced in the presence of OA. The effect of two organic ligand stripping strategies was analyses. Overall the organic removal by thermal decomposition resulted in a reduced crystal growth and the presence of relatively large amounts of carbon in the final material. Both leaded to reduced electrical thermal conductivities. At the same time, electrical conductivity was relatively low due to a very low charge carrier concentration and also to the scattering of charge carriers in the crystal boundaries (Figure 6). On the other hand, the OL displacement by metal salts had associated the introduction of a relatively large charge carrier density through the nanocrystal surface. This surface charge increased interface energy barriers, but also introduced larger charge carrier densities in the material which became degenerated. Much higher electrical conductivities, but also lower Seebeck coefficients were obtained. At the same time, due to the higher density of the materials, the larger crystal domains and the reduced phonon scattering efficiency when compared with PbSe-OL, and also due to an increase of the electronic contribution, the thermal conductivity of these materials was relatively larger.

## References

1. Cadavid, D. *et al.* Bottom-up processing of thermoelectric nanocomposites from colloidal nanocrystal building blocks: the case of Ag2Te–PbTe. *J. Nanopart. Res.* **14,** 1–10 (2012).
2. Ibáñez, M. *et al.* Core–Shell Nanoparticles As Building Blocks for the Bottom-Up Production of Functional Nanocomposites: PbTe–PbS Thermoelectric Properties. *ACS Nano* **7,** 2573–2586 (2013).

12

3. Huynh, W. U., Dittmer, J. J. & Alivisatos, A. P. Hybrid Nanorod-Polymer Solar Cells. *Science* **295,** 2425–2427 (2002).
4. Kovalenko, M. V., Scheele, M. & Talapin, D. V. Colloidal Nanocrystals with Molecular Metal Chalcogenide Surface Ligands. *Science* **324,** 1417–1420 (2009).
5. Kovalenko, M. V., Bodnarchuk, M. I., Zaumseil, J., Lee, J.-S. & Talapin, D. V. Expanding the Chemical Versatility of Colloidal Nanocrystals Capped with Molecular Metal Chalcogenide Ligands. *J. Am. Chem. Soc.* **132,** 10085–10092 (2010).
6. Kovalenko, M. V. *et al.* Semiconductor Nanocrystals Functionalized with Antimony Telluride Zintl Ions for Nanostructured Thermoelectrics. *J. Am. Chem. Soc.* **132,** 6686–6695 (2010).
7. Kovalenko, M. V., Bodnarchuk, M. I. & Talapin, D. V. Nanocrystal Superlattices with Thermally Degradable Hybrid Inorganic−Organic Capping Ligands. *J. Am. Chem. Soc.* **132,** 15124–15126 (2010).
8. Lee, J.-S., Kovalenko, M. V., Huang, J., Chung, D. S. & Talapin, D. V. Band-like transport, high electron mobility and high photoconductivity in all-inorganic nanocrystal arrays. *Nature Nanotechnol.* **6,** 348–352 (2011).
9. Dong, A. *et al.* A Generalized Ligand-Exchange Strategy Enabling Sequential Surface Functionalization of Colloidal Nanocrystals. *J. Am. Chem. Soc.* **133,** 998–1006 (2011).
10. Rosen, E. L. *et al.* Exceptionally Mild Reactive Stripping of Native Ligands from Nanocrystal Surfaces by Using Meerwein's Salt. *Angew. Chem. Int. Ed.* **51,** 684–689 (2012).
11. Nag, A. *et al.* Metal-free Inorganic Ligands for Colloidal Nanocrystals: S2–, HS–, Se2–, HSe–, Te2–, HTe–, TeS32–, OH–, and NH2– as Surface Ligands. *J. Am. Chem. Soc.* **133,** 10612–10620 (2011).
12. Fafarman, A. T. *et al.* Thiocyanate-Capped Nanocrystal Colloids: Vibrational Reporter of Surface Chemistry and Solution-Based Route to Enhanced Coupling in Nanocrystal Solids. *J. Am. Chem. Soc.* **133,** 15753–15761 (2011).
13. Koh, W., Saudari, S. R., Fafarman, A. T., Kagan, C. R. & Murray, C. B. Thiocyanate-Capped PbS Nanocubes: Ambipolar Transport Enables Quantum Dot Based Circuits on a Flexible Substrate. *Nano Lett.* **11,** 4764–4767 (2011).
14. Zhang, H. *et al.* Surfactant Ligand Removal and Rational Fabrication of Inorganically Connected Quantum Dots. *Nano Lett.* **11,** 5356–5361 (2011).
15. Nag, A. *et al.* Effect of Metal Ions on Photoluminescence, Charge Transport, Magnetic and Catalytic Properties of All-Inorganic Colloidal Nanocrystals and Nanocrystal Solids. *J. Am. Chem. Soc.* **134,** 13604–13615 (2012).
16. Tang, J. *et al.* Colloidal-quantum-dot photovoltaics using atomic-ligand passivation. *Nature Mater.* **10,** 765–771 (2011).
17. Zhitomirsky, D. *et al.* N-Type Colloidal-Quantum-Dot Solids for Photovoltaics. *Adv. Mater.* **24,** 6181–6185 (2012).
18. Ning, Z. *et al.* All-Inorganic Colloidal Quantum Dot Photovoltaics Employing Solution-Phase Halide Passivation. *Adv. Mater.* **24,** 6295–6299 (2012).
19. Klem, Ethan J.D. *et al.* Impact of dithiol treatment and air annealing on the conductivity, mobility, and hole density in PbS colloidal quantum dot solids. *Appl. phys. Lett.* **92,** 212105 (2008).
20. Ibáñez, M. *et al.* Composition Control and Thermoelectric Properties of Quaternary Chalcogenide Nanocrystals: The Case of Stannite $Cu_2CdSnSe_4$. *Chem. Mater.* **24,** 562–570 (2012).
21. Ibáñez, M. *et al.* $Cu_2ZnGeSe_4$ Nanocrystals: Synthesis and Thermoelectric Properties. *J. Am. Chem. Soc.* **134,** 4060–4063 (2012).
22. Ibáñez, M. *et al.* Extending the Nanocrystal Synthesis Control to Quaternary Compositions. *Cryst. Growth Des.* **12,** 1085–1090 (2012).
23. Shavel, A., Cadavid, D., Ibáñez, M., Carrete, A. & Cabot, A. Continuous Production of Cu_2ZnSnS_4 Nanocrystals in a Flow Reactor. *J. Am. Chem. Soc.* **134,** 1438–1441 (2012).
24. Ibáñez, M. *et al.* Crystallographic Control at the Nanoscale to Enhance Functionality: Polytypic Cu_2GeSe_3 Nanoparticles as Thermoelectric Materials. *Chem. Mater.* **24,** 4615-4622 (2012).
25. Ibáñez, M. *et al.* Colloidal Synthesis and Thermoelectric Properties of Cu_2SnSe_3 Nanocrystals. *J. Mater. Chem. A* **1,** 1421-1426 (2012).
26. Martin, J., Wang, L., Chen, L. & Nolas, G. S. Enhanced Seebeck coefficient through energy-barrier scattering in PbTe nanocomposites. *Phys. Rev. B* **79,** 115311 (2009).
27. Mentzel, T. S. *et al.* Charge transport in PbSe nanocrystal arrays. *Phys. Rev. B* **77,** 075316 (2008).
28. Ziman, J. M. *Principles of the theory of solids.* (University Press, 1972).

13

29. Parker, D. & Singh, D. J. High-temperature thermoelectric performance of heavily doped PbSe. *Phys. Rev. B* **82,** 035204 (2010).
30. Zhang, Q. *et al.* Enhancement of thermoelectric figure-of-merit by resonant states of aluminium doping in lead selenide. *Energy Environ. Sci.* **5,** 5246–5251 (2012).
31. Wang, H., Pei, Y., LaLonde, A. D. & Snyder, G. J. Heavily Doped p-Type PbSe with High Thermoelectric Performance: An Alternative for PbTe. *Adv. Mater.* **23,** 1366–1370 (2011).
32. Lee, Y. *et al.* High-Performance Tellurium-Free Thermoelectrics: All-Scale Hierarchical Structuring of p-Type PbSe–MSe Systems (M = Ca, Sr, Ba). *J. Am. Chem. Soc.***135***, 5152-5160* (2013).
33. Androulakis, J. *et al.* Thermoelectrics from Abundant Chemical Elements: High-Performance Nanostructured PbSe–PbS. *J. Am. Chem. Soc.* **133,** 10920–10927 (2011).
34. Urban, J. J., Talapin, D. V., Shevchenko, E. V. & Murray, C. B. Self-Assembly of PbTe Quantum Dots into Nanocrystal Superlattices and Glassy Films. *J. Am. Chem. Soc.* **128,** 3248–3255 (2006).
35. Ravich, Y. I., Efimova, B. A. & Tamarchenko, V. I. Semiconducting Lead Chalcogenides. *Plenum, New York* (1970).
36. Androulakis, J. *et al.* High-temperature charge and thermal transport properties of the n-type thermoelectric material PbSe. *Phys. Rev. B* **84,** 155207 (2011).
37. Scheele, M. *et al.* Thermoelectric Properties of Lead Chalcogenide Core–Shell Nanostructures. *ACS Nano* **5,** 8541–8551 (2011).
38. Wang, S. *et al.* Exploring the doping effects of Ag in p-type PbSe compounds with enhanced thermoelectric performance. *J. Phys. D: Appl. Phys.* **44,** 475304 (2011).
39. Marks B.M., Howard Jr. H. C. The Catalytic Decomposition of Oleic Acid. *J. Phys. Chem.* **32,** 1040-1048 (1928).
40. Ibáñez M. *et al.* Electron doping in bottom-up engineered thermoelectric nanomaterials through HCl-mediated ligand displacement. *J. Am. Chem. Soc.* **137,** 4046-4049 (2015).
41. Rowe D. M. *Thermoelectrics Handbook: Macro to Nano*, CRC Press: Boca Raton, FL, 2006.
42. Liu Y. *et al.* Solution-based synthesis and processing of Sn- and Bi-doped Cu_3SbSe_4 nanocrystals, nanomaterials and ring-shaped thermoelectric generators. *J. Mater. Chem. A.* **5,** 2592-2602 (2017).
43. C. Goupil, W. Seifert, K. Zabrocki, E. Müller and G. J. Snyder, Thermodynamics of Thermoelectric Phenomena and Applications. *Entropy* **13,** 1481-1517 (2011).
44. G. Min and D. M. Rowe, Ring-structured thermoelectric module. *Semicon. Sci. Techn.* **22,** 880 (2007).

TOC
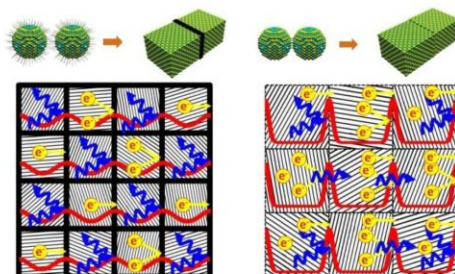
Scheme of the difference interfaces between the grains in the final nanostructured material when is obtained using PbSe-OL or PbSe-LD NCs.

14

SUPPORTING INFORMATION

Influence of the ligand striping on the transport properties of nanoparticle-based PbSe bulk nanomaterials

Doris Cadavid,[a] Silvia Ortega,[a,b] Sergio Illera,[c] Yu Liu,[a] Oscar Juan Durá,[d] Maria Ibáñez,[e,f] Alexey Shavel,[a] Yu Zhang,[a] Antonio M. López,[g] M. A. López de la Torre,[d] Joan Daniel Prades,[c] Germán Noriega,[b] Maksym Kovalenko[e,f] and Andreu Cabot*[a,h]

[a] Catalonia Institute for Energy Research - IREC, 08930 Sant Adrià de Besòs, Barcelona, Spain. E-mail: acabot@irec.cat

[b] Cidete Ingenieros S.L., Anselm Clavé 98, 08800 Vilanova i la Geltrú, Barcelona, Spain

[c] Departament d'Electrònica, Universitat de Barcelona, C. Martí i Franquès 1, 08028 Barcelona, Spain

[d] Departamento de Física Aplicada, Universidad de Castilla-La Mancha, Avd. Camilo José Cela, Edificio Politécnico, ETSII, 13071 Ciudad Real, Spain

[e] Institute of Inorganic Chemistry, Department of Chemistry and Applied Biosciences, ETH Zürich, CH-8093, Switzerland

[f] Empa-Swiss Federal Laboratories for Materials Science and Technology, Dübendorf, CH-8600, Switzerland

[g] Departament d'Enginyeria Electrònica, Universitat Politècnica de Catalunya, EPSEVG, 08800 Vilanova i la Geltrú, Barcelona, Spain

[h] ICREA, Pg. Lluís Companys 23, 08010 Barcelona, Spain

S1

Figure S1: TEM image of the PbSe NPs after ligand displacement with $NaNH_2$.
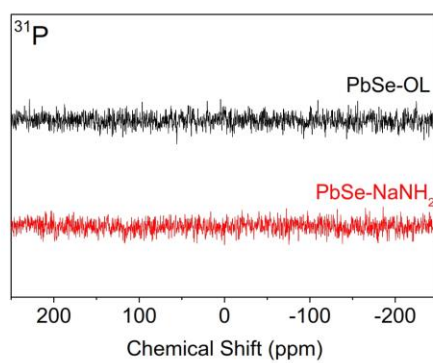
Figure S2: ^{31}P NMR spectra of PbSe-OL and PbSe-NaNH$_2$. There are not any peak that indicates the presence of TOP before or after the ligand displacement. Therefore the ligand that remains attached to the surface of the NCs is the OA.

S2
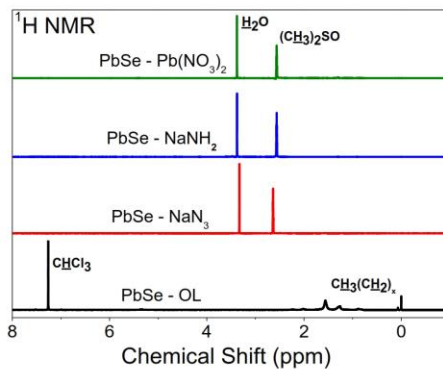
Figure S3: ¹H NMR spectra of PbSe-OL and PbSe-LD. The peaks in the PbSe-OL indicate the presence of $CH_3(CH_2)_x$ from the OL and after the ligand displacement with the different salts the spectra od the NCs only shows the presence of the solvents water and chloroform deuterated.
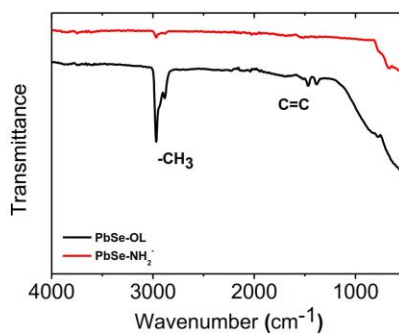
Figure S4: FTIR spectra of PbSe NCs. It is possible to observe that the peaks corresponding to CH_3 or double bonds almost desapear after LD.

S3

Modelling

In the frame of the standard Boltzmann transport equation[1] and the relaxation time approximation (RTA), considering a linear dependence of the band gap with the temperature[2,3] and the same density of states and electron/hole velocity previously used,[2,4,5] σ_i and S_i are given by:

$$\sigma_i = e^2 \int_0^\infty d\varepsilon (-\frac{\partial f_i}{\partial \varepsilon}) \Sigma_i(\varepsilon, T) \qquad (S\ 1)$$

$$S_i = \frac{e}{T\sigma_i} \int_0^\infty d\varepsilon (-\frac{\partial f_i}{\partial \varepsilon}) \Sigma_i(\varepsilon, T)(\varepsilon - \mu)^2 \qquad (S\ 2)$$

$$\Sigma_i = \frac{2}{3} \gamma_i \frac{(2m_i)^{1/2}}{\pi^2 \hbar^3} \left[\varepsilon(1 + \frac{\varepsilon}{E_g})^{3/2} (1 + \frac{2\varepsilon}{E_g})^{-1} \right] \tau_i(\varepsilon, T) \quad (S\ 3)$$

Where γ_i is the degeneracy of the conduction and valence band (i=e,h), μ is the position of the chemical potential, τ_i is the total scattering rate, e is the elemental carrier charge, f_i is the equilibrium Fermi distribution function at temperature T and chemical potential μ, and m_i is the effective mass for each band:

$$m_i = (m_l m_t^2)^{1/3} \qquad (S\ 4)$$

The temperature dependence of the parameters described above determines the temperature dependence of the transport coefficients, σ and S. In narrow bang-gap semiconductors, such as PbSe, the dependence of the energy on crystal momentum deviates from a quadratic dependence. The energy dependent effective mass reflects this non-parabolic trend. In the Kane model the energy dispersion is given by:[6]

$$\varepsilon_{\vec{k}} \left(1 + \frac{\varepsilon_{\vec{k}}}{E_g}\right) = \frac{\hbar^2}{2} \left(\frac{2k_t^2}{m_t} + \frac{k_l^2}{m_l}\right) \qquad (S\ 5)$$

where E_g is the band gap, $\hbar$ is the Plank constant, and m_l and m_t are the longitudinal and transversal effective masses, respectively. The charge carrier concentrations, n and p, given by the Kane model are:

$$n, p = \frac{\sqrt{2}}{\pi^2 \hbar^3} \gamma m^{3/2} \int_0^\infty \frac{\left[\varepsilon(1 + \frac{\varepsilon}{E_g})\right]^{1/2} \left(1 + \frac{2\varepsilon}{E_g}\right)}{\exp\left(\frac{\varepsilon - \mu}{k_B T}\right) + 1} d\varepsilon \qquad (S\ 9)$$

where k_B is the Boltzmann constant. The chemical potential strongly depends on the doping concentration and its position was obtained by numerically solving the neutrality equation taking into account the acceptor/donor doping levels:

$$n = p + N_d^+ \text{ for an n-type semiconductor} \qquad (S\ 10a)$$

$$p = n + N_a^- \text{ for a p-type semiconductor} \qquad (S\ 10b)$$

Assuming that the scattering events are independent with each other, the Mathiessen's sum rule can be used

$$\frac{1}{\tau_{tot}^i} = \frac{1}{\tau_a} + \frac{1}{\tau_o} + \frac{1}{\tau_{po}} + \frac{1}{\tau_b} \qquad \text{(S 11)}$$

where τ_{tot}^i is the total relaxation time, and the τ_a, τ_o, τ_{po} are the acoustic phonons, the optical phonons, the polar optical phonons, and the barrier scattering relaxation times, respectively. Here, i=(e,h) represents the electrons (e) and holes (h).[7,8,9] The most relevant charge scattering mechanisms in a single crystal thermoelectric material are the scattering with acoustic, optical and polar optical phonons. In nanostructured materials the charge carrier scattering at crystal interfaces may become dominant. Following previous works,[5,10] we modelled the grain interfaces as rectangular potential barriers, which charge carriers traverse with a transmission probability P and a scattering time:

$$\tau_b(\varepsilon) = \frac{1}{v}\frac{P(\varepsilon)L}{1 - P(\varepsilon)} \qquad \text{(S 12)}$$

where

$$P(\varepsilon) = \begin{cases} \left[1 + \frac{E_b \sinh^2\left[\sqrt{\frac{2mE_b w^2}{\hbar^2}\left(1 - \frac{\varepsilon}{E_b}\right)}\right]}{4\varepsilon\left(1 - \frac{\varepsilon}{E_b}\right)} \right]^{-1} &; \varepsilon < E_b \\[4ex] \left[1 + \frac{E_b \sin^2\left[\sqrt{\frac{2mE_b w^2}{\hbar^2}\left(\frac{\varepsilon}{E_b} - 1\right)}\right]}{4\varepsilon\left(\frac{\varepsilon}{E_b} - 1\right)} \right]^{-1} &; \varepsilon > E_b \end{cases} \qquad \text{(S 13)}$$

The probability term takes into account the barrier height E_b and width w. L is the mean crystal domain size and v is the average charge carrier velocity:

$$v = \sqrt{\frac{2\varepsilon(1 + \varepsilon/E_g)}{m(1 + 2\varepsilon/E_g)^2}} \qquad \text{(S 14)}$$

S5

Parameter	Value
ε_0	204
ε_∞	25
C	$4\text{X}10^{10}$
$\hbar\omega_0$	16.7
a	6.12
ρ	8270
E_{ac}	3.5-7.5
E_{0c}	2.5-7.5
$K_a = K_0$	1
E_g	$125 + \sqrt{400 + 0.256\, T^2}\ meV$
n for LE	$2.2\text{X}10^{19}\ cm^{-3}$
n for OL	$5\text{X}10^{15}\ cm^{-3}$
m_e	0.05
m_h	0.06
$Deg_e = Deg_h$	4

Table S1. Parameters used in the simulation.

References

1. Ziman, J. M. *Principles of the theory of solids*. (University Press, 1972).
2. S. Ahmad and S. D. Mahanti, *Phys. Rev. B*, 2010, **81**, 165203.
3. M. Baleva, T. Georgiev, and G. Lashkarev, *J. Phys.: Condens. Matter*, 1990, **2**, 2935.
4. C. J. Vineis, T. C. Harman, S. D. Calawa, M. P. Walsh, R. E. Reeder, R. Singh, and A. Shakouri, *Phys. Rev. B*, 2008, **77**, 235202.
5. J. Zhou, X. Li, G. Chen, and R. Yang, *Phys. Rev. B*, 2010, **82**, 115308.
6. J. J. Harris and B. K. Ridley, *Journal of Physics and Chemistry of Solids*, 1972, **33**, 1455–1464.
7. Y. I. Ravich, B. A. Efimova, and V. I. Tamarchenko, *Plenum, New York*, 1970.
8. D.M. Freik, L.I. Nykyruy, and V.M. Shperun, *Semiconductor Physics, Quantum Electronics & Optoelectronics*, **5**, 362–367.
9. Y. I. Ravich, B. A. Efimova, and V. I. Tamarchenko, *physica status solidi (b)*, 1971, **43**, 11–33.
10. A. Popescu, L. M. Woods, J. Martin, and G. S. Nolas, *Phys. Rev. B*, 2009, **79**, 205302.

Chapter 4   Thermoelectrics and nanomaterials integration

Fourth objective of this thesis was to go beyond of the fabrication of nanomaterials and devices and arrive to its integration. To reach it and finalize this dissertation, this chapter is focused on two system integration: of a TE device, and of a NP-based thermal sensor. We produced an autonomous NP-based moisture sensor system powered with a conventional TE device that was tested in-field.[109]

The system is powered by the TE generator, taking advantage of the higher temperatures present at the surface of the ground than deep inside. On the other hand, PbS colloidal NPs are used to build thermosensitive resistors since the electrical resistance of these NPs films depend on the temperature with a proper thermal coefficient. Thanks to the availability of NP-based TE inks developed under solution-processed techniques, these were deposited onto ceramic plates

by means of two solution-processed deposition techniques: spraying and brushing. Spray deposition provided better control of the thickness of the films rather than paint-brushing, even also higher resistance values. Even though, brush-painted films could be also used with the proper off-set into the circuit. Moreover, in the work is presented a low-power electronics system able to manage the power consumption and overall working operation of this autonomous sensor.

This system shows the real possibilities that TE devices and solution-processed techniques present for the fabrication of nanomaterials and devices of different kind. Together with this small example of integration, the PhD student has been working during these years in different applications and examples of TE integration, from temperature control in a hydrogen autonomous storage system to the development of a low-power consumption air condition system for electric vehicles (see CV). These examples can be translated into the confirmation of the existence of a real market for TE devices. Once high performance materials are designed, it is only necessary to point the application itself and go deeper into it to understand its necessities and challenges and adapt the technology in the best manner.

ELSEVIER

Autonomous soil moisture sensor based on nanostructured thermosensitive resistors powered by an integrated thermoelectric generator

CrossMark

Pedro C. Dias [a,b,*], Doris Cadavid [b], Silvia Ortega [b], Alejandro Ruiz [b], Maria Bernadete M. França [d], Flavio J.O. Morais [a], Elnatan C. Ferreira [a], Andreu Cabot [c,b]

[a] Department of Semiconductors, Instruments and Photonics, DSIF/FEEC, University of Campinas, Av. Albert Einstein 400, Campinas, SP 13083-820, Brazil
[b] Catalonia Institute for Energy Research (IREC), Jardins de les Dones de Negre 1, Barcelona 08930, Spain
[c] Institució Catalana de Recerca i Estudis Avançats (ICREA), Jardins de les Dones de Negre 1, Barcelona 08930, Spain
[d] State University of Londrina, UEL, Londrina, PR 86057-970, Brazil

ABSTRACT

An autonomous single heat pulse probe porous ceramic soil moisture sensor powered by a thermoelectric generator (TEG) is presented. The sensor uses nanostructured thermosensitive resistors fabricated on the same ceramic substrate of the TEG. The nanostructured resistors, fabricated by printing PbS quantum dots, present a very high thermal coefficient (-16×10^3 ppm/°C) and, used in a bridge configuration with conventional precision and low thermal coefficient SMD metal film resistors, result in a high sensitivity temperature sensor. A laboratory prototype of the sensor showed a voltage variation of 2.4 mV in the output of the bridge when the volumetric water content of the soil changed from 5% to 40%. To complete the autonomous system, we designed an ultra low-power electronic interrogator which, when powered only by the 3 F supercapacitor of the integrated TEG energy harvesting system, was able to take daily measurements up to 5 days without harvesting energy.

© 2016 Elsevier B.V. All rights reserved.

1. Introduction

Evaluation of soil water content is extremely important in advanced irrigation management systems [1]. Heat dissipation sensors, which provide estimation of the water content in soil from heat capacity measurements, are simple to use, low-cost and easy to install, being one of the most employed type of sensor used in crop fields [2]. There are two types of heat dissipation water moisture sensors: the single heat pulse probe (SHPP) [3,4] and the dual pulse heat probe (DPHP) [5,6].

Diagrams of the SHPP (with and without porous ceramic) and the DPHP soil moisture sensors are presented in Fig. 1. Both types of sensors use a heat pulse to measure the thermal conductivity of the material that surrounds the sensor. The probes used

in these sensors are made with a hypodermic tube, filled with thermal conductive epoxy, which houses the sensor's passive and active devices. In the DPHP, one of the probes contains a heater (usually a resistor) and the other probe has a temperature measurement device. A heat pulse is applied in the heating probe (usually during 6 s–8 s), and the maximum temperature measured in the other probe can be related to the soil water content [7]. In the SHPP, both heating and temperature sensing elements are placed in the same probe. The heat pulse is applied for a fixed period of time (usually in the order of 20 s–30 s) and, at the end of this period of time, the temperature rise measured in the temperature sensing element can be related to the soil water content [8].

SHPP sensors suffer from accuracy problems if the contact between the probe and the soil is not perfect. To overcome this weakness, several techniques to manufacture SHPP sensors consisting of a heating element and a temperature sensor embedded within a porous ceramic block have been proposed [9,10]. In sensors with a porous ceramic, independently of the quality of the sensors' contact with the soil, water flows between the porous ceramic and the soil until an equilibrium is reached. By measuring the thermal conductivity of the moistened porous ceramic, accurate and

* Corresponding author at: Department of Semiconductors, Instruments and Photonics, DSIF/FEEC, University of Campinas, Av. Albert Einstein 400, Campinas, SP 13083-820, Brazil.
E-mail addresses: pcdias@demic.fee.unicamp.br (P.C. Dias), dcadavid@irec.cat (D. Cadavid), sortega@irec.cat (S. Ortega), aruizr@irec.cat (A. Ruiz), mbmorais@uel.br (M.B.M. França), fjom@demic.fee.unicamp.br (F.J.O. Morais), elnatan@demic.fee.unicamp.br (E.C. Ferreira), acabot@irec.cat (A. Cabot).
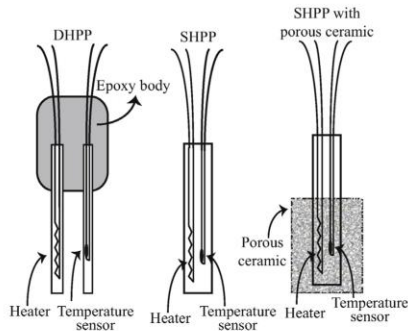
Fig. 1. Basic diagrams of the SHPP and DPHP sensors.

repetitive estimations of the water content in the soil surrounding the sensor can be obtained.

This paper presents an autonomous SHPP porous ceramic sensor, based on a bridge of semiconductor nanoparticle resistors monolithically integrated with a bismuth telluride thermoelectric generator (TEG). Besides their very high thermal coefficient (TC), an important advantage of nanoparticle-based resistors is that they can be fabricated on ceramic substrates using low-cost spray or paint-on techniques.

A basic schematic of the proposed autonomous sensor system is presented in Fig. 2. The energy harvester consists of a conventional TEG that operates from the temperature differential between a point deep into the soil and an anodized aluminium panel which is exposed to the sun radiation. The system operates using the same principle presented in [11], but instead of using a phase change material to store the heat absorbed during the day, the heat is stored into the soil.

A prototype of the energy collector was built using a 40 cm×40 cm black anodized aluminium flat-panel. To transfer the heat from the flat-panel to the TEG, which was buried 40 cm deep into the soil, a solid aluminium bar with 4 cm×4 cm area was used. The system was able to collect 34.1 J of energy during one sunny winter day, in August 12th, 2014, at Campinas, SP – Brazil, Latitude: 22° 54′. This energy is enough to charge a 3 F supercapacitor up to 5 V. An ultra-low-power electronic interrogator designed to operate with the TEG energy harvesting system was implemented to test the autonomous nanoparticle soil moisture sensor.
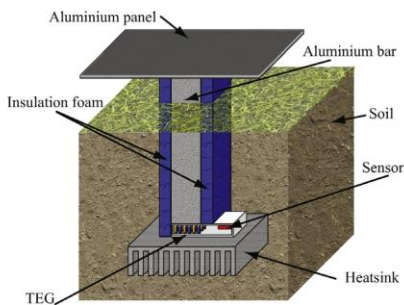

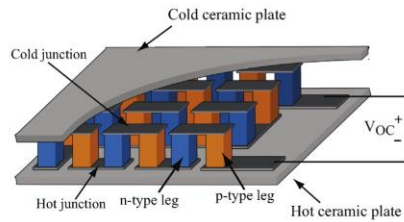Fig. 2. Basic schematic of the proposed autonomous sensor system.

Fig. 3. Schematic view of a thermoelectric generator showing the n-type and p-type thermoelectric legs which are electrically connected in series and thermally arranged in parallel, sandwiched between two ceramic plates.

2. Principle of operation of a SHPP sensor

The porous ceramic SHPP sensor consists of a heating and a temperature sensing elements embedded in a body of a porous material like ceramic [9] or felt [12]. The sensor's principle of operation is based on the measurement of the thermal conductivity of a porous material, which is dependent on the amount of water present within the porous body. A heat pulse of fixed duration is applied to the sensor and, at the end of the pulse, the temperature rise caused by the heat exchange between the heater element and the porous body is measured.

The temperature change ΔT measured in the sensing element when a heat pulse of duration $t_f - t_0$ is applied can be approximated by [8]:

$$\Delta T = T_f - T_0 = -\frac{q}{4\pi k} \ln(t_f - t_0) \qquad (1)$$

where T_0 is the initial temperature (measured at time t_0), T_f is the final temperature (measured at time t_f), q is the heat input (W) and k is the thermal conductivity of the medium ($W°C$). From Eq. (1) we can write:

$$k = -\frac{q}{4\pi \Delta T} \ln(t_f - t_0) \qquad (2)$$

Thus, for a fixed heat pulse duration $t_f - t_0$, by measuring the value of ΔT it is possible to estimate the thermal conductivity k of the system (porous ceramic + absorbed water) and, therefore, after proper calibration, correlate this value of ΔT with the soil water content. Applying an 85 mW pulse with 30 s of duration to the heater, the value of ΔT measured in a typical SHPP sensor is about 1–2 °C [9].

3. Design of the autonomous sensor integrated in a TEG

3.1. Conventional TEGs

Conventional TEGs modules are fabricated by soldering, between two ceramic plates, couples of n-type and p-type thermoelectric elements electrically in series and thermally in parallel, as shown in Fig. 3. The open circuit voltage of a TEG is given by [13]:

$$V_{OC} = N\alpha_{np} \frac{R_{\theta(n,p)}}{R_\theta + R_{\theta(n,p)}} \Delta T \qquad (3)$$

where N is the number of thermocouples elements, α_{np} is the overall Seebeck coefficient between p and n materials (given by $\alpha_p - \alpha_n$), R_θ is the thermal resistance of the ceramic plates, $R_{\theta(n,p)}$ is the thermal resistance of the thermoelectric elements and ΔT is the temperature difference between hot and cold sides of the TEG.

Typical high output voltage TEGs contain 254 thermocouples and provide a Seebeck coefficient of about 100 mV/°C. Examining Eq. (3) we see that V_{OC} is proportional to N, thus, if it is desired to
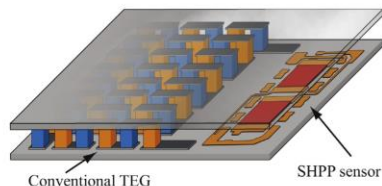
Fig. 4. A longer ceramic plate is used to fabricate the soil moisture sensor integrated with the TEG.

Table 1
Thermal coefficient of nanostructured materials.

Material	TC (ppm/°C)
$Cu_2ZnSnSe_4$	−1100
Cu_2GeSe_3	−1500
$AgSbSe_2$	−1600
Ag_2Te	−3600
Ag_2Se	−5300
$Bi_2S_{3-x}Te_x$	−10, 500
PbS	−16, 000

obtain a high output voltage V_{OC} for low values of ΔT, the number of thermocouples N has to be increased.

From Eq. (3) it is also noticed that, for a given number of couples N and a ceramic plate material with a given value of R_θ, the only parameter that can be changed in order to increase the TEG output voltage V_{OC} is the thermal resistance of the couples, $R_{\theta(n,p)}$, which has to be increased. To increase the number of thermocouples, reduce the TEG area and increase $R_{\theta(n,p)}$, relatively long thermoelectric legs with small area are necessary.

3.2. Integration of the sensor with a TEG

To build a sensor integrated with a conventional TEG, we propose to increase the ceramic plates, as shown in Fig. 4, and use this extra area to build the complete SHPP soil water content sensor. As, typically, thermoelectric elements have 1 mm^2 of area and 3 mm–5 mm in height, this is the room (between the two ceramic plates) that is available for the fabrication of the complete sensor, which includes standard surface-mount devices (SMD) components.

4. Temperature sensor based on nanoparticle thermosensitive resistors

Since the values of ΔT in SHPP sensors are generally low (1°C–2°C), if a 1% resolution is required in the measurement of the volumetric soil moisture in the agriculture range (5%–40%), a temperature measurement technique with very high accuracy and high resolution (0.01 °C) is mandatory [7]. Therefore, to simplify the design of the interrogation circuits, a sensor with high thermal sensitivity is necessary.

In the developed SHPP soil water content sensor, the heating and the temperature sensing elements are implemented with the configuration shown in the schematic diagram of Fig. 5. The temperature measurement is based on the voltage variation of two resistive voltage dividers implemented with very low thermal coefficient (TC) resistors R1–R2 (TC = 10 ppm/°C) and two thermosensitive resistors (R3–R4).

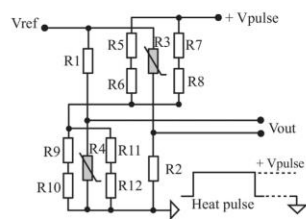**Fig. 5.** Electrical schematic of the soil moisture sensor.

The bridge configuration was used because, when compared to a single resistor divider, the differential output voltage variation is almost doubled. The heating elements are precision (±0.05 % tolerance) with very low TC (10 ppm/°C) SMD resistors (R5–R12), and the heat pulse is generated by applying a constant voltage source $+V_{pulse}$ across each pair of these resistors. We used four heating resistors around each thermosensitive resistor in order to obtain a better uniformity of the heat distribution along the substrate.

4.1. Nanoparticle thermosensitive resistors

We tested several nanomaterials to produce the thermosensitive resistors. Table 1 presents the tested nanostructured materials which showed a |TC|> 1000 ppm/°C.

As it can be seen in Table 1, PbS nanostructured films produced by printing PbS nanocrystals with sizes in the quantum refinement regime, i.e., quantum dots, were identified as the best candidate for the application, since they presented a very high TC and required simple processing, involving no post-processing. PbS quantum dot films, after being sprayed or painted on the ceramic material, required a simple 2 min baking at 80 °C in air in order to evaporate the solvent.

PbS quantum dots used to fabricate the thermosensitive resistors were prepared as follows [14]. In a typical synthesis, 4.46 g of lead (II) oxide (20 mmol, 99.9%) and 50 ml of oleic acid (0.159 mol, 90%) was mixed with 100 ml of 1-octadecene (0.312 mol, 90%). This mixture was heated to 130°C for 1 h under vacuum to form a lead oleate complex. Then the solution was flushed with Ar, and the temperature was raised to 210°C.

At this temperature, a sulfur precursor, prepared by dissolving 0.64 g of elemental sulfur (20 mmol, 99.998%) in 20 ml of distilled oleylamine (0.061 mol), was rapidly injected. The reaction mixture was maintained between 195°C and 210°C for 5 min and then quickly cooled down to room temperature, using a water bath. PbS nanocrystals were purified in an inert atmosphere by multiple precipitation/re-dispersion steps, using methanol as a non-solvent and chloroform as solvent. Afterwards, NH$_4$SCN was used to remove the electrically insulating surface capping ligands used to control the nanocrystal growth.

In a typical procedure, PbS nanocrystals (300 mg) were dispersed in 10 ml of chloroform. Then, 2 ml of a 0.1 M NH$_4$SCN solution in methanol were added and the solution was mixed with a vortex during 2 min. After this time, PbS quantum dots were precipitated by centrifugation at 30,000 rpm.

This procedure was repeated twice and finally nanocrystals were thoroughly purified using chloroform to remove the remaining organic species. Finally, PbS quantum dots were precipitated and re-dispersed in DMSO. A representative transmission electron microscopy (TEM) micrograph and the related size distribution histogram, the XRD pattern and the UV–vis spectrum of the PbS quantum dots used in this work are shown in Fig. 6.
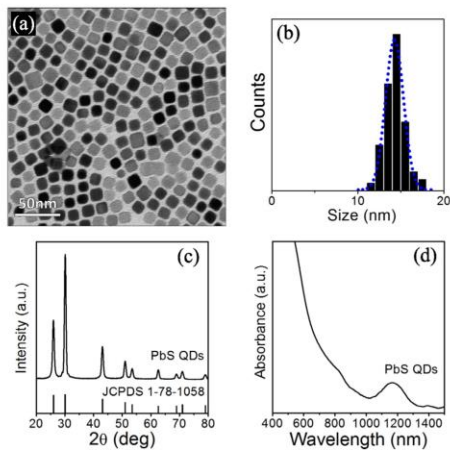
Fig. 6. Characterization of the PbS quantum dots: (a) TEM micrograph; (b) size distribution histogram; (c) XRD pattern; and (d) UV–vis spectrum.

4.2. Thermal characterization of the PbS quantum dots resistors

We tested two solution-processing technologies to fabricate the PbS quantum dot resistors on an alumina substrate: spray deposition and paint-on. Fig. 7 displays the temperature dependence of the resistance measured for resistors fabricated by spray and paint-on techniques. The measured thermal coefficient (TC) of the PbS quantum dot resistors was −1.6% /°C in both cases.

Application of the film with a spray system allowed for the fabrication of thin high resistivity films and provided a much better control of the film thickness than painting. The painted resistors showed a poor repeatability and thus a poor matching between two equal resistors (30% mismatch). This could cause an unbalance in the output of the bridge.

To solve this problem, the off-set voltage need to be cancelled with the appropriate circuit in the interrogator. For example, the microcontroller responsible for the A/D conversion in the interrogator can measure the value of V_{os} and subtract it from the measured values of V_{out}. After cancellation of the off-set voltage, a bridge with 30% mismatch in the thermosensitive resistors would present a
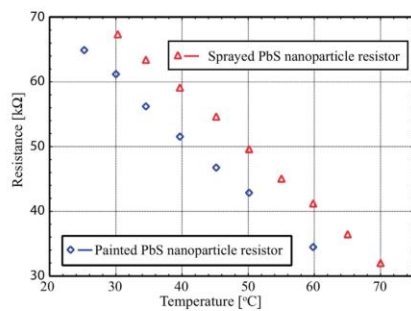

Fig. 7. Measured variation of the PbS resistors with the temperature.
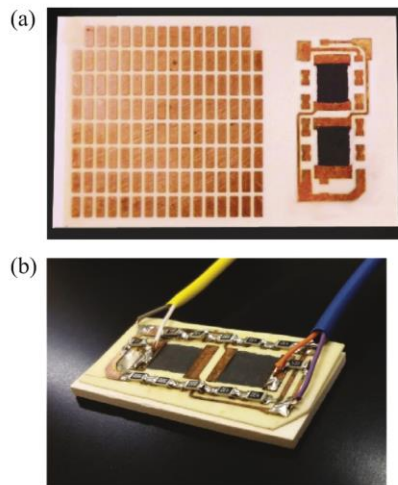

Fig. 8. (a) Photograph of the ceramic plate with TEG's soldering pads and the sensor circuit with thermosensitive quantum dots resistors; and (b) complete sensor, with a porous ceramic block glued to the bottom of the substrate.

full-scale error of only 0.0028% when the variation of temperature in the bridge is 1 °C.

4.3. Fabrication of the sensor integrated with the TEG

To fabricate the integrated sensor, we used a 96% aluminum oxide substrate (from Stellar Industries Corp) with a thickness of 0.38 mm and a 127 μm direct bonded copper foil. To define the TEG soldering pads and the interconnection traces between the components of the sensor, a conventional dry film photoresist (used for the manufacturing of PCBs) was applied to the substrate. Then the photoresist was patterned through a photofilm mask using UV light, developed and stripped. The ceramic plate with the patterned copper tracks received a new layer of dry film photoresist, and the nanoparticle resistors photofilm mask was exposed and developed, preparing the substrate to receive the spray (or paint-on) of the PbS quantum dot solution. The nanocrystal solution is applied to the ceramic, baked and the photoresist is then stripped. A photograph of the hot side ceramic plate (which contains the semiconductor nanocrystal sensor) ready for receiving the solder of the TEG's legs, SMD resistors and external connection wires is shown in Fig. 8(a).

After the SMD resistors, the TEG n-type and p-type thermoelectric legs and the external wires were soldered, an RTV silicone was applied, providing the perimeter sealing of the device. To eliminate the heat transfer between the sensor and the TEG, a slot was cut (with a dicing saw) in the ceramic plate which contains the sensor, and the slot was filled with RTV silicone. To finish the sensor, a 2 mm porous ceramic from Hidrosense, used in agricultural soil moisture sensors, was glued with a highly conductivity epoxy (Epotherm 130, from Transene, Inc.) exactly under the sensor's area.

Since one of the main interests of the work was to test and characterize the quantum dot sensor, we prepared several sensors on a small pre-cut ceramic plate, in order to make it easy to manipulate the sensor in laboratory and perform soil moisture tests. A complete sensor (with the porous ceramic glued to it) is shown in Fig. 8(b).

5

5. Interrogator circuit

Assuming that all resistors in the bridge presented in Fig. 5 are matched and equal to R_0, if a change in temperature causes a variation equal to ΔR_0 in the thermosensitive resistors (R3–R4), V_{out} is written as:

$$V_{out} = V_{REF}\frac{\Delta R_0}{2R_0 + \Delta R_0} \tag{4}$$

If the value of a thermosensitive resistor at temperature T_0 is R_0, and it is linearly dependent with temperature with a TC given by

$$\gamma = \frac{1}{R_0}\frac{dR_0}{dT}, \tag{5}$$

the expression that describes its value as a function of the temperature is written as:

$$R(T) = R_0 + R_0\gamma(T - T_0) \tag{6}$$

Thus, replacing ΔR_0 in Eq. (4) by $[R_0\gamma(T - T_0)]$, the sensitivity $S = \delta V_{out}/\delta T$ of the soil moisture sensor can be expressed as:

$$\frac{\delta V_{out}}{dT} = \frac{V_{REF}2R_0{}^2\gamma}{4R_0{}^2\left(1 + \gamma(T - T_0) + \frac{1}{4}\cdot\gamma^2(T - T_0)^2\right)} \tag{7}$$

Since thermosensitives resistors have $\gamma \ll 1$ and for SHPP sensors with porous ceramic bodies the maximum value of $(T - T_0)$ are in the range $1\,°C$–$2\,°C$, we can approximate

$$\left(1 + \gamma(T - T_0) + \frac{\gamma^2(T - T_0)^2}{4}\right) \approx 1 \tag{8}$$

and, therefore, S can be written as:

$$S = \frac{\delta V_{out}}{\delta T} \approx \frac{V_{REF}}{2}\gamma \tag{9}$$

Therefore, since the TC of the PbS thermosensitive resistors is $\gamma = 0.016\,°C^{-1}$, if a voltage reference $V_{REF} = 1.2\,V$ is used and a full scale $\Delta T = 1\,°C$ is achieved at the end of the heat pulse, a $\Delta V_{out} \approx 9.6\,mV$ would be obtained in this condition.

To test the performance of the soil water content sensor, an interrogator circuit, based on a microcontroller which has a 12 bit A/D converter (MSP430FR5959 from Texas Instruments) was designed and implemented. The MSP430FR5959 is an ultra low-power IC, as required by the interrogation system of an autonomous system powered by thermoelectric energy harvesting. The microcontroller performs the differential A/D conversion of the bridge output signal and controls both the measurement sequence and the timing of the system.

The schematic with the block diagram of the interrogator is presented in Fig. 9. An ultra low-power power management circuit, which has a current consumption of less than 0.9 μA was implemented to power the sensor's system. The circuit is based on the work presented in [15], but it uses a LTC3109 from Linear Technology, an auto-polarity switching dc-dc converter, since it is possible to harvest energy during the day and the night, when respectively positive and negative voltages are available in the TEG.

The average current consumption of the complete system (energy harvesting circuit, sensor and interrogator) is only 20.1 μA, and when powered by a 3 F supercapacitor the system can operate 5 days without harvesting any energy from the TEG when one soil water content measurement is taken per day.

The measurement sequence is as follows: firstly the microcontroller turns on the voltage reference $V_{REF} = 1.2\,V$, biasing the bridge. After $V_{REF} = 1.2\,V$ is on, the system waits 10 ms to guarantee that V_{REF} is stable, and then a 290 mW heat pulse is applied during 30 s to the heating elements.

The heat pulse is obtained by applying a 5 V pulse (Vpulse) on the heating resistors, which have a total equivalent resistance of
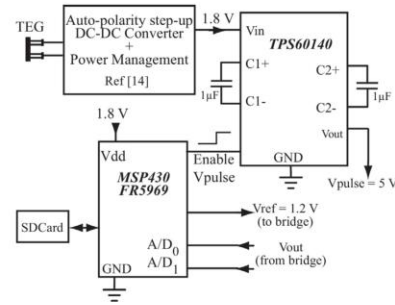

Fig. 9. Basic block diagram of the interrogator.

86 Ω. The 5 V is obtained with a charge pump regulator (TPS60140 from Texas Instruments) powered with 1.8 V in its input. At this point, we developed two different measurement strategies: one for characterization of the sensor in laboratory, and one for operation in the field.

In laboratory, after V_{REF} is stable the differential A/D conversions are started, and one measurement is taken every 1 s (actually a mean value of 20 A/D conversions taken during 10 ms). A total of 34 points are measured: four points before the heating resistors are turned-on by the microcontroller, and 30 points (30 s) under the influence of the heat pulse. In this interrogator, the measured results are stored in a SD card, so we can analyse the measured data in a computer.

Irrigation of a plantation is made only once per day, usually before 10:00 AM or after 4:00 PM, because evapotranspiration (the loss of water by transpiration of plants and by evaporation from soil and plant surfaces) can cause a great loss of water if the irrigation is made during the hottest hours of the day (10:00 AM to 4:00 PM). Soil moisture sensors are used to provide information to the irrigation management system if the soil has reached a level of water content that requires the irrigation system to be turned-on.

For example, the culture of beans requires soil moistures between 28% and 31%. It is also important to notice that once the soil reached a water content level of 31%, it will take many days before it reaches the lower limit and an irrigation procedure is required. In a complete cycle of a beans culture (monitored during 83 days, from seed planting to harvesting), irrigation was applied only in 15 days, and only once the lower water content limit of 28% was reached (on day 41, after an irrigation was done on day 31) [16].

It is important to observe that there is a delay time required for hydraulic equilibrium of the water in the soil and ceramic, which depends on both the magnitude of the water potential gradient and the hydraulic conductivity. However, in porous ceramics used in soil moisture heat dissipation sensors the delay time required for hydraulic equilibrium of the water in the soil and the ceramic is in the order of minutes or tens of minutes [9], and this delay can be completely neglected.

In the field, to save power, the system is kept in sleep mode practically during the whole day and, at a programmed time, it wakes up only during 31 s, to perform a soil water content measurement. Immediately after the application of the heat pulse ($t_0 = 100\,ms$) and just before the end of the heat pulse ($t_f = 30.1\,s$), differential A/D conversions are performed and the values T_0 and T_f are calculated. With T_0 and T_f, the value of ΔT is calculated and a soil moisture evaluation is obtained. After that, the system returns to sleep mode.
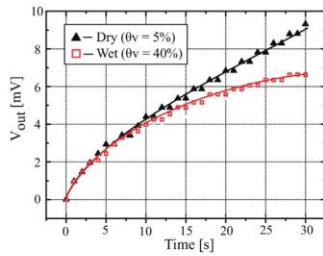
Fig. 10. Measured output voltage of the sensor, for soil water contents 5% and 40%, as a function of time.

Of course the SD card would not be available in a system applied in a crop field since, in the field, this autonomous sensor system would control an irrigation valve and, after performing a soil moisture measurement at a pre-programmed daily schedule, it would decide if it is necessary or not to irrigate the area surrounding it.

6. Experimental results

The soil water content sensor was tested in laboratory. A clay loam soil was dried in an oven and the sensor was inserted into the soil. The soil was wetted with controlled volumes of water to create volumetric moistures of $\theta_v = 5\%$ and $\theta_v = 40\%$, simulating the typical range of agriculture soil water content. The sensor was measured in these two conditions (5% and 40% of soil volumetric water content), with a heat pulse applied for 30 s. The voltage measured in the output of the bridge during the heat pulse, for both volumetric water contents, is presented in Fig. 10.

In the field, even though the sensor is buried at a depth of 40 cm, there is a small variation of the soil temperature [18], and this has to be compensated for in the sensor readings. Thus, the calibration procedure for porous ceramic heat dissipation soil moisture sensors described in [19] must be used.

To test the repeatability of the sensor, measurements were taken with the sensor out of the soil, with a controlled amount of water absorbed into the ceramic. The measurements, performed at the same temperature, with a controlled amount of water absorbed into the porous ceramic, were extremely consistent and the results fell within ± 1 LSB of the A/D converter (± 0.3 mV).

As it can be observed in the plot of Fig. 10, in dry conditions, after 30 s of heat pulse, the measured value of V_{out} in the output of the bridge was approximately 9.5 mV. According to Eq. (9), we conclude that the temperature increase in the bridge when $V_{out} = 9.5$ mV was $\Delta T = 0.99\,^\circ$C. When the volumetric water content changes from $\theta_v = 5\%$ to $\theta_v = 40\%$, the variation of the output voltage measured after 30 s of heat pulse is approximately 2.4 mV.

Although porous ceramic heat dissipation soil moisture sensors are not linear, the literature usually defines a sensitivity S, in $^\circ$C per unity change (m^3 m^{-3}), which is calculated with the ΔT measured at the extreme points of the θ_v range (5% and 40% in our case) [7,10,17]. Using this definition of sensitivity, when compared to the state-of-the-art silicon integrated dual probe heat pulse sensor presented by Valente et al [7], which has a sensitivity of $S = 1.95\,^\circ$C per unity change (m^3 m^{-3}) with an 8 J heat pulse applied when measured with $\theta_v = 5\%$ and $\theta_v = 40\%$, the developed autonomous SHPP sensor presents a better performance, $S = 2.83\,^\circ$C per unity change with a heat pulse of 8.7 J, measured under the same conditions.

If a figure of merit Γ is defined as the ratio of the sensitivity per the energy of the heat pulse, we have a 37.5% increase in Γ, since the developed sensor has $\Gamma = 0.33\,^\circ$C J^{-1} per unity change while the

silicon integrated sensor in [7] presents $\Gamma = 0.24\,^\circ$C J^{-1} per unity change.

7. Conclusions

An autonomous SHPP soil water content sensor based on nanostructured thermosensitive resistors integrated with a conventional TEG was developed. The fabrication process of the nanoparticle based sensor is compatible with the conventional TEG fabrication steps. The developed sensor was tested in laboratory and the presents a sensitivity $S = 2.83\,^\circ$C per unity change (m^3 m^{-3}) when driven by a low power (290 mW) heat pulse during 30 s. An ultra-low-power harvesting and interrogator circuit was developed and when the sensor is buried into the ground, attached to the heatsink end of a solar flat-panel collector, it can harvest all the energy required for its operation from the environment. This type of integration opens the doors to novel developments in the area of autonomous nanoparticles integrated sensors which can harvest the energy necessary to their operation from environmental temperature gradients. The autonomous system, when powered by a 3 F supercapacitor, can operate 5 days without harvesting energy from the TEG when one measurement is taken per day.

References

[1] X. Dong, C. Vuran, S. Irmak, Autonomous precision agriculture through integration of wireless sensor networks with center pivot irrigation systems, Ad Hoc Netw. 11 (2013) 1975–1987.
[2] Keith L. Bristow, Ronald D. Whit, Gerard J. Kluitenberg, Comparison of single and dual probes for measuring soil thermal properties with transient heating, Aust. J. Soil Res. 32 (1994) 447–464.
[3] J.H. Norikane, J.J. Prenger, D.T. Rouzan-Wheeldon, H.G. Levine, A comparison of soil moisture sensors for space flight applications, Appl. Eng. Agric. 21 (2005) 211–216.
[4] Pedro C. Dias, Roque Wellington, Elnatan C. Ferreira, José A.Siqueira Dias, Proposal of a novel heat dissipation soil moisture sensor, in: CSS'11 Proceedings of the 5th WSEAS International Conference on Circuits, Systems and Signals, 2011, pp. 124–127.
[5] G.S. Campbell, K. Calissendorff, J.H. Williams, Probe for measuring soil specific heat using a heat-pulse method, Soil Sci. Soc. Am. J. 55 (1991) 291–293.
[6] A. Valente, R. Morais, A. Tuli, J.W. Hopmans, G.J. Kluitenberg, Multi-functional probe for small-scale simultaneous measurements of soil thermal properties, water content, and electrical conductivity, Sens. Actuators A 132 (2006) 70–77.
[7] A. Valente, R. Morais, C. Couto, J.H. Correia, Modeling, simulation and testing of a silicon soil moisture sensor based on the dual-probe heat-pulse method, Sens. Actuators A 115 (2004) 434–439.
[8] S. Shiozawa, G. Campbell, Soil thermal conductivity, Remote Sens. Rev. 5 (1990) 301–310.
[9] Campbel, 229 Heat Dissipation Matric Water Potential Sensor Instruction Manual, 2006.
[10] Pedro.C. Dias, Roque Wellington, Elnatan C. Ferreira, Jose A.Siqueira Dias, A high sensitivity single-probe heat pulse soil moisture sensor based on a single *npn* junction transistor, Comput. Electron. Agric. 96 (2013) 139–147.
[11] Amen Agbossou, Qi Zhang, Gael Sebald, Daniel Guyomar, Solar micro-energy harvesting based on thermoelectric and latent heat effects. Part I: theoretical analysis, Sens. Actuators A 163 (2010) 277–283.
[12] L. Matile, R. Berger, D. Wächter, R. Krebs, Characterization of a new heat dissipation matric potential sensor, Sensors 13 (2013) 1137–1145.
[13] W. Glatz, S. Muntwyler, C. Hierold, Optimization and fabrication of thick flexible polymer based micro thermoelectric generator, Sens. Actuators A 132 (2006) 337–345.

Thermoelectrics and nanomaterials integration

7

[14] M. Ibáñez, R. Korkosz, Z. Luo, P. Riba, D. Cadavid, S. Ortega, A. Cabot, M. Kanatzidis, Electron doping in bottom-up engineered thermoelectric nanomaterials through HCl-mediated ligand displacement, J. Am. Chem. Soc. 137 (12) (2015) 4046–4049.

[15] Pedro C. Dias, Flavio O. Morais, Maria B. França, Elnatan C. Ferreira, Andreu Cabot, José A.Siqueira Dias, Autonomous multi-sensor system powered by a solar thermoelectric energy harvester with ultra-low power management circuit, IEEE Trans. Instrum. Meas. 64 (11) (2015) 2918–2925, http://dx.doi.org/10.1109/TIM.2015.2444253.

[16] M.W. Roque, Soil Physical-Hydric Attributes Spatial Variability for Different Irrigated Bean Tillage Systems, University of Campinas, 2007, Ph.D. thesis.

[17] T. Kamai, G.J. Kluitenberg, J.W. Jopmans, Design and numerical analysis of a button type heat pulse probe for soil water content measurement, Vadose J. 8 (2009) 167–173.

[18] A. Chanzy, J-C. Gaudu, Olivier Marloie, Correcting the temperature influence of soil capacitance sensors using diurnal temperature and water content cycles, Sensors 12 (2012) 9773–9790, http://dx.doi.org/10.3390/s120709773.

[19] A.L. Flint, G.S. Campbell, K.M. Ellett, C. Calissendorff, Calibration and temperature correction of heat dissipation matric potential sensors, Soil Sci. Soc. Am. J. 66 (2002) 1439–1445.

Biographies

Pedro Carvalhaes Dias received the received the B.S. degree from Unisal, Campinas, SP, Brazil, and the M.Sc. and Ph.D. degrees from FEEC/UNICAMP, Campinas, SP, Brazil, all in electrical engineering. He is currently a postdoctorate researcher at the Centro de Componentes Semicondutores e Nanopartículas and at the Department of Semiconductors, Instruments and Photonics – School of Electrical and Computer Engineering, FEEC/UNICAMP, in cooperation with the Catalonia Institute for Energy Research – IREC, Barcelona, Spain. His main research interests are in electronics instrumentation, embedded systems, energy harvesting, applications of nanostructured materials and sensors.

Doris Cadavid received the B.Sc. in Physics at National University of Colombia in 2005, and she continued her M.Sc. studies in Physics at the same university until 2008. She was a research assistant during two years at Atomic Center Bariloche – Argentina. She obtained her Ph.D. degree in March 2014 at the University of Barcelona, her research was focused in the solution processed bottom-up strategy for the production of efficient thermoelectric nanostructured materials. Since June 2014 she is a research engineer in the Advanced Materials Department at the Catalonia Institute for Energy Research - IREC. Her research interest is the production and characterization of nanostructured materials with different electronic, structural and thermal properties for the application in the field of energy conversion and storage.

Silvia Ortega graduated in Physics in 2012 and received her M.Sc. in Nanotechnology from the University of Barcelona. In 2014 she received a fellowship to enroll an industrial PhD program between the Functional Nanomaterials Group in the Catalonia Institute for Energy Research – IREC and the company CIDETE Ingenieros S.L. in Barcelona. Since then, her field of work is the preparation and characterization of solution processed bottom-up thermoelectric materials and the design of new thermoelectric modules.

Alejandro Ruiz Romeu graduated in Physics in 2012 and received his M.Sc. in Nanoscience and Nanotechnology in 2013 both at the University of Barcelona. In 2013 started a Ph.D. program between the Functional Nanomaterials Group in the Catalonia Institute for Energy Research – IREC and the Politechnic University of Catalonia – UPC. Since then, his field of work is the research on perovskite and nanostructured solar cells and their characterization.

Maria Bernadete de Morais França received the B.S. and the M.Sc. from the Federal University of Campina Grande, Campina, PB, Brazil in 1996 and 1998, and the Ph.D. from the School of Electrical and Computer Engineering, FEEC/UNICAMP, all in electrical engineering. She is a Professor and Researcher at the Laboratory of Automation and Intelligent Instrumentation in the State University of Londrina, PR, Brazil. Her current research interests include electronic instrumentation, microelectronics, and sensors for precision agriculture.

Flavio José Oliveira Morais received the B.S. degree in Computing Engineering from PUC of Goiás in 2009 and the M.Sc. degree in Electrical Engineering from FEEC/UNICAMP in 2011. He is currently working toward the Ph.D. degree in Electrical Engineering at the School of Electrical and Computer Engineering, FEEC/UNICAMP. His main research interests are in electronics instrumentation, energy metering, embedded systems, energy harvesting, and sensors networks.

Elnatan C. Ferreira received the B.S. degree in physics from University of Ceará, CE, Brazil in 1981, and the M.S. and the Ph.D. degrees in electrical engineering from University of Campinas, UNICAMP, respectively in 1984 and 1991. He joined the School of Electrical and Computer Engineering FEEC/UNICAMP as a Teaching Assistant in 1985, where he is currently an Associate Professor at the Department of Electronics and Microelectronics. His research interests include electronic instrumentation, signal processing, fiber optics gyroscopes and fiber optics sensors.

Andreu Cabot received his PhD from the University of Barcelona in 2003. From 2004 to 2007, he worked as a postdoctoral researcher in Prof. A. Paul Alivisatos group in the University of California at Berkeley and the Lawrence Berkeley National Laboratory. In 2009 he formed the Functional Nanomaterials Group and joined the Catalonia Institute for Energy Research – IREC, where he is currently ICREA Research Professor. His research interests include the design and preparation of nanomaterials, the characterization of their functional properties and their use in the field of energy conversion.

Conclusions

This dissertation has been focused in three main topics: i) synthesis and engineering of NP-building blocks for the production of efficient TE nanocomposites; ii) TE device fabrication; iii) integration of TE devices and solution-processed NPs. These topics are englobed and follow the reviewed strategy for the production of bottom-up engineering of TE nanomaterials and devices from solution-processed NP building blocks. The main conclusions that can be drawn for all the prior works are:

1. Solution-processed NPs are useful for the production of bulk TE nanomaterials and nanocomposites.

2. Taking advantage of the chemical engineering of the NPs surface is possible to improve the TE performance of the nanomaterials.

3. Strategies on nanocomposite formation presented, heterostructured NPs and blending of NPs, allow the enhancement of TE properties of the materials in a facile and straightforward way.

4. Electronic doping can be accomplished by the assembly of proper combinations of solution-processed NPs.

5. Solution-processed NPs can be used for the fabrication of TE devices with multiple architectures.

6. The production of TE nanomaterials from NP building blocks present many challenges, but also many possibilities to precisely control the parameters of the materials and thus optimize the performance.

Future work

I have been lucky to work during my PhD thesis in two exciting fields, the design and engineering of nanomaterials from the bottom-up assembly of colloidal NPs, and TE. When combined, the emerging technology is even more attracting and full of possibilities, although still in its very initial stages. A lot of work is thus needed for its further development.

As far as I am concerned, I plan to continue my research in the following directions:

1. Extending the chemical engineering of the NPs surface and the assembly routes for the fabrication of nanocomposites to other materials more environmentally friendly.

2. Developing other TE devices with different flexible or conformable architectures, based on our solution-processed NP-based nanomaterials.

3. Proving the suitability of the solution-processed route for the fabrication of TE devices and push for its introduction to the market.

References

1. EC 2020 Energy Strategy, https://ec.europa.eu/energy/sites/ener/files/documents/2011_energy2020_en_0.pdf.
2. 2012 Energy Efficiency Directive, http://eur-lex.europa.eu/legal-content/EN/TXT/?qid=1399375464230&uri=CELEX:32012L0027.
3. 2016 LLNL Energy Flow Chart, https://flowcharts.llnl.gov/.
4. D. M. Rowe, ed., *Thermoelectrics Handbook: Macro to Nano*, CRC Press: Boca Raton, FL, 2006.
5. A. Ziabari, M. Zebarjadi, D. Vashaee and A. Shakouri, *Reports on Progress in Physics*, 2016, 79, 095901.
6. Q. H. Zhang, X. Y. Huang, S. Q. Bai, X. Shi, C. Uher and L. D. Chen, *Advanced Engineering Materials*, 2016, 18, 194-213.
7. Sub-watt thermoelectric energy harvesting: industry and market analysis, http://www.infinergia.com/en/services-market-research.
8. M. G. Kanatzidis, *MRS Bulletin*, 2015, 40, 687-695.
9. Gentherm Global Power, http://www.genthermglobalpower.com/.
10. D. Champier, *Energy Conversion and Management*, 2017, 140, 167-181.
11. S. Twaha, J. Zhu, Y. Yan and B. Li, *Renewable and Sustainable Energy Reviews*, 2016, 65, 698-726.
12. X. Zheng, C. Liu, Y. Yan and Q. Wang, *Renewable and Sustainable Energy Reviews*, 2014, 32, 486-503.
13. BioLite Wood Burning Campstove, https://www.amazon.com/BioLite-BL-CSA-Wood-Burning-Campstove/dp/B00BQHET9O.
14. Nabla Thermoelectrics, http://www.nablatherm.com/.
15. Definitiv-box, https://definitiv-box.de/.
16. J.-H. Bahk, H. Fang, K. Yazawa and A. Shakouri, *Journal of Materials Chemistry C*, 2015, 3, 10362-10374.

17. M. H. Elsheikh, D. A. Shnawah, M. F. M. Sabri, S. B. M. Said, M. H. Hassan, M. B. A. Bashir and M. Mohamad, *Renewable and Sustainable Energy Reviews*, 2014, 30, 337-355.

18. IDTechEx report Thermoelectric Energy Harvesting 2012-2022. Updated 2016-2026, http://www.idtechex.com/research/reports/thermoelectric-energy-harvesting-2016-2026-000473.asp.

19. Y. Chen, Y. Zhao and Z. Liang, *Energy & Environmental Science*, 2015, 8, 401-422.

20. S. J. Kim, J. H. We and B. J. Cho, *Energy & Environmental Science*, 2014, 7, 1959-1965.

21. J. Y. Oh, J. H. Lee, S. W. Han, S. S. Chae, E. J. Bae, Y. H. Kang, W. J. Choi, S. Y. Cho, J.-O. Lee and H. K. Baik, *Energy & Environmental Science*, 2016, 9, 1696-1705.

22. K. Yazawa and A. Shakouri, *Environmental science & technology*, 2011, 45, 7548-7553.

23. S. LeBlanc, S. K. Yee, M. L. Scullin, C. Dames and K. E. Goodson, *Renewable and Sustainable Energy Reviews*, 2014, 32, 313-327.

24. C. B. Vining, *Nature Materials*, 2009, 8, 83-85.

25. L. E. Bell, *Science*, 2008, 321, 1457-1461.

26. G. J. Snyder and E. S. Toberer, *Nature Materials*, 2008, 7, 105-114.

27. C. Goupil, W. Seifert, K. Zabrocki, E. Müller and G. J. Snyder, *Entropy*, 2011, 13, 1481-1517.

28. L.-D. Zhao, S.-H. Lo, Y. Zhang, H. Sun, G. Tan, C. Uher, C. Wolverton, V. P. Dravid and M. G. Kanatzidis, *Nature*, 2014, 508, 373-377.

29. A. Shakouri, *Annual Reviews of Materials Research*, 2011, 41, 399-431.

30. Northwestern Thermoelectrics Group, http://thermoelectrics.matsci.northwestern.edu/thermoelectrics/history.html.

31. L. D. Hicks and M. S. Dresselhaus, *Physical Review B*, 1993, 47, 12727-12731.

32. L. D. Hicks and M. S. Dresselhaus, *Physical Review B*, 1993, 47, 16631-16634.

33. G. A. Slack and D. M. Rowe, *CRC Handbook of Thermoelectrics*, 1995.

34. Alphabet Energy, https://www.alphabetenergy.com/.

35. Otego, http://www.otego.de/en/index.php.

36. Marlow, http://www.marlow.com.

37. Thermonamic, http://www.thermonamic.com/.

38. D. K. Aswal, R. Basu and A. Singh, *Energy Conversion and Management*, 2016, 114, 50-67.

39. T. Zhu, Y. Liu, C. Fu, J. P. Heremans, J. G. Snyder and X. Zhao, *Advanced Materials*, 2017.

40. W. Liu, X. Yan, G. Chen and Z. Ren, *Nano Energy*, 2012, 1, 42-56.

41. G. Tan, L.-D. Zhao and M. G. Kanatzidis, *Chemical Reviews*, 2016, 116, 12123-12149.

42. W. Kim, J. Zide, A. Gossard, D. Klenov, S. Stemmer, A. Shakouri and A. Majumdar, *Physical Review Letters*, 2006, 96, 045901.

43. M. Beekman, D. T. Morelli and G. S. Nolas, *Nature Materials*, 2015, 14, 1182-1185.

44. J. R. Sootsman, D. Y. Chung and M. G. Kanatzidis, *Angewandte Chemie Interntional Edition*, 2009, 48, 8616-8639.

45. C. J. Vineis, A. Shakouri, A. Majumdar and M. G. Kanatzidis, *Advanced Materials*, 2010, 22, 3970-3980.

46. M. Zebarjadi, K. Esfarjani, M. S. Dresselhaus, Z. F. Ren and G. Chen, *Energ. Environ. Sci.*, 2012, 5, 5147-5162.

47. A. J. Minnich, M. S. Dresselhaus, Z. F. Ren and G. Chen, *Energy & Environmental Science*, 2009, 2, 466-479.

48. K. Biswas, J. He, I. D. Blum, C.-I. Wu, T. P. Hogan, D. N. Seidman, V. P. Dravid and M. G. Kanatzidis, *Nature*, 2012, 489, 414-418.

49. D. Wu, L.-D. Zhao, X. Tong, W. Li, L. Wu, Q. Tan, Y. Pei, L. Huang, J.-F. Li and Y. Zhu, *Energy & Environmental Science*, 2015, 8, 2056-2068.

50. R. Venkatasubramanian, E. Siivola, T. Colpitts and B. O'Quinn, *Nature*, 2001, 413, 597-602.

51. T. C. Harman, P. J. Taylor, M. P. Walsh and B. E. LaForge, *Science*, 2002, 297, 2229-2232.

52. D.-K. Ko, Y. Kang and C. B. Murray, *Nano letters*, 2011, 11, 2841-2844.

53. J. P. Heremans, V. Jovovic, E. S. Toberer, A. Saramat, K. Kurosaki, A. Charoenphakdee, S. Yamanaka and G. J. Snyder, *Science*, 2008, 321, 554-557.

54. M. Orrill and S. LeBlanc, *Journal of Applied Polymer Science*, 2016.

55. K. F. Hsu, S. Loo, F. Guo, W. Chen, J. S. Dyck, C. Uher, T. Hogan, E. K. Polychroniadis and M. G. Kanatzidis, *Science*, 2004, 303, 818-821.

56. J. Yang, H. L. Yip and A. K. Y. Jen, *Advanced Energy Materials*, 2013, 3, 549-565.

57. B. Poudel, Q. Hao, Y. Ma, Y. Lan, A. Minnich, B. Yu, X. Yan, D. Wang, A. Muto, D. Vashaee, X. Chen, J. Liu, M. S. Dresselhaus, G. Chen and Z. Ren, *Science*, 2008, 320, 634-638.

58. M. Rull-Bravo, A. Moure, J. Fernandez and M. Martin-Gonzalez, *RSC Advances*, 2015, 5, 41653-41667.

59. W.-S. Liu, B.-P. Zhang, J.-F. Li, H.-L. Zhang and L.-D. Zhao, *Journal of Applied Physics*, 2007, 102, 103717.

60. Matres, http://www.matres.org/Sito/Home.html.

61. C.-L. Chen, H. Wang, Y.-Y. Chen, T. Day and G. J. Snyder, *Journal of Materials Chemistry A*, 2014, 2, 11171-11176.

62. S. K. Yee, S. LeBlanc, K. E. Goodson and C. Dames, *Energy & Environmental Science*, 2013, 6, 2561-2571.

63. S. LeBlanc, *Sustainable Materials and Technologies*, 2014, 1, 26-35.

64. M. Ibáñez, D. Cadavid, U. Anselmi-Tamburini, R. Zamani, S. Gorsse, W. Li, A. M. López, J. R. Morante, J. Arbiol and A. Cabot, *Journal of Materials Chemistry A*, 2013, 1, 1421-1426.

65. M. Ibáñez, R. Zamani, W. Li, D. Cadavid, S. Gorsse, N. A. Katcho, A. Shavel, A. M. López, J. R. Morante, J. Arbiol and A. Cabot, *Chemistry of Materials.*, 2012, 24, 4615–4622.

66. M. Ibáñez, R. Zamani, A. Lalonde, D. Cadavid, W. Li, A. Shavel, J. Arbiol, J. R. Morante, S. Gorsse, G. J. Snyder and A. Cabot, *Journal of the American Chemical Society*, 2012, 134, 4060-4063.

67. M. Ibáñez, D. Cadavid, R. Zamani, N. García-Castelló, V. Izquierdo-Roca, W. Li, A. Fairbrother, J. D. Prades, A. Shavel, J. Arbiol, A. Pérez-Rodríguez, J. R. Morante and A. Cabot, *Chemistry of Materials*, 2012, 24, 562-570.

68. M. Scheele, N. Oeschler, I. Veremchuk, S.-O. Peters, A. Littig, A. Kornowski, C. Klinke and H. Weller, *ACS Nano*, 2011, 5, 8541-8551.

69. M. V. Kovalenko, B. Spokoyny, J.-S. Lee, M. Scheele, A. Weber, S. Perera, D. Landry and D. V. Talapin, *Journal of the American Chemical Society*, 2010, 132, 6686-6695.

70. M. Scheele, N. Oeschler, K. Meier, A. Kornowski, C. Klinke and H. Weller, *Advanced Functional Materials*, 2009, 19, 3476-3483.

71. Y. Yin and A. P. Alivisatos, *Nature*, 2005, 437, 664-670.

72. C. B. Murray, C. R. Kagan and M. G. Bawendi, *Annual Review of Materials Research*, 2000, 30, 545-610.

73. J. Y. Rempel, M. G. Bawendi and K. F. Jensen, *Journal of the American Chemical Society*, 2009, 131, 4479-4489.

74. M. Ibáñez and A. Cabot, *Science*, 2013, 340, 935-936.

75. Y. Liu, G. García, S. Ortega, D. Cadavid, P. Palacios, J. Lu, M. Ibáñez, L. Xi, J. D. Roo, A. M. López, S. Martí-Sánchez, I. Cabezas, M. d. l. Mata, Z. Luo, C. Dun, O. Dobrozhan, D. L. Carroll, W. Zhang, J. Martins, M. V. Kovalenko, J. Arbiol, G. Noriega, J. Song, P. Wahnón and A. Cabot, *Journal of Materials Chemistry* A, 2016, 5, 2592-2602.

76. A. Shavel, D. Cadavid, M. Ibáñez, A. Carrete and A. Cabot, *Journal of the American Chemical Society*, 2012, 134, 1438-1441.

77. Y. Liu, D. Cadavid, M. Ibáñez, J. De Roo, S. Ortega, O. Dobrozhan, M. V. Kovalenko and A. Cabot, *Journal of Materials Chemistry C*, 2016, 4, 4756-4762.

78. M. V. Kovalenko, L. Manna, A. Cabot, Z. Hens, D. V. Talapin, C. R. Kagan, V. I. Klimov, A. L. Rogach, P. Reiss and D. J. Milliron, *ACS Nano*, 2015, 9, 1012-1057.

79. D. V. Talapin, J.-S. Lee, M. V. Kovalenko and E. V. Shevchenko, *Chemical Reviews*, 2010, 110, 389-458.

80. M.-R. Gao, Y.-F. Xu, J. Jiang and S.-H. Yu, *Chemical Society Reviews*, 2013, 42, 2986-3017.

81. C. Coughlan, M. Ibáñez, O. Dobrozhan, A. Singh, A. Cabot and K. M. Ryan, *Chemical Reviews*, 2017.

82. A. Nurmikko, *Nature Nanotechnology*, 2015, 10, 1001-1004.

83. M. V. Kovalenko, *Nature Nanotechnology*, 2015, 10, 994-997.

84. S. Carregal-Romero, P. Guardia, X. Yu, R. Hartmann, T. Pellegrino and W. J. Parak, *Nanoscale*, 2015, 7, 570-576.

85. W. Li, R. Zamani, P. Rivera Gil, B. Pelaz, M. Ibáñez, D. Cadavid, A. Shavel, R. A. Alvarez-Puebla, W. J. Parak, J. Arbiol and A. Cabot, *ournal of the American Chemical Society*, 2013, 135, 7098-7101.

86. C. R. Kagan, E. Lifshitz, E. H. Sargent and D. V. Talapin, *Science*, 2016, 353, aac5523.

87. S. W. Finefrock, H. Yang, H. Fang and Y. Wu, *Annual review of chemical and biomolecular engineering*, 2015, 6, 247-266.

88. R. J. Mehta, Y. Zhang, C. Karthik, B. Singh, R. W. Siegel, T. Borca-Tasciuc and G. Ramanath, *Nature Materials*, 2012, 11, 233-240.

89. T. Varghese, C. Hollar, J. Richardson, N. Kempf, C. Han, P. Gamarachchi, D. Estrada, R. J. Mehta and Y. Zhang, *Scientific Reports*, 2016, 6.

90. S. H. Park, S. Jo, B. Kwon, F. Kim, H. W. Ban, J. E. Lee, D. H. Gu, S. H. Lee, Y. Hwang and J.-S. Kim, *Nature Communications*, 2016, 7.

91. Z. Lu, M. Layani, X. Zhao, L. P. Tan, T. Sun, S. Fan, Q. Yan, S. Magdassi and H. H. Hng, *Small*, 2014, 10, 3551-3554.

92. D. Liang, H. Yang, S. W. Finefrock and Y. Wu, *Nano letters*, 2012, 12, 2140-2145.

93. S. Ortega, M. Ibáñez, Y. Liu, Y. Zhang, D. Cadavid and A. Cabot, *Chemical Society Reviews*, 2017.

94. S. Ortega, M. Ibáñez, D. Cadavid and A. Cabot, *International Journal of Nanotechnology*, 2014, 11, 955-970.

95. M. Ibáñez, R. J. Korkosz, Z. Luo, P. Riba, D. Cadavid, S. Ortega, A. Cabot and M. G. Kanatzidis, *Journal of the American Chemical Society*, 2015, 137, 4046-4049.

96. M. Ibáñez, Z. Luo, A. Genç, L. Piveteau, S. Ortega, D. Cadavid, O. Dobrozhan, Y. Liu, M. Nachtegaal, M. Zebarjadi, J. Arbiol, M. V. Kovalenko and A. Cabot, *Nature Communications*, 2016, 7, 10766.

97. S. N. Girard, J. He, X. Zhou, D. Shoemaker, C. M. Jaworski, C. Uher, V. P. Dravid, J. P. Heremans and M. G. Kanatzidis, *Journal of the American Chemical Society*, 2011, 133, 16588-16597.

98. J. Androulakis, C.-H. Lin, H.-J. Kong, C. Uher, C.-I. Wu, T. Hogan, B. A. Cook, T. Caillat, K. M. Paraskevopoulos and M. G. Kanatzidis, *Journal of the American Chemical Society*, 2007, 129, 9780-9788.

99. S. N. Girard, K. Schmidt-Rohr, T. C. Chasapis, E. Hatzikraniotis, B. Njegic, E. M. Levin, A. Rawal, K. M. Paraskevopoulos and M. G. Kanatzidis, *Advanced Funtional Materials*, 2013, 23, 747-757.

100. L.-D. Zhao, S.-H. Lo, J. He, H. Li, K. Biswas, J. Androulakis, C.-I. Wu, T. P. Hogan, D.-Y. Chung and V. P. Dravid, *Journal of the American Chemical Society*, 2011, 133, 20476-20487.

101. M. Ibáñez, R. Zamani, S. Gorsse, J. Fan, S. Ortega, D. Cadavid, J. R. Morante, J. Arbiol and A. Cabot, *ACS Nano*, 2013, 7, 2573-2586.

102. A. Nag, H. Zhang, E. Janke and D. V. Talapin, *Zeitschrift für Physikalische Chemie*, 2015, 229, 85-107.

103. J. Androulakis, D.-Y. Chung, X. Su, L. Zhang, C. Uher, T. C. Hasapis, E. Hatzikraniotis, K. M. Paraskevopoulos and M. G. Kanatzidis, *Physical Review B*, 2011, 84, 155207.

104. Z. Quan, Z. Luo, W. S. Loc, J. Zhang, Y. Wang, K. Yang, N. Porter, J. Lin, H. Wang and J. Fang, *Journal of the American Chemical Society*, 2011, 133, 17590-17593.

105. J. Androulakis, I. Todorov, J. He, D.-Y. Chung, V. Dravid and M. Kanatzidis, *Journal of the American Chemical Society*, 2011, 133, 10920-10927.

106. Y. Liu, D. Cadavid, M. Ibáñez, S. Ortega, S. Martí-Sánchez, O. Dobrozhan, M. V. Kovalenko, J. Arbiol and A. Cabot, *APL Materials*, 2016, 4, 104813.
107. G. Min and D. M. Rowe, *Semiconductor Science and Technology*, 2007, 22, 880.
108. A. Schmitz, C. Stiewe and E. Müller, *Journal of electronic materials*, 2013, 42, 1702.
109. J. Baek, P. M. Allen, M. G. Bawendi and K. F. Jensen, *Angewandte Chemie Interntional Edition*, 50, 627-630.

CURRICULUM VITAE

Silvia Ortega Torres

Born in 16th October 1987 in Barcelona. Physicist and science passionate. I strongly believe in technology transfer from the lab to the industry.

Passatge de la Pau, 5, 1-1
08970 Sant Joan Despí
Barcelona – Spain

Tel.: +34 619607177
silvia.ortega.torres@gmail.com
sortega@irec.cat
sortega@cidete.com

Academic Qualifications

2012-2013	Master in Nanoscience and Nanotechnology. University of Barcelona. Thesis: Bottom-up processing of efficient thermoelectric materials. Supervisor: Prof. Dr. Andreu Cabot and Dr. Maria Ibáñez. Overall average: 9.3 (5-10)
2012-2013	Postgraduate in Project Management. National Distance Education University – UNED.
2006-2012	Bachelor in Physics. University of Barcelona Overall average: 7.38 (5-10)

Research Interests

After finishing my Bachelor in Physics, I joint IREC to develop my Master thesis in the field of thermoelectrics, as a part of the Nanoscience and Nanotechnology Master program. This topic has become the aim of my research career and my passion. During my day-by-day working, I put all my efforts to make this technology a more efficient one, pursuing its definitive market widespread and, above all, contributing for a more sustainable energy production. My field of work is the preparation and characterization of solution-processed bottom-up thermoelectric materials, the design of new thermoelectric modules and their application for cooling and energy harvesting.

Professional Experience

2013 – Present   Technical Project Manager
                     CIDETE Ingenieros S.L.
                     Vilanova i la Geltrú, Barcelona – Spain

2010 – 2011   Private Tutor
                     El Sol Blau, Pedagogical Association
                     Molins de Rei, Barcelona – Spain

2007   Private Tutor
                     Aula d'Estudi, Study Advice
                     Barcelona – Spain

Participation in Research Projects

In my present position, I have fully participated in the following research projects funded by the European Commission. My main tasks are hereby described.

JOSPEL – Low Energy Passenger Comfort Systems Based on the Joule and Peltier Effects. May 2015 – present. H2020. http://jospel-project.eu/
Coordinator: Dr. Begoña Galindo. AIMPLAS, Plastics Technology Centre.
Main task(s): Development of a low consumption thermoelectrics-based AC system of an electric vehicle.

EDEN – High Energy Density Mg-Based Metal Hydrides Storage System. March 2013 – July 2016. FP7. http://www.h2eden.eu/
Coordinator: Dr. Luigi Crema. Bruno Kessler Foundation.
Main task(s): Thermal management of the autonomous hydrogen storage system. Coordination of the demonstration activities of the technology in the city of Barcelona with the collaboration of the Barcelona Energy Agency.

UNION – Ultra-Versatile Nanoparticle Integration into Organized Nanoclusters. March 2013 – January 2016. FP7. http://www.fp7-union.eu/
Coordinator: Prof. Dr. Dermot Brougham. Dublin City University.
Main task(s): Fabrication of a thermoelectric device from solution-processed engineered nanoclusters. Coordination of the dissemination activities within the project.

MERGING – Membrane-Based Phonon Engineering for Energy Harvesting. March 2013 – December 2015. FP7. http://www.merging.eu/
Coordinator: Prof. Dr. Clivia Sotomayor. Catalan Institute of Nanoscience and Nanotechnology.
Main task(s): Design of the integration route for a membrane-based thermoelectric device.

NEXTEC – Next Generation Nano-Engineered Thermoelectric Converters – From Concept to Industrial Validation. March 2013 – May 2014. FP7.
http://cordis.europa.eu/project/rcn/99282_en.html
Coordinator: Prof. Dr. Mamoun Muhammed. KTH Royal Institute of Technology.
Main task(s): Development and fabrication of a ring-shaped thermoelectric generator for SEAT car exhausts.

Scientific Production

Title: Influence of the ligand striping on the transport properties of nanoparticle-based PbSe bulk nanomaterials
Author(s): Doris Cadavid, Silvia Ortega, Sergio Illera, Yu Liu, Oscar Juan Durá, Maria Ibáñez, Alexey Shavel, Yu Zhang, Antonio M. López, M. A. López de la Torre, Joan Daniel Prades, Germán Noriega, Maksym V. Kovalenko and Andreu Cabot
Citation: ACS Appl. Mater. Interfaces, 2017, Submitted.

Title: Bottom-up engineering of thermoelectric nanomaterials and devices from solution-processed nanoparticle building blocks
Author(s): Silvia Ortega, Maria Ibáñez, Yu Liu, Yu Zhang, Maksym V. Kovalenko, Doris Cadavid and Andreu Cabot
Citation: Chem. Soc. Rev., 2017, DOI: 10.1039/c6cs00567e.

Title: Solution-based synthesis and processing of Sn- and Bi-doped Cu_3SbSe_4 nanocrystals, nanomaterials and ring-shaped thermoelectric generators
Author(s): Yu Liu, Gregorio García, Silvia Ortega, Doris Cadavid, Pablo Palacios, Jinyu Lu, Maria Ibáñez, Lili Xi, Jonathan De Roo, Antonio M. López, Sara Martí-Sánchez, Ignasi Cabezas, María de la Mata, Zhishan Luo, Chaochao Dun, Oleksandr Dobrozhan, David L. Carroll, Wenqing Zhang, José Martins, Maksym V. Kovalenko, Jordi Arbiol, Germán Noriega, Jiming Song, Perla Wahnón and Andreu Cabot
Citation: J. Mater. Chem. A, 2017, 5, 2592-2602.

Title: High-performance thermoelectric nanocomposites from nanocrystal building blocks
Author(s): Maria Ibáñez, Zhishan Luo, Aziz Genç, Laura Piveteau, Silvia Ortega, Doris Cadavid, Oleksandr Dobrozhan, Yu Liu, Maarten Nachtegaal, Mona Zebarjadi, Jordi Arbiol, Maksym V Kovalenko and Andreu Cabot
Citation: Nat. Commun., 2016, 7, 10766.

Title: Colloidal $AgSbSe_2$ nanocrystals: surface analysis, electronic doping and processing into thermoelectric materials
Author(s): Yu Liu, Doris Cadavid, Maria Ibáñez, Jonathan de Roo, Silvia Ortega, Oleksandr Dobrozhan, Maksym V Kovalenko and Andreu Cabot
Citation: J. Mat. Chem. C, 2016, 4 (21), 4756-4762.

Title: Thermoelectric properties of semiconductor-metal composites produced by particle blending
Author(s): Yu Liu, Doris Cadavid, Maria Ibáñez, Silvia Ortega, Sara Martí-Sánchez, Oleksandr Dobrozhan, Maksym V Kovalenko, Jordi Arbiol and Andreu Cabot
Citation: APL Mater., 2016, 4, 104813.

Title: Autonomous soil moisture sensor based on nanostructured thermosensitive resistors powered by an integrated thermoelectric generator
Author(s): Pedro C Dias, Doris Cadavid, Silvia Ortega, Alejandro Ruiz, Maria Bernadete M França, Flavio JO Morais, Elnatan C Ferreira and Andreu Cabot
Citation: Sens. Actuators A, 2016, 239, 1–7.

Title: Electron Doping in Bottom-Up Engineered Thermoelectric Nanomaterials through HCl-Mediated Ligand Displacement.
Author(s): Maria Ibáñez, Rachel J. Korkosz, Zhishan Luo, Pau Riba, Doris Cadavid, Silvia Ortega, Andreu Cabot and Mercouri G. Kanatzidis.
Citation: J. Am. Chem. Soc., 2015, 137, pp 4046-4049.

Title: Bottom-Up Processing of PbTe-PbS Thermoelectric Nanocomposites
Author(s): Silvia Ortega, Maria Ibáñez, Doris Cadavid and Andreu Cabot.
Citation: Int. J. Nanotechnol., 2014, 11, pp 955-970.

Title: Core-Shell Nanoparticles as Building Blocks for the Bottom-Up Production of Functional Nanocomposites: PbTe-PbS Thermoelectric Properties
Author(s): Maria Ibáñez, Reza Zamani, Stéphane Gorsse, Jiandong Fan, Silvia Ortega, Doris Cadavid, Joan Ramon Morante, Jordi Arbiol and Andreu Cabot.
Citation: ACS Nano, 2013, 7 (3), pp 2573-2586.

Participation in Conferences

E-MRS 2017 Spring Meeting – May 2017, Strasbourg – France.
Oral Presentation: Nanomaterial-solutions to shape-adaptable thermoelectric devices.

Improving Energy Efficiency in Electric Vehicles Workshop. November 2016, Bologna – Italy.
Oral Presentation: Thermoelectric cooling. Thermoelectrics for a low energy thermal management.

Summer Thermoelectrics School. July 2016, Golden – Colorado. USA.

Autumn Thermoelectrics School. October 2015, Duisburg – Germany.

Hydrogen Storage: A Key Element for Future Energy Systems. November 2015, Trento – Italy.

34th Annual International Conference on Thermoelectrics and 13th European Conference on Thermoelectrics – July 2015, Dresden – Germany.
Oral Presentation: Solution-Processed Enhanced Thermoelectric Nanocomposites – From Materials to Devices.

Thermoelectrics Industry Workshop "Ultra-versatile Nanoparticle Integration into Organized Nano-clusters" – June 2015, Barcelona – Spain.

12th European Conference on Thermoelectrics – September 2014, Madrid – Spain.
Poster Presentations: Bottom-Up Bulk Thermoelectric Materials, Ultra-Versatile Nanoparticle Integration into Organized Nanoclusters

IX Barcelona Global Energy Challenges – June 2014, Barcelona – Spain.

E-MRS 2013 Spring Meeting – May 2013, Strasbourg – France.

Other Research Merits and Awards

InnoEnergy PhD School grant. InnoEnergy Knowledge Innovation Community, 2016.

Industrial Doctorates program grant 2014 DI-10. AGAUR, Catalonia Government.

Co-supervisor of the Master student Edson Johan Uribe under the framework of the Renewable and Sustainable Energy Master program, University of Barcelona. 2013-2014. Title: Flexible Thermoelectric Modules. Supervisors: Prof. Dr. Andreu Cabot and Silvia Ortega.

Additional Training

June 2017, Entrepreneurship Summer School. ESADE, Barcelona – Spain.

March 2017, R&D Management: Technology transfer, innovation and entrepreneurship. University of Barcelona, Barcelona – Spain.

Autumn 2015, Project Management and Transversal Skills: Leadership, coordination, project management and negotiation. DI – Knowledge Innovation Market – KIM. Barcelona – Spain.

Languages

Spanish: Native

Catalan: Native

English: CEFR C1 Level. School of Modern Languages. University of Barcelona, 2013.